AEROELASTIC STABILITY PREDICTION USING FLUTTER FLIGHT TEST DATA

A THESIS SUBMITTED TO
THE GRADUATE SCHOOL OF NATURAL AND APPLIED SCIENCES
OF
MIDDLE EAST TECHNICAL UNIVERSITY

BY

ERDİNÇ NURİ YILDIZ

IN PARTIAL FULFILLMENT OF THE REQUIREMENTS
FOR
THE DEGREE OF DOCTOR OF PHILOSOPHY
IN
MECHANICAL ENGINEERING

JULY 2007

Approval of the thesis:

AEROELASTIC STABILITY PREDICTION USING FLUTTER FLIGHT TEST DATA

submitted by **ERDİNÇ NURİ YILDIZ** in partial fulfillment of the requirements for the degree of **Doctor of Philosophy in Mechanical Engineering Department, Middle East Technical University** by,

Prof. Dr. Canan Özgen _____
Dean, Graduate School of **Natural and Applied Sciences**

Prof. Dr. Kemal İder _____
Head of Department, **Mechanical Engineering**

Prof. Dr. Bülent E. Platin _____
Supervisor, **Mechanical Engineering Dept., METU**

Dr. Mutlu D. Cömert _____
Co-Supervisor, **TÜBİTAK-SAGE**

Examining Committee Members:

Prof. Dr. Tuna Balkan _____
Mechanical Engineering Dept., METU

Prof. Dr. Bülent E. Platin _____
Mechanical Engineering Dept., METU

Dr. Mutlu D. Cömert _____
Chief Researcher, TÜBİTAK-SAGE

Prof. Dr. Yavuz Yaman _____
Aerospace Engineering Dept., METU

Assoc. Prof. Dr. M. Önder Efe _____
Electric and Electronics Engineering Dept., TOBB-ETU

Date: 23.07.2007

I hereby declare that all information in this document has been obtained and presented in accordance with academic rules and ethical conduct. I also declare that, as required by these rules and conduct, I have fully cited and referenced all material and results that are not original to this work.

Name, Last name :

Signature :

ABSTRACT

AEROELASTIC STABILITY PREDICTION USING FLUTTER FLIGHT TEST DATA

Yıldız, Erdinç Nuri
Ph.D., Department of Mechanical Engineering
Supervisor : Prof. Dr. Bülent E. Platin
Co-Supervisor: Dr. Mutlu D. Cömert

July 2007, 224 pages

Flutter analyses and tests are the major items in flight certification efforts required when a new air vehicle is developed or when a new external store is developed for an existing aircraft. The flight envelope of a new aircraft as well as the influence of aircraft modifications on an existing flight envelope can be safely determined only by flutter tests. In such tests, the aircraft is instrumented by accelerometers and exciters. Vibrations of the aircraft at specific dynamic pressures are measured and transmitted to a ground station via telemetry systems during flutter tests. These vibration data are analyzed online by using a flutter test software with various methods implemented in order to predict the safety margin with respect to flutter. Tests are performed at incrementally increasing dynamic pressures and safety regions of the flight envelope are determined step by step. Since flutter is a very destructive instability, tests are performed without getting too close to the flutter speed and estimations are performed by extrapolation.

In this study, pretest analyses and flutter prediction methods that can be used in various flight conditions are investigated. Existing methods are improved and their applications are demonstrated with experiments. A novel method to predict limit cycle oscillations that are encountered in some modern fighter aircraft is developed. The prediction method developed in this study can effectively be used in cases where the nonlinearities in aircraft dynamics and air flow reduce the applicability of the classical prediction methods. Some further methods to reduce the adverse effects of these nonlinearities on the predictions are also developed.

Keywords: Flutter, Flutter Test, Flutter Flight Test, Aeroelasticity, Limit Cycle Oscillation.

ÖZ

ÇIRPINTI UÇUŞ TESTİ VERİLERİNİ KULLANARAK AEROELASTİK KARARLILIK KESTİRİMİ

Yıldız, Erdinç Nuri
Doktora, Makina Mühendisliği Bölümü
Tez Yöneticisi : Prof. Dr. Bülent E. Platin
Ortak Tez Yöneticisi : Dr. Mutlu D. Cömert

Temmuz 2007, 224 sayfa

Yeni bir hava aracı geliştirilmesi ya da mevcut bir uçağa yeni harici yükler takılması durumunda yapılması gereken, uçuşa uygunluk çalışmalarının önemli bir maddesini çırpıntı analiz ve testleri oluşturmaktadır. Yeni bir hava aracının uçuş zarfının belirlenmesi yanında mevcut bir hava aracında yapılacak değişikliklerin uçuş zarfına olan etkilerinin belirlenmesi ancak çırpıntı uçuş testleri ile güvenilir bir şekilde gerçekleştirilebilmektedir. Çırpıntı uçuş testlerinde uçak ivmeölçerler ve sarsıcılar ile donatılmaktadır. Uçağın belirli bir dinamik basınç değerlerindeki titreşimleri ölçülmekte ve yer istasyonuna telemetre ile aktarılmaktadır. Bu titreşim verileri bir çırpıntı testi yazılımında bulunan çeşitli yöntemler kullanılarak gerçek zamanda işlenmekte ve çırpıntı emniyet payı uçuş sırasında anında hesaplanmaktadır. Dinamik basınç değeri adım adım arttırılarak bu testler yinelenmekte ve bu şekilde uçuş zarfının güvenli olduğu bölgeler adım adım belirlenmektedir. Çırpıntı olayı son

derece yıkıcı bir karasızlık olduğu için, çırpıntı hızına belirli bir paydan fazla yaklaşılmamakta ve çırpıntı hızı kestirimi ekstrapolasyon ile yapılmaktadır.

Bu çalışmada, uçuş testleri öncesi yapılması gereken ön analizler ve uçuş testlerinde çırpıntı hızının kestirilmesi için çeşitli uçuş koşullarında kullanılabilecek yöntemler incelenmiştir. Mevcut yöntemler iyileştirilmiş ve uygulamaları deneylerle gösterilmiştir. Bunun yanı sıra bazı modern savaş uçaklarında görülen limitli döngü titreşimlerinin kestirilmesi için özgün bir yöntem geliştirilmiştir. Uçak dinamiğinde ve hava akışındaki doğrusalsızlıkların bulunduğu durumlarda birçok klasik kestirim yönteminin uygulanması kısıtlanırken, bu çalışmada geliştirilen yöntem etkin bir şekilde uygulanabilmektedir. Ayrıca, bu doğrusalsızlıkların çırpıntı kestirimine olumsuz etkilerini azaltacak yöntemler de geliştirilmiştir.

Anahtar Kelimeler: Çırpıntı, Çırpıntı Testi, Çırpıntı Uçuş Testi, Aeroelastisite, Limitli Döngü Titreşimi.

TABLE OF CONTENTS

ABSTRACT iv

ÖZ vi

TABLE OF CONTENTS viii

LIST OF TABLES xii

LIST OF FIGURES xiii

LIST OF SYMBOLS AND ABBREVIATIONS xix

CHAPTER

1 INTRODUCTION 1

1.1 General 1

1.2 Scope of the Study 4

1.3 Flutter Flight Test 4

1.4 Historical Overview 5

1.5 Literature Survey 8

1.6 Objectives of the Thesis 10

1.7 Outline of the Thesis 11

2 FLUTTER FLIGHT TEST 12

2.1 Test Techniques 12

2.1.1 Excitation 12

2.1.2 Instrumentation 14

2.1.3 Flutter Prediction 15

2.2 Selection of Best Excitation Points 16

2.3 Selection of Best Measurement Points 17

2.4 Flutter Prediction Methods 18
2.4.1 Damping Extrapolation 18
2.4.1.1 Literature Survey 19
2.4.1.2 Frequency Domain Methods 21
2.4.1.3 Time Domain Methods 22
2.4.1.4 Implementation of Nonlinear Least Squares Fit 23
2.4.1.5 FRF Improvement 24
2.4.1.5.1 Modal Filter 25
2.4.1.5.2 Singular Value Decomposition 26
2.4.2 Envelope Function 27
2.4.2.1 Implementation of Envelope Function 30
2.4.3 Zimmerman-Weissenburger Flutter Margin 30
2.4.3.1 Implementation of Flutter Margin 31
2.4.4 Discrete-Time ARMA Modeling 33
2.4.4.1 Implementation of the ARMA Modeling Method 34
2.4.5 Flutterometer 37
2.4.5.1 Literature Survey 39
2.4.5.2 Nominal Aeroelastic Analysis 40
2.4.5.3 Robust Aeroelastic Analysis 44
2.4.5.4 Incorporating Flight Data 47
2.5 Summary 51
3 SIMULATION STUDIES WITH A LINEAR AEROELASTIC MODEL 53
3.1 Aeroelastic Model 53
3.2 Numerical Study for Mild Flutter 55
3.2.1 Best Measurement Points 59
3.2.2 Best Excitation Points 60
3.2.3 Flutter Prediction with Damping Extrapolation 61
3.2.3.1 Modal Filtering 71
3.2.3.2 Singular Value Decomposition Filtering 76
3.2.4 Flutter Prediction with Envelope Function 78

3.2.5 Flutter Prediction with Flutter Margin 84
3.2.6 Flutter Prediction with ARMA Modeling 87
3.2.7 Flutter Prediction with Flutterometer 92
3.2.7.1 State Space Formulation 92
3.2.7.2 Nominal Flutter Analysis 96
3.2.7.3 Robust Flutter Analysis 98
3.2.7.4 Flutter Prediction 106
3.3 Numerical Study for the ATS 111
3.3.1 Flutter Prediction with Damping Extrapolation 113
3.3.2 Flutter Prediction with Envelope Function 122
3.3.3 Flutter Prediction with Flutter Margin 124
3.3.4 Flutter Prediction with ARMA Modeling 126
3.3.5 Flutter Prediction with Flutterometer 127
3.4 Comparison of Results and Summary 131
4 NONLINEAR AEROELASTIC SYSTEMS 134
4.1 Introduction 134
4.2 Analysis of Nonlinear Aeroelastic Systems 135
4.3 Nonlinear Typical Section Model 138
4.4 LCO Prediction with Wavelet Analysis 142
4.5 Volterra Series 150
4.6 Nonlinear Flutter Prediction 159
4.7 Summary 163
5 EXPERIMENTAL STUDIES 165
5.1 The Aeroservoelastic Test Setup (ATS) 165
5.2 Experiment 169
5.3 Flutter Estimation 175
5.3.1 Flutter Prediction with Damping Extrapolation 178
5.3.2 Flutter Prediction with Envelope Function 184
5.3.3 Flutter Prediction with Flutter Margin 186

5.3.4 Flutter Prediction with ARMA Modeling 187
5.3.5 Flutter Prediction with Flutterometer 188
5.4 Summary 195

6 SUMMARY AND CONCLUSIONS 197

6.1 Summary 197
6.2 Conclusions and Contributions 198
6.3 Recommended Future Work 202

REFERENCES 204

APPENDICES

A Lift and Moment on A Typical Section for Incompressible Flow 210

B Simulink Model 217

CURRICULUM VITAE 224

LIST OF TABLES

Table 1. Mode shapes of the selected typical section. 57
Table 2. Expanded mode shape matrix. 59
Table 3. Summary of modal extraction. 69
Table 4. Results of filtered FRF. 78
Table 5. Envelope function results. 83
Table 6. Flutter Margin results. 86
Table 7. AIC table for various noise order and speed. 87
Table 8. ARMA Modeling results without filtering 89
Table 9. ARMA Modeling results with filtering. 92
Table 10. Physical parameter changes. 107
Table 11. Results for flutterometer. 110
Table 12. Summary of modal extraction. 121
Table 13. Comparison of methods for the mild flutter case. 132
Table 14. Comparison of methods for the ATS case. 133
Table 15. Number of kernels to be identified for sample memory lengths 152
Table 16. Flutterometer solutions. 162
Table 17. Summary of modal extraction. 182
Table 18. Comparison of methods for the real ATS. 195

LIST OF FIGURES

Figure 1. Comparison of critical speeds [1]. 2
Figure 2. Typical frequency response of a two DOF, structurally damped airfoil at various airspeeds [2]. 3
Figure 3. Typical modern flutter flight test process [3]. 6
Figure 4. Von Schlippe's flutter flight test method [3]. 7
Figure 5. LFT system for nominal stability analysis in the μ framework. 44
Figure 6. LFT system for robust stability analysis in the μ framework. 45
Figure 7. Flowchart to generate plant and uncertainty operators from a system model and flight data with the μ method [18]. 49
Figure 8. LFT system for robust stability analysis and model validation. 49
Figure 9. The typical section [1]. 54
Figure 10. Mode shapes of the selected typical section. 57
Figure 11. Pulse response of the selected typical section below the critical speed. 58
Figure 12. Pulse response of the selected typical section above the critical speed. 58
Figure 13. Best measurement points for the model (higher is better). 60
Figure 14. Best excitation points for the model (higher is better). 61
Figure 15. FRF estimates for 20 m/s. 62
Figure 16. FRF estimates for 50 m/s. 63
Figure 17. FRF estimates for 80 m/s. 63
Figure 18. Change of H1 with air speed. 64
Figure 19. Fit results for 20 m/s. 64
Figure 20. Fit results for 30 m/s. 65
Figure 21. Fit results for 40 m/s. 65
Figure 22. Fit results for 50 m/s. 66
Figure 23. Fit results for 60 m/s. 66
Figure 24. Fit results for 70 m/s. 67

Figure 25. Fit results for 80 m/s. 67
Figure 26. Fit results for 85 m/s. 68
Figure 27. Damping versus speed graph. 68
Figure 28. Natural frequency versus speed graph. 69
Figure 29. Damping extrapolation result. 70
Figure 30. Decoupled FRF at U=20 m/s. 72
Figure 31. Decoupled FRF at U=30 m/s. 72
Figure 32. Decoupled FRF at U=40 m/s. 73
Figure 33. Decoupled FRF at U=50 m/s. 73
Figure 34. Decoupled FRF at U=60 m/s. 74
Figure 35. Decoupled FRF at U=70 m/s. 74
Figure 36. Decoupled FRF at U=80 m/s. 75
Figure 37. Decoupled FRF at U=85 m/s. 75
Figure 38. Singular values of the FRF matrix. 76
Figure 39. SVD filtering result on H1 77
Figure 40. SVD filtering result on H3 77
Figure 41. Envelope functions for leading edge accelerometer. 80
Figure 42. Envelope functions for leading edge accelerometer, zoomed. 80
Figure 43. Variation of shape parameters with speed, t_{max}=10s. 81
Figure 44. Variation of shape parameters with speed, t_{max}=5s. 81
Figure 45. Variation of shape parameters with speed, t_{max}=2s. 82
Figure 46. Envelope function result, t_{max}=10s. 83
Figure 47. Envelope function result, t_{max}=5s. 84
Figure 48. Flutter Margin fit for 6 data points. 85
Figure 49. Flutter Margin fit for 5 data points. 85
Figure 50. Flutter Margin fit for 4 data points. 86
Figure 51. Variation of ARMA *Fz* with dynamic pressure without filtering. 88
Figure 52. ARMA Modeling fit for 5 points without filtering. 88
Figure 53. Variation of ARMA *Fz* with dynamic pressure with filtering. 90
Figure 54. ARMA Modeling fit for 11 points with filtering. 91
Figure 55. ARMA Modeling fit for 4 points with filtering. 91

Figure 56. Nominal flutter analysis of the typical section. 98
Figure 57. Robust flutter analysis for 1% uncertainty, parameters='a'. 102
Figure 58. Robust flutter analysis for 1% uncertainty, parameters='a'. 103
Figure 59. Robust flutter analysis for 1% uncertainty, parameter=default. 103
Figure 60. Robust flutter analysis for 1% uncertainty, parameters=default. 104
Figure 61. Robust flutter analysis for 10% real uncertainty, parameter='a' 105
Figure 62. Validation norm, uncertainty=1%, U=60m/s. 109
Figure 63. Validation norm with changed parameters, uncertainty=1%, U=60m/s. 109
Figure 64. Flutterometer result for U=60 m/s. 110
Figure 65. FRF estimates for 10 m/s. 114
Figure 66. FRF estimates for 17.5 m/s. 114
Figure 67. FRF estimates for 25 m/s. 115
Figure 68. Change of H5 with air speed. 115
Figure 69. Fit results for 10 m/s. 116
Figure 70. Fit results for 12.5 m/s. 116
Figure 71. Fit results for 15 m/s. 117
Figure 72. Fit results for 17.5 m/s. 117
Figure 73. Fit results for 20 m/s. 118
Figure 74. Fit results for 22.5 m/s. 118
Figure 75. Fit results for 25 m/s. 119
Figure 76. Damping versus speed graph. 119
Figure 77. Natural frequency versus speed graph. 120
Figure 78. Damping extrapolation result with 6 data. 120
Figure 79. Damping extrapolation result with 5 data. 121
Figure 80. Envelope functions for the trailing edge accelerometer. 123
Figure 81. Envelope functions for the trailing edge accelerometer, zoomed. 123
Figure 82. Variation of shape parameters with speed, t_{max}=10s. 124
Figure 83. Flutter Margin fit for 6 data points. 125
Figure 84. Flutter Margin fit for 5 data points. 125
Figure 85. Variation of ARMA Fz with dynamic pressure. 127
Figure 86. Nominal flutter analysis of the ATS. 128

Figure 87. Validation norm, uncertainty=1%, U=15 m/s. 130
Figure 88. Flutterometer result for U=15 m/s. 130
Figure 89. Flutterometer result for U=20 m/s. 131
Figure 90. Nonlinear aeroelastic Simulink model. 141
Figure 91. Nonlinear correction force block. 141
Figure 92. Nonlinear simulation results for U=25 m/s. 142
Figure 93. Real Morlet Wavelet for a=1 and τ=0. 143
Figure 94. Wavelet transforms, left U=5 m/s, right U=10 m/s. 145
Figure 95. Wavelet transforms, left U=15 m/s, right U=20 m/s. 145
Figure 96. Wavelet transforms, left U=25 m/s, right U=30 m/s. 145
Figure 97. Magnitude of dominant scales for U=5 m/s. 146
Figure 98. Dominant scales for U=5 m/s. 147
Figure 99. Envelope of the dominant scales for U=5 m/s, left: pure Hilbert, right: curve fit. 147
Figure 100. Left: Envelope of dominant scales. Right: Derivative of dominant scales. 148
Figure 101. Maximum slope and maximum slope time results. 148
Figure 102. LCO prediction function. 149
Figure 103. Pitch response U=20 m/s. 153
Figure 104. Identified first order kernel, U=25 m/s. 157
Figure 105. Derived FRF, U=25 m/s. 158
Figure 106. Identified second order kernel, U=25 m/s. 158
Figure 107. FRF estimates for all speeds. 159
Figure 108. Curve fit result for damping extrapolation, U=20 m/s. 160
Figure 109. Estimated damping variation. 161
Figure 110. Flutter margin solution. 161
Figure 111. Uninstalled ATS. 166
Figure 112. View of ATS from test room. 167
Figure 113. View of ATS below the test room. 167
Figure 114. Installed ATS. 168
Figure 115. Excitation at 15 m/s. 170

Figure 116. Torsional response at 15 m/s. 170
Figure 117. Plunge response at 15 m/s..... 171
Figure 118. Leading edge accelerometer data at 15 m/s. 171
Figure 119. Trailing edge accelerometer data at 15 m/s. 172
Figure 120. Filtered accelerometer data at 15 m/s. 172
Figure 121. Torsional response at 37.6 m/s. 173
Figure 122. Plunge response at 37.6 m/s. 174
Figure 123. Torsional response at 40 m/s. 174
Figure 124. Plunge response at 40 m/s..... 175
Figure 125. FRF estimations for leading edge with impulsive input. 176
Figure 126. FRF estimations for trailing edge with impulsive input. 177
Figure 127. FRF estimations for leading edge with sinesweep input. 177
Figure 128. FRF estimations for trailing edge with sinesweep input. 178
Figure 129. Fit results for 10 m/s. 179
Figure 130. Fit results for 15 m/s. 179
Figure 131. Fit results for 19.9 m/s. 180
Figure 132. Fit results for 24.8 m/s. 180
Figure 133. Fit results for 29.9 m/s. 181
Figure 134. Fit results for 34.9 m/s. 181
Figure 135. Fit results for 37.6 m/s. 182
Figure 136. Damping versus speed graph. 183
Figure 137. Natural frequency versus speed graph. 183
Figure 138. Damping extrapolation result with 5 data pairs. 184
Figure 139. Envelope functions for trailing edge accelerometer. 185
Figure 140. Variation of shape parameter with speed, t_{max}=3s. 185
Figure 141. Flutter Margin fit for 5 data points. 186
Figure 142. Flutter Margin fit for 6 data points. 187
Figure 143. Nominal plant and ATS FRF at 10 m/s. 189
Figure 144. Nominal plant and ATS FRF at 15 m/s. 189
Figure 145. Nominal plant and ATS FRF at 19.9 m/s. 190
Figure 146. Nominal plant and ATS FRF at 24.8 m/s. 190

Figure 147. Validation norm, uncertainty=1%, U=10m/s. 192
Figure 148. Flutterometer result for U=10m/s. 192
Figure 149. Validation norm, uncertainty=1%, U=15m/s. 193
Figure 150. Flutterometer result for U=15m/s. 193
Figure 151. Validation norm, uncertainty=1%, U=19.9m/s. 194
Figure 152. Flutterometer result for U=19.9m/s. 194
Figure 153. Simulink model for a two DOF aeroelastic system. 221
Figure 154. Detail of the “Transducers” Simulink sub-block. 222
Figure 155. Detail of the “Noise and Antialias Filter” Simulink sub-block. 222

LIST OF SYMBOLS AND ABBREVIATIONS

$[A]$: Generalized aerodynamic influence coefficients matrix.

$[A_p]$: Predictor matrix.

$[C]$: Generalized viscous damping matrix.

$[H]$: FRF matrix.

$[K]$: Generalized linear stiffness matrix.

$[M]$: Generalized mass matrix.

$[Q(s)]$: Unsteady aerodynamics matrix.

$[T]$: Transformation matrix.

$[\Delta]$: Uncertainty matrix.

$[\Phi]$: Mode shape matrix.

$[\psi]$: Modal filter matrix.

$\{e\}$: Error vector.

$\{f\}$: Vector of generalized external forces.

$\{H\}$: Array of Volterra kernels.

$\{\eta\}$: Vector of generalized displacements.

a : Nondimensional distance of the elastic axis from the midchord / wavelet scale.

a_∞ : Speed of sound.

b : Semichord length.

c : Chord length.

$c_{1,2,3,4}$: Aerodynamic coefficients.

$C(k)$: Theodorsen's function.

h : Plunge motion of airfoil.

$h_{1,2,n}$: Volterra kernels.

I_α : Mass moment of inertia of the typical section.

k : Reduced frequency, Strouhal's number.

K_h : Flexural stiffness of the typical section.

K_α : Torsional stiffness of the typical section.

l : Span of the typical section.

L : Aerodynamic lift force acting at the elastic axis.

m : Mass of the typical section / number of modes.

M : Mach number / Volterra kernel memory length.

M_y : Aerodynamic moment about the elastic axis.

N : Number of DOF.

p : Laplace transform variable.

q : Dynamic pressure.

s : Nondimensional time (distance traveled in terms of reference length, b).

S : Wing area / shape parameter.

S_α : First mass moment of the control surface about the elastic axis.

t : Time.

$\bar{t}$: Time centroid.

U : Free stream flow speed.

α : Pitch motion of airfoil.

τ : Wavelet time shift.

x_α : Nondimensional static unbalance distance from elastic axis.

η : Structural damping proportionality constant.

ρ : Density of air.

ω : Angular frequency / natural frequency.

ϕ : Wagner's function.

$\phi(U)$: LCO prediction function.

δ : Uncertainty perturbation.

$_rA$: Modal constant.

M^R : Lower residue.

K^R : Higher residue.

(.) : Differentiation with respect to time.

(') : Differentiation with respect to s.

(~) : Laplace transform.

AIC : Akaike's information criterion.
ARMA: Auto Regressive Moving Average.
ATS : Aeroservoelastic Test Setup of TÜBİTAK-SAGE.
DOF : Degree of Freedom.
FFT : Fast Fourier Transform.
FM : Flutter Margin.
FRF : Frequency Response Function.
LCO : Limit Cycle Oscillation.
LMI : Linear Matrix Inequality.
LTI : Linear Time Invariant.
MIMO : Multi Input Multi Output.
ODP : Optimum Driving Point.
SAGE : Defense Industries Research and Development Institute.
SISO : Single Input Single Output.
SVD : Singular Value Decomposition.
TÜBİTAK : The Scientific and Technological Research Council of Turkey.

CHAPTER 1

INTRODUCTION

1.1 General

Designing a flying machine is still one of the most difficult engineering problems, because expectations from an aircraft increase with the increasing engineering knowledge in both civil and military applications. Although many engineering problems are well understood and satisfactory analysis tools are developed for design phase, every new design and modification should be carefully tested and certified in real conditions to avoid unexpected failures of these expensive machines. The flight envelope of a new or modified aircraft is always determined by flight tests after engineering analyses. Military aircraft are subject to strict rules for any modification that is not already certified, involving many integrity tests, aeroelastic analyses, and flight tests. Military handbook MIL-HDBK-1763 "Aircraft/Stores Compatibility: Systems Engineering Data Requirements and Test Procedures" is one of the main guides that describes how to perform these tests when new external stores, such as fuel tanks or munitions, are to be certified on a certain aircraft.

One of the first engineering problems in aeronautics was the aeroelastic instabilities that were not realized until the flight tests. In order to reduce the weight, the elastic stiffnesses of the early aircraft structures were so low that they were not able to overcome the aerodynamic forces and stabilize at a deformed shape, resulting in a phenomenon called divergence. The divergence is one of the simplest aeroelastic instabilities because it is a static phenomenon like control system reversal. Engineers soon solved static aeroelastic instability problems with new structure designs that had

higher stiffnesses. As the airspeeds increased, new and complicated aeroelastic instabilities were encountered such as flutter and buffeting which are much more difficult to overcome. Since these instabilities occur because of the coupling of structural dynamics and unsteady aerodynamic forces, they are called dynamic aeroelastic instabilities. Presently, the advances in embedding of computational fluid dynamics tools into structural finite element analysis tools, allow to perform flutter analyses which are often verified by wind tunnel flutter models and ground vibration tests.

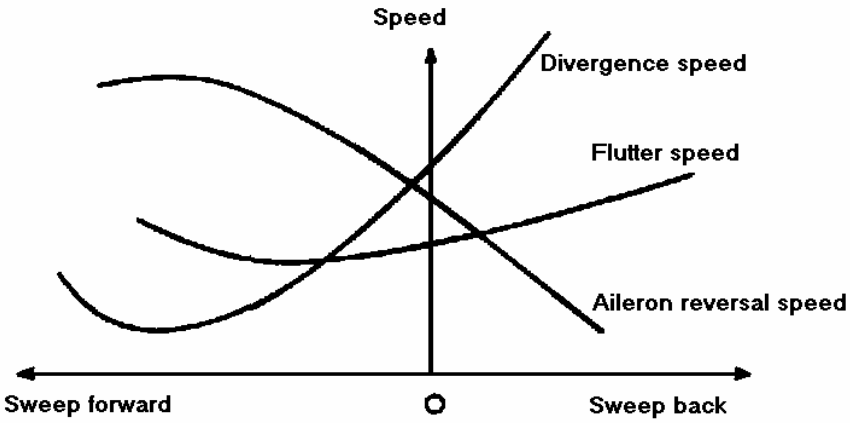

Figure 1. Comparison of critical speeds [1].

Figure 1 shows the typical instability behaviors as the speed and wing sweep angle changes. Sweep forward wings have a great advantage of lifting forces when they are rigid. However, this advantage introduces drawbacks in low divergence speeds. High performance aircraft that have sweep forward wings, like Russian Su-47, can only be operated with active divergence compensation control systems that are built in the flight control system of the aircraft. As the speed requirements of aircraft increased, wing configurations were changed to sweep back to increase the divergence speed. However, in the sweep back configuration, speed limits of the aircraft are determined by flutter. There are various ways to increase the flutter speed by passive methods such as mass balancing and stiffness improvements besides the use of active control systems. Aileron reversal, also named as control system reversal is the condition in

which the intended effects of displacing a given component of the control system are completely nullified by elastic deformations of the structure. In fact, the aileron reversal is not an instability; but should be considered in flight control system to compensate the lift lost.

Among all aeroelastic instabilities, flutter is the most dangerous instability not only for the aircraft but also for civil structures like bridges. Flutter may occur in any flexible structure that has an interaction with fluids, like pumps. The severity of flutter can be observed in Figure 2, which illustrates the typical flutter mechanism in relation to frequency and airspeed.

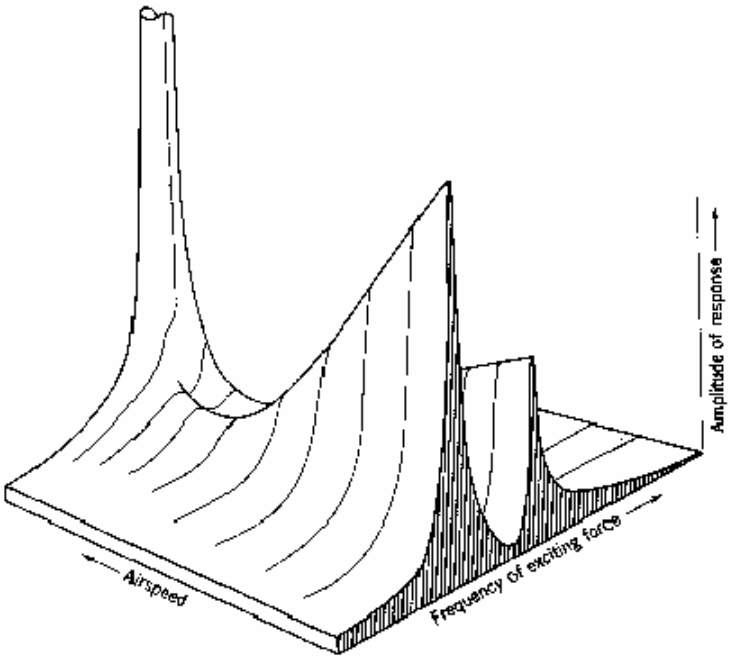

Figure 2. Typical frequency response of a two DOF, structurally damped airfoil at various airspeeds [2].

The unsteady aerodynamic forces introduce a damping effect on the response of the structure at low speeds. As the speed increases the aerodynamic damping contribution increases. At a critical speed, some of the elastic modes of the structure

are coupled by the aerodynamic forces such that the energy is transferred from the airflow to the structure, causing increasing oscillations. With a very little further speed increment, oscillations increase so rapidly that pilots usually do not have enough time to decrease the speed before a structural failure occurs. At this point, the equivalent damping of at least one mode becomes negative, causing a dynamic instability.

1.2 Scope of the Study

This study investigates the pretest and analysis tools used in flutter flight testing. The flutter flight testing involves many engineering disciplines to study on, such as modal analysis, instrumentation, data acquisition, signal processing, telemetry, system identification, and flutter prediction. The flutter prediction is the most critical item, which still needs a considerable human intervention and experience. The application of other items is relatively straightforward, but needs an adaptation to the flutter testing. This study mainly focuses on the flutter prediction methods for linear and nonlinear systems. Some classical and modern methods are evaluated and improved with new tools developed in this study. The results are demonstrated by means of simulations and wind tunnel experiments.

1.3 Flutter Flight Test

Today's aircraft designs undergo sophisticated aeroelastic analyses to ensure that the design is free of flutter within the flight envelope. The mathematical models used in the analysis are often verified by wind tunnel flutter models and ground vibration tests. The flutter flight testing provides the final verification of the analytical predictions throughout the flight envelope [3].

After analytical verifications, an aircraft is instrumented with accelerometers and/or strain gauges to measure the response of the structure to excitations, which are usually produced by exciters located at proper locations of the structure during flight.

Successive measurements at different altitudes and speeds are used to estimate the critical flutter speeds by the help of flutter estimation methods. A flutter flight test has three main aspects; excitation, measurement, and prediction. Critical flutter speeds or higher speeds are never tested, so predictions are always realized by extrapolations. A reliable extrapolation is usually difficult to achieve due to low signal to noise ratios and nonlinear behavior of the damping. Damping is the main indicator of the flutter margin for most of the methods. The flutter prediction is still a developing research area. Next to very old data based techniques; new, model based, robust, and limit cycle detectable techniques are still in progress.

Usually it is preferred to make predictions during testing to reduce the test time and also to decide on the next safe test point. The evaluation of the test data is usually performed in a ground station, so a telemetry system is commonly used in a modern test practice. Figure 3 shows a typical modern flutter flight test process.

Early test engineers were faced with inadequate instrumentation, excitation methods, and stability determination techniques. Since then, considerable improvements were made in flutter flight test techniques, instrumentation, and response data analysis. The flutter testing, however, is still a hazardous test for several reasons. First, one still must fly close to the actual flutter speeds before imminent instabilities can be detected. Second, subcritical damping trends can not be accurately extrapolated to predict the stability at higher airspeeds. Third, the aeroelastic stability may change abruptly from a stable condition to the one that is unstable with only a few knots' change in airspeed [3].

1.4 Historical Overview

A brief historical overview of the flutter flight testing is given in reference [3]. In the early years of aviation, there was no formal flutter testing procedure. The aircraft was forced to fly within the speed and altitude limits to demonstrate the aeroelastic stability of the vehicle. The first formal flutter test was carried out by Von Schlippe

in 1935 in Germany, although the first recorded flutter incident was on a Handley Page O/400 twin engine biplane bomber in 1916 in Britain. The flutter mechanism in this test consisted of a coupling of the fuselage torsion mode with an antisymmetric elevator rotation mode. The elevators on this airplane were independently actuated. The solution brought to the flutter problem was to interconnect the elevators with a torque tube.

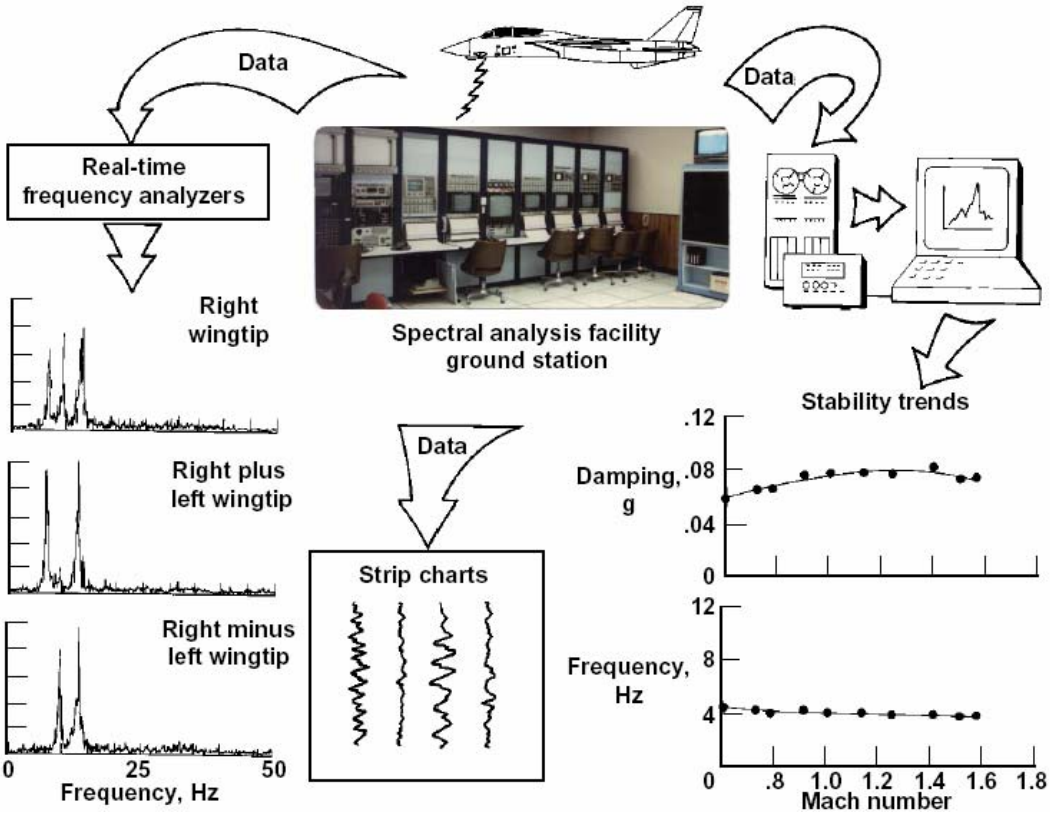

Figure 3. Typical modern flutter flight test process [3].

On the other hand, Von Schlippe's approach was to vibrate the aircraft at its resonant frequencies at progressively higher speeds and to plot the amplitude as a function of airspeed, as in Figure 2. A raise in amplitude would suggest a reduced damping with the flutter occurring at the asymptote of the theoretical infinite amplitude as shown in Figure 4. This idea was applied successfully to several German aircraft until a Junker JU90 fluttered and crashed during flight tests in 1938. An inadequate structural

excitation equipment, unsatisfactory response measurement, and insufficient recording equipment were identified as probable causes for this accident. In these tests, Von Schlippe was using a rotating unbalance for excitation.

In late 1950's, excitation systems consisted of inertia shakers, manual control surface pulses, and thrusters. The instrumentation was improved and the response signals were telemetered to the ground for display and analysis. Many experimenters realized the importance of adequate structural excitation for obtaining a high signal to noise ratio. The use of oscillating vanes to excite the structure was considered during this time.

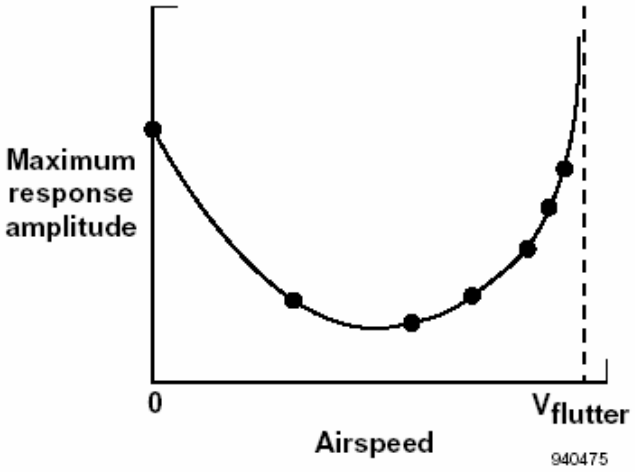

Figure 4. Von Schlippe's flutter flight test method [3].

From the 1950's until the 1970's, many aircraft were equipped with excitation systems. Frequency sweeps were employed to identify resonances. These sweeps were often followed by a frequency dwell quick stop at each resonant frequency. The flight analysis was usually limited to log the decrement analysis of accelerometer decay rates on strip charts to determine the damping.

Since 1970's, digital computers have significantly affected flutter flight testing techniques. The use of computers allowed the rapid calculation of fast Fourier

transform of the measured response. Computers fostered the development of more sophisticated data processing algorithms that were useful for the analysis of response data to either steady state or transient excitations. The frequency and damping are now estimated with parameter identification techniques. Such analysis is accomplished online in a near real time manner. Frequency and damping trends are established as a function of airspeed or Mach number. These trends are extrapolated to determine the stability at the next higher airspeed test point. As computer speeds increased, the time required to conduct flutter flight testing per test point decreased.

Although flutter flight test techniques advanced considerably, today's techniques are still based upon the same three components as back in Von Schlippe's method: structural excitation, response measurement, and data analysis for stability [3].

1.5 Literature Survey

There are some survey papers as excellent sources for other important references [3-6]. Through these invaluable survey papers, it is possible to observe the progress in this field, shortcomings, evolution, and comparison of methods. It is seen that as in many engineering fields, there exits no perfect method that is suitable for all cases, and there are still serious problems in this field. Furthermore, the aeroelastic testing community suffers from the lack of knowledge sharing because the results are usually kept confidential and not published.

In the early days of flutter flight testing, the only way to estimate the flutter speed was to analyze the time domain signals and calculate the logarithmic decrement of signals. The damping was then estimated from this logarithmic decrement information. However, this method was prone to human errors and close modes were hard to analyze. To find the antisymmetric and symmetric modes, time signals were added and subtracted to improve the signals associated with symmetric and antisymmetric modes. With the implementation of fast Fourier transform (FFT) on computers, the test engineers began to use frequency domain data to estimate the

frequency response functions (FRF) of the system. The estimation methods were adopted from the classical modal analysis techniques starting from the simple single-DOF curve fitting and processing to some sophisticated multi-DOF curve fitting techniques in years. As the computer speeds increased, parallel to the development of modal analysis techniques, the time domain analysis techniques reappeared. However, instead of using raw time domain signals directly, Inverse Fourier transform (IFT) of frequency response functions were utilized. Since IFT of FRF is the ideal impulse response of a system, time domain curve fittings can be used to estimate the modal parameters of the system. Nowadays, some sophisticated modal analysis techniques, such as polyreference, use both frequency and time domain data to accurately estimate the modal parameters with filters being employed in each domain. However, these powerful modal analysis techniques can not be used in flutter flight testing since the test quality in a ground testing can not be achieved in flutter flight testing.

In parallel to the development in damping estimation techniques, some other techniques that were unfamiliar to modal test engineers were developed. These methods use different stability criteria developed by control engineers. Since the main aim was to measure the stability of the aircraft, which was a major field of study in control engineering, the stability criteria that were developed by control engineers were adapted to the flutter flight testing.

Several comparisons of methods with both simulated and real data are available in the literature. Cooper [4] summarized the advantages and defects of old and newly developed methods. Despite the advances in this field; the estimation with close modes and high noise, prediction of error bounds on estimated parameters, application of phase resonance method, online estimation, and nonlinear estimation methods were listed as topics that require research on. Cooper *et al*. [7] compared the curve fitting algorithms using simulated data and showed the variation of estimates with noise. Dimitriadis *et al*. [8] compared the classic methods using simulated data and found that sometimes the simplest methods gave more reliable results than the

complex ones. It was stated that “there is no specific method that works with every aeroelastic model”. Kehoe [9] performed some real flight tests and approved the conclusion reached by Dimitriadis. Ramsay [10] described the test setup for Eurofighter 2000 flutter test and listed results of complex time and frequency domain methods without giving any conclusions. An overview of the flight tests performed by NASA Dryden is given in reference [5]. The modern methods like robust flutter margin and wavelet analysis were also investigated and were found promising. Lind *et al.* [11] compared a robust flutter margin method, which was named as the “flutterometer”, with classical methods and demonstrated that the flutterometer is a reliable method even at low speeds.

A detailed literature survey for each method investigated in this study is given in its associated section.

1.6 Objectives of the Thesis

The main objective of the thesis is to gain knowledge on major aspects of the flutter flight test. A safe and efficient execution of the flutter flight test requires an experience on the aeroelasticity, instrumentation, test planning, telemetry, and flutter prediction. It is not possible to investigate all components of the flutter flight test in detail with a single study. However, the flutter prediction is the most critical phase of the flutter flight test. The aim of the study is mainly to investigate the flutter prediction methods. The study aims to

- guide the test engineer to instrument the test object properly,
- implement some commonly used flutter prediction methods on computer,
- investigate the effectiveness of the flutter prediction methods,
- improve the effectiveness of the flutter prediction methods,
- investigate the applicability of some auxiliary tools, such as modal filters and singular value decomposition in flutter prediction algorithms,
- investigate the effect of structural nonlinearities on flutter prediction,
- develop tools to decrease the effect of nonlinearities,

- develop tools to predict limit cycle oscillations,
- demonstrate the investigated flutter prediction methods and the developed tools on a wind tunnel setup.

1.7 Outline of the Thesis

This brief introduction chapter is followed by a detailed chapter, Chapter 2 about flutter flight testing. In that chapter, some pretest studies such as excitation and measurement location selection methods and flutter prediction methods are investigated. The application of measurement and excitation location selection, and flutter prediction methods are demonstrated with the simulated data in the next chapter, Chapter 3. These demonstrations are performed with realistic simulation models. In Chapter 4, some methods that can be used for nonlinear aeroelastic systems are investigated. The performance of flutter prediction methods on nonlinear systems are examined. Wavelet analysis and Volterra series are introduced to improve flutter prediction methods and limit cycle oscillation prediction. The results of wind tunnel experiments are given in Chapter 5. Finally, in Chapter 6, some concluded remarks, observations, and contributions to the literature are stated.

CHAPTER 2

FLUTTER FLIGHT TEST

2.1 Test Techniques

2.1.1 Excitation

A structural excitation is the necessary part of a flutter flight testing methodology. The detection of impending aeroelastic instabilities cannot be made without any adequate excitation. An adequate excitation provides the energy needed to excite all of the selected vibration modes, usually up to 60 Hz in aircraft flutter test applications, with sufficiently large magnitudes to accurately assess the stability from the response data. Low excitation levels tend to give a large scatter in the damping values estimated from the response data. In addition, the estimated values suggest lower aerodynamic damping values than actually existing levels [3].

An excitation system must not only provide adequate force levels but must also provide an adequate excitation over the desired frequency range of interest. In aerospace applications, it should also be light weight so as not to affect the modal characteristics of the airplane used in tests and have power requirements that this airplane can meet. It is difficult for any one system to meet all these requirements simultaneously. Over the years, several types of excitation techniques were tried with varying degrees of success.

Manual control surface pulses were the first means of excitation. Depending on the type of the control system, modes up to about 10 Hz can be excited by this way. Two

benefits of this type of excitation are that no special excitation equipment is required and that the transient response signature of the structure is easy to analyze for stability. The test duration is short, so many pulses can be applied at each test point. However, there exist several drawbacks of this method. First, it is difficult to get repeatable pulses, and thus the degree of excitation is inconsistent. Second, either the pilot cannot provide a sharp enough input or the control system is unable to provide a sharp enough disturbance. Most modern fly by wire flight control systems have low pass filters in the stick input path. In such cases the flight control system should be reprogrammed to allow sharp control surface pulses. Reprogramming of the flight control system of an aircraft introduces a considerable preparation period and workmanship. Flight control surface pulses are still used today as an excitation techniques for flutter flight testing [3].

Oscillating control surfaces, commanded from an external signal were also used in the early days. The primary advantage of this type of system is that no additional hardware is required except for an excitation control box located in the cockpit. A disadvantage of this type of system is the frequency response limitations of the control surface actuators. Often, some special actuators are required to excite the critical high frequency modes.

Thrusters, sometimes known as bonkers, ballistic exciters or impulse generators, are early devices circa 1940 used for structural excitation. Thrusters are simple, lightweight, small, single shot, calibrated solid propellant rocket devices that generally do not affect the modal characteristics of the airplane. A single shot usage is the biggest drawback of these devices [3].

Inertial exciters, rotating unbalance exciters, and inertia shakers were also tried as structural excitation systems. Since the rotating unbalance produces a force proportional to the square of rotation speed, the excitation capability is limited at lower frequencies and excessive at higher frequencies. Often weight and size requirements preclude the use of such inertial exciters. However, inertia shakers,

which are usually hydraulically powered and electrically controlled, are in acceptable size and weight [3].

Another way to produce the excitation force is to use aerodynamic force itself. Aerodynamic vanes consist of a small airfoil that is usually mounted on the tip of wing or stabilizer. The vane is generally mounted on a shaft, driven either electrically or hydraulically, and oscillates about some mean angle. The advantage of this type system is that it can excite low frequencies well. The main disadvantage is that the maximum force produced varies with the square of the equivalent airspeed. Other disadvantages are the addition of mass to the wing structure, disturbance of the normal airflow around the wingtip, and large power requirements.

The random atmospheric turbulence was used for structural excitation in many flutter flight test programs. The greatest attraction to this type of excitation is that no special onboard exciter hardware is required. The atmospheric turbulence excites all surfaces simultaneously, which causes both symmetrical and antisymmetric modes excited at the same time. This method eliminates the need to perform symmetric or antisymmetric sweeps. Although this method was used with some success over the years, it has several disadvantages. The turbulence is often not intense enough to produce a sufficient excitation, which causes scattered and lower damping estimates. The turbulence usually excites only lower frequency modes for most airplanes. Long data records are required to obtain results with a sufficiently high statistical confidence level. The signal to noise ratio of the response data is often low [3].

2.1.2 Instrumentation

The instrumentation used to record the structural response of an airplane to an excitation is another critical component of the flutter flight testing methodology. The response data must be measured at enough number of locations and be of high enough quality that the flight can be conducted safely. The most commonly used transducers to measure the excited response of a structure were accelerometers and

strain gage bridges. Today, the more commonly used device is the accelerometer, since accelerometers are more compact than they were and exhibit practically invariant behavior under operational temperature changes [3].

Regarding the transfer of measured signals to the ground station, the pulse code modulation (PCM) or digital telemetry was initiated in the 1960's, although FM/FM telemetry was still widely used for flutter testing because of the frequency bandwidth required. In FM/FM transmission, the analog signals are modulated with frequencies that are in FM band and transmitted to the ground antenna. However, in PCM telemetry, the signals are first digitized and then transmitted to the ground. The PCM telemetry significantly increases the number of parameters that can be transmitted to the ground but requires a filter to prevent frequency aliasing of the analog response signal during its digital sampling. The frequency bandwidth of PCM systems increased significantly by the 1980's. A frequency bandwidth of 200 Hz is easily attainable nowadays and sufficient for most flutter applications. As a result, PCM telemetry is now usually preferred for most flutter flight testing [3].

2.1.3 Flutter Prediction

There are various commercial companies that provide necessary equipment customized to specific needs of a flutter flight test. The selection of an appropriate excitation method and associated instrumentation depends on the aircraft type under test, which is usually straightforward, and on the flutter prediction method to be used. Once the response data is acquired, it has to be analyzed very carefully to achieve the final goal. Several methods were developed with the goal of predicting flutter speeds and improving flight testing [12]. These methods include approaches based on extrapolating damping trends [1], envelope function [13], the Zimmerman-Weissenburger flutter margin [14], discrete time autoregressive moving average model [15], and the flutterometer [12, 16-20]. These methods were all demonstrated on simple test cases and flight tests. However, each method has certain strengths and weaknesses, and still needs further improvements.

The prediction methods can be classified as data based and model based methods according to the way that they use the measured data. Some methods rely entirely on flight data or models derived from flight data. Some others use both flight data and theoretical models.

2.2 Selection of Best Excitation Points

One of the most severe problems in flutter testing is the low signal to noise ratio. This occurs because the structure of the airplane may not be excited such that the response is not obtained at sufficiently large levels in the various modes of interest. In order to ensure that a required mode is excited, it is necessary to ensure that the excitation point is not at or close to a nodal line of that mode. An optimum driving point (ODP) function can be defined as

$$ODP(j) = \prod_{r} \left| \Phi_{rj} \right| \tag{2-1}$$

where [Φ] is the mode shape matrix, r denotes the modes considered and j is the specific degree of freedom. This function is a measure of the cumulative observability of all modes in interest. The degrees of freedom that have high ODP values are the best excitation points [21].

Since most of the time it is not possible to excite the structure with a rotary exciter, a new set of translational coordinates can be defined. The original eigenvector matrix can be transformed according to the new set of coordinates with additional dependent coordinates at different locations of the airfoil. Thereafter, the most suitable excitation point can be selected according to the ODP values. In the selection of the exciter locations, both ODP and practical installation constraints should be considered.

2.3 Selection of Best Measurement Points

In the selection of measurement locations there are a number of considerations; but two major ones are as follows.

- points at which measurements are taken so as to present a visually informative display of the resulting mode shapes, and
- DOFs which are necessary to measure in order to ensure an unambiguous correlation between the test and analysis models.

The former consideration essentially calls for a fairly uniform distribution of points with a sufficiently fine mesh that the essential features of the various mode shapes can be seen without aliasing effects. However, the second consideration is more critical. Since a limited number of sensors are used in a flutter testing, it is very crucial to sense the contribution of each mode in every sensor so as to accurately resolve the modes and their parameters. A number of different algorithms were proposed to select the best measurement points. However the most popular one is the "effective independence technique" [21] which is briefly explained below.

If there are m number of modes that are in interest, then each mode shape must be defined at a minimum m DOF, otherwise, the submatrix of eigenvectors will necessarily be singular. Since it is not possible to measure all critical DOF, because of difficulties in accessing and measuring rotary DOF, it is prudent to define each mode shape at more than this minimum number. Thus it is necessary to develop a procedure that can rank the various DOF in a descending order of importance. A predictor matrix, $[A_p]_{mxm}$, and its associate, $[E]_{NxN}$, are computed for the incomplete set of m mode shapes as below.

$$\left[A_p\right]_{mxm} = \left[\Phi\right]^T_{mxN}\left[\Phi\right]_{Nxm} \tag{2-2}$$

$$\left[E\right]_{NxN} = \left[\Phi\right]_{Nxm}\left[A_p\right]^{-1}_{mxm}\left[\Phi\right]^T_{mxN} \tag{2-3}$$

The matrix [*E*] is then used to eliminate successively those DOF from the full set of *N* which contribute least to the rank of [*E*]. By simply sorting the diagonal elements of [*E*], the most important DOF, which cause highest values in the diagonal can be selected. By discarding the least important DOF and the DOF that are unavailable for measurement, a new iteration can be performed to sort the remaining DOF. This iteration can be repeated until the rank of [*E*] get close to the desired number of sensors. Distribution of the sensors that is determined by this method may not present a visually informative display for the animation of mode shapes. However, the measurements from these locations will not result in rank deficient FRF matrices during modal parameter extraction. The measurements from these locations would result in useful FRFs.

2.4 Flutter Prediction Methods

2.4.1 Damping Extrapolation

The flutter speed prediction from the damping trend is one of the most popular methods used by the aeroelastic testing community. This method can be considered as a data based method because it relies entirely on analysis of flight data with no consideration of theoretical models of the specific system being tested. This approach is actually straightforward to understand conceptually. Simply stated, the damping of at least one mode becomes zero at the onset of flutter. The flutter prediction method consists of noting the variations in modal damping with airspeed and extrapolating those variations to an airspeed at which damping should become zero. This resulting airspeed is considered as the predicted flutter speed. The principle behind this method is quite sound; however, there are often some difficulties in practice. One area of difficulty is the extraction of modal damping. Aeroelastic flight data often have low signal to noise ratios, and so sophisticated techniques may be required for processing. Another area of difficulty is the extrapolation method. The damping can be a highly nonlinear function of airspeed so that the extrapolation must be carefully performed to ensure that it accurately

accounts for any high order nonlinearity. For highly coupled systems, the damping of the modes decreases all of a sudden although it is measured in a monotonically increasing trend up to that speed. So it may not be possible to measure this reversal trend of the damping until speeds get very close to the flutter speed, which is not an acceptable condition. Such a flutter phenomenon is called as the “explosive flutter”. In addition, highly coupled systems usually have lower flutter speeds than loosely coupled systems. Aeroelastic systems are designed with an optimum mass and stiffness distribution to have higher flutter speeds with mild behavior.

There are several methods developed by modal test engineers to extract modal damping and the other modal properties of the system from the response data, which can be divided into two main categories; namely, frequency and time domain methods. In all frequency and some time domain methods, the frequency response function of the system should be determined first. Since the calculated FRF is itself an estimation, the reliability of damping calculations from these estimated FRFs depends on their quality. Thus, adverse effects like noise and poor excitation will cause a scattered damping estimation [22]. Another drawback of a modal test is that, all modal analysis methods require a human intervention hence are open to human errors, which precludes the development of a robust and automated code. Because of time considerations during flight test, the analysis tool should require a minimum human intervention to calculate the damping.

2.4.1.1 Literature Survey

Although aeroelastic tests had been performed long before Koenig [22], Koenig was the first to emphasize the problems on damping estimation. The computational power, measurement quality, and modal analysis methods of that time were insufficient to predict the flutter speed. Since FRF calculations were not reliable due to the noise problems, it was not possible to establish FRFs without using any filter. Koenig used flight vibration test results of Airbus A310 aircraft and estimated the modal damping by fitting curves to the measured FRF. He also sent the time and

frequency domain data to seven different experts in four European countries for modal data analysis. The results were disappointing with some large scatters up to 5% in the mean frequency and up to 43% in the mean damping. Since the flutter estimation depends on the damping estimation, such a high variation in damping forced Koenig to conclude that, the state of the art of flight vibration analysis is poor and insufficient. The earlier studies on aeroelastic testing can be found in reference [23] which is a conference proceeding, published in 1975 by NASA. Bennett and Abel [24] were the first that encountered the failure of flutter prediction in real life. They used the impulse response function and performed a least squares curve fit in time domain. The instrumented drone was lost because of flutter despite the online flutter monitoring. The analysis tools did not even indicate the onset of flutter.

The least squares curve fit of time domain data was commonly used in early days despite its limitations such as the excessive computer time required and accuracy loss for systems that have more than three modes. These limitations were eliminated by the study of Smith [25]. However, nowadays computers allow the implementation of nonlinear least squares curve fit algorithms for the modal parameter estimation in both time and frequency domain.

Cooper [4] summarized the important points in using time and frequency domain methods. It was stated that, “In the modal analysis community it is considered to perform a global curve fit, simultaneously using data from a number (often large) of shakers and transducers (MIMO approach). Such an approach is not recommended for flight testing, as there is a likelihood of there being a wide scatter of damping, and even frequency, estimates between individual transducers”. It was recommended to use SISO formulations if there were no need to use any mode shape information for analysis. Although there were advanced FRF estimation methods such as H^c (three channel FRF estimator / instrumental variable FRF estimator), it was recommended to use traditional H_1 estimate.

2.4.1.2 Frequency Domain Methods

When using parameter estimation methods, an engineer has the choice of whether to use a simple single-DOF method or some more sophisticated multi-DOF methods. For a multi-DOF system with well separated modes, the parameters of each mode on the FRF can be found by examining each circle on the Nyquist plot, or each peak on the Bode plot, individually. Such approaches are called as single-DOF methods. It is common to assume that the damping is small enough so that the damped natural frequency is the same as the undamped natural frequency. The damping values can be found from either the half power points, or a number of points around the circle (or peak), or by curve-fitting. The problems with using such methods is that the mathematical model becomes invalid if the modes are sufficiently close to each other (usually defined by overlapping the half-power bandwidths) resulting in some poor damping estimates. In the extreme case, one mode will dominate another mode to such an extent that only the parameters of the dominant mode are estimated. However, the use of such methods is still very commonplace for flutter flight testing, particularly for military aircraft, due to their ease of use. In civilian aircraft however, where there is a much greater likelihood of close modes due to engines mounted on the wings, the use of such methods is not so common. Often a number of transformations between the time and frequency domains are required in order to isolate all the modes [4].

In multi-DOF methods, the FRF is modeled as some form of rational fraction expansion that includes contributions from all the modes. Therefore, no problem arises when close modes are analyzed. As well as the contribution of individual modes including complex amplitude terms, the upper and lower residuals should also be included in order to take into account the modal behavior outside the frequency range of interest. The majority of techniques in this category employ an iterative nonlinear least squares curve-fit to the FRF model over the frequency range of interest. These methods require initial frequency and damping estimates for the iterative process and the convergence speed can be very sensitive to these initial

estimates. The alternative approach is to produce a linearized model and to find the estimates using a direct procedure. Such methods include the rational fraction polynomial method.

The method developed by Nissim and Gilyard [26] uses a model that directly estimates the physical mass, stiffness, and damping matrices. A maximum likelihood approach was developed [27] including both input and measurement noise models. Theoretically, such an approach should provide the best statistical estimates of the parameters. However, there can be convergence problems when using such sophisticated methods on systems with low damping and high modal densities.

The non-linear iterative curve-fit approach is the most popular method used in the aerospace industry [4]. This methods requires an initial analysis to decrease the computational time during flight tests. However, such an analysis are usually conducted in practice before the flight tests.

2.4.1.3 Time Domain Methods

The time domain parameter identification became feasible with the development of the digital computers. Such methods are based upon a time series representation of a system model, which can be related to the state space model, often used in the control field. Although it is possible to develop methods based upon a model relating inputs and outputs, the modal analysis community has tended to use methods that curve-fit the impulse response function. The impulse response function of a system can be calculated from the inverse Fourier transform of the FRF and the time response to an impulse. It is also possible to generate the impulse response function from the response to an unknown random input. A large number of mathematically rigorous time domain techniques exist in the signal processing field. However, the direct application of such methods to modal analysis or flutter flight testing is very difficult due to high modal densities and low damping values.

One inherent problem with the use of time domain methods is their incapability to model the residual effects directly. Such effects result in some leakage errors due to filtering modes outside the frequency range of interest, which can cause problems.

Multi-DOF curve fitting methods model the impulse response as a summation of exponentially damped sinusoids. Often, a least squares minimization of a difference equation representation relating the structural response at different time instants is used. This difference equation formulation gives rise to some biased estimates when the data is corrupted. The most common remedy is to increase the number of modes in the fitted model. Although such an approach removes most of the bias, the user then has to distinguish between the system modes and the spurious modes. In real structures such as aircraft, this differentiation can be difficult, and a fair amount of user interpretation is required in order to get the best out of the methods [4].

2.4.1.4 Implementation of Nonlinear Least Squares Fit

In this study, the method of multi-DOF nonlinear least squared fit (NLSF) in frequency domain is used for damping extrapolation, since close modes case is usually encountered in practice and NLSF has been around for a long time. In order to improve the fit, low and high residual modes will be included in the FRF expression. The mathematical model of an FRF can be expressed as

$$H_{jk}(\omega) \cong -\frac{1}{\omega^2 M_{jk}^R} + \sum_{r=m_1}^{m_2} \frac{{}_rA_{jk}}{{\omega_r}^2 - \omega^2 + i\eta_r {\omega_r}^2} + \frac{1}{K_{jk}^R} \tag{2-4}$$

Here index j stands for the response DOF, k for the excitation DOF and r for the mode number. M^R and K^R represent the low and high residues, respectively. Boundaries m_1 and m_2 define the number of modes that will be included in the fit. Finally, ${}_rA$, ω_r, and η_r represent the modal constant, natural frequency, and modal damping of the r^{th} mode, respectively. The error function can be defined as

$$e_i = \sum_k \sum_j \left| H_{measured\ jk}(\omega_i) - H_{jk}(\omega_i) \right| \tag{2-5}$$

The norm minimization of vector $\{e\}$ with respect to the modal parameters and frequencies that are in interest would result in an optimum curve fit. The modal parameters are directly obtained without performing other operations on the curve. Matlab software is used for solving this optimization problem.

It is possible to fit multiple FRF simultaneously. For a single excitation point, the error expression (2-5) can be rewritten such that it is compatible to the Matlab's "lsqnonlin" function as follows.

$$\{e\} = \begin{bmatrix} \left| H_1(\omega_1) - H_{measured_1}(\omega_1) \right| \\ \vdots \\ \left| H_1(\omega_p) - H_{measured_1}(\omega_p) \right| \\ \hline \left| H_n(\omega_1) - H_{measured_n}(\omega_1) \right| \\ \vdots \\ \left| H_n(\omega_p) - H_{measured_n}(\omega_p) \right| \end{bmatrix} \tag{2-6}$$

where ω_1 and ω_p define the frequency range of interest.

Necessary Matlab codes are prepared to calculate the FRF from time signals and to fit an analytical FRF. Once the modal dampings are estimated, a polynomial fit to damping versus flight speed can be used to predict zero damping speed by extrapolation.

2.4.1.5 FRF Improvement

The measured FRF can be improved by orthogonality checks and elimination of weak signals. Modal filters and singular value decomposition can be used for such

improvements. Such approaches are suggested in the literature but not studied in detail. In this study, the application of modal filtering and SVD decomposition to flight testing is investigated.

2.4.1.5.1 Modal Filter

A modal filter is simply a coordinate transformation from the physical to modal coordinates. The concept of modal filter was developed by the control community in order to deal with the problem of control spillover. The vibration suppression of large structures, such as space structures, is usually achieved by means of active control. Since actuators have limited bandwidths, the out-of-range modes can not be controlled, but may be excited accidentally. So it is crucial to filter the contribution of the controllable modes from the overall response data. Once the responses of the particular modes are extracted, appropriate control signals can be generated that affect only the particular modes of interest. Modal filters can be used to subtract FRF of individual modes from measured FRF. Then, by using simple single degree of freedom methods, the modal parameters can be extracted quite easily. In addition, any spatially uncorrelated measurement noise can be generally reduced by the spatial averaging that is inherent in the modal filter calculation [28].

A modal filter is a matrix whose columns are a set of reciprocal modal vectors. By definition, these reciprocal modal vectors are orthogonal to the modal vectors in a given frequency range. There are several ways to calculate the modal filters. A straightforward solution for a modal filter is merely the generalized inverse of the modal matrix with rows corresponding to the sensor locations. Another method is the reciprocal modal vector method which calculates the modal filter from a measured FRF matrix and modal parameters estimated from the FRF matrix [28]. So, the modal properties of the structure must be known to calculate the modal filter during flight. Usually, a ground vibration test is carried out on the structure before the flight test, so the mode shape matrix of the structure is known at the zero flow speed. Since modal filters are spatial filters, they are not affected from the natural frequency or

damping changes as long as the mode shapes do not change. So it will be assumed that mode shapes of the structure do not change severely with changing flight speed.

The modal filter, $[\psi]$ can be calculated by the inverse of mode shape matrix, $[\Phi]$ as

$$[\psi] = [\Phi]^{-1} \tag{2-7}$$

Usually it is not possible to obtain the full mode shape matrix. It is also possible to calculate the modal filter from the truncated mode shape matrix by pseudo inverse operation.

The modal coordinate responses, $\{\eta\}$, can be calculated from the vector of physical response measurements, $\{x\}$, as

$$\{\eta\} = [\psi]^T \{x\} \tag{2-8}$$

The decoupled FRF matrix, $[H_{decoupled}]$, can be calculated from the FRF matrix, $[H]$, as

$$\left[H_{decopuled}\right] = [H][\psi]^T \tag{2-9}$$

The effectiveness of the method will be investigated in Chapter 3.

2.4.1.5.2 Singular Value Decomposition

The singular value decomposition (SVD) is another tool that can be used to improve the measured FRF. Furthermore, SVD provides an information about the number of independent FRF and the number of modes within the analyzed frequency range. Finding the number of modes from FRF may become very difficult in the presence of repeated or close modes and measurement noise. So, SVD also provides a way to automate the curve fitting algorithms.

The augmented FRF matrix,

$$[H]_{Lxnp} = \left[\{H_{11}(\omega)\}_{Lx1} \cdots \{H_{np}(\omega)\}_{Lx1}\right] \tag{2-10}$$

can be decomposed by SVD as follows.

$$[H]_{Lxnp} = [U]_{LxL}[\Sigma]_{Lxnp}[V]^T_{npxnp} \tag{2-11}$$

Then the decomposed matrix [Σ], whose diagonal elements are the singular values, gives the amplitude information of modes. The matrix [U] gives the frequency distribution of the amplitudes and the matrix [V] gives the spatial distribution of the amplitudes. The number of nonzero singular values defines the number of modes within the analyzed frequency range. Singular values below a specified threshold should be treated as zero. Once the number of nonzero singular values is determined, the decomposed matrices can be reconstructed and combined back to obtain the new FRF matrix as follows.

$$[\overline{H}] = [[U_r] \quad [U_0]] \begin{bmatrix} [\Sigma_r] & 0 \\ 0 & [\Sigma_0] \\ 0 & 0 \end{bmatrix} \begin{bmatrix} [V_r] \\ [V_0] \end{bmatrix}^T \tag{2-12}$$

The noise reduction and mode number estimation capability of SVD will be investigated in Chapter 3.

2.4.2 Envelope Function

Flutter speeds can be predicted using a method based on an envelope function, namely, the “envelope function” method [13]. This method, like the damping extrapolation approach, is a data based approach that predicts the onset of flutter based entirely on the analysis of flight data. The data used by this method are simply

the time domain measurements from sensors in response to an impulse excitation. The fundamental nature of this method is somewhat similar to the method based on damping extrapolation. However, this method does not directly use the estimates of modal damping. Instead, it notes that the envelope bounding the impulse response gets larger as the damping decreases. Thus, the size and shape of the response envelope can be used to indicate a loss of damping and, consequently, the onset of flutter. An envelope function that bounds an impulse response can be computed in several ways. The current formulation considers an approach based on the Hilbert transform. A signal *y(t)* is related to its Hilbert transform $y_H(t)$ as being similar in magnitude but differing in phase by 90°. An envelope function that bounds the impulse response is easy to compute by using the phase difference between *y(t)* and $y_H(t)$ as follows.

$$env(t) = \sqrt{y(t)^2 + y_H(t)^2} \tag{2-13}$$

This envelope will clearly increase in size as the data indicate impulse responses of a system with decreasing modal damping. Unfortunately, the amplitude of this envelope can be also affected by the size and shape of the impulse given to the system. Thus, the time centroid is needed as a further indication of the stability of a system. This centroid, $\bar{t}$, is computed with respect to a maximum length of time window, t_{max}, within which the data lie as

$$\bar{t} = \frac{\int_0^{t_{\max}} env(t)\, t\, dt}{\int_0^{t_{\max}} env(t)\, dt} \tag{2-14}$$

A shape parameter is used for the actual prediction of flutter. This parameter S is simply the inverse of the time centroid such that $S = 1/\bar{t}$. This shape parameter is then assumed to be a polynomial function of airspeed as

$$S = S_0 + S_1 V + S_2 V^2 + \ldots \tag{2-15}$$

The prediction of the flutter speed is accomplished by noting that $S=2/t_{max}$ when the system has the critical damping at the onset of flutter. The flutter speed is, thus, predicted by noting the value of the polynomial at which this condition is satisfied. However, this condition is valid only for single-DOF systems. For multi-DOF systems, the shape parameter, S, will reduce rapidly with decreasing damping but not to a value of $2/t_{max}$, because of the effect of the other damped modes. However, it is known that as the speed approaches the critical flutter speed, the flutter mode shape dominates on the response of the structure. So, it is possible to estimate the flutter speed by using the envelope function for multi-DOF systems with critical condition $S=2/t_{max}$. The envelope function is a useful and fast method in monitoring the overall damping during flight. It can be used as a quick check tool which may indicate whether the damping has changed significantly since the last test.

An estimate for $\bar{t}$, and therefore S, may be obtained very quickly from the raw time data without any transformation by using the following approximation of Equation 2-14 [13].

$$\bar{t} \approx \frac{\int_0^{t_{\max}} t\left|y(t)\right| dt}{\int_0^{t_{\max}} \left|y(t)\right| dt} \tag{2-16}$$

2.4.2.1 Implementation of Envelope Function

The impulse response of the aeroelastic structure, which is necessary to calculate the shape parameter, *S*, can be obtained in two ways. One way is the direct measurement of the aircraft's response to an impulsive excitation obtained by a control stick jerk or by using a pyrotechnic thruster. The other method is by taking the inverse Fourier transform of FRF, which can be obtained by any kind of excitation. In practice, it is usually not possible to produce a perfect impulsive excitation by a stick jerk. However exciters such as thrusters are designed to produce some appropriate impulsive loads that can excite all modes within the frequency range of interest. The use of FRF data allows averaging and windowing so that the effect of noise can be reduced. The impulse responses can be exponentially weighted to improve the signal to noise ratio.

The acceleration, velocity or displacement impulse responses can be used to calculate the shape parameter. Since the acceleration data is the only data for most cases, the velocity and displacement impulse responses must be calculated by the inverse Fourier transform of the velocity and displacement FRF, which can be calculated by dividing the acceleration FRF by $i\omega$ and $-\omega^2$, respectively. Since the high frequency content is inherently filtered in the velocity and displacement response, the contribution of responses that belong to the low frequency modes to the shape parameter can be increased by using either velocity or displacement impulse response. However, when using displacement impulse response, care must be taken with rigid body responses. The effects of rigid body modes must be filtered by high-pass filters. If the flutter frequency is high, the acceleration data must be used. The acceleration data can also be filtered to eliminate the effect of higher modes that are out of the frequency range of interest.

2.4.3 Zimmerman-Weissenburger Flutter Margin

Another method developed to predict the onset of flutter uses the concept of flutter margin [14]. This method is also a data based method in the sense that it only uses

the information obtained directly from the flight data. In this case, the flutter margin makes use of the information about the poles of the transfer function obtained from the data. The flutter margin, as originally formulated by this approach, is an indicator of the distance to flutter in terms of dynamic pressure. The development of this method is based on the equations of motion for a classical aeroelastic system with bending and torsion modes. The method was formulated for a two mode flutter mechanism but has since been extended to consider one mode or three mode instabilities [29, 30]. The essence of the method is to consider the characteristic polynomial that describes the continuous time aeroelastic system. The stability of this system can be evaluated by applying the Routh stability criterion. In this way, both damping and frequency properties of the system are used to estimate the instability. It is very difficult to measure damping from test data especially in the presence of measurement noise. However, the damping estimation is the core of the most classical flutter prediction methods. With this approach, a control engineering point of view is used in the modal analysis field.

2.4.3.1 Implementation of Flutter Margin

Assume that the system is indeed a two mode system with two complex conjugate pairs of distinct poles given by $\lambda_{1,2}$ and $\lambda_{3,4}$ with parameters to represent the real and imaginary parts of these poles such that $\lambda_{1,2} = \beta_1 \pm j\omega_1$ and $\lambda_{3,4} = \beta_2 \pm j\omega_2$. Then the characteristic equation becomes

$$(s-\lambda_1)(s-\lambda_2)(s-\lambda_3)(s-\lambda_4) = 0 \tag{2-17}$$

The flutter margin (FM) is formulated by applying the Routh stability criterion to the two mode system. This criterion results in a parameter that must be positive if the corresponding system is stable. Recall that for a fourth order system such as that given in Equation 2-18, the Routh stability criteria can be constructed as in condition 2-19.

$$s^4 + A_3 s^3 + A_2 s^2 + A_1 s + A_0 = 0 \tag{2-18}$$

$$\left[A_2 \left(\frac{A_1}{A_3} \right) - \left(\frac{A_1}{A_3} \right)^2 - A_0 \right] > 0$$

or

$$F = \left\{ \left[\left(\frac{A_2}{2} \right)^2 - A_0 \right] - \left[\frac{A_2}{2} - \frac{A_1}{A_3} \right]^2 \right\} > 0 \tag{2-19}$$

By comparing Equations 2-17 and 2-18, the stability parameter, F, can be written in terms of the system poles as

$$F = \left[\frac{\left({\omega_2}^2 - {\omega_1}^2 \right)}{2} + \frac{{\beta_2}^2 - {\beta_1}^2}{2} \right]^2 + 4\beta_1\beta_2 \left[\frac{\left({\omega_2}^2 + {\omega_1}^2 \right)}{2} + 2\left(\frac{\beta_2 + \beta_1}{2} \right)^2 \right] - \left[\frac{\beta_2 - \beta_1}{\beta_2 + \beta_1} \frac{{\omega_2}^2 - {\omega_1}^2}{2} + 2\left(\frac{\beta_2 + \beta_1}{2} \right)^2 \right]^2 \tag{2-20}$$

The flutter margin is obviously zero if either $\beta_1 = 0$ or $\beta_2 = 0$. This parameter is, thus, an indicative of the stability of a system; however, that does not necessarily make it valuable for predicting the onset of flutter. The nature of a flutter margin arises by noting, subject to some assumptions, that the parameter F varies with the dynamic pressure, q. Some studies noted that this variation may be considered linear. The proposed formulation assumes that this variation is quadratic; that is

$$F = f_0 + f_1 q + f_2 q^2 \tag{2-21}$$

The dynamic pressure associated with flutter is predicted by computing F from data taken at test points with different values of dynamic pressure. The roots of this equation for F give the dynamic pressure at which the onset of flutter is predicted to occur.

The main advantage of this method is that the flutter margin is insensitive to the damping scatter. However, it is sensitive to the fundamental frequencies, which can be determined more precisely than damping. Another advantage is that, the stability plots are expected to be monotonic contrary to the damping plots. So this method is also useful for the detection of moderate and explosive flutter. Although the method is limited to 2 or 3-DOF systems, it was also successfully used with multi-DOF systems with acceptable accuracy [31].

2.4.4 Discrete-Time ARMA Modeling

Since measurements are available at sampled time intervals, the discrete time identification techniques can be used to describe the aeroelastic system. Then, the stability analysis of discrete systems can be used to predict the flutter speed. The discrete time autoregressive moving average (ARMA) modeling [32] is such a technique that is adapted to flutter estimation. This method is a data based approach; however, the type of data used by this method is different from the data used by the previous methods. The discrete time approach relies on time domain measurements from the system in response to a random excitation. This type of data is usually provided by sensor measurements that record the response to atmospheric turbulence. The analysis of turbulence data have both advantages and disadvantages compared to other methods. The method does not require any onboard excitation system, but uses turbulence as the input to the system. However, it is often difficult to get the response levels in which all modes are sufficiently observed with the turbulence. The system is assumed to be represented accurately by an ARMA model. This type of model uses autoregressive measurements and a moving average of white noise input to describe the dynamics. This is because the method requires data measured in

response to turbulence which is known to be almost random. The coefficients associated with the autoregressive measurements are associated with the stability characteristics.

2.4.4.1 Implementation of the ARMA Modeling Method

The measured response, *y(t)*, of a wing excited by air turbulence, *e(t)*, which is assumed to be pure white noise, during steady flow conditions can be written as a discrete time series with weighting coefficients α and β as

$$y(k)+\alpha_1 y(k-1)+\ldots+\alpha_n y(k-n)=e(k)+\beta_1 e(k-1)+\ldots+\beta_m e(k-m) \tag{2-22}$$

This ARMA model can be expressed in short notation as

$$\alpha(z^{-1})y(k)=\beta(z^{-1})e(k) \tag{2-23}$$

where

$$\begin{aligned}\alpha(z^{-1})&=1+\alpha_1 z^{-1}+\ldots\alpha_n z^{-n}\\ \beta(z^{-1})&=1+\beta_1 z^{-1}+\ldots\beta_m z^{-m}\end{aligned} \tag{2-24}$$

The coefficients α and β describe the AR and MA parts of the ARMA model, respectively. The coefficients α and β, orders n and m, and variance of the noise should be determined to identify the system. These unknowns can be determined by any suitable search algorithm such as the maximum likelihood estimation. The optimum order of the system can be determined by the help of Akaike's information criterion (AIC), which is developed by Hirotsugu Akaike in 1971 and it is a measure of the goodness of the fit of an estimated statistical model using the concept of entropy. The combination of n and m that gives the minimum AIC is the optimum

order of the ARMA model. As in flutter margin method, ARMA method assumes interaction of two dominant modes. So AR order, *n*, should be set as *n=4*. The order of the noise, *m*, can be set to *n-1* if it is not possible to perform a pre-analysis with AIC.

The characteristics polynomial, *G(z)*, of the system that is defined in Equation 2-22 as a function of the discrete time variable *z* can be defined as

$$G(z) = z^4 + \alpha_1 z^3 + \alpha_2 z^2 + \alpha_3 z + \alpha_4 = (z - z_1)(z - z_1^*)(z - z_2)(z - z_2^*) \tag{2-25}$$

This form for the characteristic polynomial assumes that the dynamics are described by two modes. There are four poles in the dynamics, but they are restricted to be complex conjugate pairs. The stability of the system can be computed by applying the Jury determinant method. This method guarantees the stability of discrete time systems if a certain set of conditions are satisfied. A discrete system is stable if all of the following Jury's stability parameters are positive.

$$\begin{aligned} G(1) &= 1 + \alpha_1 + \alpha_2 + \ldots \\ G(-1) &= 1 - \alpha_1 + \alpha_2 - \ldots \\ F^+(1) &= 1 + \alpha_n \\ F^-(1) &= 1 - \alpha_n \\ F^+(k) &= \det([X_k] + [Y_k]) \\ F^-(k) &= \det([X_k] - [Y_k]) \end{aligned} \tag{2-26}$$

where

$$[X_k]=\begin{bmatrix}1 & \alpha_1 & \cdots & \alpha_{k-1}\\ 0 & 1 & \ddots & \vdots\\ \vdots & \ddots & \ddots & \alpha_1\\ 0 & \cdots & 0 & 1\end{bmatrix},\ [Y_k]=\begin{bmatrix}\alpha_{n-k-1} & \cdots & \alpha_{n-1} & \alpha_n\\ \vdots & \ddots & \alpha_n & 0\\ \alpha_{n-1} & \ddots & \ddots & \vdots\\ \alpha_n & 0 & \cdots & 0\end{bmatrix},\ k=1,3,\ldots,n-1 \qquad (2\text{-}27)$$

The conditions can be also written in terms of the poles, z_i. There are many conditions to be satisfied, however, the condition defined as $F^-(3)$ for the fourth order system is of particular interest.

$$F^-(3)=\det\left([X_3]-[Y_3]\right)=\left(\left|1-z_1z_2\right|^2\right)\left(\left|1-z_1z_2^*\right|^2\right)\left(1-\left|z_1\right|^2\right)\left(1-\left|z_2\right|^2\right)$$

$$[X_3]=\begin{bmatrix}1 & \alpha_1 & \alpha_2\\ 0 & 1 & \alpha_1\\ 0 & 0 & 1\end{bmatrix},\ [Y_3]=\begin{bmatrix}\alpha_2 & \alpha_3 & \alpha_4\\ \alpha_3 & \alpha_4 & 0\\ \alpha_4 & 0 & 0\end{bmatrix} \qquad (2\text{-}28)$$

The stability of a discrete time system is ensured if all poles have magnitudes less than unity. This result implies that a stable system will always have $F^-(3)>0$. Furthermore, the value of $F^-(3)$ goes to zero as the system approaches instability. Thus, $F^-(3)$ was used as the stability predictor whose trend toward zero indicates the onset of flutter [32-34]. Unfortunately, $F^-(3)$ was noted to have some potentially adverse behaviors with the dynamic pressure; therefore, the behavior of a similar parameter, $F^-(1)$, was considered.

$$F^-(1)=1-\alpha_4=\left(1-\left|z_1\right|^2\left|z_2\right|^2\right) \qquad (2\text{-}29)$$

The behavior of $F^-(3)$ is somewhat improved by associating it with $F^-(1)$. This forms the basis for the discrete time ARMA flutter margin, F_z [35, 36, and 15] as

$$F_z = F^-(3)/F^-(1)^2 \tag{2-30}$$

The flutter margin is used to predict the onset of flutter by expressing F_z as a function of flight conditions. Specifically, a standard approach is to express F_z as a quadratic function of dynamic pressure, q, as

$$F_z = f_0 + f_1 q + f_2 q^2 \tag{2-31}$$

The dynamic pressure associated with the flutter is predicted by computing F_z at several different flight conditions. The coefficients in Equation 2-31 are calculated by applying a curve fit to the results. The flutter is expected at the dynamic pressure at which F_z becomes zero.

Note that this method has some similarities to the Zimmerman–Weissenburger flutter margin approach. In fact they are mathematically equivalent.

2.4.5 Flutterometer

The studies in the literature showed that the classical methods discussed above are able to estimate the critical flutter speed but the reliability of these methods depends on the test points. Estimations were only reliable when the processed measurements were acquired close to critical flutter speed, which is an undesired condition. The estimations were based on only the measured data without knowing the behavior of the system. In case of explosive flutter instability, the extrapolated estimation of the system behavior may result in some catastrophic failures. Although air vehicles are designed to be free of such instabilities, it is not possible to prove without real tests that this is indeed the case. Classical methods depend on the parameters, such as natural frequency and damping, estimated from the measurements. Although there are very efficient system identification techniques, the quality of the estimation depends on the quality of the measured data. In contrast to ground testing, the quality

of the flight testing measurements are very poor because of the unmeasured disturbances and insufficient excitation. Although the natural frequencies can be estimated very accurately, the damping which is the most important parameter for these methods, can not be estimated that accurately. An accurate damping estimation problem is not specific to the flight testing but is also encountered in the ground testing.

In this section, a recent and promising technique called flutterometer is investigated. In contrast to the classical methods, this method uses both experimental measurements and an assumed system behavior. Having an idea for the system behavior greatly improves the reliability of the estimations. In order to use this method, a mathematical representation of the test item is required. Since the ground vibration tests are always performed before a flight test, a very accurate structural model can be constructed with the ground test data. Sometimes some aerodynamic experiments are also performed which can be used to model the aerodynamic behavior. However, the aerodynamic model is often derived from approximate aerodynamic theories. Panel methods are extensively used in aerodynamic modeling. Once the flight data is incorporated to the mathematical model, the critical flutter speed can be estimated by the stability margin calculations that are used by control engineers. The predictions derived from stability margins would be more reliable than the predictions derived from damping. A robust stability measure which is called μ norm is used as the stability margin measure.

The flutterometer was developed in NASA Dryden Flight Research Center. Basically, the flutterometer uses both flight data and theoretical models to predict the onset of flutter. The flight data under consideration are frequency domain transfer functions which are derived from flight test results. The model to be analyzed is the corresponding theoretical transfer function with some estimated uncertainty descriptions. The flutter speed is, thus, computed as the largest increase in airspeed for which the theoretical model remains robustly stable with respect to the uncertainty. The initial step is to compute an uncertainty description for the model at

a specific flight condition. This step is performed by noting the differences between the theoretical and measured transfer functions. The uncertainty is introduced to the model as variations such that the resulting range of theoretical transfer functions bound the measured transfer function. The next step is to compute the robust flutter speed. This step is performed by a straightforward application of μ method analysis on the theoretical model that contains the uncertainty variations. In this way, the flutterometer predicts a realistic and reliable flutter speed. The flutterometer can also be used as pre flutter analysis tool, when the uncertainties except the dynamic pressure are neglected.

2.4.5.1 Literature Survey

The flutterometer method was first presented by Lind and Brenner in 1997 [37-40]. The method was demonstrated with an F/A-18 SRA (Systems Research Aircraft) flutter flight test data that was recorded between 1994 and 1995 [37-39]. These offline demonstrations showed that the flutterometer can estimate the flutter speeds accurately. The details of the method were published in 1998 [18, 19]. The performance of the method with simulated flight conditions was demonstrated in 2000 [16]. The longest computation time among different test points was 2.5 minutes with some powerful computers of that time. Afterwards, some specific flight tests were performed to test the method and to compare the performance of the new method with the data based classical prediction methods. A set of experiments were conducted with a separate wing that was mounted on an F-15 body called Aerostructures Test Wing (ATW). The comparison of results showed that the flutterometer is capable of predicting flutter speed with a reasonable conservatism [11, 17, 31, and 41]. However, the conservatism was not reduced even at speeds close to the critical flutter speed where the accuracy of classical methods increases inherently.

The flutterometer requires an accurate mathematical model of the test item. Although it is not possible to model the aerodynamics accurately even with a wind tunnel

testing, the structural parameters and the associated uncertainties can be modeled accurately with the help of ground vibration test data. Potter and Lind [42] demonstrated such a use of ground vibration test data and observed that analyzing the data using an ∞-norm approach generates a model with less uncertainty than the corresponding 1-norm or 2-norm approaches. Smaller uncertainty definitions are useful for flight tests because the associated robust flutter speeds can be computed with less conservatism. The Aerostructures Test Wing was used to demonstrate the procedure.

2.4.5.2 Nominal Aeroelastic Analysis

The first step in the flutterometer method is to construct a mathematical model of the structure with an unsteady aerodynamic coupling. The aerodynamic equations are usually derived from unsteady panel codes such as MSC.Nastran Aeroelasticity modules. Thus a general formulation will be given here such that the outputs of the unsteady aeroelastic codes are compatible with the formulation. However, the typical section, which will be used as a case study, has a specific formulation and it will be shown that a nondimensional time formulation is more suitable to use with this method.

Consider the generalized equation of motion for the structural response, $\{\eta\}$, of the aircraft by considering it as a system with n modes as

$$[M]\{\ddot{\eta}\}+[C]\{\dot{\eta}\}+[K]\{\eta\}+q[Q(s)]\{\eta\}=\{0\} \tag{2-32}$$

where $[M] \in \boldsymbol{R}^{nxn}$ is the mass matrix, $[C] \in \boldsymbol{R}^{nxn}$ is the viscous damping matrix, $[K] \in \boldsymbol{R}^{nxn}$ is the stiffness matrix, $q \in \boldsymbol{R}$ is a scalar representing the dynamic pressure, $[Q(s)] \in \boldsymbol{C}^{nxn}$ as the matrix of unsteady aerodynamic forces, and s is the Laplace variable. This equation is valid for a particular Mach number, since $[Q(s)]$ changes with Mach number. The frequency dependent values of $[Q(s)]$ can be derived using

finite element structural models of the aircraft and panel methods for unsteady aerodynamic force calculations. Unsteady aerodynamic forces can be approximated with lag terms as Padé approximation or finite dimensional state space systems as Karpel's method, [43]. Assume [*Q(s)*] in state space form to be similar to Karpel's form as shown below.

$$[Q(s)] = \left[\begin{array}{c|c} [A_Q] & [B_Q] \\ \hline [C_Q] & [D_Q] \end{array}\right] = [D_Q] + [C_Q](s[I] - [A_Q])^{-1}[B_Q] \tag{2-33}$$

Given the number of generalized states, n, and the number of aerodynamic states, $\{n_Q\}$, define $[A_Q] \in \boldsymbol{R}^{n_Q \times n_Q}$, $[B_Q] \in \boldsymbol{R}^{n_Q \times n}$, $[C_Q] \in \boldsymbol{R}^{n \times n_Q}$, $[D_Q] \in \boldsymbol{R}^{n \times n}$ as the elements of the state space system approximation. Consider the force vector, $\{y\}$, generated by the state vector, $\{\eta\}$. Define $\{x\} \in \boldsymbol{R}^{n_Q}$ as the vector of aerodynamic states.

$$\{y\} = [Q(s)]\{\eta\} \Leftrightarrow \begin{bmatrix} \{\dot{x}\} \\ \{y\} \end{bmatrix} = \begin{bmatrix} [A_Q] & [B_Q] \\ [C_Q] & [D_Q] \end{bmatrix} \begin{bmatrix} \{x\} \\ \{\eta\} \end{bmatrix} \tag{2-34}$$

Then the equation of motion becomes

$$\begin{aligned} \{0\} &= [M]\{\ddot{\eta}\} + [C]\{\dot{\eta}\} + [K]\{\eta\} + q[Q(s)]\{\eta\} \\ &= [M]\{\ddot{\eta}\} + [C]\{\dot{\eta}\} + [K][\eta] + q\{y\} \\ &= [M]\{\ddot{\eta}\} + [C]\{\dot{\eta}\} + [K]\{\eta\} + q\left([C_Q]\{x\} + [D_Q]\{\eta\}\right) \\ &= [M]\{\ddot{\eta}\} + [C]\{\dot{\eta}\} + \left([K] + q[D_Q]\right)\{\eta\} + q[C_Q]\{x\} \end{aligned} \tag{2-35}$$

where

$$\{\dot{x}\} = \left[A_Q\right]\{x\} + \left[B_Q\right]\{\eta\}. \tag{2-36}$$

So the state space representations of the system including the aerodynamic states can be formed as

$$\begin{bmatrix}\{\dot{\eta}\}\\ \{\ddot{\eta}\}\\ \{\dot{x}\}\end{bmatrix} = \begin{bmatrix}[0] & [I] & [0]\\ -[M]^{-1}\left([K]+q\left[D_Q\right]\right) & -[M]^{-1}[C] & -q[M]^{-1}\left[C_Q\right]\\ \left[B_Q\right] & [0] & \left[A_Q\right]\end{bmatrix}\begin{bmatrix}\{\eta\}\\ \{\dot{\eta}\}\\ \{x\}\end{bmatrix} \tag{2-37}$$

The flutter occurs when the system becomes unstable at a particular dynamic pressure and Mach number. This stability problem can be solved by the robust stability concept by introducing a perturbation to the dynamic pressure as an additive uncertainty, $\delta_q \in \boldsymbol{R}$, on the nominal dynamic pressure, q_0, as

$$q = q_0 + \delta_q \tag{2-38}$$

Substituting the new dynamic pressure term in the equation of motion and separating the terms that involve δ_q, one obtains

$$\begin{aligned}\{0\} &= [M]\{\ddot{\eta}\} + [C]\{\dot{\eta}\} + \left([K]+q\left[D_Q\right]\right)\{\eta\} + q\left[C_Q\right]\{x\}\\ &= [M]\{\ddot{\eta}\} + \left[[C]\{\dot{\eta}\} + \left([K]+q_0\left[D_Q\right]\right)\{\eta\} + q_0\left[C_Q\right]\{x\}\right] + \delta_q\left[\left[D_Q\right]\{\eta\} + \left[C_Q\right]\{x\}\right]\\ &= \{\ddot{\eta}\} + \left[[M]^{-1}[C]\{\dot{\eta}\} + [M]^{-1}\left([K]+q_0\left[D_Q\right]\right)\{\eta\} + q_0[M]^{-1}\left[C_Q\right]\{x\}\right]\\ &\quad + \delta_q\left[[M]^{-1}\left[D_Q\right]\{\eta\} + [M]^{-1}\left[C_Q\right]\{x\}\right]\end{aligned} \tag{2-39}$$

The term $\left[\left[M\right]^{-1}\left[D_Q\right]\{\eta\}+\left[M\right]^{-1}\left[C_Q\right]\{x\}\right]$ is a linear combination of states and can be treated as an output, $\{z\}$, of the plant which will be fed to the uncertainty block. Define, $\{w\}$ related to $\{z\}$ such that

$$\{w\}=\delta_q\{z\}. \tag{2-40}$$

Then the system equation becomes

$$\begin{aligned}\{0\} &= \{\ddot{\eta}\}+\left[\left[M\right]^{-1}\left[C\right]\{\dot{\eta}\}+\left[M\right]^{-1}\left(\left[K\right]+q_0\left[D_Q\right]\right)\{\eta\}+q_0\left[M\right]^{-1}\left[C_Q\right]\{x\}\right]+\delta_Q\{z\}\\ &= \{\ddot{\eta}\}+\left[\left[M\right]^{-1}\left[C\right]\{\dot{\eta}\}+\left[M\right]^{-1}\left(\left[K\right]+q_0\left[D_Q\right]\right)\{\eta\}+q_0\left[M\right]^{-1}\left[C_Q\right]\{x\}\right]+\{w\}\end{aligned} \tag{2-41}$$

which can be represented in state space form as

$$\left[\begin{array}{c}\{\dot{\eta}\}\\ \{\ddot{\eta}\}\\ \{\dot{x}\}\\ \hline \{z\}\end{array}\right]=\left[\begin{array}{ccc|c} [0] & [I] & [0] & [0]\\ -\left[M\right]^{-1}\left(\left[K\right]+q_0\left[D_Q\right]\right) & -\left[M\right]^{-1}\left[C\right] & -q_0\left[M\right]^{-1}\left[C_Q\right] & -[I]\\ \left[B_Q\right] & [0] & \left[A_Q\right] & [0]\\ \hline \left[M\right]^{-1}\left[D_Q\right] & [0] & \left[M\right]^{-1}\left[C_Q\right] & [0]\end{array}\right]\left[\begin{array}{c}\{\eta\}\\ \{\dot{\eta}\}\\ \{x\}\\ \hline \{w\}\end{array}\right] \tag{2-42}$$

The perturbation, δ_q, is not an explicit parameter in the state space model because δ_q only affects the plant through a feedback relationship $\{w\}=\delta_q\{z\}$. Define the transfer function matrix $[P(s)]$ such that $\{z\}=[P(s)]\{w\}$ and the stability problem can be expressed in μ framework as in Figure 5.

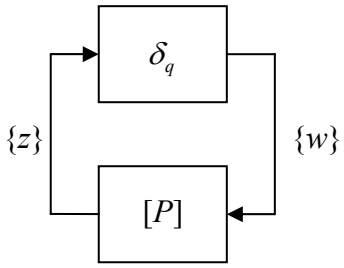

Figure 5. LFT system for nominal stability analysis in the μ framework.

The question now becomes "What is the largest perturbation to dynamic pressure for which the nominal aeroelastic dynamics remains stable?" Using robust stability analysis tools and small gain theorem, this largest perturbation to dynamic pressure for which the nominal aeroelastic system is still stable can be found. For a stable system with $\mu([P]) < 1/\alpha$, $\|\delta_q\|_\infty = \alpha$ is the largest perturbation to dynamic pressure for which the nominal aeroelastic system is stable. Instead of calculating the μ norm, a pole tracking of the closed system with various perturbation levels would also give the critical flutter speed with less mathematical calculations.

2.4.5.3 Robust Aeroelastic Analysis

Analytical model of an aeroelastic system is prone to many uncertainties such as stiffness, damping, and aerodynamic force uncertainties. These uncertainties must be estimated or measured by some ground tests. Overestimated uncertainties will result in too conservative flutter margins. On the other hand, underestimated uncertainties will result in a less robust flutter estimation. However, in either case, the estimated flutter boundary will be more conservative than the estimation obtained from P-K method or nominal aeroelastic model.

Figure 6 shows the stability formulation in μ framework with an additional structured uncertainty block, which represents the structural and aerodynamic uncertainties

such that $\left\|[\Delta]\right\|_\infty \le 1$. The uncertainties associated with the structure can be represented by stiffness and damping matrix variations in the form of additive or multiplicative uncertainties and/or by a dynamic uncertainty in the input or output. Aerodynamic uncertainties can be represented by pole location uncertainty or aerodynamic matrix uncertainty in the form of additive or multiplicative uncertainties.

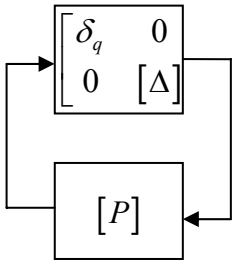

Figure 6. LFT system for robust stability analysis in the μ framework.

Imposing the norm bound for δ_q operators as $\left\|\delta_q\right\|_\infty \le 1$ may seem overly restrictive because the units of δ_q are the same as the units of q in the model. This condition implies that the total uncertainty block considers the range of flight conditions $q = q_0 \pm 1$ Pa for plants formulated by dynamic pressure in units of Pa. Such small range of flight conditions is not useful for a stability analysis unless q_0 is extremely close to the flutter pressure. This limitation is avoided by introducing a weighting function, W_q, to the computation of q.

$$q = q_0 + W_q \delta_q \tag{2-43}$$

A $W_q > 1$ allows a large range of flight conditions to be considered despite the unity norm bound constraint on δ_q. This weighting is incorporated into the stability analysis by scaling the feedback signals between the δ_q operator and the plant [P] to form the scaled plant, $\left[\overline{P}\right]$.

$$\left[\bar{P}\right] = [P]\begin{bmatrix} W_q[I] & [0] \\ [0] & [I] \end{bmatrix} \tag{2-44}$$

A robust flutter margin is computed by analyzing μ($\left[\bar{P}\right]$) with respect to uncertainties. The robust flutter pressure is determined by iterating over scales of W_q until the smallest pressure $q=q_0+W_q$ is found for which the $\left[\bar{P}\right]$ is just robustly stable.

The uncertainty description can contain structural, aerodynamic, unmodeled dynamic, and measurement uncertainties. Although it is possible to model the structure accurately with high quality ground vibration test data, the flight test item will be slightly different than the ground test item. Each aircraft would have a different set of structural parameters because of manufacturing processes and wear. Some parameters would also change during flight tests because of the fuel consumption which will cause changes in the mass distribution, because of differences in hydraulic pressure, and because of temperature variations. But the changes in structural parameters are expected to be the least changing parameters compared to other uncertainties. The stiffness and damping matrices are modeled with additive or multiplicative uncertainty descriptions. The uncertainty descriptions on inverted parameters such as mass matrix, which is inverted to get the state space equations of motion, can result in an ill conditioning. On the other hand, the aerodynamic parameters are the most difficult parameters to estimate. Thus uncertainties on the aerodynamic parameters usually show high variations. The effects of higher structural modes that are not included in the model and inaccurate mode shapes can be described by dynamic uncertainties with less conservatism compared to the parametric uncertainties. These dynamic uncertainties are typically complex in order to represent the errors in both magnitude and phase. If the data acquisition system that is used to collect measurements have serious reliability problems with some known error bounds, or the excitation signal is not measured but

assumed, or the flight conditions are known to be variable during the acquisition, then a frequency varying uncertainty can be added to the output signals to describe all these problems. These uncertainties are not because of the mathematical modeling but because of the test setup and test conditions. The modeled uncertainties associated with the test setup and test conditions will further increase the conservatism on flutter predictions.

The most appropriate type of the uncertainty description is completely problem dependent. Each uncertainty description will increase the conservatism on flutter prediction and unrealistic uncertainties will cause unrealistic results rather then robust results. So each uncertainty description and type should be selected carefully. The selection of an uncertainty as parametric, complex, frequency varying, additive or multiplicative requires some extensive pre-analysis studies supported with experiments.

The mathematical modeling for robust flutter analysis can be performed in a similar way as that presented on nominal flutter analysis, which is given through Equations 2-7 to 2-10.

2.4.5.4 Incorporating Flight Data

Generating a model by analyzing flight data is essential for a reliable stability analysis. A nominal model generated purely from the analytical equations of the predicted aircraft dynamics may not accurately describe the true aircraft. A model must be generated that accounts for the flight data to ensure the predicted dynamics represent the true dynamics.

The most direct method of generating a model from the flight data is to identify a system model entirely from the data measurements. Several such system identification algorithms exist that have become standard tools for systems and control engineers. The direct application of these methods to aeroelastic systems

rarely produces an accurate model that accounts for the dynamics of the aircraft. The aeroelastic response data is typically of poor quality relative to the ground vibration test data because of its low signal to noise ratio. The noise and unobserved dynamics in flight test may drastically lower the effectiveness of the system identification algorithms. An alternative method is to use the nominal aircraft dynamical model as an initial estimate to model the true aircraft. The flight data are then used to update the elements of this model.

Two basic methods are proposed to update the full structural model using comparisons between experimental and predicted data. One method updates the mass and stiffness matrices of the finite element model [44]. This method suffers from the lack of physical interpretation of the matrix updates and possible numerical ill conditioning. Another approach is to update some specific parameters in the model. This approach is usually accurate for small systems but may require an excessive computational cost for large systems.

The approach used by the flutterometer method is to update only the uncertainty operators of the robust aeroelastic model by using the flight data, and leave the nominal dynamics model unchanged. Figure 7 shows the flow of information through the μ method.

To update the uncertainty operators, the system must be converted to a LFT system as given in Figure 8, with forcing and response signals. The uncertainty should be scaled until $F_u([P],[\Delta])$ could generate the set of observed data y with input u.

The input-output relation in the vicinity of uncertainties can be used with the measured signals to decide on the scaling of uncertainties. The upper LFT would give the input-output relation

$$\{y\} = F_u\left([P],[\Delta]\right)\{u\} \tag{2-45}$$

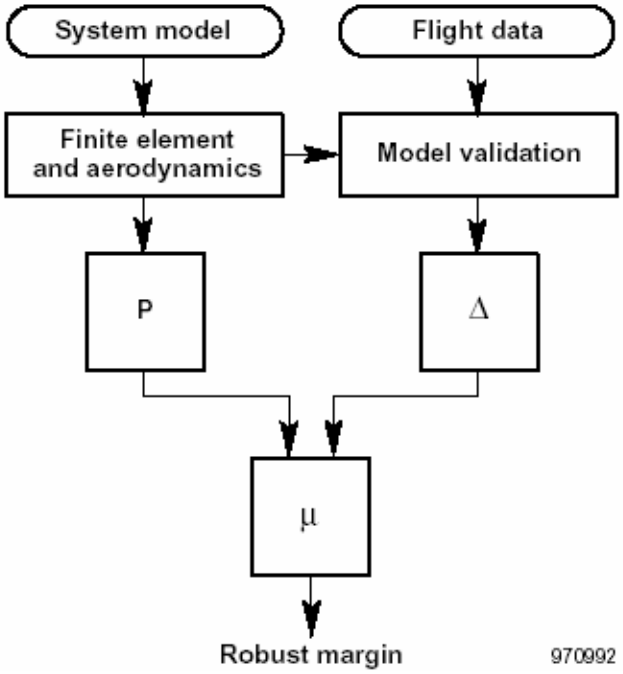

Figure 7. Flowchart to generate plant and uncertainty operators from a system model and flight data with the μ method [18].

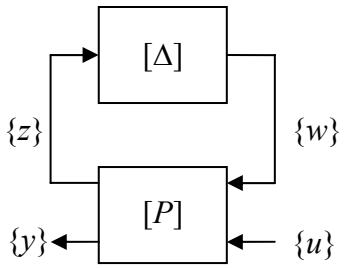

Figure 8. LFT system for robust stability analysis and model validation.

The plant, $[P]$, is partitioned to be used in LFT framework as

$$\begin{Bmatrix} \{z\} \\ \{y\} \end{Bmatrix} = \begin{bmatrix} [P_{11}] & [P_{12}] \\ [P_{21}] & [P_{22}] \end{bmatrix} \begin{Bmatrix} \{w\} \\ \{u\} \end{Bmatrix} \tag{2-46}$$

Then the upper LFT can be expressed as

$$F_u\left([P],[\Delta]\right)=[P_{22}]+[P_{21}][\Delta]\left([I]-[P_{11}][\Delta]\right)^{-1}[P_{12}] \tag{2-47}$$

By inserting Equation 2-47 into 2-45, the input-output relation can be found as in Equation 2-48.

$$y=[P_{22}]u+[P_{21}][\Delta]\left([I]-[P_{11}][\Delta]\right)^{-1}[P_{12}]u \tag{2-48}$$

The time domain signals *u* and *y* can be converted into frequency domain to combine them with the plant dynamics. Converting the signals and plant models into frequency domain and extracting the output signal from Equation 2-48 results in a useful expression as

$$[0]=\left[[P_{22}]u(j\omega)-y(j\omega)\right]+[P_{21}][\Delta]\left([I]-[P_{11}][\Delta]\right)^{-1}\left[[P_{12}]u(j\omega)\right] \tag{2-49}$$

which can be used for uncertainty updating.

Using the definitions

$$\begin{aligned}\left[\bar{P}_{12}\right]&=[P_{12}]u(j\omega)\\ \left[\bar{P}_{22}\right]&=[P_{22}]u(j\omega)-y(j\omega)\end{aligned} \tag{2-50}$$

Equation 2-49 becomes

$$[0]=\left[\bar{P}_{22}\right]+[P_{21}][\Delta]\left([I]-[P_{11}][\Delta]\right)^{-1}\left[\bar{P}_{12}\right] \tag{2-51}$$

Note that Equation 2-51 is in LFT form; so if there exists a $\|[\Delta]\| \leq 1$ that makes this LFT zero, then the postulated model can produce the output from the input data. Kumar and Balas [45] showed that the system [P] with associated uncertainty [Δ] is not invalidated if Equation 2-52 is satisfied. In this respect, the model validation test is actually an inverted robust stability test.

$$\mu\left([P_{11}]-[\bar{P}_{12}][\bar{P}_{22}]^{-1}[P_{21}]\right)>1 \tag{2-52}$$

The scaling of [Δ] is equivalent to the scaling of [P_{11}], so a model validation can be performed by scaling [P_{11}] until Equation 2-52 is just satisfied. In fact, it is not possible to say that the model is certainly validated, because it is only guaranteed that the model is not invalidated with the selected uncertainty description and used measured signals. After deciding on the uncertainty scaling, the critical flutter speed can be calculated from the robust aeroelastic analysis as mentioned in the previous section.

2.5 Summary

In this chapter, three basic steps of flight flutter testing are investigated. These basic steps are test setup design with reference to excitation and measurement arrangements, and , and flutter prediction.

The excitation setup design depends on the available sources of excitation mechanisms. Onboard excitation systems such as inertial shakers, thrusters, aerodynamic vanes, and aircraft control surfaces can be used as excitation sources. In such cases, the excitation can be measured and controlled directly. The air turbulence can also be used as an excitation source alone. Since it is not possible to measure the turbulence excitation, some special flutter estimation methods that do not require any excitation information should be used with turbulence excitation. Advantages and disadvantages of the excitation mechanisms are discussed. Another important point in excitation system design is the selection of the excitation location. The excitation

location should be selected such that sufficient energy is transferred to the structure within the frequency range of interest to obtain useful FRFs. An optimum driving point selection algorithm is given.

The instrumentation setup design includes sensor selection and sensor location selection. Nowadays, accelerometers are commonly used to measure the response of the structure, since modern accelerometers are light, small, accurate, and easy to install. Measurement locations should be selected such that all modes of interest are observed. An optimum measurement location selection algorithm is given.

Once the aircraft is instrumented with exciters, accelerometers, and telemetry system, the actual flutter speeds of the aircraft can be predicted with the flight test data using special prediction methods. There exist several data based classical and model based modern flutter estimation methods. Commonly used methods are discussed and their mathematical implementations are given.

CHAPTER 3

SIMULATION STUDIES WITH A LINEAR AEROELASTIC MODEL

3.1 Aeroelastic Model

To simulate the experimental data, a mathematical model representing an aeroelastic 2-DOF typical section in subsonic flow is utilized in this section. This model is also used to represent the dynamics involved in the Aeroservoelastic Test Setup (ATS), which has been produced for aeroelastic and aeroservoelastic experiments in TÜBİTAK-SAGE. The details of the ATS is presented in Chapter 5.

The typical section was first devised during the 1930's by aeroelastic pioneers such as Theodorsen and Garrick, seeking a system suitable for the elementary examination of flutter and divergence problems. They suggested that the dynamics of an actual wing might be simulated by choosing the properties of the typical section to match those at a station 70-75% of the distance from root to tip. The subsequent experience confirmed their judgment in situations where the aspect ratio is large, the sweep is small, and the sectional characteristics vary smoothly across span. The typical section is not only suitable for cantilever wing simulation but also for control surface simulations.

Figure 9 shows the conventions used for positive lift, moment, vertical and angular displacement, and some important geometric properties of a typical section.

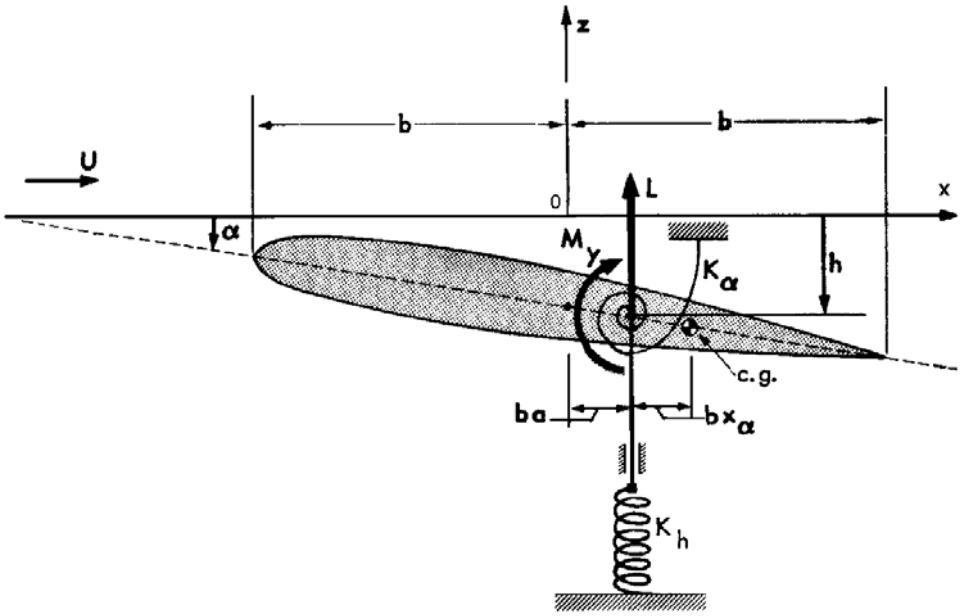

Figure 9. The typical section [1].

This convention configuration is called Theodorsen's notation, which is perfectly general. The general dynamic equations of motion for the typical section with linear structural parameters, which are commonly used in the literature for harmonic analysis, are given as follows.

$$m\ddot{h} + S_\alpha \ddot{\alpha} + (1 + i\eta)K_h h = -L + F^{ext} \tag{3-1}$$

$$S_\alpha \ddot{h} + I_\alpha \ddot{\alpha} + (1 + i\eta)K_\alpha \alpha = M_y + M^{ext} \tag{3-2}$$

where

$$S_\alpha = mbx_\alpha \tag{3-3}$$

The parameter S_α is sometimes called as the “static unbalance” or “static mass moment” of the typical section about its elastic axis located at $x=ba$. It is positive

when the center of mass is aft of the elastic axis. I_α is the mass moment of inertia about the elastic axis. Although no viscous damping is included in the equations, which is physically convenient, necessary terms can be added to the equations if needed.

Lift and moment predictions for typical sections are available for both compressible and incompressible flows for steady and unsteady cases. Calculating steady aerodynamic forces is rather simpler than calculating unsteady aerodynamic forces. This is because while calculating the dynamic response of an aerodynamic body, often steady forces are used. However, this approximation can not be used for the flutter analysis of airfoils, which are designed to obtain considerable lift. Unsteady aerodynamic forces should be used in the analysis of lifting surfaces because steady flow expressions do not contain the phase difference information, which is an important parameter in flutter calculations. With unsteady aerodynamic forces, it is also possible to observe the divergence since the asymptotic values of unsteady forces converge to steady forces as the frequency reaches zero.

Lift and moment expressions for steady flow, harmonic motion and arbitrary motion are given in Appendix A.

3.2 Numerical Study for Mild Flutter

The first numerical study is about a system that has a mild flutter behavior. The term "mild flutter" is used for cases where damping trends are smooth and do not change abruptly. The ATS is designed to have a low flutter speed. This is achieved by highly coupling the DOF via a large static unbalance. However a large static unbalance results in explosive type flutter, where damping decreases rapidly with flow speed. That case is studied as a separate case.

The parameters of the first system analyzed are derived from the parameters of ATS, but are modified to get a mild flutter at relatively high speeds. The resulting system

has natural frequencies similar to a real fighter aircraft. The parameters for the first system are selected as follows.

m = 12.4 kg : Total mass of moving parts of the system.
I_α = 0.065 kg.m^2 : Moment of inertia of rotating parts.
K_h = 28,444 N/m : Flexural stiffness of the airfoil.
K_α = 70.5 N.m/rad : Torsional stiffness of the airfoil.
a = -0.5 : Normalized distance between the elastic axis and midchord.
b = 0.135 m : Semichord length of the airfoil.
l = 0.54 m : Span of the airfoil.
x_α = 0.03 : Normalized distance between the elastic axis and mass center.

This airfoil has a critical flutter speed of 86.47 m/s (~0.256 Mach) at 1.1341 kg/m^3 air density (corresponding to ~800 m altitude), which is found by plotting the roots of the system versus the flight speed. The uncoupled natural frequencies are 5.24 Hz for torsion and 7.63 Hz for plunge modes.

A Matlab Simulink model is prepared for simulation studies. The details of the Simulink model are given in Appendix B. The response of the system to a half-sine pulse of 400 N peak value and 10 ms duration at the leading edge for speeds 10 m/s below and above of the critical speed are given in Figure 11 and Figure 12, respectively.

The mode shapes of the selected typical section are given in Table 1 and Figure 10. The natural frequencies of the system are 5.23 Hz and 7.65 Hz. Note that these natural frequencies are close to the uncoupled natural frequencies, which is an indication of very weak coupling.

Table 1. Mode shapes of the selected typical section.

	Mode 1 (5.23 Hz)	Mode 2 (7.65 Hz)
h	-0.0141	-0.2842
α	-3.9066	0.4136

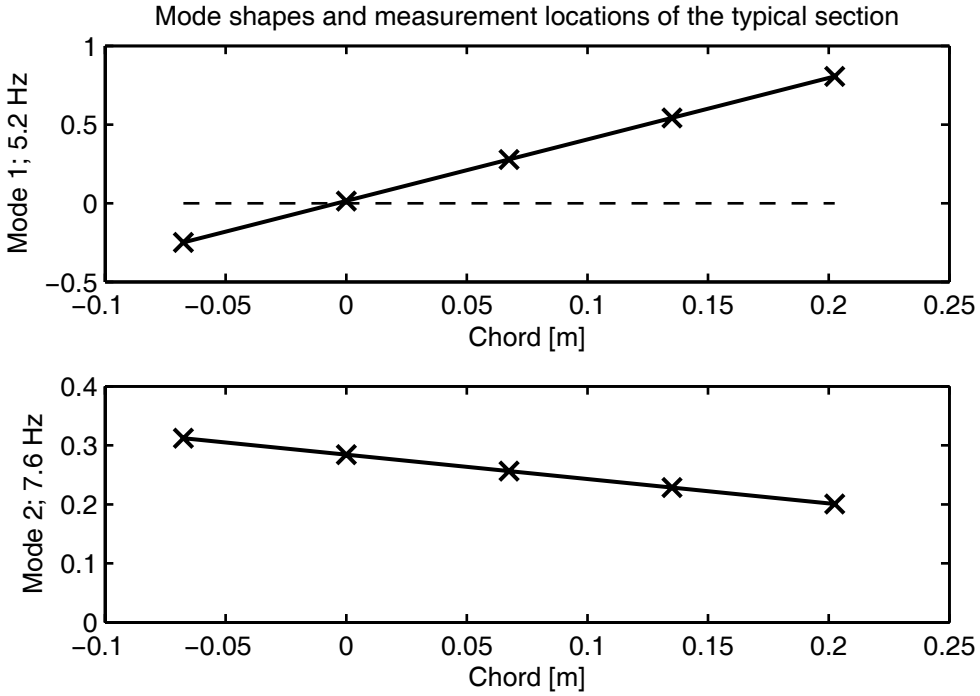

Figure 10. Mode shapes of the selected typical section.

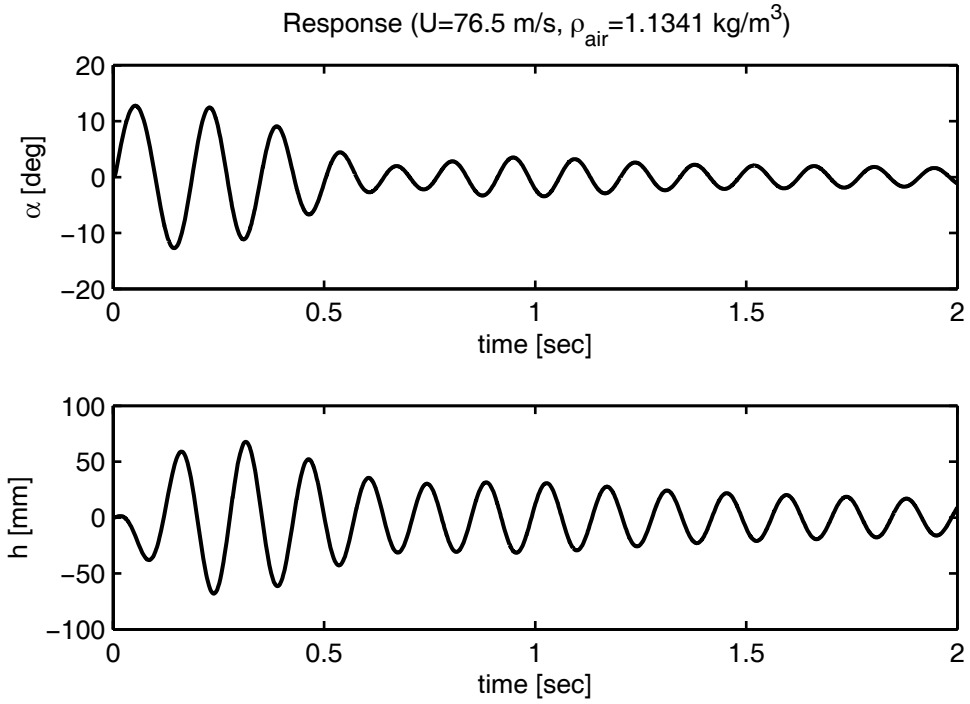

Figure 11. Pulse response of the selected typical section below the critical speed.

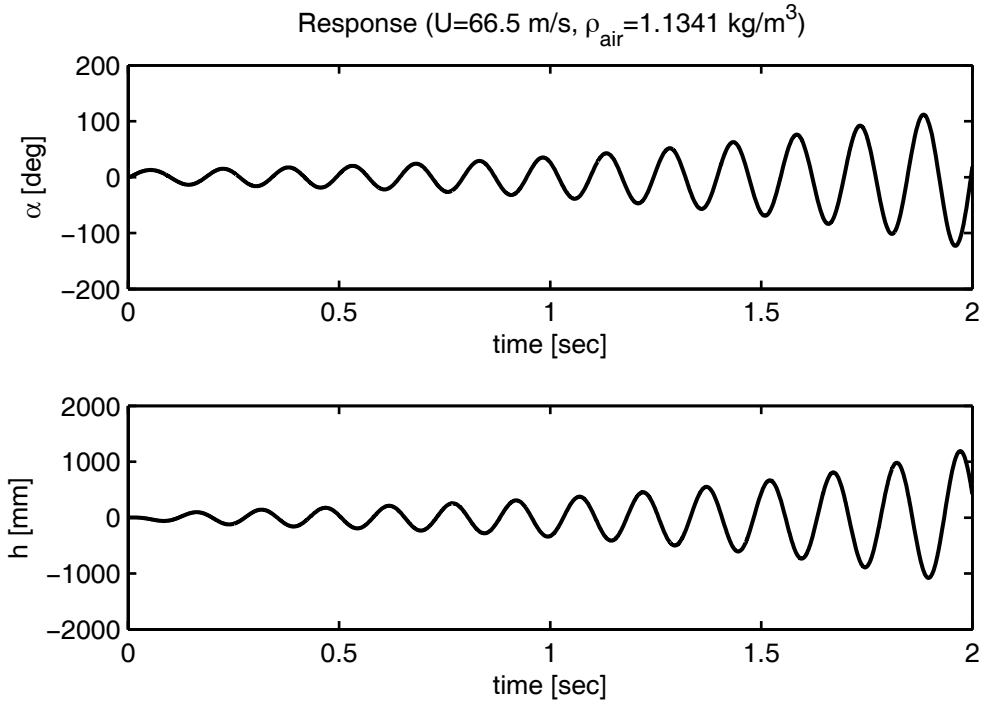

Figure 12. Pulse response of the selected typical section above the critical speed.

3.2.1 Best Measurement Points

Assume that five equally spaced locations are suitable for the measurements as shown in Figure 10. The new mode shape matrix can be constructed from the original matrix by a simple transformation in the following manner.

$$\left[\Phi^{new}\right]_{5x2} = \left[T\right]_{5x2}\left[\Phi\right]_{2x2} \tag{3-4}$$

where

$$\left[T\right] = \begin{bmatrix} -1 & 0.5b \\ -1 & 0 \\ -1 & -0.5b \\ -1 & -b \\ -1 & -1.5b \end{bmatrix} \tag{3-5}$$

The resulting new mode shape matrix is given in Table 2. In fact, the new mode shape matrix is not an eigenvector matrix in the modal sense, since only two of the five degrees of freedom are independent. In real cases, instead of this artificial expansion, the real mode shape matrix should be used to find the best measurement and excitation points.

Table 2. Expanded mode shape matrix.

Node	Description	Mode 1	Mode 2
1	Vertical displacement at x=–b/2 chord point (leading edge)	-0.2496	0.3121
2	Vertical displacement at origin x=0	0.0141	0.2842
3	Vertical displacement at x=b/2 chord point	0.2778	0.2563
4	Vertical displacement at x=b chord point	0.5415	0.2284
5	Vertical displacement at x= 3/2b chord point (trailing edge)	0.8052	0.2005

Equations 2-2 and 2-3 can be used to find the best locations for measurement. The result is given in Figure 13. As seen from the figure, the best measurement locations are around the leading and trailing edges. Since the model is a 2-DOF system and both modes are of interest, at least two measurement locations should be chosen. In real cases, it is not possible to know the number of modes within the frequency range of interest without performing some modal tests. However, all five measurement locations are used to investigate the mode extraction performance of some methods.

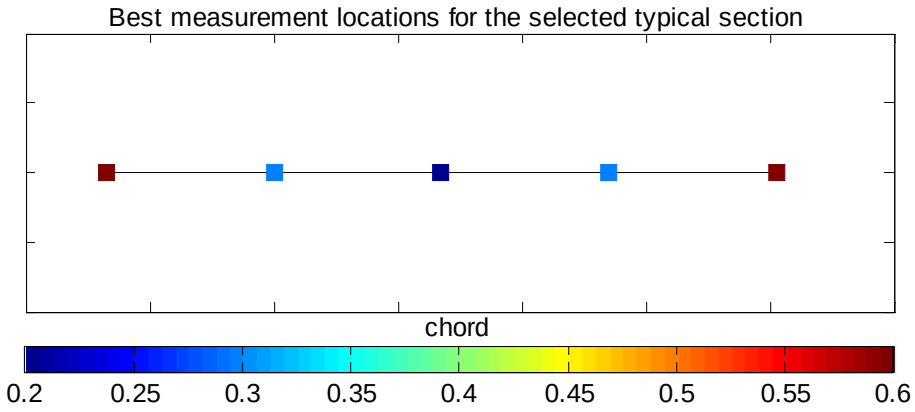

Figure 13. Best measurement points for the model (higher is better).

3.2.2 Best Excitation Points

Assume that the same measurement locations are available for excitation in the vertical direction. The ODP value of each point can be calculated by Equation 2-1. The result is given in Figure 14. As seen from the figure, the best excitation point is the trailing edge of the typical section. The number of excitation points in real cases is very limited due to the geometric and structural difficulties. Thus, in the simulations, only single excitation at the trailing edge are used.

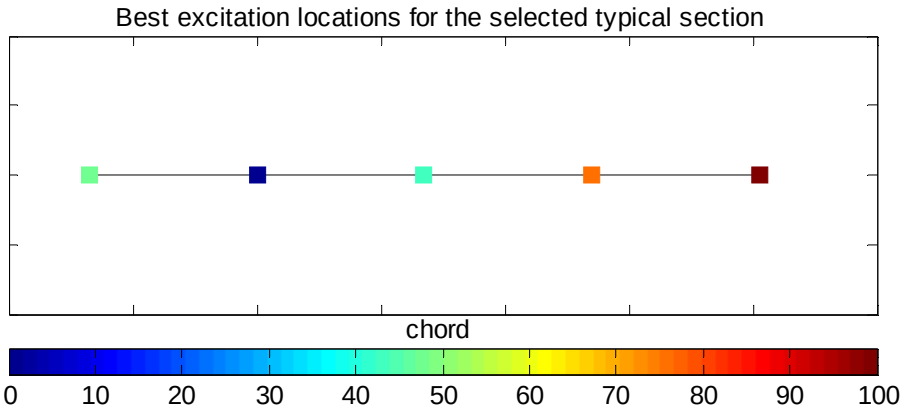

Figure 14. Best excitation points for the model (higher is better).

3.2.3 Flutter Prediction with Damping Extrapolation

The prepared Simulink model is run with different air speeds. The forcing and measurement signals are saved for an offline processing. Forcing and measurement signals are saved for airspeeds of 20, 30, 40, 50, 60, 70, 80, and 85 m/s. Here, it should be noted that the last airspeed is very close to the flutter speed. Some FRF estimations obtained by the "tfestimate" command of Matlab are given in Figure 15, Figure 16 and Figure 17. It can be seen from these figures that the best estimates belong to the leading edge (H_1) and trailing edge (H_5) measurement points. The qualities of the FRF agree with the best measurement point ranking.

The two distinct modes can be easily seen at low air speeds. As the speed increases, the damping of second mode first increases and then decreases. Meanwhile, the second natural frequency shifts to some lower values and the frequency of the first mode increases. This flutter mechanism can be observed from the FRF plots in Figure 18.

The convergence of the nonlinear least squares fit method used for fitting analytical curves to the experimental FRF's depends on the initial guess. The method can converge to a different local minimum if a proper initial guess is not used. The

coupled natural frequencies of the system can be used to construct the required initial guess. However, a pre-study is required to establish a good initial guess for the lowest speed. Once the curve fit converges, the determined parameters can be used as initial guess for the next speed.

The curve fit is performed for a frequency range of 2 to 11 Hz, which covers both modes. The fit results for all air speeds are given in figures Figure 19 to Figure 26. As seen from the figures, the curve fits performed are successful. The damping value for a nearly unstable speed, 85 m/s, is estimated to be positive near zero. The V-g plots are given in Figure 27 and Figure 28.

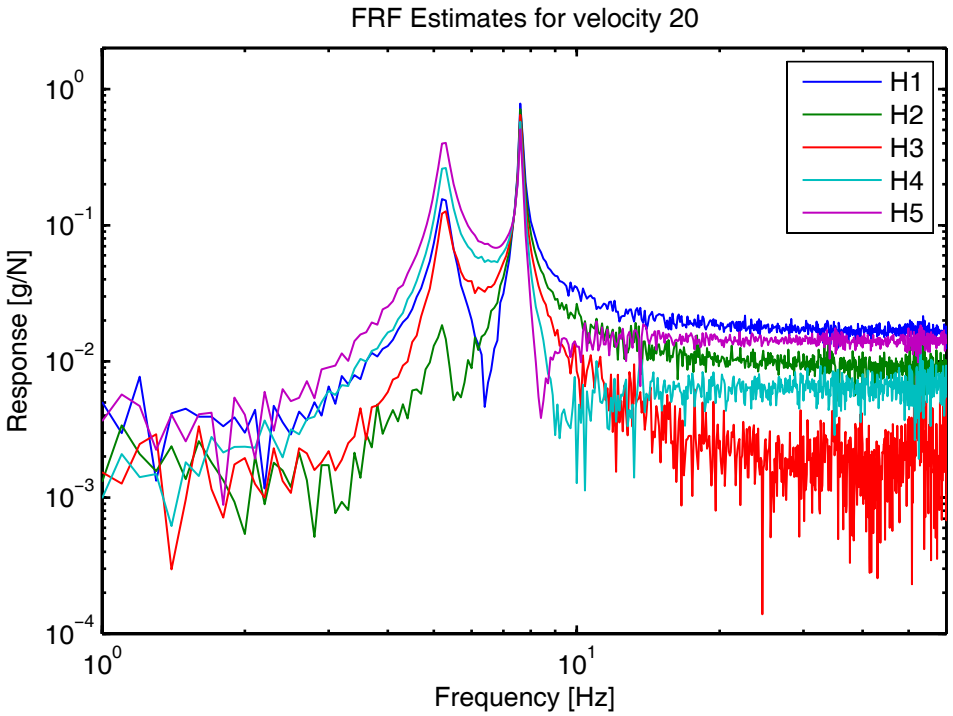

Figure 15. FRF estimates for 20 m/s.

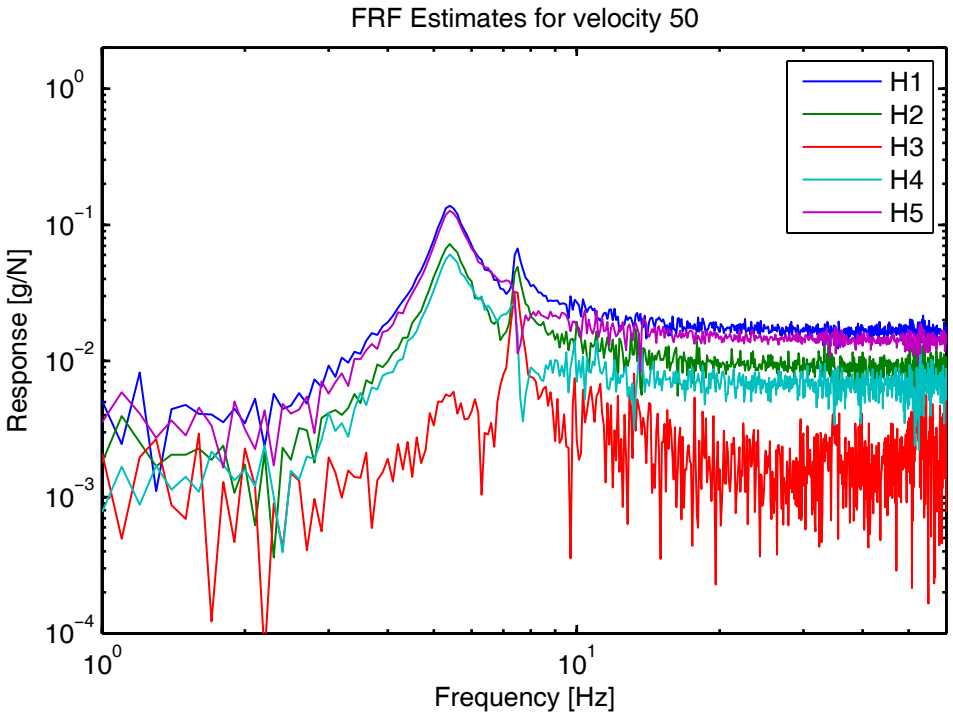

Figure 16. FRF estimates for 50 m/s.

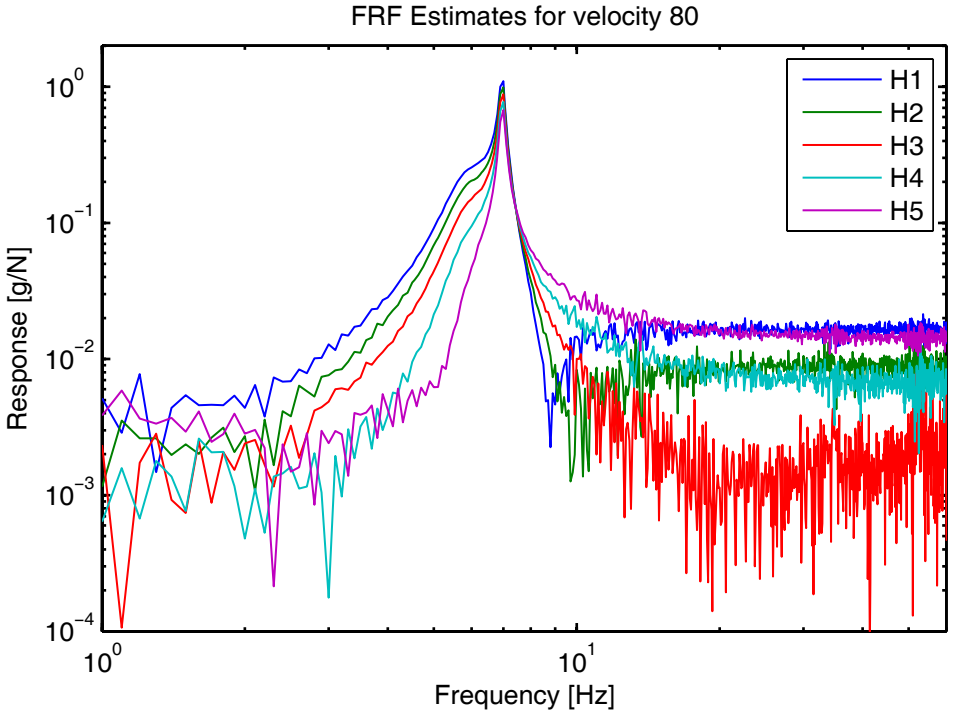

Figure 17. FRF estimates for 80 m/s.

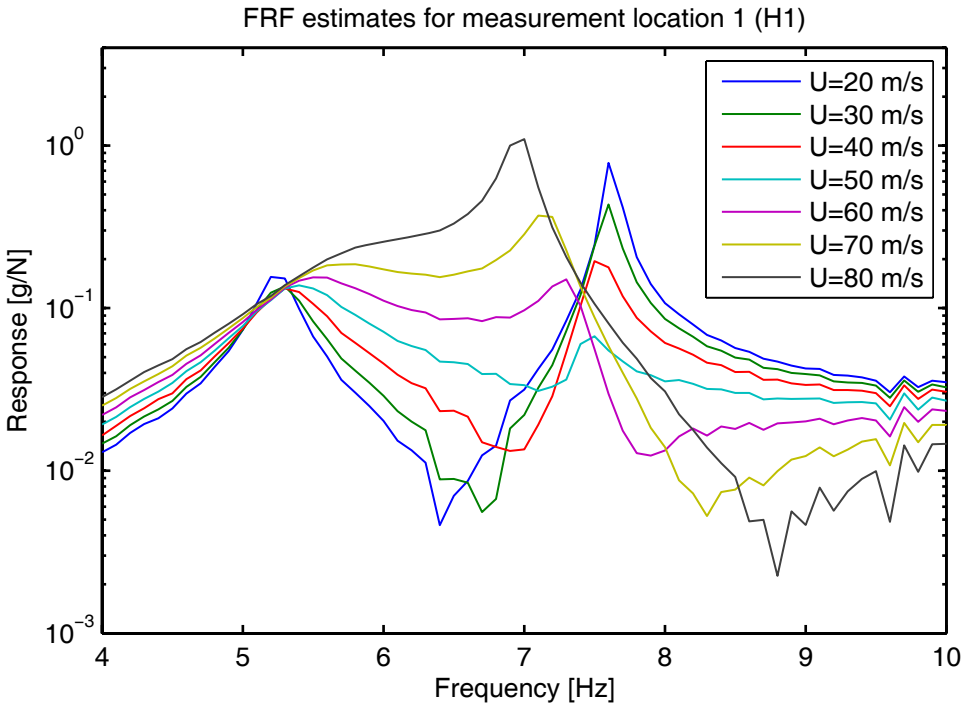

Figure 18. Change of H1 with air speed.

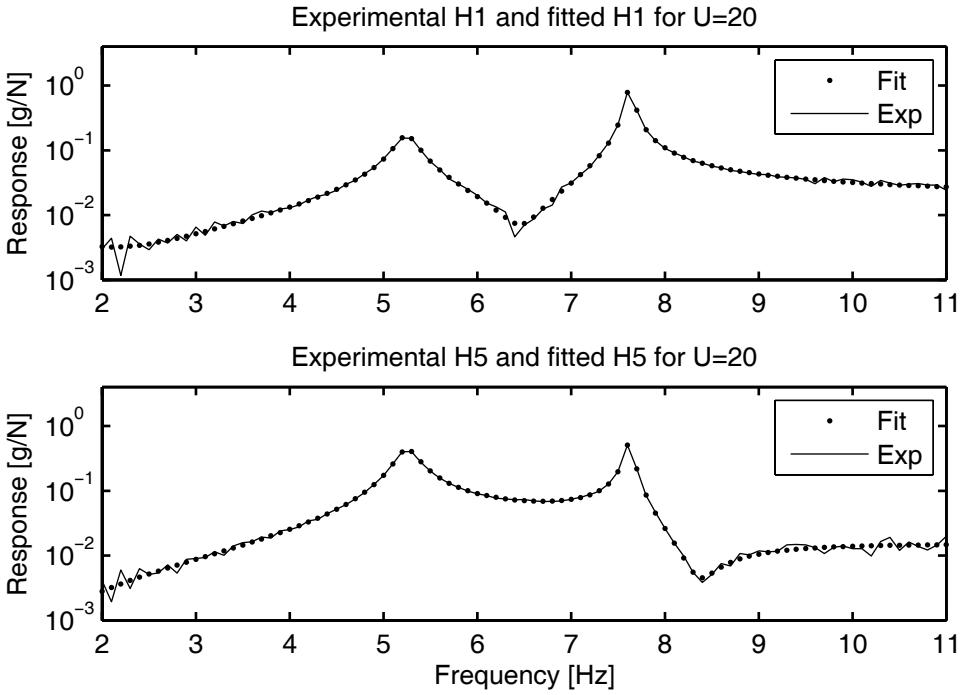

Figure 19. Fit results for 20 m/s.

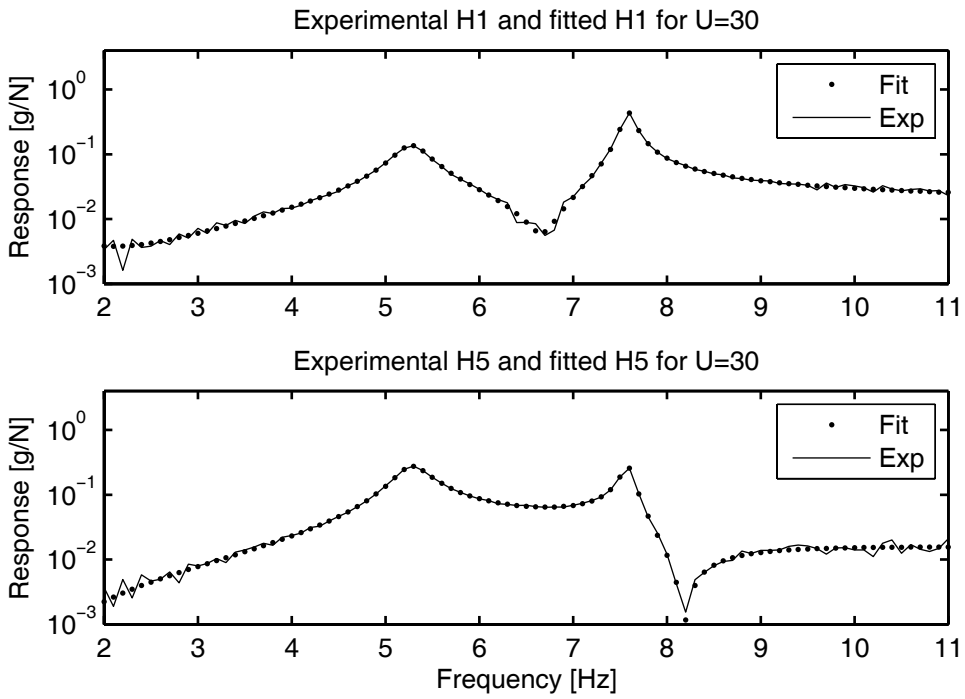

Figure 20. Fit results for 30 m/s.

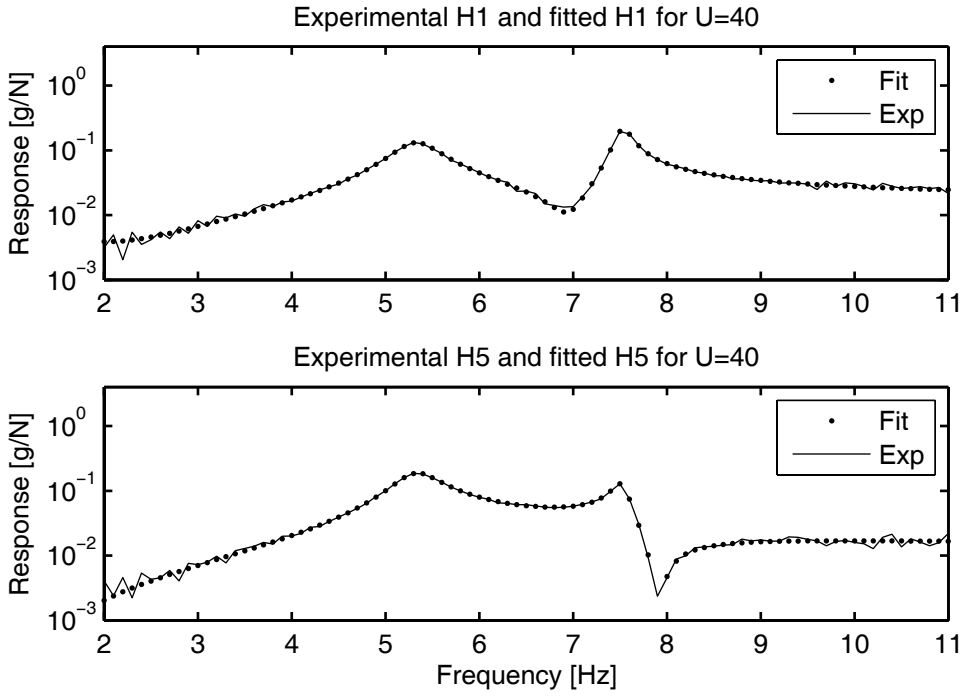

Figure 21. Fit results for 40 m/s.

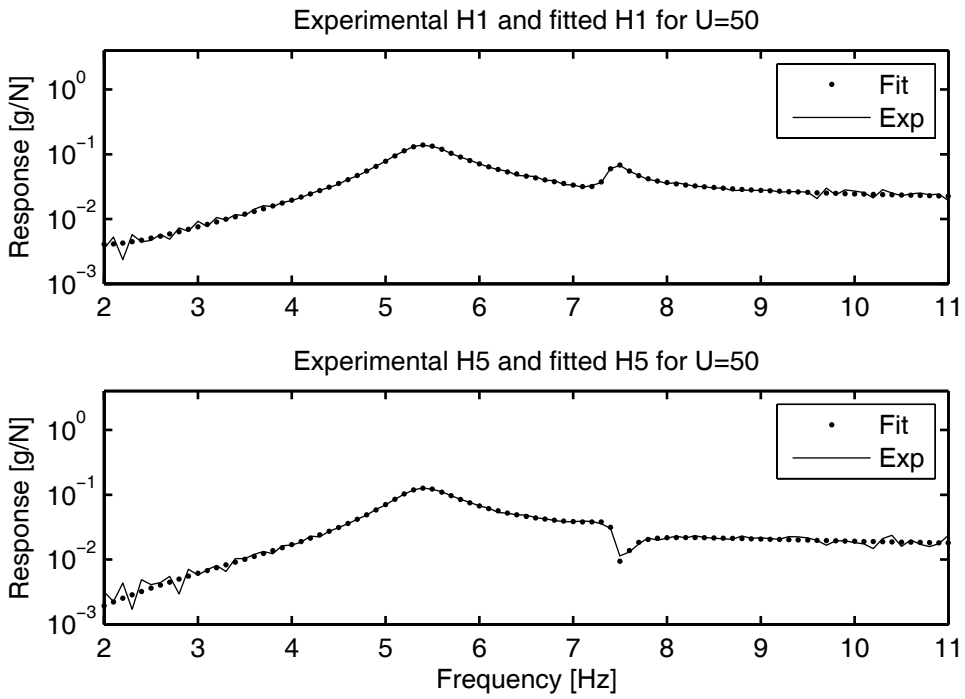

Figure 22. Fit results for 50 m/s.

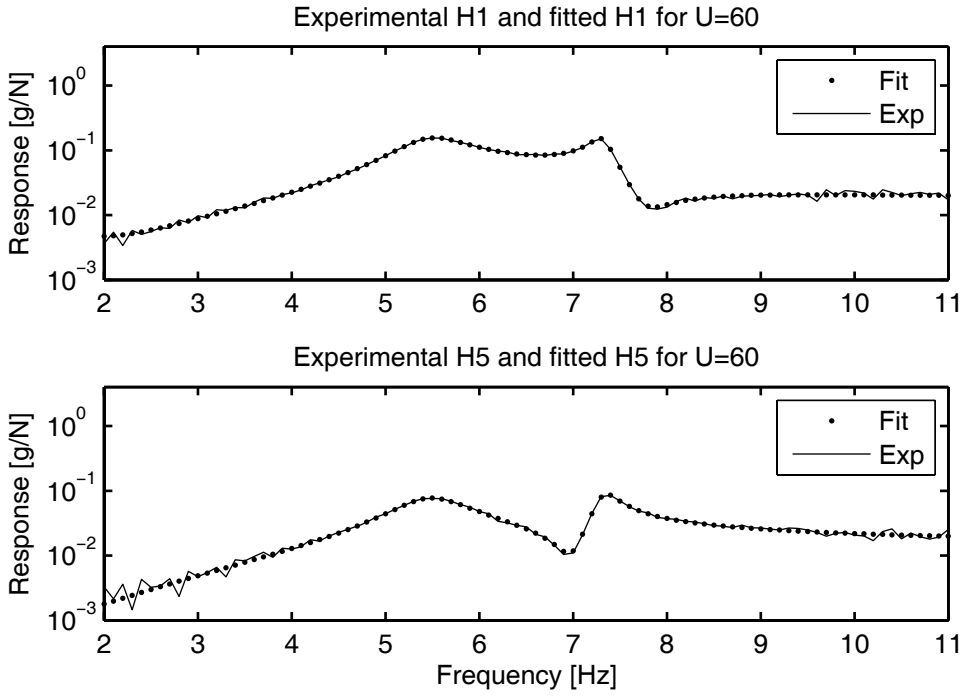

Figure 23. Fit results for 60 m/s.

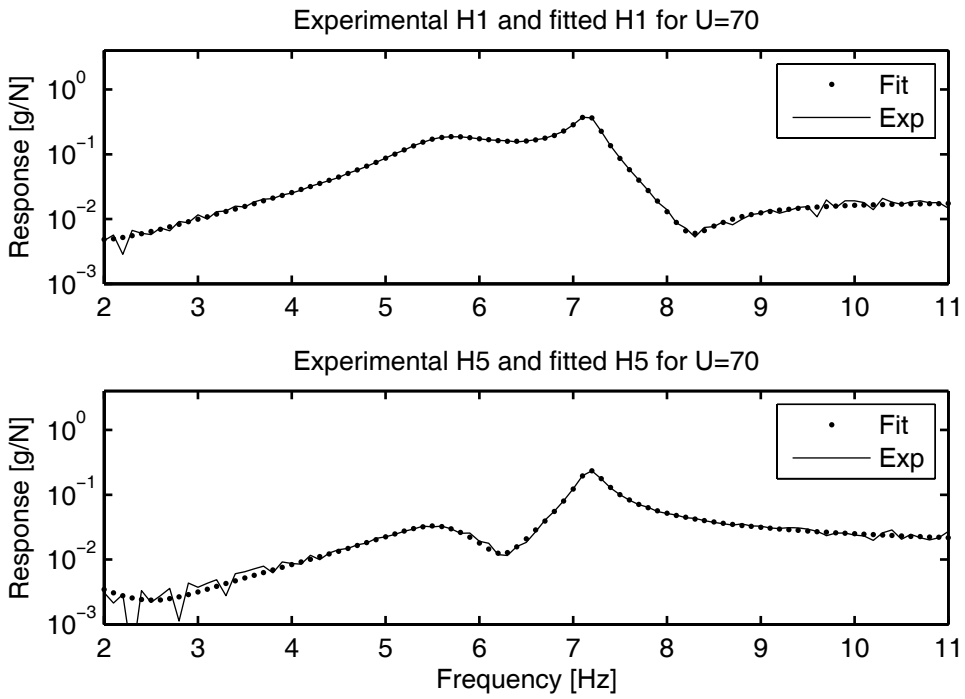

Figure 24. Fit results for 70 m/s.

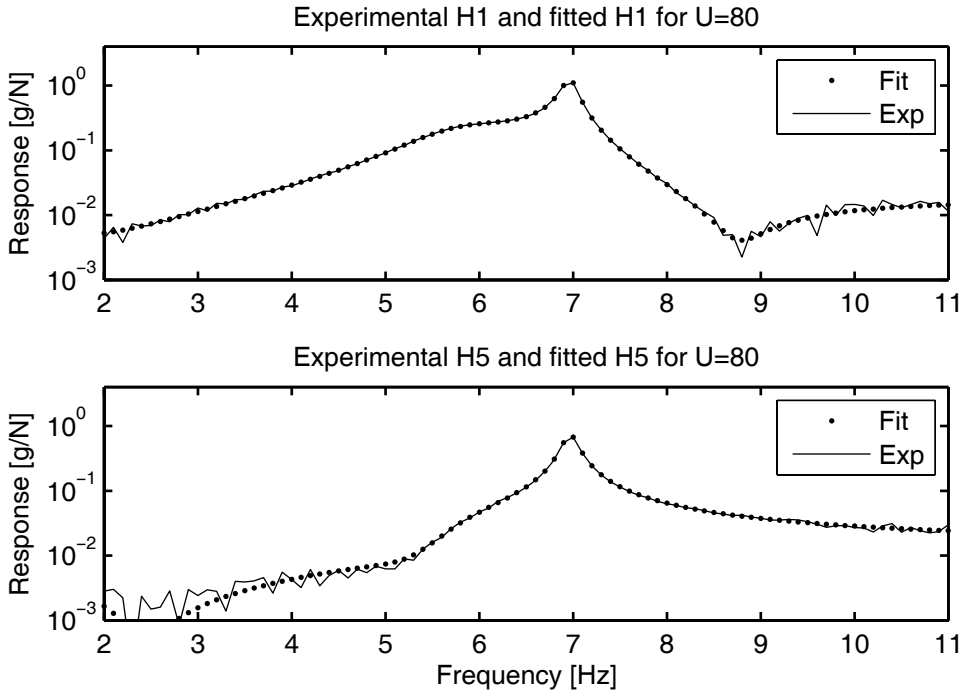

Figure 25. Fit results for 80 m/s.

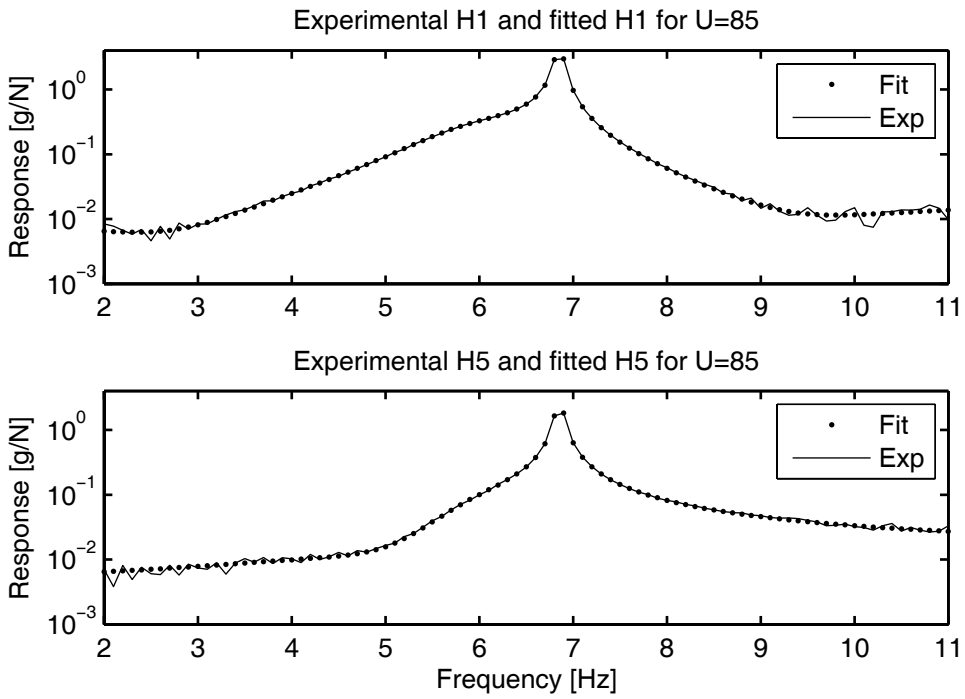

Figure 26. Fit results for 85 m/s.

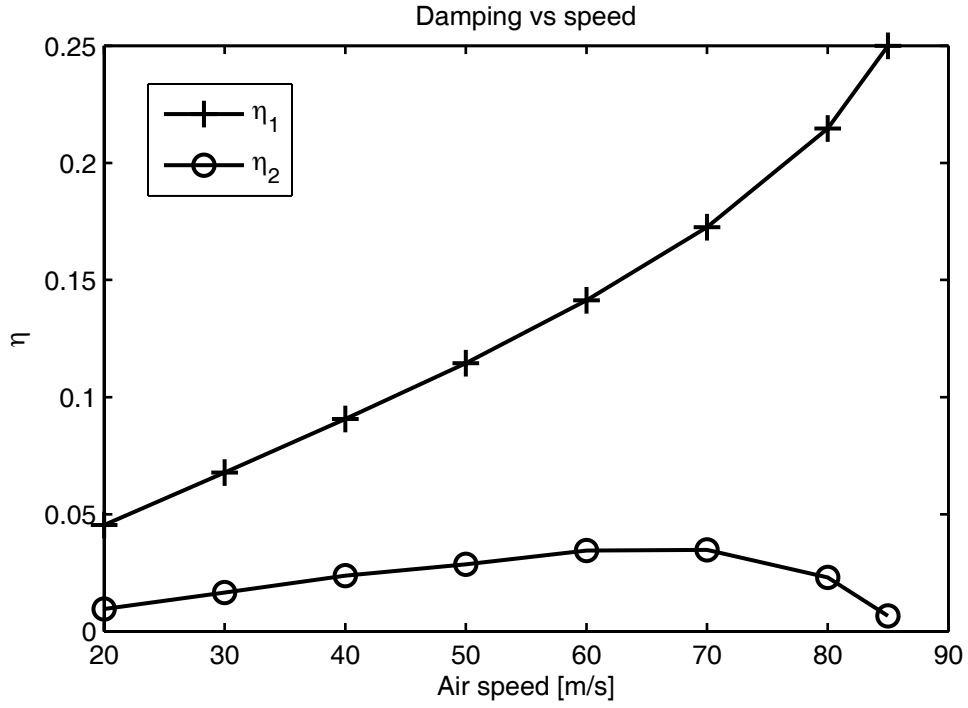

Figure 27. Damping versus speed graph.

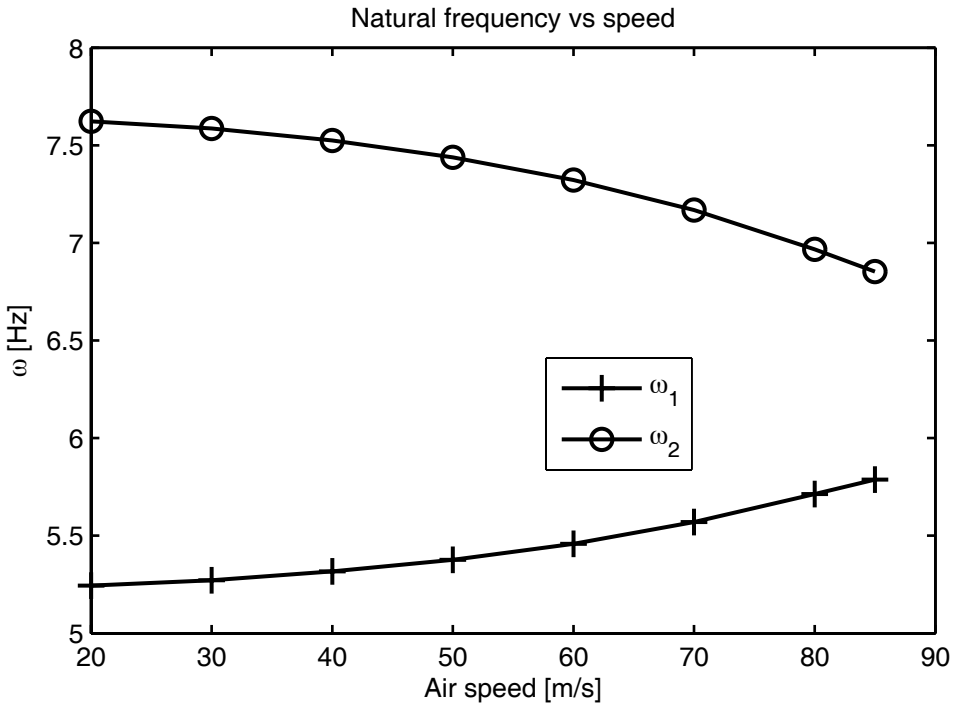

Figure 28. Natural frequency versus speed graph.

Table 3. Summary of modal extraction.

U [m/s]	20	30	40	50	60	70	80	85
η_1	0.0454	0.0678	0.0907	0.1145	0.1413	0.1725	0.2147	0.2500
η_2	0.0095	0.0166	0.0238	0.0286	0.0345	0.0348	0.0230	0.0066
ω_1 [Hz]	5.2441	5.2719	5.3166	5.3764	5.4578	5.5697	5.7131	5.7874
ω_2 [Hz]	7.6228	7.5856	7.5244	7.4385	7.3220	7.1687	6.9664	6.8531

After all these calculations, the damping extrapolation can be performed. Although there are eight flight conditions, only the low speed results can be used in real situations. Since the flutter speed is not known during real tests, it is not possible to extend the test up to 80 or 85 m/s. Before extrapolation, the order of the polynomial fit should be determined. This usually requires a preliminary study with the

aeroelastic model of the system. Usually, orders between 3 and 6 are used for extrapolation. However, high order fits such as 6th order should be used with care if damping estimates have some scatter. It is possible to fit up to 5th order polynomial with six flight conditions. However, in this case 3rd and 4th fits are investigated. The damping extrapolations with 3rd and 4th order polynomials are given in Figure 29. The extrapolation with a 3rd order polynomial results in flutter speed of 106.2 m/s, whereas the extrapolation with a 4th order polynomial results in 90.42 m/s. Both estimates are over the true flutter speed, 86.47 m/s. During real tests, the conservative estimate should be used. So, the flutter speed estimation by damping extrapolation is concluded to be 90.42 m/s, which is 4.6% higher than the real value.

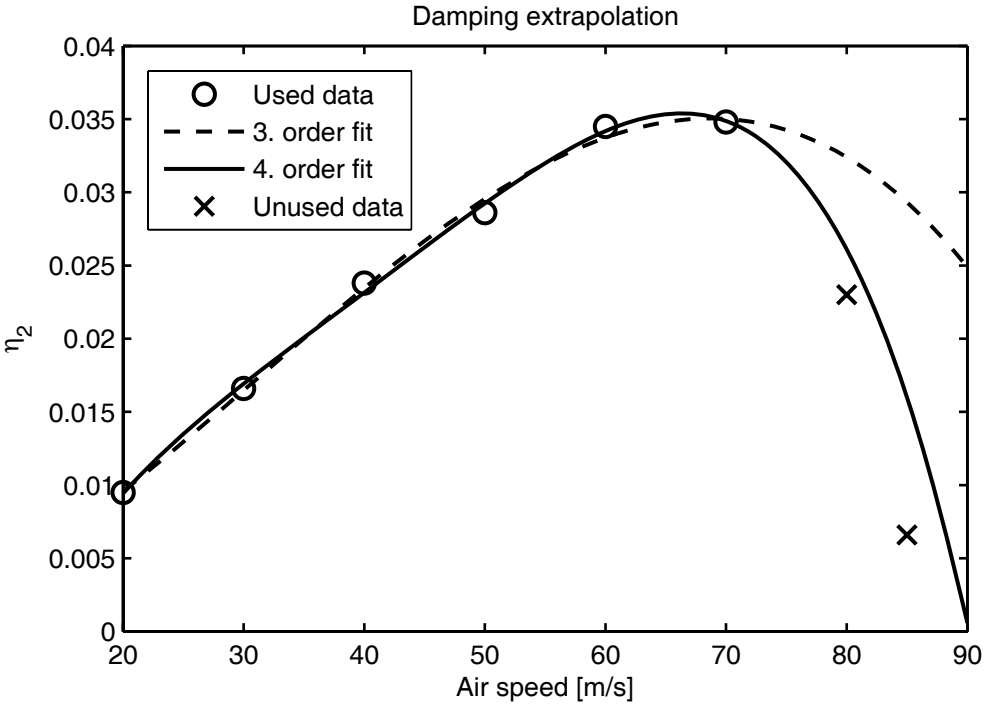

Figure 29. Damping extrapolation result.

3.2.3.1 Modal Filtering

The decoupled FRF plots calculated by using the method given in Section 2.4.1.5.1 are given in Figure 30 through Figure 37. The expanded mode shape matrix at zero air speed is used to calculate the modal filter.

$$[\psi] = \left[\Phi^{new}\right]^{-1} \tag{3-6}$$

As can be seen from these figures, the decoupling performance of the proposed method decreases with increasing velocity. The main reason is the change of phase relation between the mode shapes with increasing velocity, which is the main mechanism of flutter. Therefore, in order to use modal filters efficiently, the modal filters must be also calculated and updated during flight. This can only be done if the modal parameters at that flight condition are known. So, the modal parameters must be estimated first. Afterwards, the modal filters can be calculated. In such conditions, the pseudo inverse method is not recommended since complete and accurate estimates of all modal vectors in the frequency range of interest are required, which is difficult to obtain during flight. An incomplete model or errors in the estimate of any modal vector can propagate to all calculated modal filter vectors. However, the reciprocal or modified reciprocal modal vector method requires a least squares solution for the calculation of modal filters. Furthermore, the updating procedure requires some additional iterations to calculate the updated modal filters.

Once the modal parameters are estimated, the flutter calculations can be performed without modal filters. Thus modal filters in this case can be used as an additional post processing tool but their use is not practical for an online analysis. Because of these facts, modal filter calculations will not be carried out as further analysis in this study.

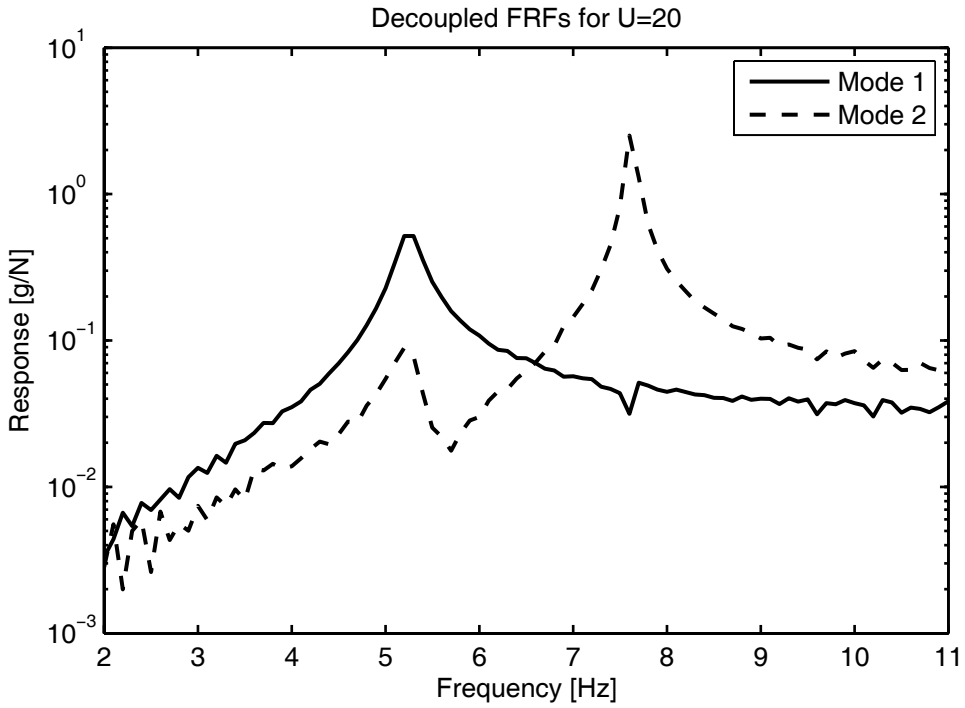

Figure 30. Decoupled FRF at U=20 m/s.

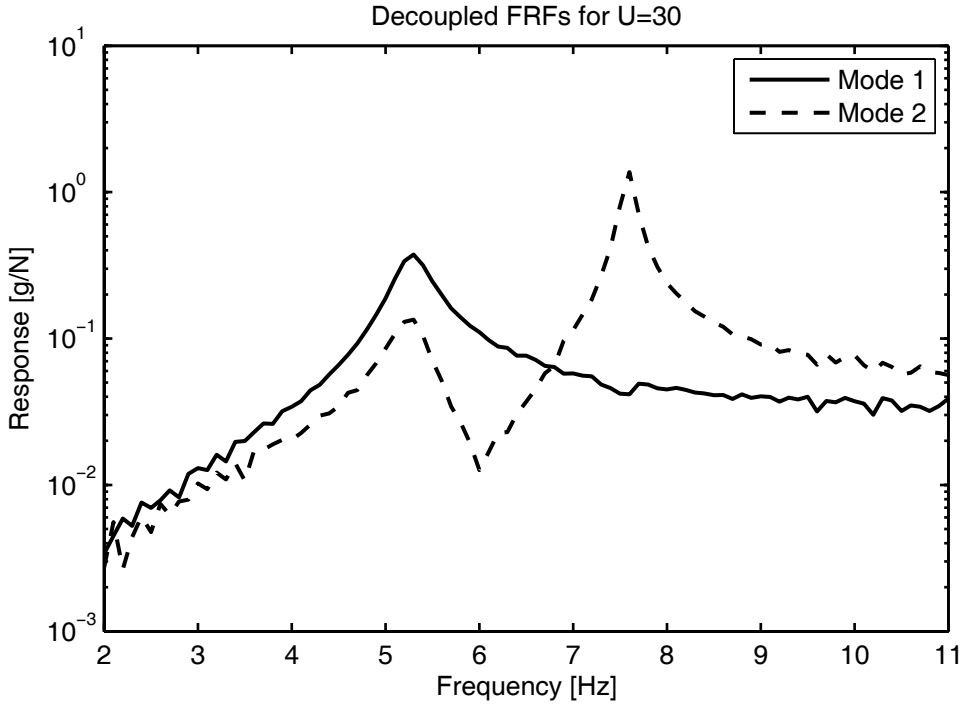

Figure 31. Decoupled FRF at U=30 m/s.

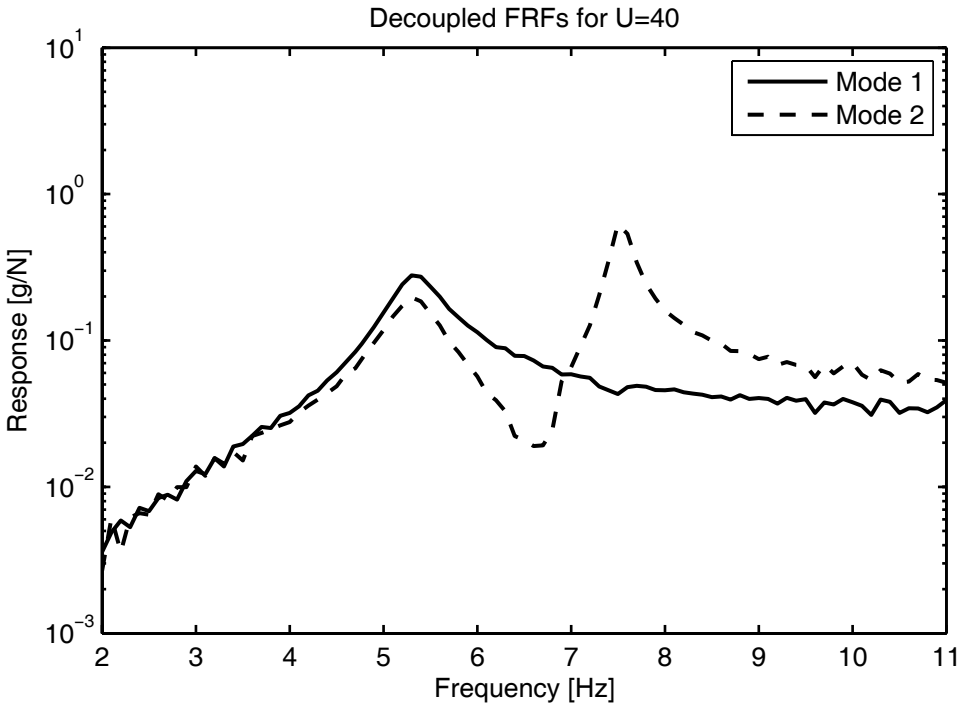

Figure 32. Decoupled FRF at U=40 m/s.

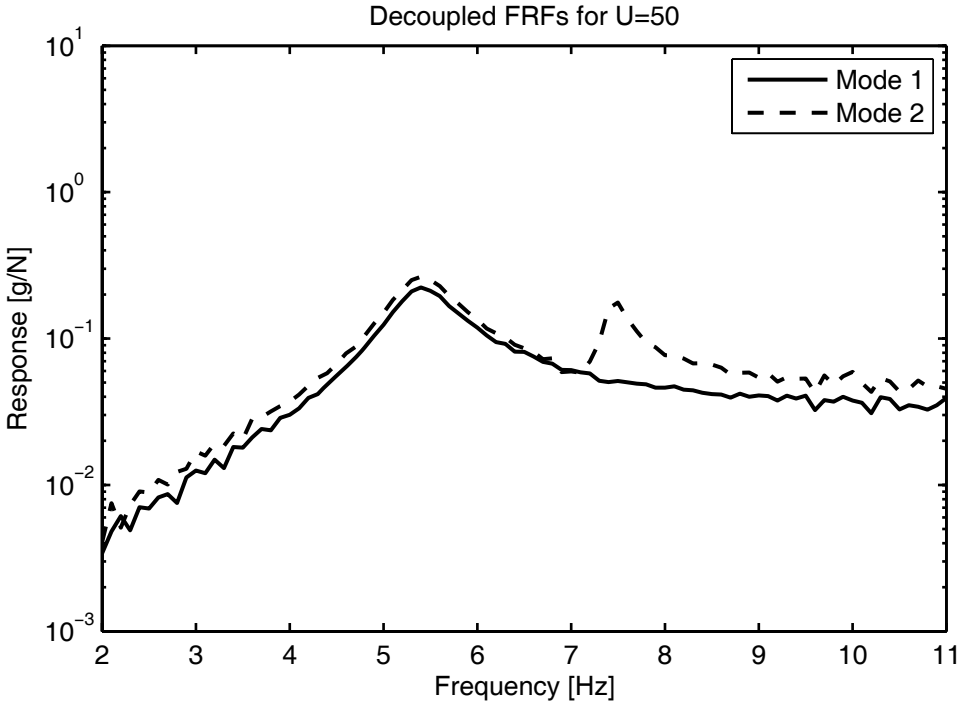

Figure 33. Decoupled FRF at U=50 m/s.

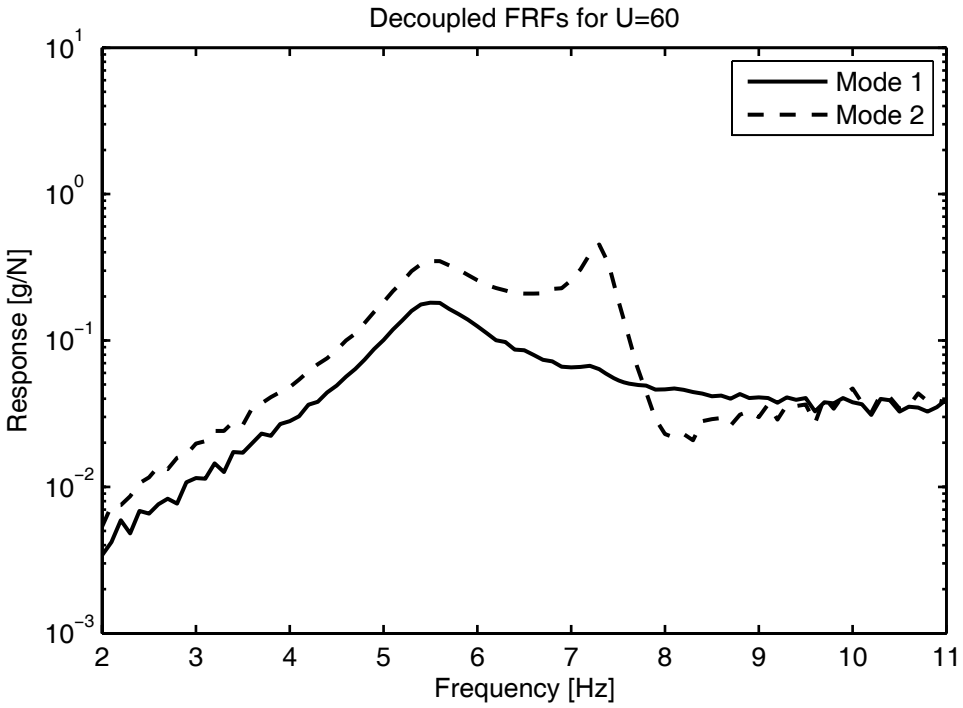

Figure 34. Decoupled FRF at U=60 m/s.

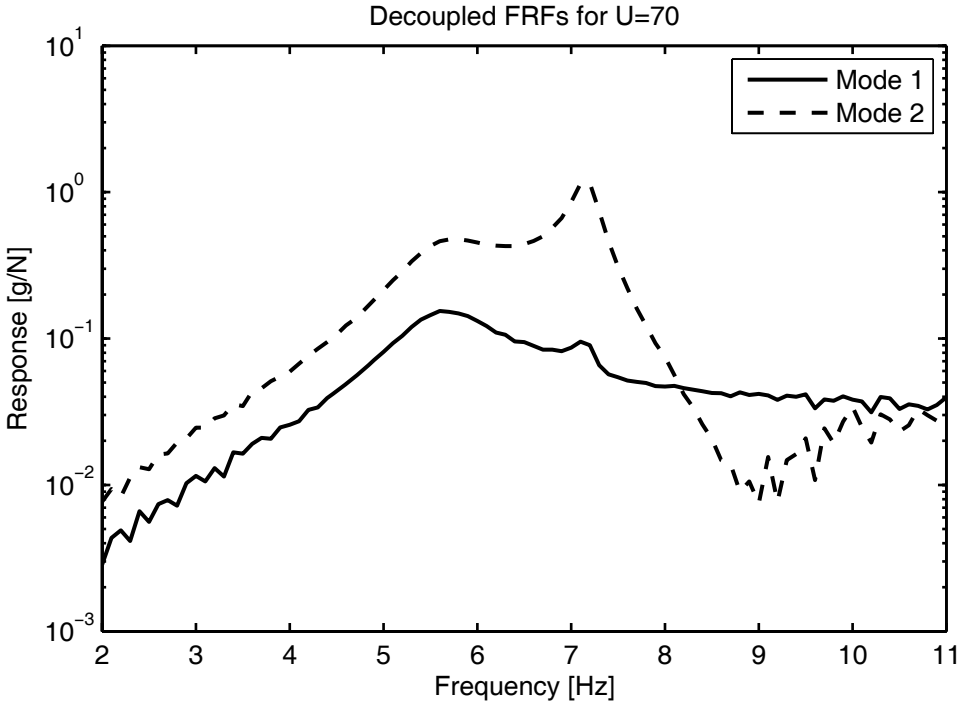

Figure 35. Decoupled FRF at U=70 m/s.

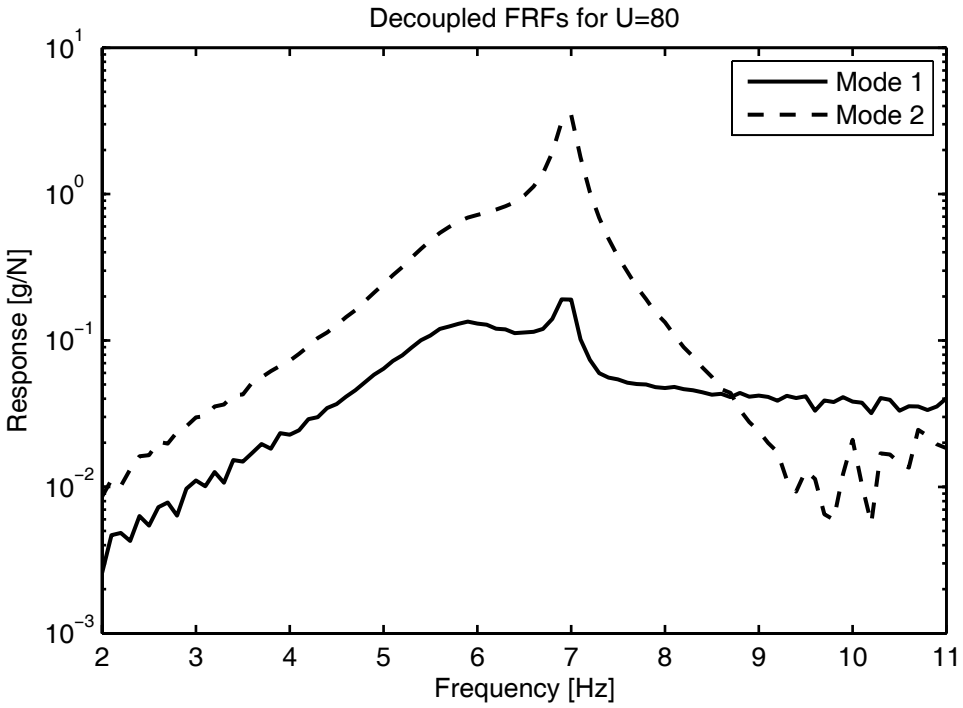

Figure 36. Decoupled FRF at U=80 m/s.

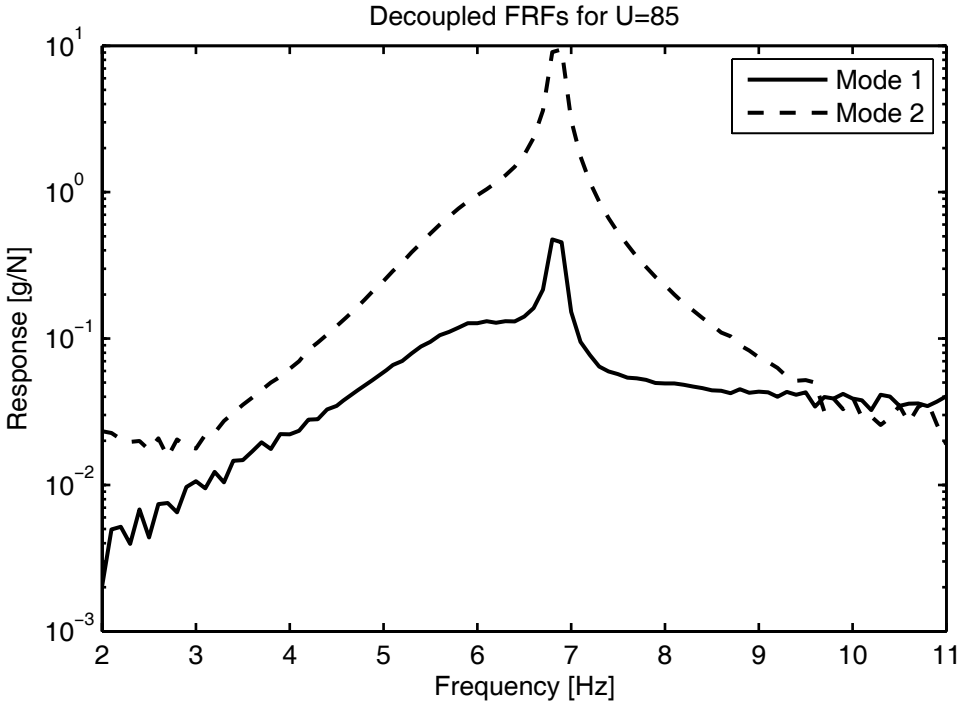

Figure 37. Decoupled FRF at U=85 m/s.

3.2.3.2 Singular Value Decomposition Filtering

Figure 38 shows the singular values of the FRF matrix at airflow speed 20 m/s. The number of modes can be easily identified from this figure. Results of SVD filtering are given in Figure 39 and Figure 40. Figure 39 shows that the filtering the best measurement point's FRF did not improve the FRF much because of the inherent high signal to noise ratio. The improvement on the worst measurement point (Figure 40) is more significant at frequencies at which response level is low.

The modal parameters are recalculated using filtered FRF data. The results are given in Table 4 with a subscript *f* next to previous values given in Table 3. Since there is no significant change in modal parameters, the predicted flutter speeds remain the same. Although, the SVD improves the FRF, these improvements are at frequencies far away from the natural frequencies. The signal to noise ratio at natural frequencies are high in this case. Since the error around natural frequencies dominates the error function used in curve fitting, the improvements around distant frequencies have no effect on the results.

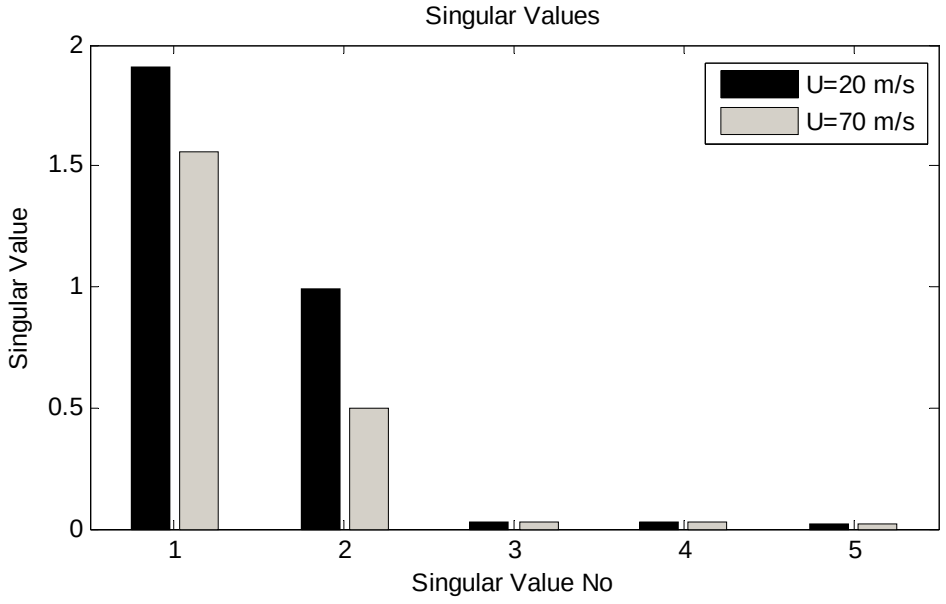

Figure 38. Singular values of the FRF matrix.

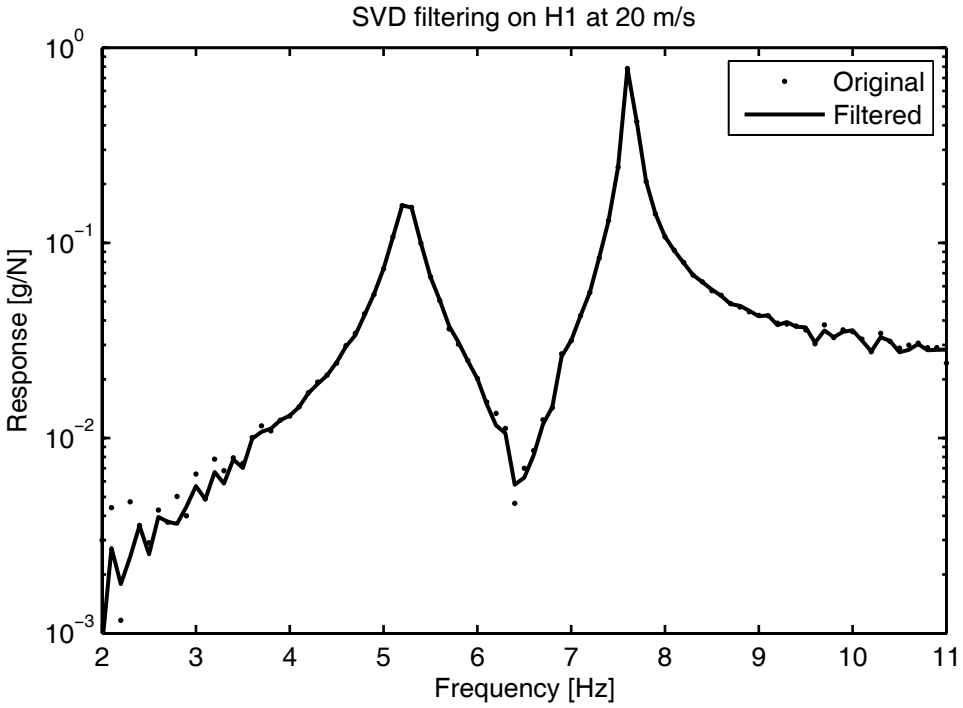

Figure 39. SVD filtering result on H1.

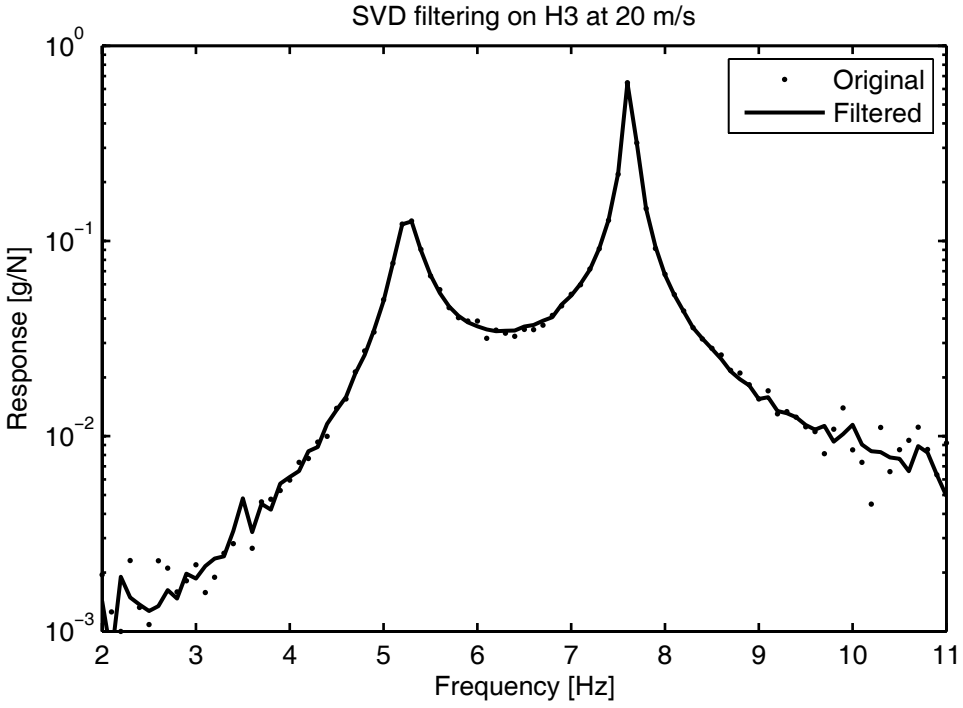

Figure 40. SVD filtering result on H3.

Table 4. Results of filtered FRF.

U [m/s]	20	30	40	50	60	70	80	85
η_1	0.0454	0.0678	0.0907	0.1145	0.1413	0.1725	0.2147	0.2500
η_{1f}	0.0455	0.0681	0.0913	0.1158	0.1417	0.1727	0.2166	0.2496
η_2	0.0095	0.0166	0.0238	0.0286	0.0345	0.0348	0.0230	0.0066
η_{2f}	0.0095	0.0166	0.0238	0.0292	0.0346	0.0348	0.0229	0.0066
ω_1 [Hz]	5.2441	5.2719	5.3166	5.3764	5.4578	5.5697	5.7131	5.7874
ω_{1f} [Hz]	5.2442	5.2726	5.3143	5.3740	5.4592	5.5710	5.7194	5.7908
ω_2 [Hz]	7.6228	7.5856	7.5244	7.4385	7.3220	7.1687	6.9664	6.8531
ω_{2f} [Hz]	7.6228	7.5856	7.5239	7.4331	7.3234	7.1687	6.9668	6.8532

3.2.4 Flutter Prediction with Envelope Function

In order to represent the thruster exciters, half sine pulses are used with the simulation model. Thus, the acceleration response of the typical section model to this nearly impulse excitation can be used to calculate the shape parameter at different speeds. The acceleration measurements are filtered with a cut-off frequency of 60 Hz to eliminate the high frequency content. A Matlab code is prepared to calculate the time centroid defined in Equation 2-16 and to accomplish the further processing in order to estimate the flutter speed of the model.

The envelope functions of the leading edge acceleration obtained for various air speeds are given in Figure 41. As seen from the figure, the envelope functions are not pure exponential decays at low air speeds because of the multi-DOF response. As the speed approaches the critical flutter speed, the envelopes increase in magnitude which indicates a serious decrease in damping.

To calculate the time centroid, a time limit must be chosen. The calculated shape parameter changes are given in Figure 43, Figure 44, and Figure 45 with various time limits. As seen from these figures, the damping trends change drastically with the chosen time limits. Although, the damping of the mode of interest at air speeds 60 and 70 m/s are almost the same as shown in Table 4, the shape parameter graphs with shorter time limits show a drastic change in damping, which seems to be very useful in flutter estimation. However, the main reason of the drastic shape parameter change can be understood from Figure 42, where the calculated envelope functions for the leading edge accelerometer are shown in more detail up to 1.2 s. It can be seen that the impulse response behavior of the system changes with the air speed. This behavior dominates the shape parameter change for short time limits. As the air speed increases, the coupled response after the impulsive excitation increases first and then decays. If this is a universal rule, then a new approach can be developed regarding this phenomenon. The validity of the rule must be checked with higher order models. Once proved, it is obvious that the envelope function would be a perfect indicator of stability even in the cases where damping changes are small.

Besides choosing the time limit, a proper sensor should be chosen to estimate the flutter speed. As seen from the figures, the leading edge sensor outputs are more suitable for extrapolation. Although, the trailing edge sensor has a similar rank, the large time limit graph, Figure 43, shows a flat response up to the speeds that are very close to the flutter. This is the usual behavior for this method which is observed in literature, [8]. Hence, usually it is not possible to predict flutter speed at low speeds, but some reliable estimates can be made with the high speed data. The shape parameter variation for the leading edge sensor in Figure 43 shows a similar behavior of modal damping.

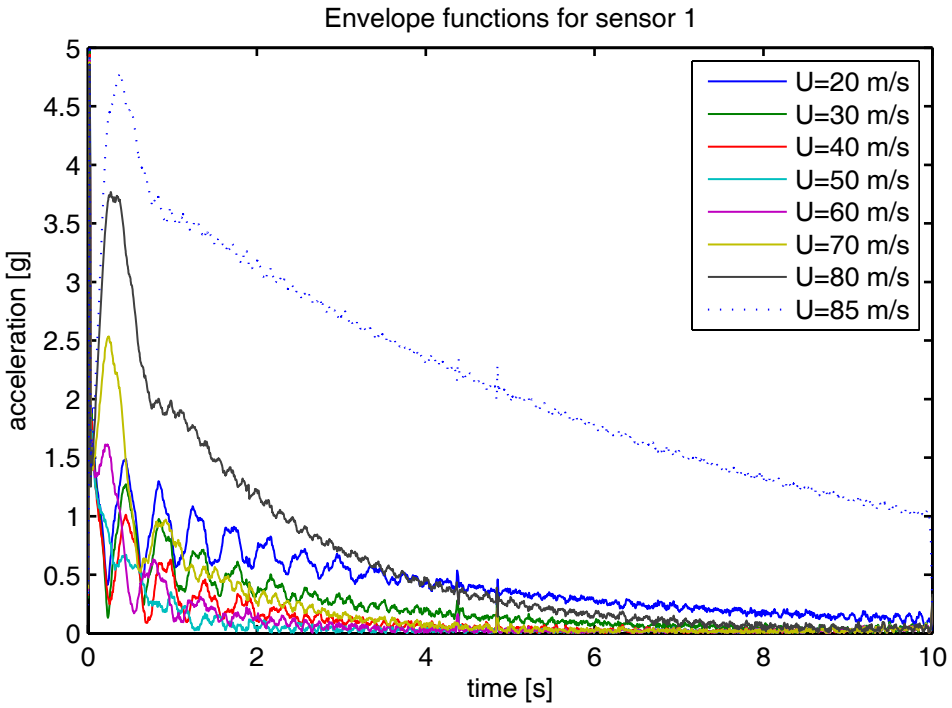

Figure 41. Envelope functions for leading edge accelerometer.

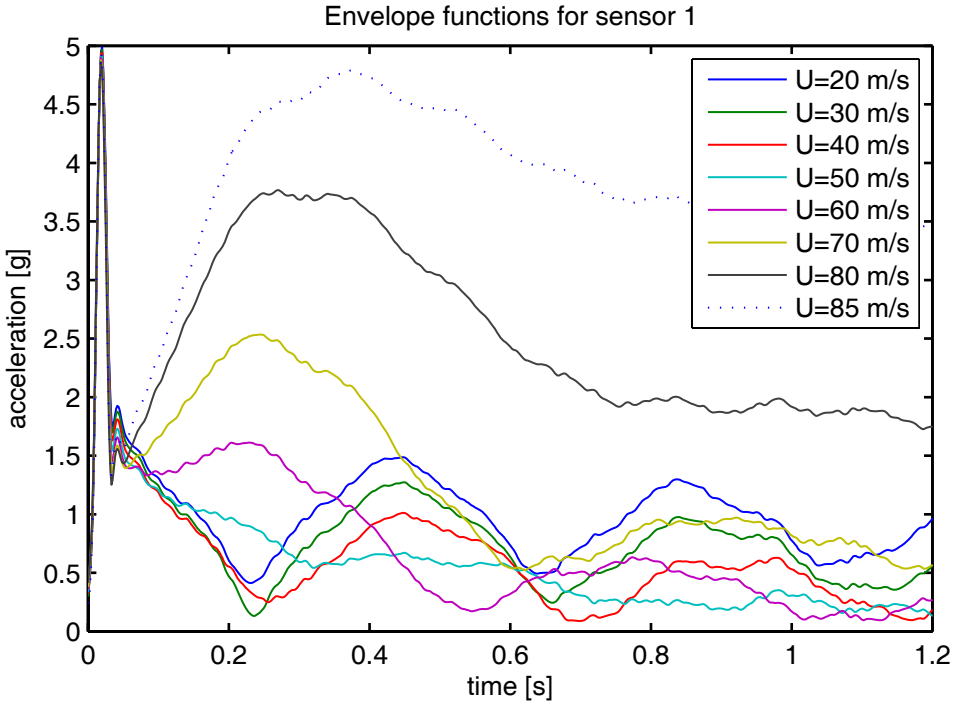

Figure 42. Envelope functions for leading edge accelerometer, zoomed.

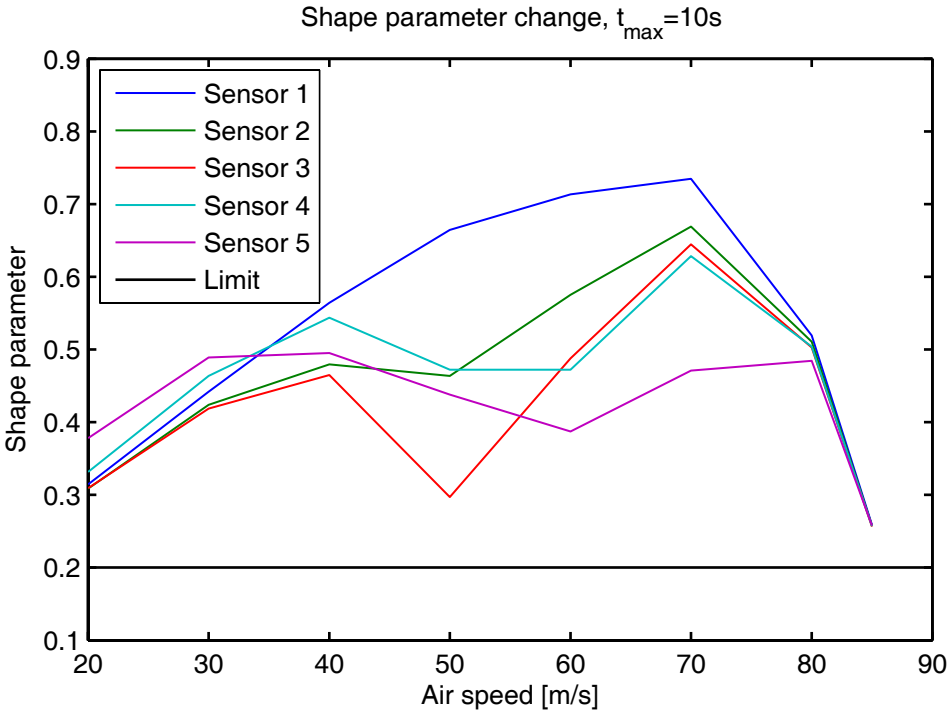

Figure 43. Variation of shape parameters with speed, t_{max}=10s.

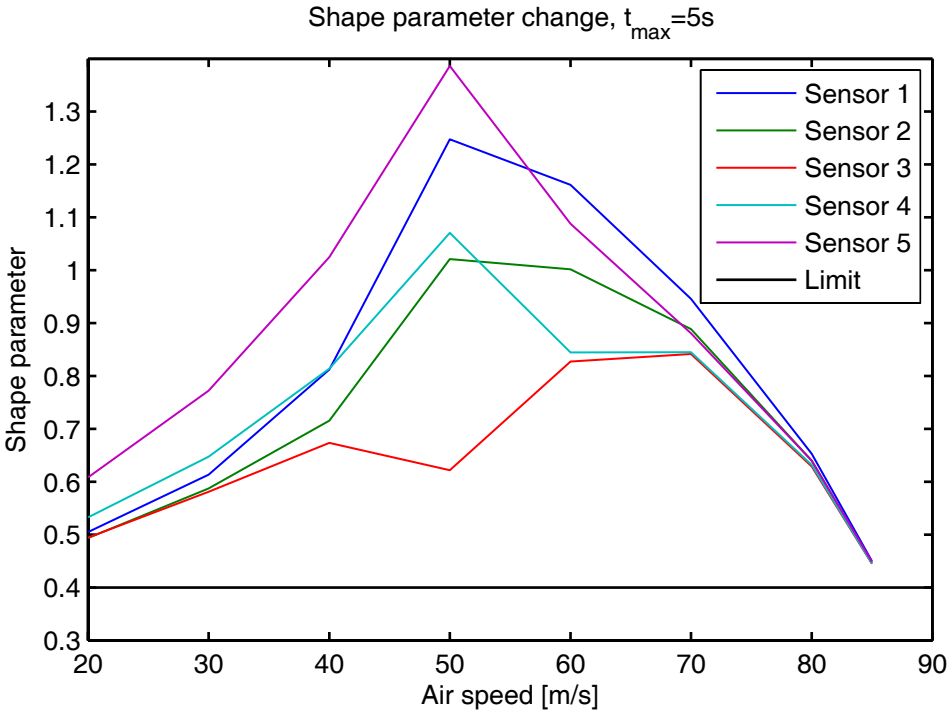

Figure 44. Variation of shape parameters with speed, t_{max}=5s.

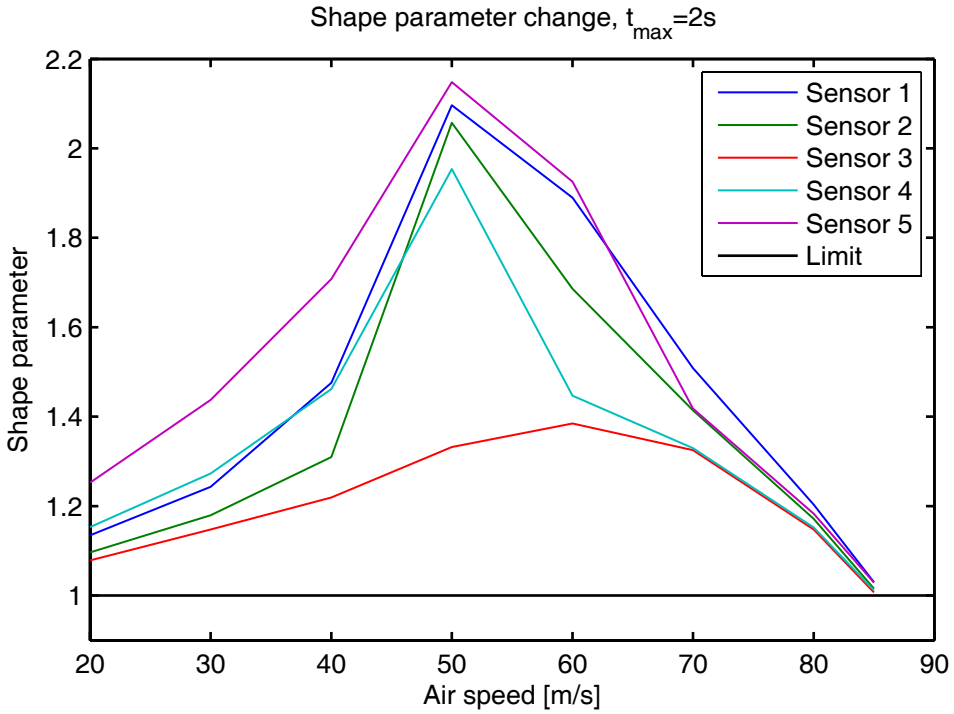

Figure 45. Variation of shape parameters with speed, t_{max}=2s.

It is assumed that the data at speeds 80 and 85 m/s are not available as is the case in the damping extrapolation method. The curve fit results are given in Figure 46 and Figure 47 for different time limits. The solution with time limit of 2 s is not presented here since 2 s is not long enough to describe the decay of the response. The estimation results are given in Table 5. As seen from this table, it is not possible to perform a reliable estimation with full span time data. On the other hand, estimations with lower time limit yield better and even conservative estimations.

The selection of the order of the polynomial fit is another problem as in damping extrapolation. The best polynomial order changes with the time limit and speed range. Orders up to six are used in the literature. Such high orders are necessary when the speed range that will be processed is large.

Table 5. Envelope function results.

t_{max} [s]	Fit order	Flutter speed estimate [m/s]	Error [%]
10	2	135.04	56
10	3	107.18	24
5	2	95.12	10
5	3	76.93	-11

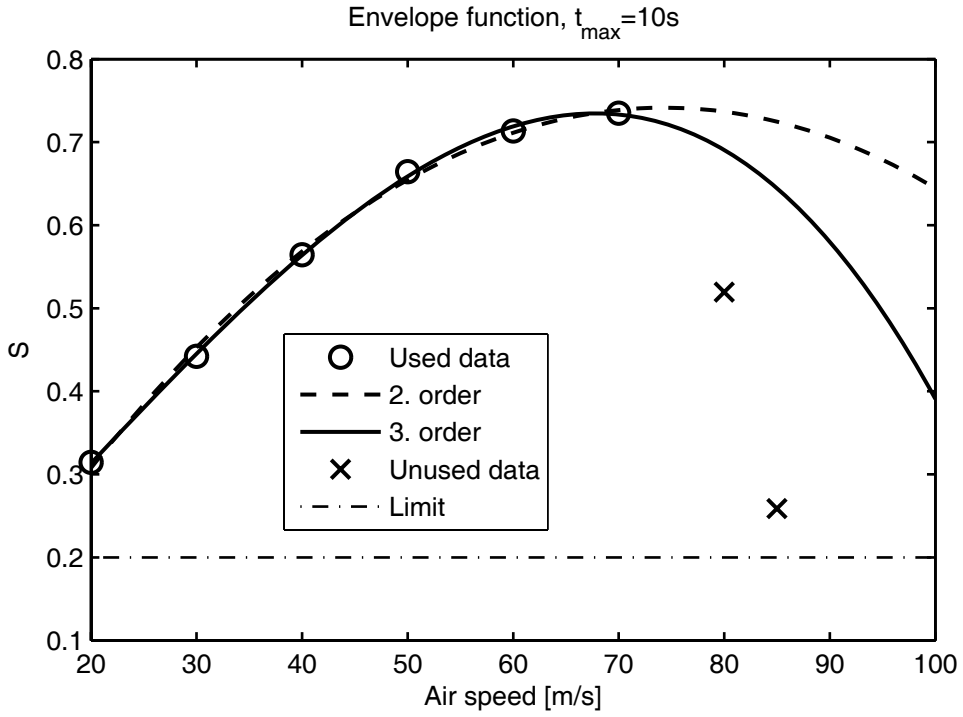

Figure 46. Envelope function result, t_{max}=10s.

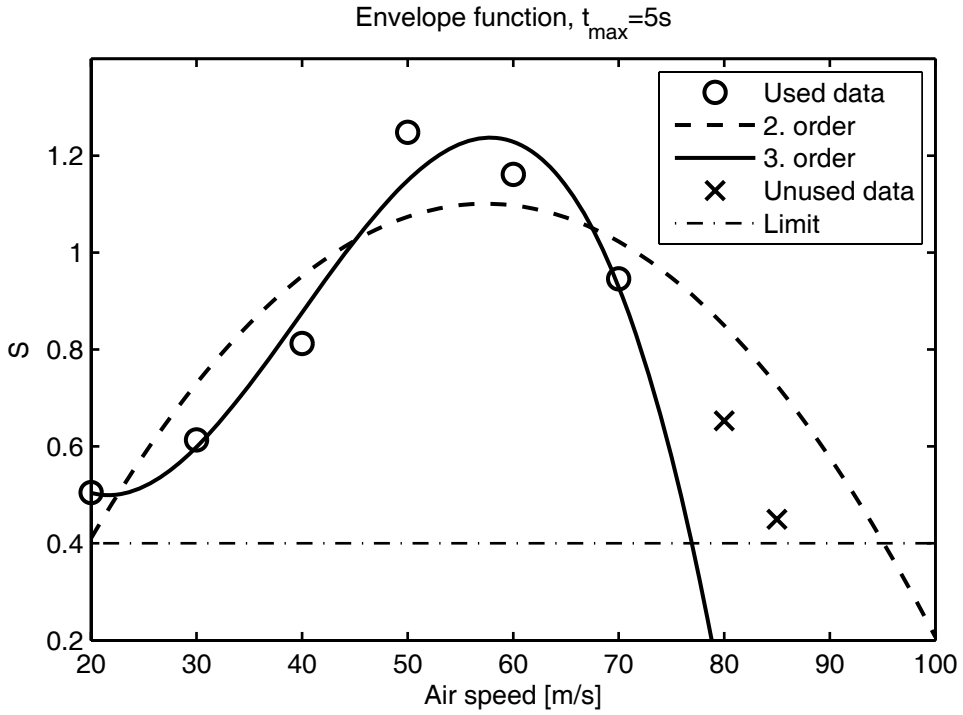

Figure 47. Envelope function result, t_{max}=5s.

3.2.5 Flutter Prediction with Flutter Margin

The flutter margin calculations and curve fit results using the approach presented in Section 2.4.3 are given in Figure 48, Figure 49, and Figure 50 using different number of data points for fit. The flutter estimates are given in Table 6. As seen from these figures and the table, the second order fit gives conservative and close estimates in every case considered. Using the data obtained at higher speeds is observed to improve the estimates. The results are completely as expected and compatible with the literature, since the method best works with 2-DOF systems. The almost linear behavior should be noted.

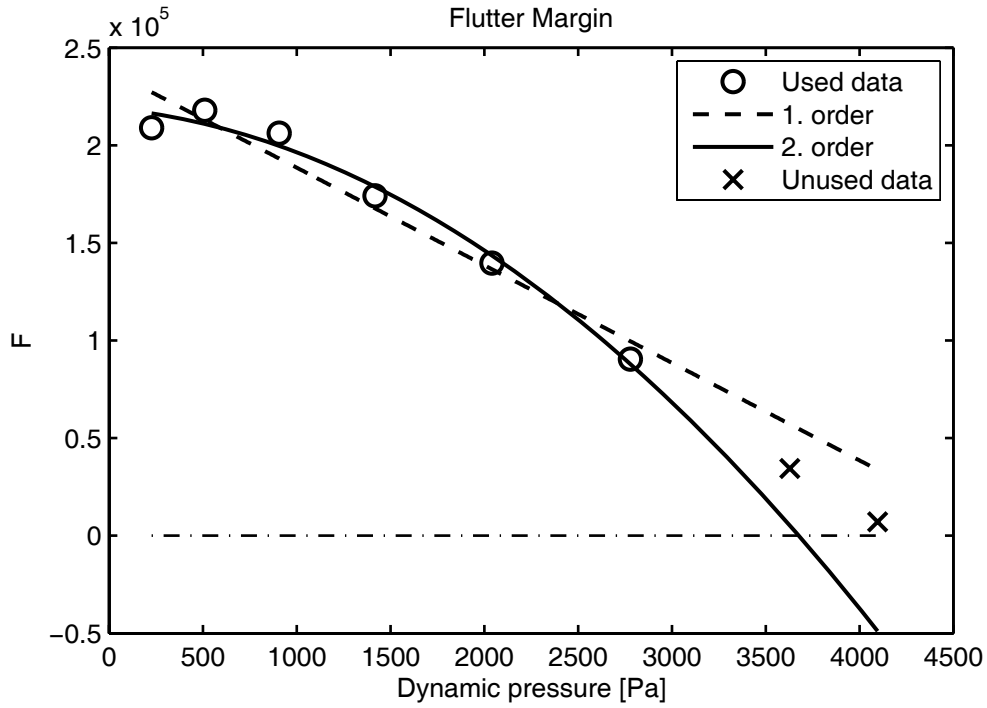

Figure 48. Flutter Margin fit for 6 data points.

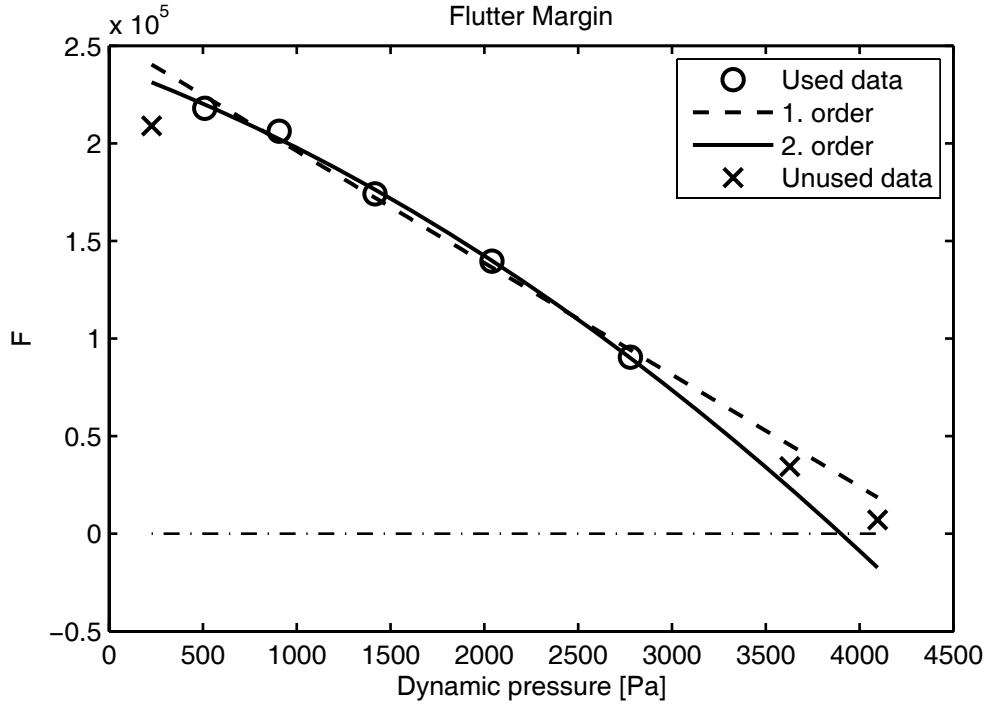

Figure 49. Flutter Margin fit for 5 data points.

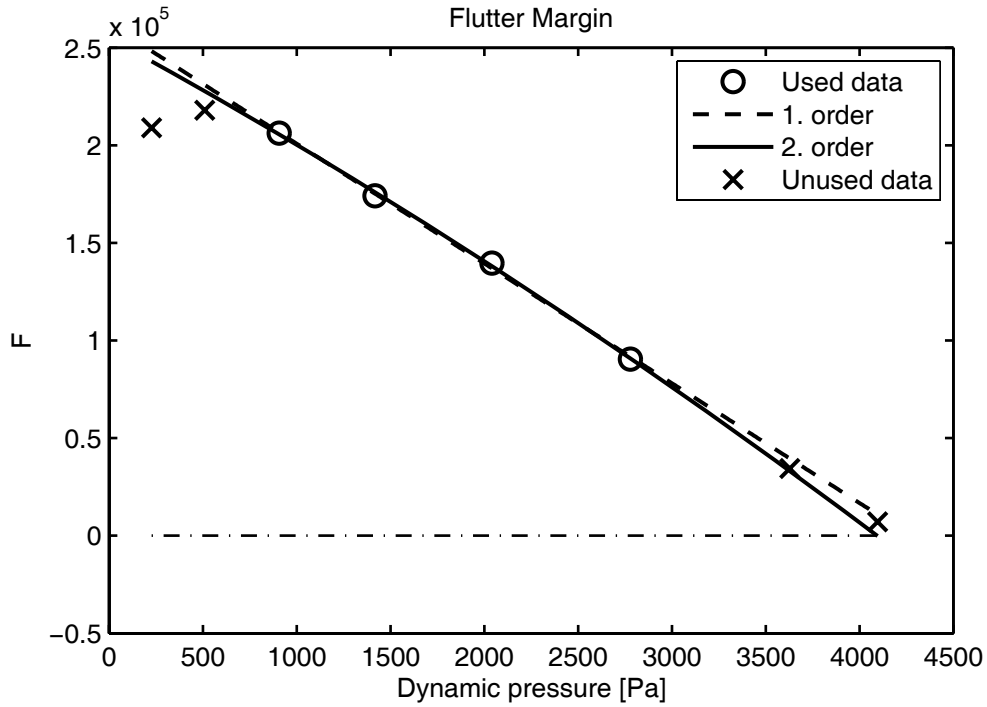

Figure 50. Flutter Margin fit for 4 data points.

Table 6. Flutter Margin results.

Fit order	Used velocities [m/s]	Flutter speed estimate [m/s]	Error [%]
1	20, 30, 40, 50, 60, 70	91.73	6.1
2	20, 30, 40, 50, 60, 70	80.52	-6.9
1	30, 40, 50, 60, 70	88.30	2.1
2	30, 40, 50, 60, 70	82.95	-4.1
1	40, 50, 60, 70	86.81	0.4
2	40, 50, 60, 70	84.97	-1.7

3.2.6 Flutter Prediction with ARMA Modeling

The Simulink model is modified to excite the system with a normal distribution noise that has a variance value of 100 N. The response to random noise is used to find the ARMA coefficients by using the method explained in Section 2.4.4. ARMA fits are performed with different noise orders to select a suitable noise order. Table 7 summarizes the pre-analysis results. As seen from the table AIC values are close to each other, which means any noise order is suitable for modeling. Order of the system is 4. So, the order of the noise model can be selected as 3 as a general rule. The estimation is performed with an ARMA(4,3) model.

Table 7. AIC table for various noise order and speed.

U	20 m/s	30 m/s	40 m/s	50 m/s	60 m/s	70 m/s	80 m/s	85 m/s
m=1	4.7086	4.7139	4.6622	4.6064	4.7793	4.8164	4.8068	4.7911
m=2	4.7136	4.8871	4.6624	4.8943	4.8297	4.8368	4.9101	4.9192
m=3	4.7215	4.7147	4.8672	4.9105	4.8871	4.924	4.9044	4.8001

Since a turbulence excitation is always present in the structure, practically more test points can be defined for the test. Measurements are collected for 14 speed points ranging from 20 to 85 m/s with 5 m/s steps. The stability variations for leading and trailing edge measurement points are given in Figure 51. As seen from the figure, the variations are not monotonic for both optimum sensor locations. The trailing edge measurements for air speeds greater than 50 m/s (dynamic pressure of 1,418 Pa) are used to perform the extrapolation. Although the method seems to work for low speeds, it is obvious that no useful data can be extracted from the low speed data. There is no need to perform a second order curve fitting for the high speeds since a second order fit would never cross the zero axis. The upper limit for the speed is taken as 70 m/s as in all previously studied methods. The estimation results are given in Figure 52 and Table 8.

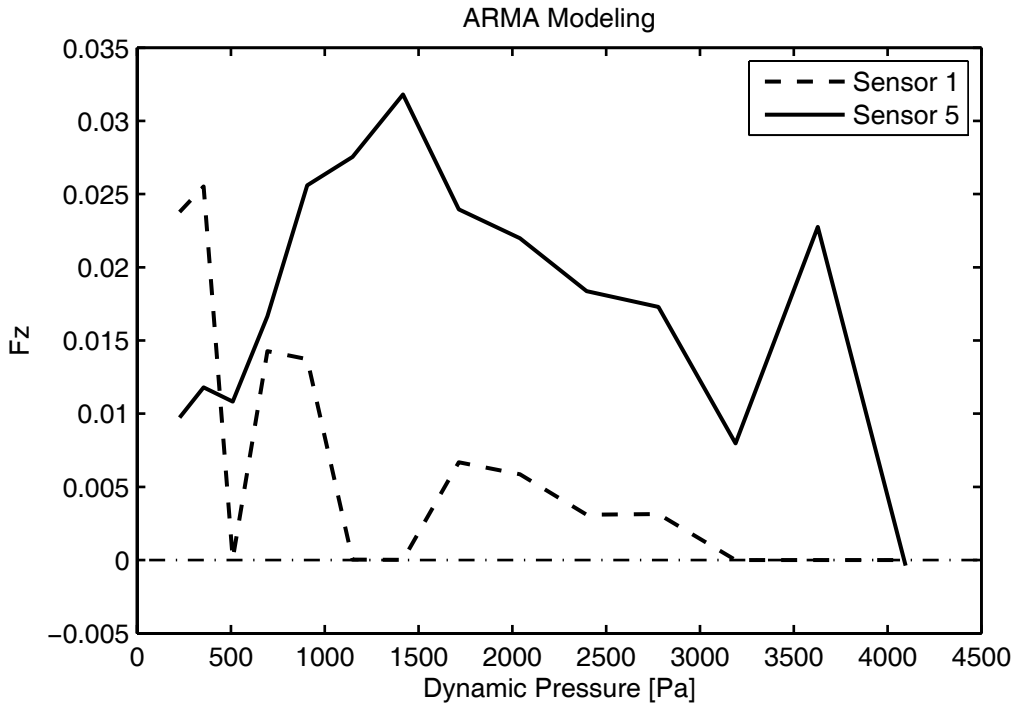

Figure 51. Variation of ARMA *Fz* with dynamic pressure without filtering.

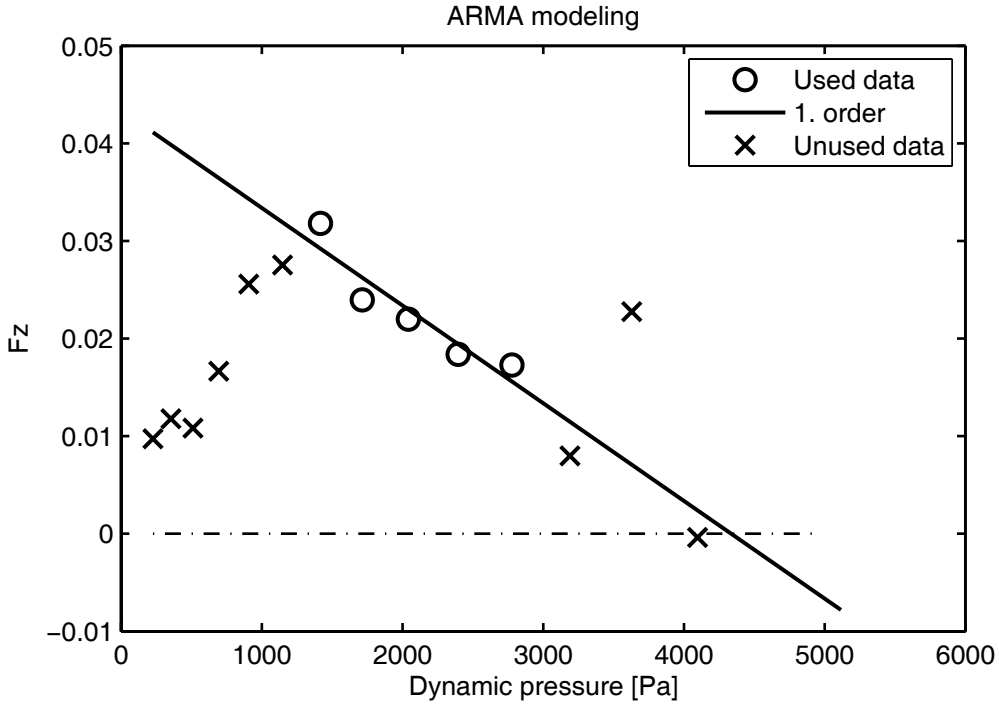

Figure 52. ARMA Modeling fit for 5 points without filtering.

Table 8. ARMA Modeling results without filtering.

Fit order	Used velocities [m/s]	Flutter speed estimate [m/s]	Error [%]
1	50, 55, 60, 65, 70	94.08	8.8
1	50, 55, 60, 65	89.4	3.4
1	55, 60, 65, 70	98.12	13.5

Clearly, the estimation process turns out to be neither robust nor reliable compared to the studies reported in the literature. After investigating the estimated models, it is found that the poles of the estimated models are not complex conjugate pairs. Although the structural part has two pairs of oscillatory poles, the unsteady aerodynamics introduces two additional real poles to the complete aeroelastic system. It is found that the ARMA procedure always converges to one pair of complex pole and two distinct real poles, which violates the fundamental assumption of the method. Since the method assumes interaction of two modes, signals that are not associated with these modes should be filtered out before estimating the ARMA model. The importance of filtering is also stated in the literature [15, 36]. To resolve this problem the measurements are pre-filtered by a sixth order Butterworth filter with a cutoff frequency of 30 Hz. The new poles are checked and verified that they are formed as complex conjugate pairs. The variations of the stability parameter *Fz* with the dynamic pressure are considerably different at all measurement locations as seen in Figure 53. However, the stability margin calculated from the trailing edge, Sensor 5, shows a flat variation for low speeds. So, only a second order curve fit is enough to give accurate results. However, without using high speed data, it is still not possible to perform a meaningful second order curve fit. The monotonic decrease behavior is observed in the leading edge measurement, which is more suitable for a first order curve fit. The results of the curve fit for the leading edge measurement with different number of data points are given in Figure 54 and Figure 55. If some high speed data were available for curve fitting, a third order fit might give very accurate results. However, such high order curve fits are never recommended in the

literature. In fact, the stability variation is expected to be linear as in flutter margin method.

The results of the discrete time ARMA Modeling method are given in Table 9. As seen from the table, a second order fit does not give any result, which is usually the case for this method because of scatter.

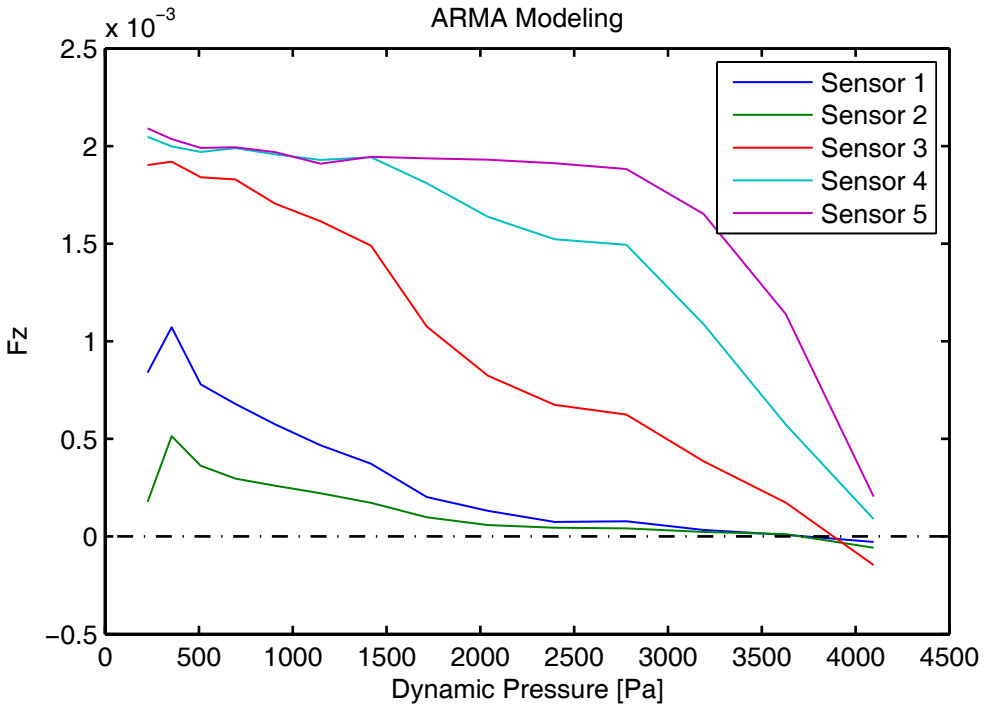

Figure 53. Variation of ARMA *Fz* with dynamic pressure with filtering.

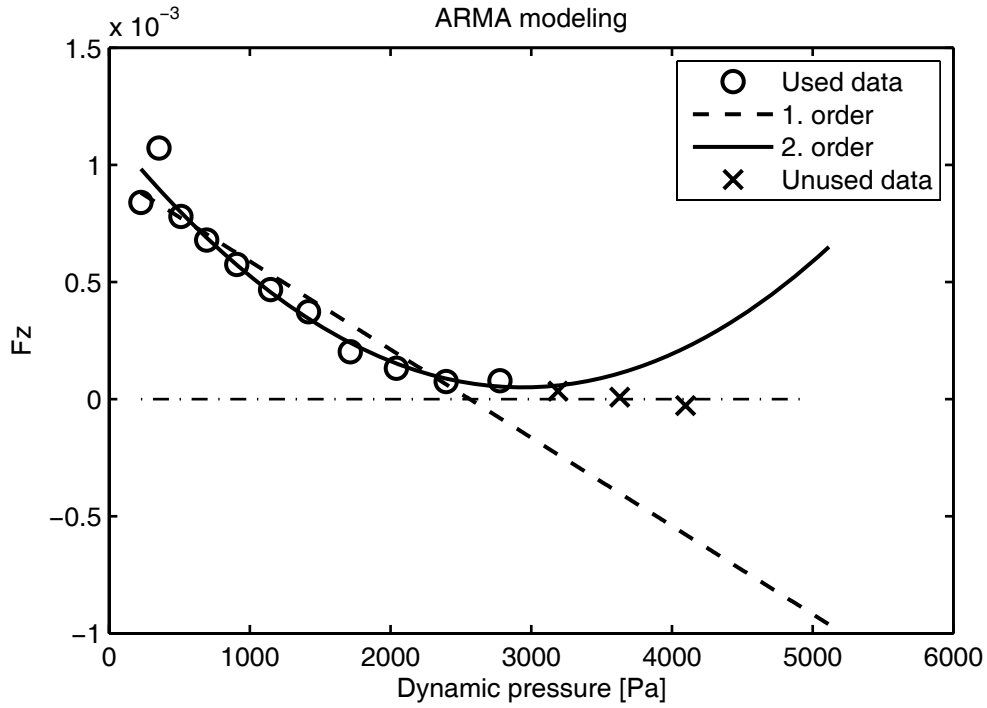

Figure 54. ARMA Modeling fit for 11 points with filtering.

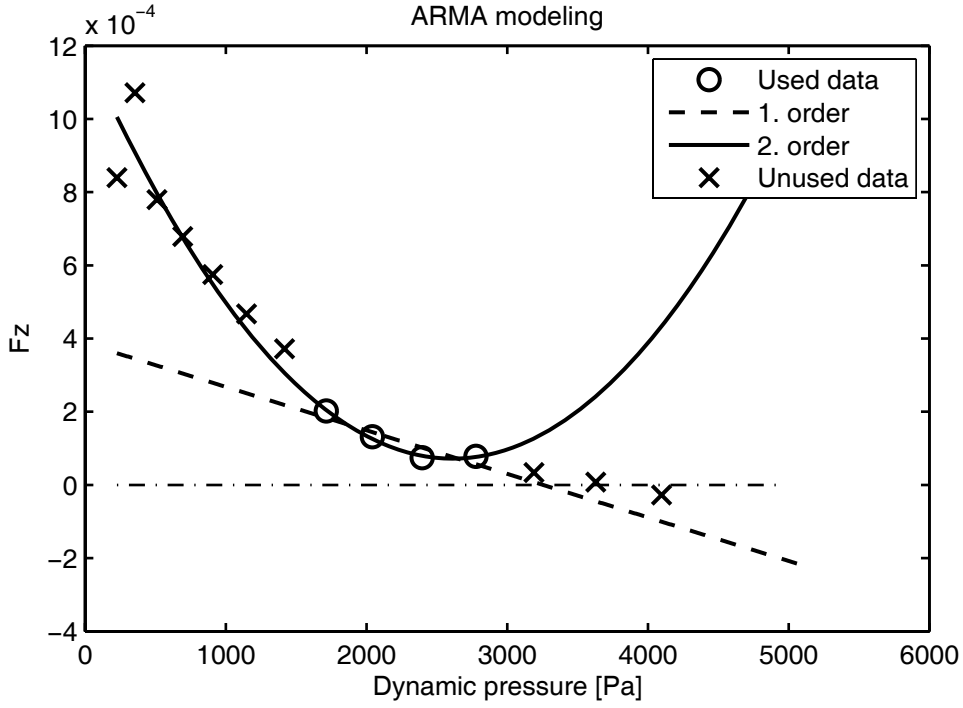

Figure 55. ARMA Modeling fit for 4 points with filtering.

Table 9. ARMA Modeling results with filtering.

Fit order	Used velocities [m/s]	Flutter speed estimate [m/s]	Error [%]
1	20 to 70 by 5	68.17	-21.17
2	20 to 70 by 5	-----	-----
1	55 to 70 by 5	74.73	-13.6
2	55 to 70 by 5	-----	-----

3.2.7 Flutter Prediction with Flutterometer

3.2.7.1 State Space Formulation

The equations of motion of the typical section, which are presented in Appendix B, are based on Laplace transformation in order to deal more easily with the complex aerodynamic terms. However, a state-space formulation is more suitable for robust analysis. For this reason, the equations of motion are derived in the state space form. Recall that basic equations for two degrees of freedom typical section are as in Equations 3-7 and 3-8.

$$m\ddot{h} + S_\alpha \ddot{\alpha} + K_h h = -L + F^{ext} \tag{3-7}$$

$$S_\alpha \ddot{h} + I_\alpha \ddot{\alpha} + K_\alpha \alpha = M_y + M^{ext} \tag{3-8}$$

where

$$S_\alpha = mbx_\alpha \tag{3-9}$$

Unsteady aerodynamic lift and moment expressions are given below.

$$L = \pi\rho b^2 l\left[\ddot{h} + U\dot{\alpha} - ba\ddot{\alpha}\right] + 2\pi\rho UblC(k)\left[\dot{h} + U\alpha + b\left(\tfrac{1}{2} - a\right)\dot{\alpha}\right] \tag{3-10}$$

$$M_y = \pi\rho b^2 l\left[ba\ddot{h} - Ub\left(\tfrac{1}{2}-a\right)\dot{\alpha} - b^2\left(\tfrac{1}{8}+a^2\right)\ddot{\alpha}\right]$$
$$+ 2\pi\rho U b^2 l\left(a+\tfrac{1}{2}\right)C(k)\left[\dot{h} + U\alpha + b\left(\tfrac{1}{2}-a\right)\dot{\alpha}\right] \tag{3-11}$$

where

$$k = \frac{\omega b}{U} \tag{3-12}$$

is the nondimensional frequency called as the "reduced frequency". The circulatory part of the aerodynamic forces depend on the Theodorsen's function *C(k)*. A useful approximation for Theodorsen's function is given in Equation 3-13 and 3-14. It is possible to derive aerodynamic state equations with these equations.

$$C(k) = 1 - \frac{0.165}{1 - i\dfrac{0.0455}{k}} - \frac{0.335}{1 - i\dfrac{0.3}{k}} \quad \text{for } k<0.5 \tag{3-13}$$

$$C(k) = 1 - \frac{0.165}{1 - i\dfrac{0.041}{k}} - \frac{0.335}{1 - i\dfrac{0.32}{k}} \quad \text{for } k\geq 0.5 \tag{3-14}$$

In order to describe the dynamic pressure uncertainty, the density and square of air speed parameters should be collected to form the dynamic pressure. However, Equations 3-10 and 3-11 clearly show that it is not possible to separate the dynamic pressure terms without leaving individual density and speed terms in the equations of motion. To overcome this difficulty, a nondimensional time scaling *s* defined as

$$s = \frac{Ut}{b} \tag{3-15}$$

is used to derive the equations of motion. It is shown that the switching to the nondimensional time scale eliminates all speed terms from the equations and it is possible to have a proper state equation that is valid at a specific altitude.

The differentiation with respect to time can be replaced with the differentiation with respect to nondimensional time as in Equations 3-16 and 3-17.

$$\frac{d}{dt} = \frac{ds}{dt}\frac{d}{ds} = \left(\frac{U}{b}\right)\frac{d}{ds} \tag{3-16}$$

$$\frac{d^2}{dt^2} = \left(\frac{U}{b}\right)^2 \frac{d^2}{ds^2} \tag{3-17}$$

Laplace representation of Theodorsen's function with respect to reduced frequency can be expressed as

$$C(\tilde{p}) = \frac{1}{2} + \frac{c_1\tilde{p} + c_2}{\tilde{p}^2 + c_3\tilde{p} + c_4} \tag{3-18}$$

where

$$\begin{gathered} c_1=0.1080075,\ c_2=0.006825,\ c_3=0.3455,\ c_4=0.01365 \text{ for } k \le 0.5 \\ c_1=0.113965,\ c_2=0.00656,\ c_3=0.361,\ c_4=0.01312 \text{ for } k > 0.5 \end{gathered} \tag{3-19}$$

So, the equations of motion in nondimensional time become

$$\begin{aligned} &\left(\frac{2m}{\rho b^2} + 2\pi l\right)qh'' + \left(\frac{2S_\alpha}{\rho b^2} - 2\pi bla\right)q\alpha'' + 2\pi lqh' + 2\pi l\left(\tfrac{3}{2} - a\right)q\alpha' \\ &+ K_h h + 2\pi blq\alpha + 4\pi l\, {c_1}/{b}\; qx_a' + 4\pi l\, {c_2}/{b}\; qx_a = F^e \end{aligned} \tag{3-20}$$

$$\begin{aligned} &\left(\frac{2S_\alpha}{\rho b^2} - 2\pi bla\right)qh'' + \left(\frac{2I_\alpha}{\rho b^2} + 2\pi b^2 l\left(\tfrac{1}{8} + a^2\right)\right)q\alpha'' - 2\pi bl\left(\tfrac{1}{2} + a\right)qh' \\ &+ 2\pi b^2 l\left(\tfrac{1}{2} - a\right)^2 q\alpha' + K_\alpha\alpha - 2\pi b^2 l\left(\tfrac{1}{2} + a\right)q\alpha \\ &- 4\pi l\left(\tfrac{1}{2} + a\right)c_1 qx_a' - 4\pi l\left(\tfrac{1}{2} + a\right)c_2 qx_a = M^e \end{aligned} \tag{3-21}$$

$$x_a'' + c_3 x_a' + c_4 x_a = bh' + b^2\alpha + b^2\left(\tfrac{1}{2} - a\right)\alpha' \tag{3-22}$$

where x_a in Equation 3-22 defines the extra aerodynamic states introduced by the denominator of the Theodorsen's function. Here, it should be noted that the equations of motion do not involve the speed term explicitly. The equations can be expressed in matrix notation as in Equation 3-23.

$$\begin{gathered}[M]q\{\eta''\} + [C]q\{\eta'\} + \left([K] + [K_a]q\right)\{\eta\} + [D]q\{x\} = \{f\} \\ \{x'\} = [F]\{x\} + [E_1]\{\eta'\} + [E_2]\{\eta\}\end{gathered} \tag{3-23}$$

where

$$[M] = \begin{bmatrix} 2m/\rho b^2 + 2\pi l & 2S_\alpha/\rho b^2 - 2\pi bla \\ 2S_\alpha/\rho b^2 - 2\pi bla & 2I_\alpha/\rho b^2 + 2\pi b^2 l\left(\tfrac{1}{8} + a^2\right) \end{bmatrix}$$

$$[C] = \begin{bmatrix} 2\pi l & 2\pi bl\left(\tfrac{3}{2} - a\right) \\ -2\pi bl\left(\tfrac{1}{2} + a\right) & 2\pi b^2 l\left(\tfrac{1}{2} - a\right)^2 \end{bmatrix}$$

$$[K] = \begin{bmatrix} K_h & 0 \\ 0 & K_\alpha \end{bmatrix}$$

$$[K_a] = \begin{bmatrix} 0 & 2\pi bl \\ 0 & -2\pi b^2 l\left(\tfrac{1}{2} + a\right) \end{bmatrix}$$

$$[D] = \begin{bmatrix} 4\pi l\, c_2/b & 4\pi l\, c_2/b \\ -4\pi l\left(\tfrac{1}{2} + a\right)c_2 & -4\pi l\left(\tfrac{1}{2} + a\right)c_1 \end{bmatrix}$$

$$[F]=\begin{bmatrix} 0 & 1 \\ -c_4 & -c_3 \end{bmatrix}$$

$$[E_1]=\begin{bmatrix} 0 & 0 \\ b & b^2\left(\tfrac{1}{2}-a\right) \end{bmatrix}$$

$$[E_2]=\begin{bmatrix} 0 & 0 \\ 0 & b^2 \end{bmatrix}$$

$$\{\eta\}=\begin{Bmatrix} h \\ \alpha \end{Bmatrix},\ \{x\}=\begin{Bmatrix} x_a \\ x_a' \end{Bmatrix}$$

(3-24)

Finally, the state space representation of the typical section can be formed as shown below.

$$\begin{Bmatrix} \{\eta'\} \\ \{\eta''\} \\ \{x'\} \end{Bmatrix}=\begin{bmatrix} [0] & [I] & [0] \\ -[M]^{-1}\left(\left[K\right]/q+[K_a]\right) & -[M]^{-1}[C] & -[M]^{-1}[D] \\ [E_2] & [E_1] & [F] \end{bmatrix}\begin{Bmatrix} \{\eta\} \\ \{\eta'\} \\ \{x\} \end{Bmatrix}+\begin{bmatrix} [0] \\ [M]^{-1}/q \\ [0] \end{bmatrix}\{f\}$$

(3-25)

3.2.7.2 Nominal Flutter Analysis

The LFT form of the system can be derived by applying a perturbation to the dynamic pressure term in Equation 3-23 such as

$$q=q_0+W_q\delta_q \tag{3-26}$$

Collecting the perturbation terms after the substitution of Equation 3-26 into the equation of motion results in Equation 3-27.

$$\{\eta''\}+[M]^{-1}[C]\{\eta'\}+[M]^{-1}\left([K]/q_0+[K_a]\right)\{\eta\}+[M]^{-1}[D]\{x\}$$

$$+\left(\{\eta''\}+[M]^{-1}[C]\{\eta\}+[M]^{-1}[K_a]\{\eta\}+[M]^{-1}[D]\{x\}\right)W_q/q_0\,\delta q=[M]^{-1}/q_0\{f\} \tag{3-27}$$

Define the perturbation term as

$$\left(\{\eta''\}+[M]^{-1}[C]\{\eta\}+[M]^{-1}[K_a]\{\eta\}+[M]^{-1}[D]\{x\}\right)W_q/q_0\,\delta q=\{z\}\,\delta q=\{w\} \tag{3-28}$$

Note that $\{z\}$ contains $\{\eta''\}$ term, so another substitution is necessary to eliminate this term. By substituting Equation 3-29, which is derived from Equation 3-27 and the definition 3-28, into 3-28, the definition of the perturbation equation is obtained as follows.

$$\{\eta''\}=-[M]^{-1}[C]\{\eta'\}-[M]^{-1}\left([K]/q_0+[K_a]\right)\{\eta\}-[M]^{-1}[D]\{x\}-\{w\}+[M]^{-1}/q_0\{f\} \tag{3-29}$$

$$\{z\}=-[M]^{-1}[K]W_q/q_0^2\{\eta\}-W_q/q_0\{w\}+[M]^{-1}W_q/q_0^2\{f\} \tag{3-30}$$

Forcing input and measurement output is not necessary in nominal flutter analysis. The state space equation for nominal flutter analysis is given in Equation 3-31.

$$\begin{Bmatrix}\{\eta'\}\\ \{\eta''\}\\ \{x'\}\\ \hline \{z\}\end{Bmatrix}=\left[\begin{array}{ccc|c}[0] & [I] & [0] & [0]\\ -[M]^{-1}\left([K]/q_0+[K_a]\right) & -[M]^{-1}[C] & -[M]^{-1}[D] & -[I]\\ [E_2] & [E_1] & [F] & [0]\\ \hline -[M]^{-1}[K]W_q/q_0^2 & [0] & [0] & -W_q/q_0\end{array}\right]\begin{Bmatrix}\{\eta\}\\ \{\eta'\}\\ \{x\}\\ \hline \{w\}\end{Bmatrix} \tag{3-31}$$

Figure 56 shows the variation of the real part of the pole that is related to the flutter with different dynamic pressure perturbations. The point where the real part becomes positive is marked on the figure. The calculated flutter speed, 88.6 m/s, is almost the same with the previously calculated value, 86.5 m/s, which was obtained from the equations of motion derived by Laplace transform. Since other system poles are always stable, they are not given in the figure.

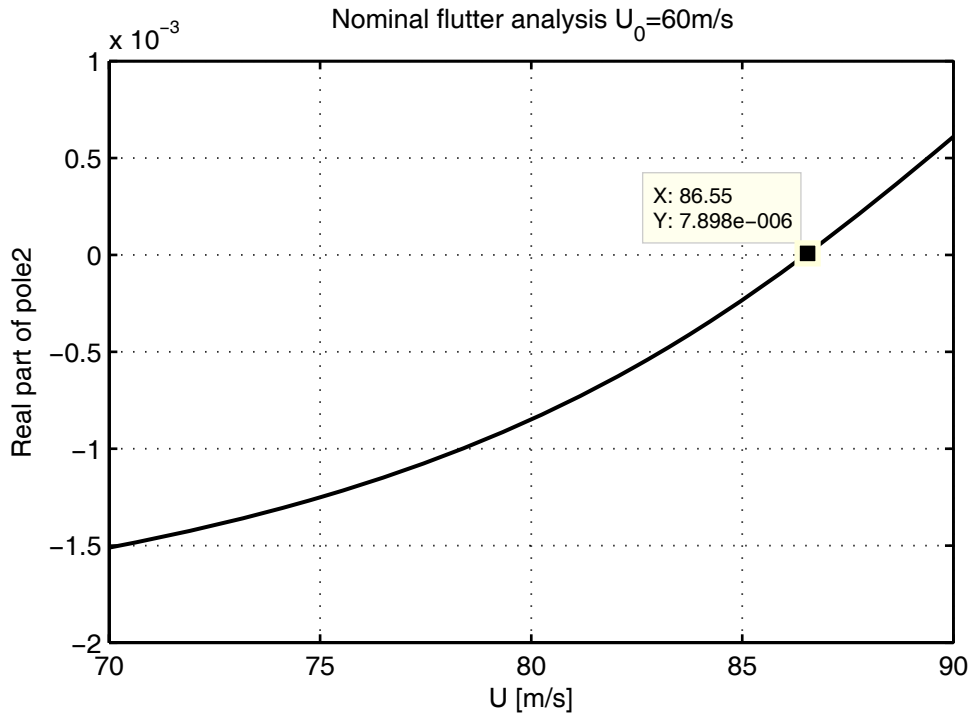

Figure 56. Nominal flutter analysis of the typical section.

3.2.7.3 Robust Flutter Analysis

It is convenient to model the uncertainties of the stiffness, damping, and aerodynamic parameters of the systems that have limited number of DOFs with parametric uncertainties. Since no structural damping is included in the typical section model, a complex parametric uncertainty would cover both stiffness and aerodynamic damping uncertainties. Thin airfoils are usually in good agreement with steady aerodynamic theories. However, unsteady aerodynamic coefficients are usually calculated with a curve fitting. Thus, the unsteady aerodynamic parameters

can be modeled with a complex or scalar parametric uncertainty. For parametric uncertainties, multiplicative and additive descriptions are equivalent to each other. Thus, it will be convenient to use an additive uncertainty for the aerodynamic coefficients and the structural stiffness matrix. The structural stiffness matrix and aerodynamic coefficients with perturbation can be defined as below.

$$\begin{gathered}[K]=[K_0]+[W_K]\delta_K \\ c_i = c_{i_0} + W_{c_i}\delta_{c_i},\ \text{for } i=1..4\end{gathered} \tag{3-32}$$

Since stiffness matrix, [*K*], is explicitly available in the state space equations, rewriting these equations with a defined uncertainty is straightforward. However, the aerodynamic coefficients are embedded in the system matrices and a decomposition of the related matrices is necessary. The aerodynamic coefficients are used in the system matrices [*D*] and [*F*]. Consider the matrix [*D*]

$$[D]=4\pi l\begin{bmatrix} 1/b & 1/b \\ -a-\tfrac{1}{2} & -a-\tfrac{1}{2}\end{bmatrix}\begin{bmatrix} c_2 & 0 \\ 0 & c_1\end{bmatrix}=[D_1]\begin{bmatrix} c_2 & 0 \\ 0 & c_1\end{bmatrix} \tag{3-33}$$

The coefficient matrix in Equation 3-33 can be decomposed as follows.

$$\begin{bmatrix} c_2 & 0 \\ 0 & c_1\end{bmatrix}=\begin{bmatrix} c_{2_0} & 0 \\ 0 & c_{1_0}\end{bmatrix}+\begin{bmatrix} W_{c_2} & 0 \\ 0 & 0\end{bmatrix}\delta_{c_2}+\begin{bmatrix} 0 & 0 \\ 0 & W_{c_1}\end{bmatrix}\delta_{c_1} \tag{3-34}$$

So the matrix [*D*] can be expressed as

$$\begin{gathered}[D]=[D_1]\begin{bmatrix} c_{2_0} & 0 \\ 0 & c_{1_0}\end{bmatrix}+[D_1]\begin{bmatrix} W_{c_2} & 0 \\ 0 & 0\end{bmatrix}\delta_{c_2}+\begin{bmatrix} 0 & 0 \\ 0 & W_{c_1}\end{bmatrix}\delta_{c_1} \\ [D]=[D_0]+[D_2]\delta_{c_2}+[D_3]\delta_{c_1}\end{gathered} \tag{3-35}$$

Similarly, the matrix [*F*] can be decomposed as

$$[F]=\begin{bmatrix} 0 & 1 \\ -c_4 & -c_3 \end{bmatrix}=\begin{bmatrix} 0 & 1 \\ -c_{4_0} & -c_{3_0} \end{bmatrix}+\begin{bmatrix} 0 & 0 \\ 0 & -W_{c_4} \end{bmatrix}\delta_{c_4}+\begin{bmatrix} 0 & 0 \\ 0 & -W_{c_3} \end{bmatrix}\delta_{c_3}$$
$$[F]=[F_0]+[F_1]\delta_{c_4}+[F_2]\delta_{c_3} \tag{3-36}$$

Substituting uncertainty descriptions given by Equations 3-32 (stiffness), 3-35, and 3-36 into Equation 3-23 results in the following set of new equations of motion with some dynamic pressure, stiffness, and aerodynamic uncertainties.

$$\{\eta''\}=-[M]^{-1}\left([K_0]/q_0+[K_a]\right)\{\eta\}-[M]^{-1}[C]\{\eta'\}-[M]^{-1}[D_0]\{x\}$$
$$-\{w\}-\{w_K\}-\{w_{c_2}\}-\{w_{c_1}\}+[M]^{-1}/q_0\{f\}$$

$$\{x'\}=[E_2]\{\eta\}+[E_1]\{\eta'\}+[F_0]\{x\}+\{w_{c_4}\}+\{w_{c_3}\}$$

$$\{w_K\}=[M]^{-1}/q_0[W_K]\{\eta\}\delta_K=\{z_K\}\delta_K$$

$$\{w_{c_1}\}=[M]^{-1}[D_3]\{x\}\delta_{c_1}=\{z_{c_1}\}\delta_{c_1}$$

$$\{w_{c_2}\}=[M]^{-1}[D_2]\{x\}\delta_{c_2}=\{z_{c_2}\}\delta_{c_2}$$

$$\{w_{c_3}\}=[F_2]\{x\}\delta_{c_3}=\{z_{c_3}\}\delta_{c_3}$$

$$\{w_{c_4}\}=[F_1]\{x\}\delta_{c_4}=\{z_{c_4}\}\delta_{c_4}$$

$$\{w\}=\left(-[M]^{-1}/{q_0}^2[K_0]\{\eta\}-W_q/q_0\{w_K\}-W_q/q_0\{w\}+[M]^{-1}W_q/{q_0}^2\{f\}\right)\delta_q$$
$$=\{z\}\delta_q$$

(3-37)

The state space representation of the system without any forcing input and measurement output is given as

$$\begin{Bmatrix} \{\eta'\} \\ \{\eta''\} \\ \{x'\} \\ \hline \{z\} \\ \{z_K\} \\ \{z_{c_1}\} \\ \{z_{c_2}\} \\ \{z_{c_3}\} \\ \{z_{c_4}\} \end{Bmatrix} = \left[\begin{array}{ccc|cccccc} [0] & [I] & [0] & [0] & [0] & [0] & [0] & [0] & [0] \\ -[M]^{-1}([K_0]/q_0+[K_a]) & -[M]^{-1}[C] & -[M]^{-1}[D_0] & -[I] & -[I] & -[I] & -[I] & [0] & [0] \\ E_2 & E_1 & F_0 & 0 & 0 & 0 & 0 & I & I \\ \hline -[M]^{-1}[K_0]W_q/{q_0}^2 & [0] & [0] & -W_q/q_0[I] & -W_q/q_0[I] & [0] & [0] & [0] & [0] \\ [M]^{-1}[W_K]/q_0 & [0] & [0] & [0] & & \cdots & & & [0] \\ [0] & [0] & [M]^{-1}[D_3] & & & & & & \\ [0] & [0] & [M]^{-1}[D_2] & \vdots & & \ddots & & & \vdots \\ [0] & [0] & [F_2] & & & & & & \\ [0] & [0] & [F_1] & [0] & & \cdots & & & [0] \end{array}\right] \begin{Bmatrix} \{\eta\} \\ \{\eta'\} \\ \{x\} \\ \hline \{w\} \\ \{w_K\} \\ \{w_{c_1}\} \\ \{w_{c_2}\} \\ \{w_{c_3}\} \\ \{w_{c_4}\} \end{Bmatrix} \tag{3-38}$$

A Matlab script code is prepared for the robust flutter analysis of the typical section using the given formulation. The μ norm is calculated with the "mussv" function of the "Robust Control Toolbox" of Matlab.

Figure 57 shows a case study with a 1% complex stiffness uncertainty and 1% real parametric uncertainty for each aerodynamic coefficient. Here, the nominal speed is 60 m/s and an initial perturbation of 25 m/s is applied. The μ norm indicates that the dynamic pressure perturbation should be 1/1.122 of the predicted value for stability, which corresponds to 22 m/s perturbation in speed. Figure 58 shows the new μ norm for 21 m/s perturbation, and the norm is now close to unity. Hence, the robust flutter speed for this typical section is estimated to be 82 m/s, which is less than the nominal flutter speed (85.5 m/s) as expected. However, both figures show that there is a convergence problem in μ norm calculation. Its upper and lower bounds should converge for a reliable answer. The upper bounds are calculated with the greatest accuracy, which is denoted by parameter='a' in the title of figures. This parameter invokes the linear matrix inequality (LMI) solver with an automatic prescaling and increases the computation time seriously. The computation time depends on the number of uncertainty descriptions and on the type of the uncertainty. A pure real uncertainty description decreases the convergence speed of the norm computations. This is actually why it is always advised to include some complex uncertainty to

increase the convergence speed. The speed of norm calculation with default parameters is much higher than the LMI solution. Nevertheless, the default solver has a serious accuracy problem. Figure 59 shows the same solution as in Figure 57 obtained using the default solver. When these figures are investigated, it is seen that neither the norm value nor the destabilizing frequency is correct. The robust flutter calculation based on Figure 59 converges to a flutter speed of 71 m/s, which is given in Figure 60. Actually, such a mathematical conservatism will increase the actual flutter test time which contradicts with the aim of the method.

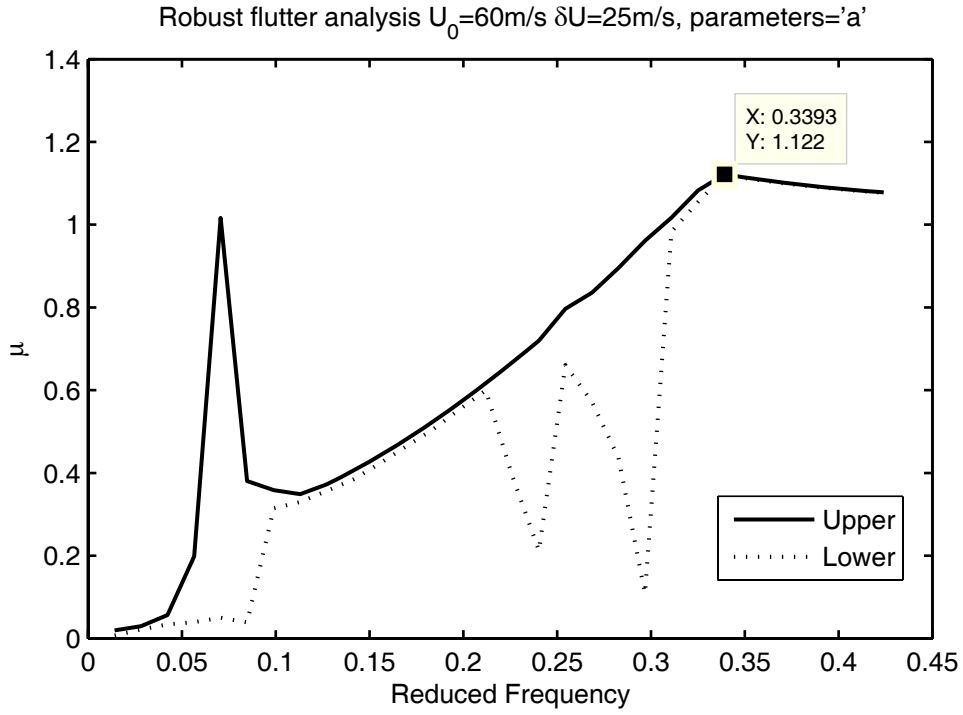

Figure 57. Robust flutter analysis for 1% uncertainty, parameters='a'.

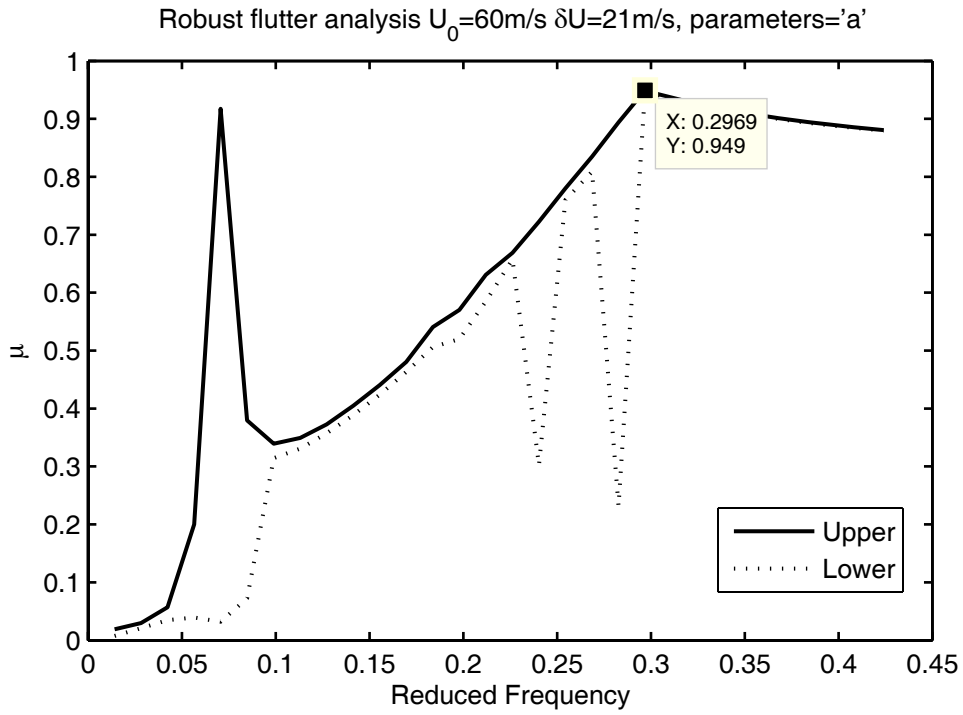

Figure 58. Robust flutter analysis for 1% uncertainty, parameters='a'.

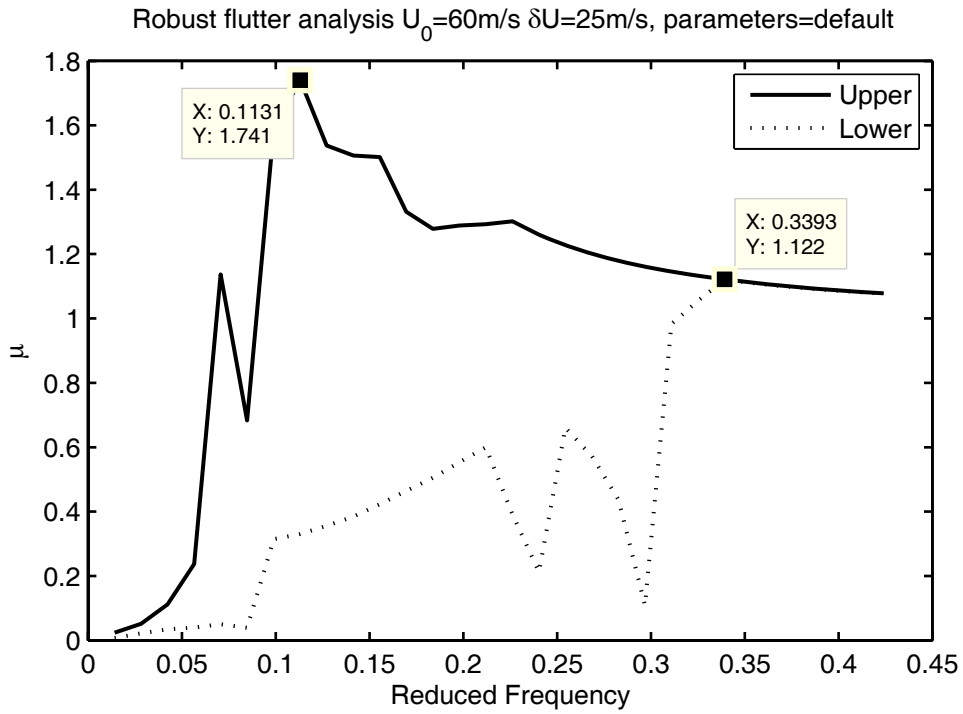

Figure 59. Robust flutter analysis for 1% uncertainty, parameter=default.

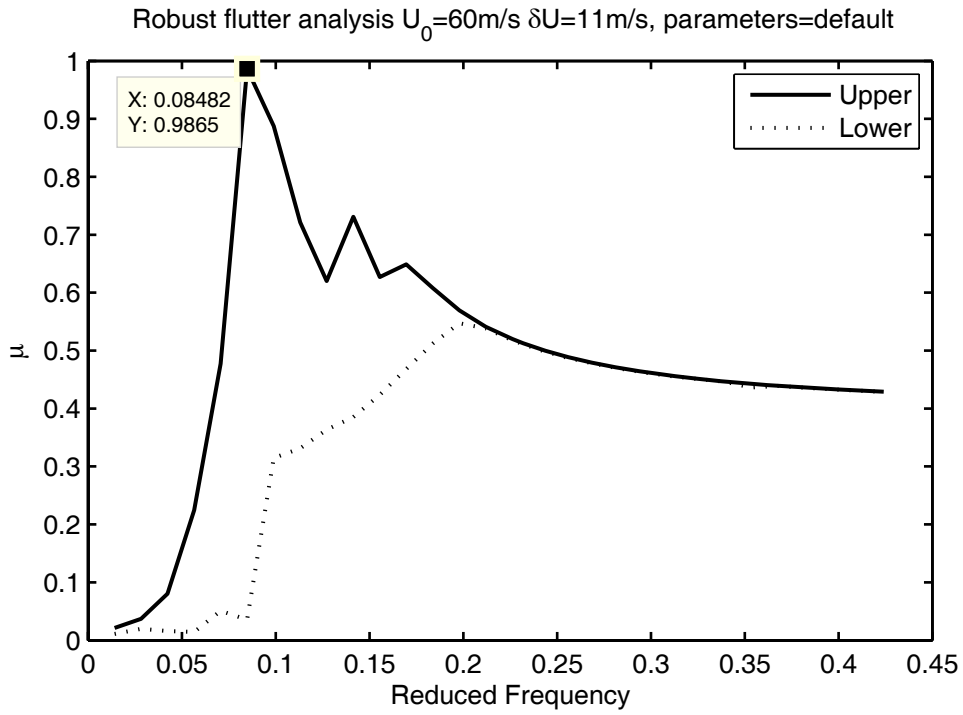

Figure 60. Robust flutter analysis for 1% uncertainty, parameters=default.

Another case is solved with uncertainty descriptions increased to 10%. Since the structural stiffness is modeled with a complex uncertainty, an artificial damping is introduced to the model, which might be expected to increase the flutter speed. However, the method also considers the other case where the damping decreases because of the symmetry of the uncertainty. The method considers the worst case and it is seen that the μ norm never decreases to unity even at very low speeds. Such a high conservatism can be eliminated by changing the complex stiffness uncertainty to a real uncertainty. Figure 61 shows the converged result when the structural stiffness is modeled with a real parametric uncertainty. The robust flutter speed is calculated as 77 m/s, which has less conservatism. This case demonstrates the importance of uncertainty modeling. The uncertainty levels and types should be selected carefully, preferably depending on experimental results.

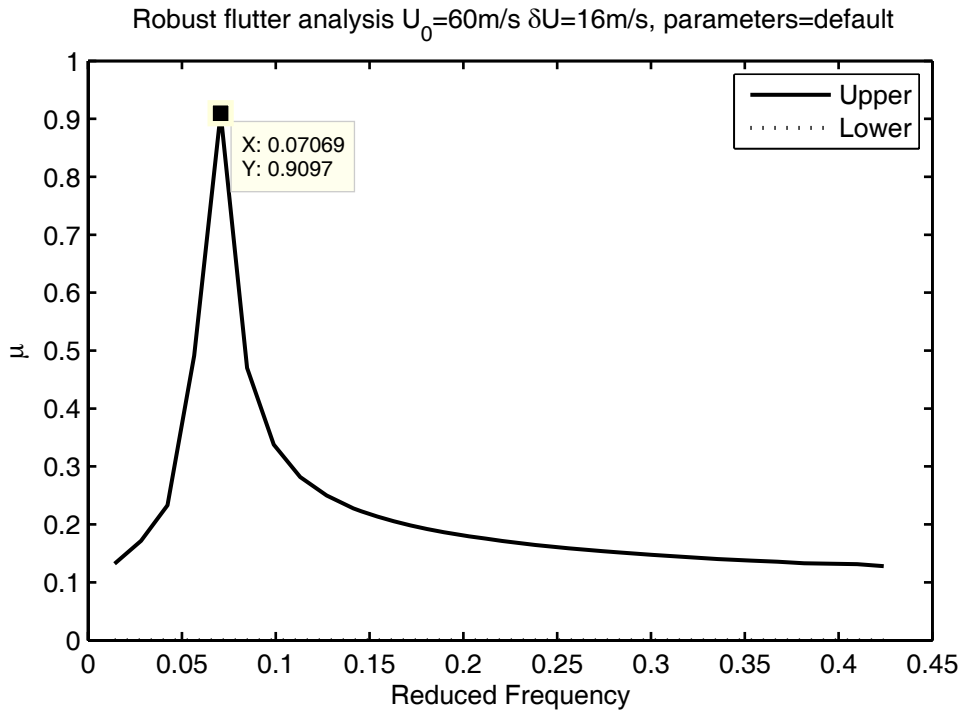

Figure 61. Robust flutter analysis for 10% real uncertainty, parameter='a'.

Another important point is the selection of nominal and perturbation speeds. Since Matlab's "mussv" function always assumes a symmetrical deviation from the nominal value, negative dynamic pressures occur when the perturbation is bigger than the nominal value. Although a negative dynamic pressure is mathematically possible, solutions in such cases are not physically meaningful. Therefore, a nominal pressure just below the assumed flutter pressure should be selected with a small perturbation compared to nominal pressure. In aeroservoelastic cases, not only the upper pressure bound should be checked but the stability at and beyond the lower bound should also be checked. In other cases, only the upper pressure bound is important. So a new μ norm function can be developed regarding only the upper bound for dynamic pressure. This would also decrease the computational time.

3.2.7.4 Flutter Prediction

The structural states of a typical section can be measured easily in an experiment. However, in real flutter tests, it is usually not possible to measure structural displacements or speeds directly. Strain gauges would give measurements proportional to the relative displacement, but it is difficult to calibrate the sensor and to mathematically model the input-output relation. Accelerometers are the main sensors used in flutter flight testing. So, the state space model of the typical section should output vertical accelerations. Recall that the trailing edge of the typical section is found as the best measurement point. The vertical acceleration of the trailing edge in terms of state variables can be found by the following simple transformation.

$$y = -h'' - \tfrac{3}{2} b\alpha'' = \begin{bmatrix} -1 & -\tfrac{3}{2} b \end{bmatrix} \begin{Bmatrix} h'' \\ \alpha'' \end{Bmatrix} = [T_1]\{\eta''\} \tag{3-39}$$

The forcing on the typical section is simply a impulsive force acting on the trailing edge, which also creates a moment proportional to the moment arm of $\tfrac{3}{2} b$.

$$\{f\} = \begin{bmatrix} 1 \\ \tfrac{3}{2} b \end{bmatrix} f^e = [T_2] f^e \tag{3-40}$$

Accelerations can be calculated with the first expression of Equation 3-37.

$$\begin{aligned} y = &-[T_1][M]^{-1}\left([K_0]/q_0 + [K_a]\right)\{\eta\} - [T_1][M]^{-1}[C]\{\eta'\} - [T_1][M]^{-1}[D_0]\{x\} \\ &-[T_1]\{w\} - [T_1]\{w_K\} - [T_1]\{w_{c_1}\} - [T_1]\{w_{c_2}\} + [T_1][M]^{-1}[T_2]/q_0 \, f^e \end{aligned} \tag{3-41}$$

Equation 3-37 with the output 3-41 can be represented in state space form as given in Equation 3-42.

$$\begin{Bmatrix} \{\eta'\} \\ \{\eta^*\} \\ \{x'\} \\ \hline \{z\} \\ \{z_K\} \\ \{z_{c_1}\} \\ \{z_{c_2}\} \\ \{z_{c_3}\} \\ \{z_{c_4}\} \\ y \end{Bmatrix} = \left[\begin{array}{ccc|cccccccc} [0] & [I] & [0] & [0] & [0] & [0] & [0] & [0] & [0] & [0] \\ -[M]^{-1}([K_0]/q_0+[K_a]) & -[M]^{-1}[C] & -[M]^{-1}[D_0] & -[I] & -[I] & -[I] & -[I] & [0] & [0] & [M]^{-1}[T_2]/q_0 \\ [E_2] & [E_1] & [F_0] & [0] & [0] & [0] & [0] & [I] & [I] & [0] \\ \hline -[M]^{-1}[K_0]W_q/q_0^2 & [0] & [0] & -W_q/q_0[I] & -W_q/q_0[I] & [0] & [0] & [0] & [0] & [M]^{-1}[T_2]W_q/q_0^2 \\ [M]^{-1}[W_K]/q_0 & [0] & [0] & [0] & & \cdots & & & & [0] \\ [0] & [0] & [M]^{-1}[D_3] & & & & & & & \\ [0] & [0] & [M]^{-1}[D_2] & \vdots & & \ddots & & & & \vdots \\ [0] & [0] & [F_2] & & & & & & & \\ [0] & [0] & [F_1] & [0] & & \cdots & & & & [0] \\ -[T_1][M]^{-1}([K_0]/q_0+[K_a]) & -[T_1][M]^{-1}[C] & -[T_1][M]^{-1}[D_0] & -[T_1] & -[T_1] & -[T_1] & -[T_1] & -[T_1] & -[T_1] & [T_1][M]^{-1}[T_2]/q_0 \end{array}\right] \begin{Bmatrix} \{\eta\} \\ \{\eta'\} \\ \{x\} \\ \hline \{w\} \\ \{w_K\} \\ \{w_{c_1}\} \\ \{w_{c_2}\} \\ \{w_{c_3}\} \\ \{w_{c_4}\} \\ f^e \end{Bmatrix} \tag{3-42}$$

A Matlab script code is prepared to find the appropriate scale of the initial uncertainty definition. As stated in the method, the dynamic pressure uncertainty is not taken into account during updating. After updating the uncertainty definition, a robust flutter analysis is performed to estimate the critical flutter speed. Input and output time signals are converted into discrete frequency domain functions by Fourier transformation. The initial uncertainty scale is estimated to be 1% for all parameters. The structural stiffness is modeled with a complex uncertainty and all other parameters are modeled with a real parametric uncertainty. Figure 62 shows the validation norm. This norm should be just greater than unity to ensure that model is not invalidated. As seen from this figure, the norm is much higher than unity, which means that 1/192 of the uncertainty description is sufficient for validation. 1/192 of 1% is almost negligible but such a low value was expected because simulations are already performed with the exact parameters. The original mathematical model is so accurate that no uncertainty description is necessary. In real life, there will be errors in the mathematical model of the test item. Thus, the parameters of the typical section are perturbed artificially as in Table 10 for a meaningful analysis.

Table 10. Physical parameter changes.

Parameter	K_h	K_α	c_1	c_2	c_3	c_4
Change	5%	-5%	10%	-10%	-10%	10%

The result with the perturbed parameters is given in Figure 63. As seen from the figure, the norm is reduced significantly. The validation algorithm indicates that 1/1.286 of the initial uncertainty description is enough for validation. So, the perturbation will be selected as 1/1.286*1%=0.78% for the related speed. Figure 64 shows the result of the flutterometer method. The perturbation on the dynamic pressure should be slightly lowered to get unity norm. The estimated flutter speed can be calculated as shown below.

$$q_{new} = q_0 + W_q / \mu(P)$$
$$V_f = \sqrt{2 q_{new} / \rho} \tag{3-43}$$

Various flight speeds and dynamic pressure perturbation levels are used to demonstrate the method. Results are given in Table 11. The comparison of the method with other methods is given in Table 13. Although flutterometer is said to be always conservative, the estimations at high speeds show that the estimated flutter speeds can be higher than the actual values. The conservatism seems to decrease with increasing speed.

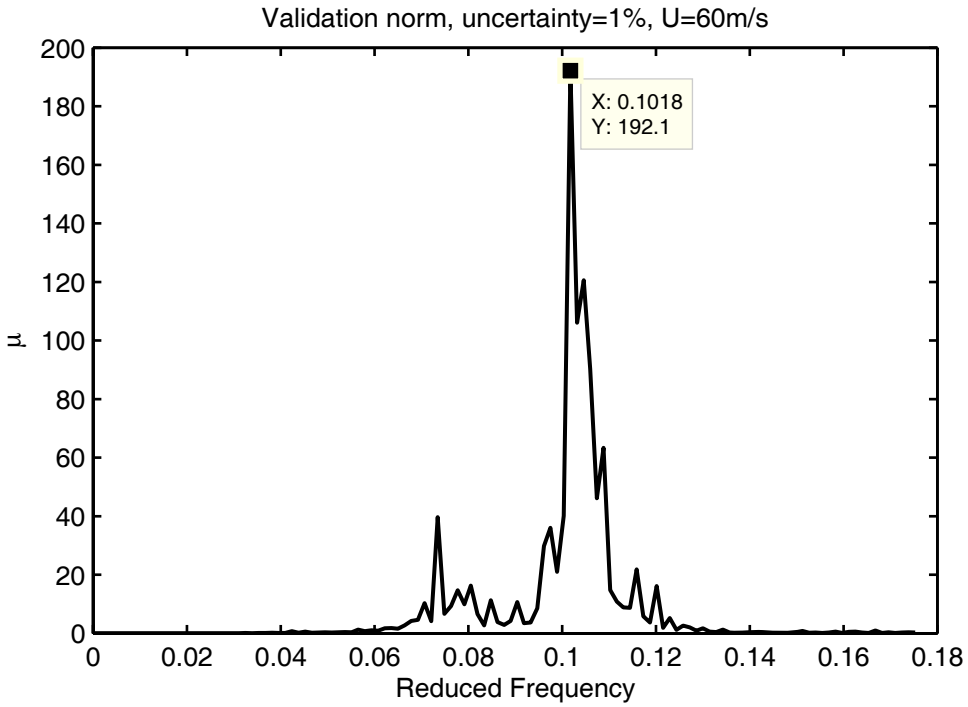

Figure 62. Validation norm, uncertainty=1%, U=60m/s.

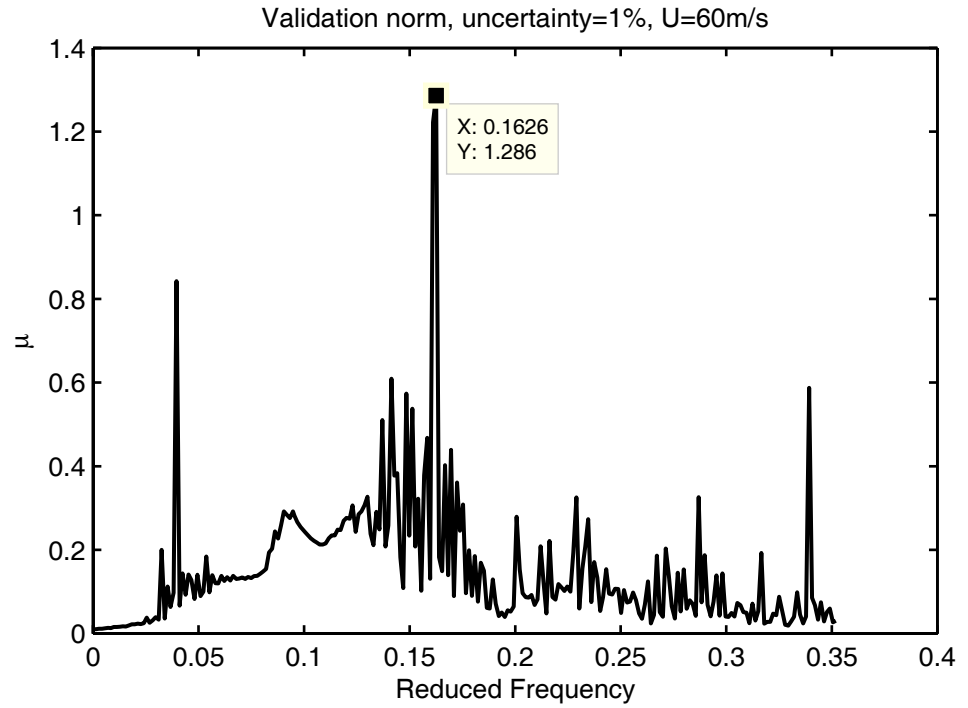

Figure 63. Validation norm with changed parameters, uncertainty=1%, U=60m/s.

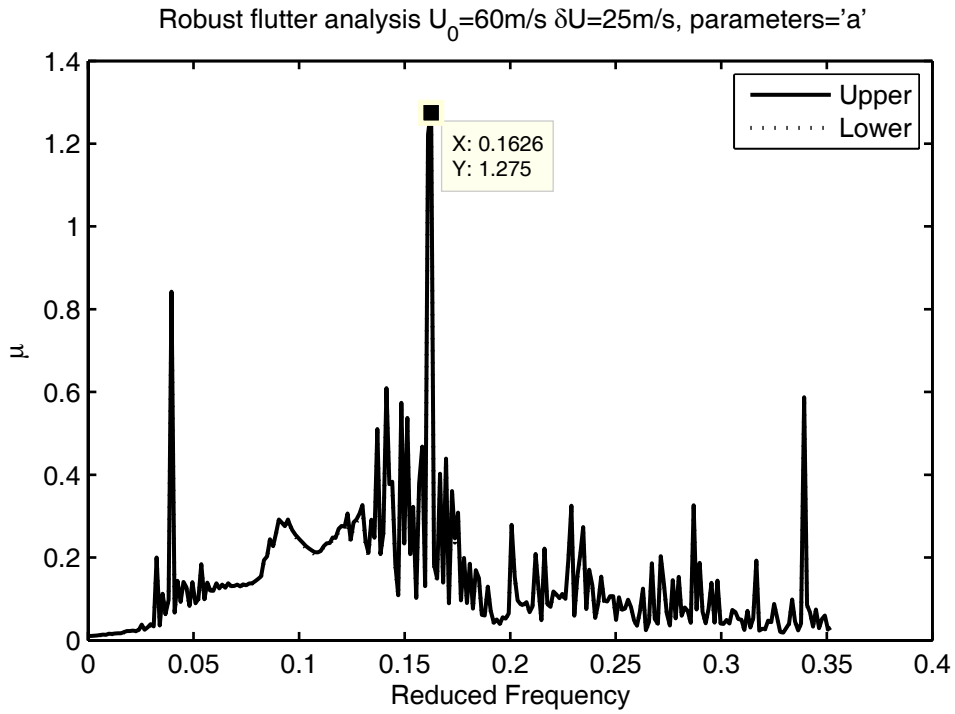

Figure 64. Flutterometer result for U=60 m/s.

Table 11. Results for flutterometer.

Test	Flight Speed [m/s]	Uncertainty [%]	Speed Perturbation [m/s]	Estimated Flutter Speed [m/s]	Error [%]
1	50	0.18	40	70.6	-18.4
2	50	0.18	20	70.5	-18.5
3	60	0.78	25	83.3	-3.7
4	60	0.78	23	83	-4
5	70	0.6	20	97.3	12.5
6	70	0.6	10	95	9.9

3.3 Numerical Study for the ATS

The original aeroservoelastic test setup was a highly nonlinear system because of the high friction levels on the linear guides. The flutter speed of the original setup was much higher than the theoretical value because of the high damping introduced by this friction. The setup improved by replacing linear guides with better ones. The linear springs are also replaced to have a higher preload to avoid backlash in plunge motion. The actual parameters of the ATS are as follows.

m = 38 kg : Total mass of moving parts of the system (airfoil and base).
$m_{airfoil}$ = 11 kg : Mass of the rotating parts (airfoil).
I_α = 0.1 kg.m^2 : Mass moment of inertia of the rotating parts.
K_h = 19,200 N/m : Flexural stiffness of the airfoil.
K_α = 44.6 N.m/rad : Torsional stiffness of the airfoil.
a = -0.6 : Normalized distance between the elastic axis and midchord.
b = 0.15 m : Semichord length of the airfoil.
l = 0.6 m : Span of the airfoil.
x_α = 0.409 : Normalized distance between the elastic axis and mass center of airfoil.

This system has a theoretical flutter speed of 25.7 m/s with 1.1341 kg/m^3 air density (corresponding to ~800 m altitude), which is found by plotting the roots of the system versus the flight speed. The uncoupled natural frequencies are 3.36 Hz for torsion and 3.58 Hz for plunge. The natural frequencies of the system are 2.98 Hz and 4.3 Hz. Recall that uncoupled and coupled natural frequencies of the mild flutter case are close to each other. However ATS has considerably different coupled and uncoupled natural frequencies. This is an indication of high coupling and is because of the high value of x_α. The mass unbalance is one of the most important parameters that effects the flutter speed. A high mass unbalance is not only reduces the flutter speed but also changes the behavior of the flutter mechanism. Usually an explosive type flutter occurs in such systems. The term “explosive flutter” is used for cases

where the damping of the system decreases rapidly at speeds close to the flutter speed.

The ATS is excited by a servo system mounted on the torsional degree of freedom of the system. The base of the torsional spring is displaced by a desired angle with this stiff servo system. Recall that the excitation for mild flutter case is an impulsive force. An angular base excitation is added to the previously prepared Simulink model. Note that the parameter *a,* which defines the location of the elastic axis is also different. The elastic axis is at the quarter chord for mild flutter case. The center of pressure for thin airfoils at subsonic speeds is at the quarter chord, a=-0.5, of the airfoil. However, the elastic axis of the ATS is slightly ahead of the quarter chord, a=-0.6, to have an equilibrium at the zero angle attack. The transformation given in Equation 3-6, which converts the angular and flexural motions of the typical section to vertical motions of the typical section at various measurement points must be redefined because of this shift in the elastic axis. The new transformation matrix is given in Equation 3-44. The locations of leading and trailing edge accelerometers are corrected, but the locations of intermediate accelerometers are not changed. The best measurement location for ATS is found to be the trailing edge, which is denoted as sensor 5.

$$[T]=\begin{bmatrix} -1 & 0.4b \\ -1 & 0 \\ -1 & -0.5b \\ -1 & -b \\ -1 & -1.6b \end{bmatrix} \tag{3-44}$$

The simulations are re-run with the typical section parameters given above. The simulation results are analyzed with the same tools used in the mild flutter case.

3.3.1 Flutter Prediction with Damping Extrapolation

The Simulink model developed is run with air speeds of 10, 12.5, 15, 17.5, 20, 22.5, and 25 m/s. A shifted half cosine is used for excitation. The excitation has a peak of 5° and 62.5 ms of duration, which corresponds to 8 Hz. Some FRF estimations obtained by the "tfestimate" command of Matlab are given in Figure 65, Figure 66 and Figure 67. The variation of FRF at the trailing edge with speed is given in Figure 68.

A curve fit is performed for a frequency range of 2 to 6 Hz, which covers both modes. The fit results for all air speeds are given in Figure 69 through Figure 75, and in Table 12. The V-g plots are given in Figure 76 and Figure 77.

Damping extrapolations with 3^{rd} and 4^{th} order fit are given in Figure 78 and Figure 79 with various data pairs used. The extrapolation with the first 6 data pairs results in a flutter speed of 41.3 m/s for the 3^{rd} order fit and 26.8 m/s for the 4^{th} order fit. The 4^{th} order fit result is very close to the true value, 25.7 m/s. Extrapolation with the first 5 data pairs results in a flutter speed of 24 m/s only with the 4^{th} order fit.

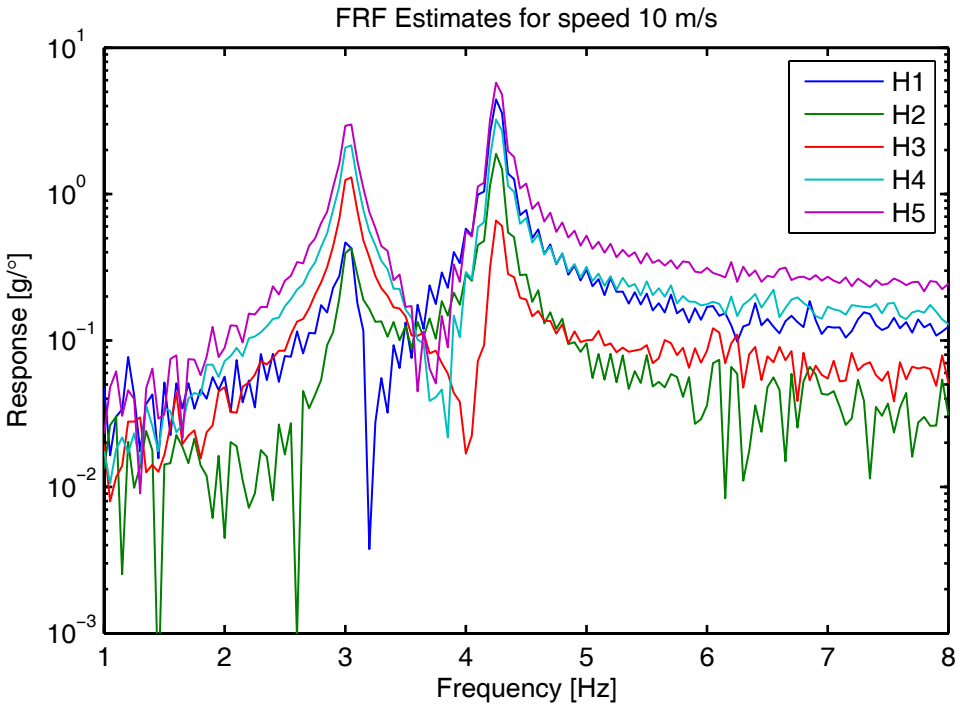

Figure 65. FRF estimates for 10 m/s.

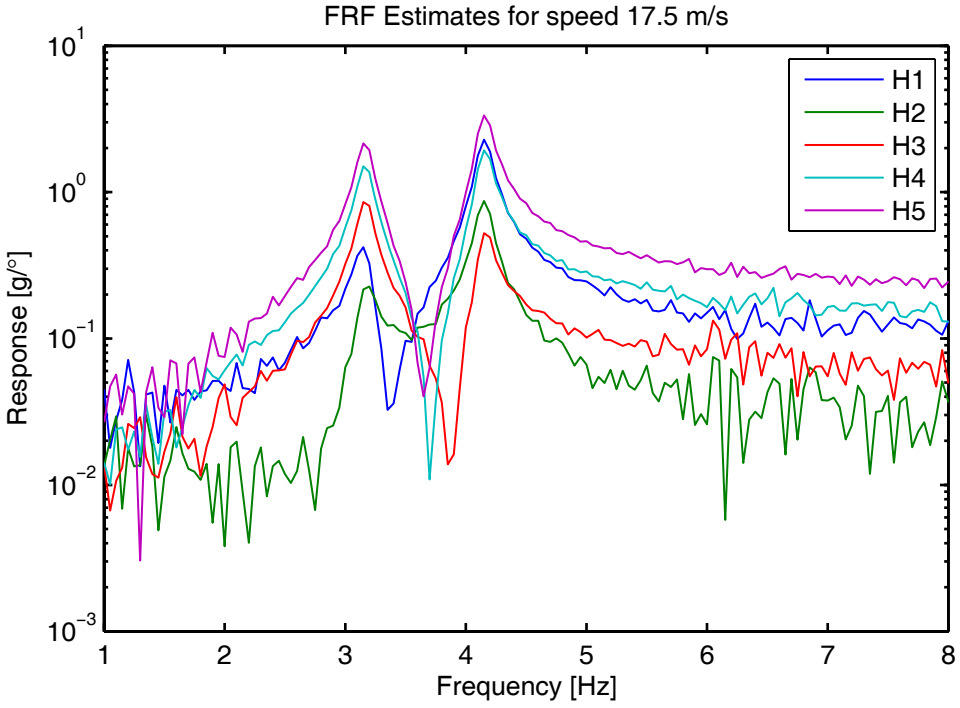

Figure 66. FRF estimates for 17.5 m/s.

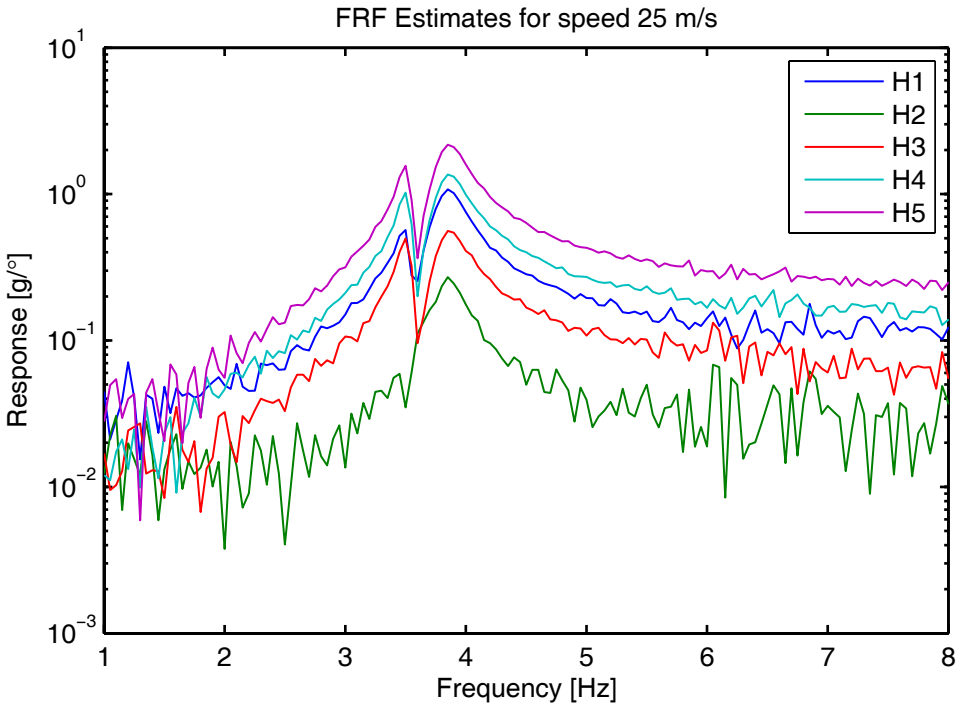

Figure 67. FRF estimates for 25 m/s.

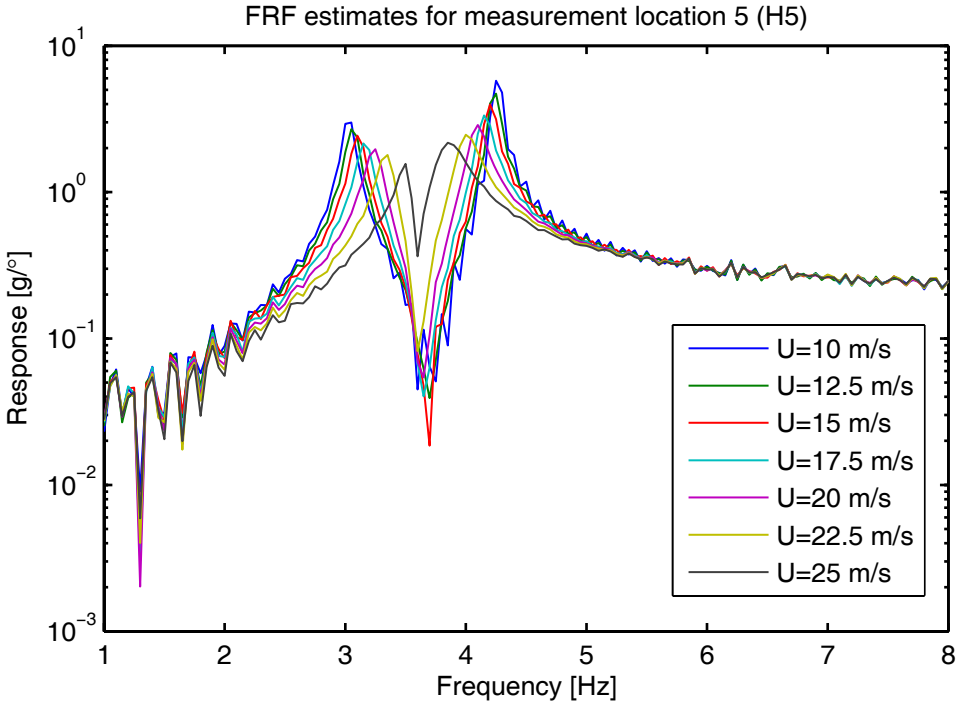

Figure 68. Change of H5 with air speed.

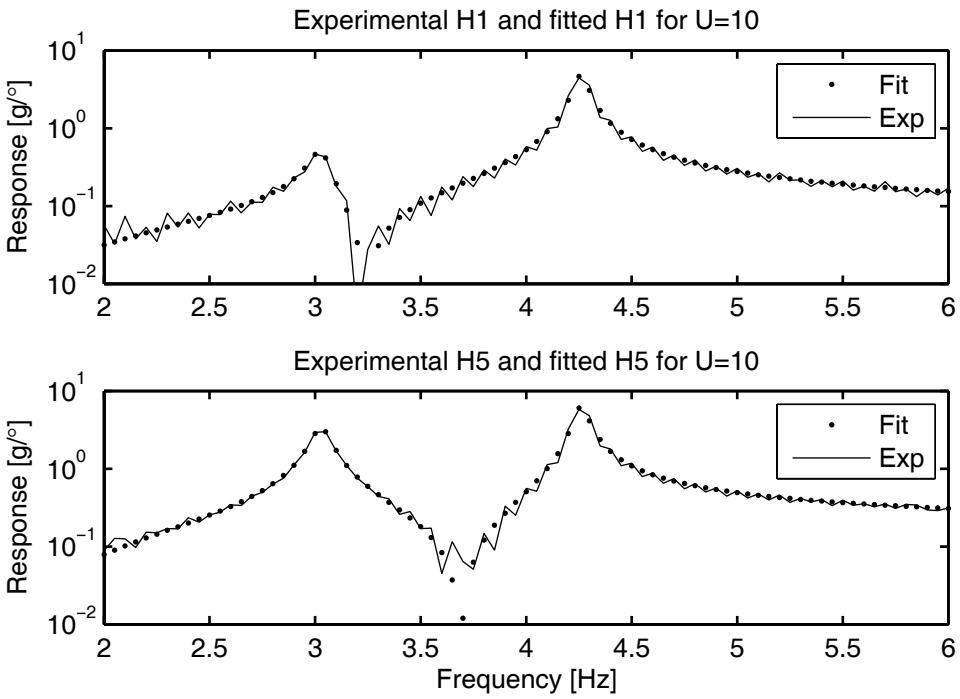

Figure 69. Fit results for 10 m/s.

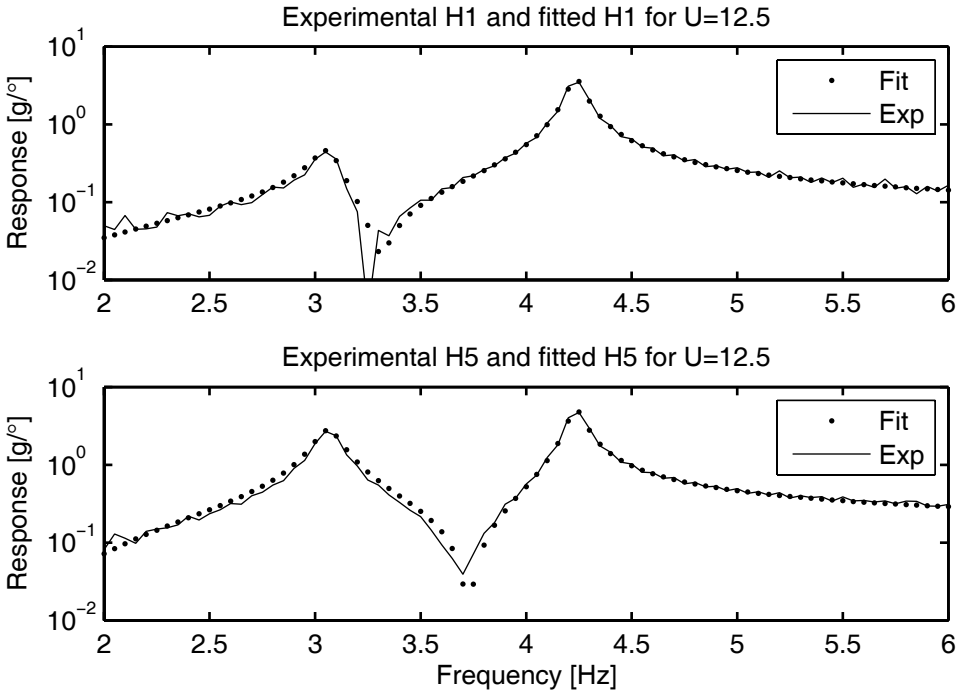

Figure 70. Fit results for 12.5 m/s.

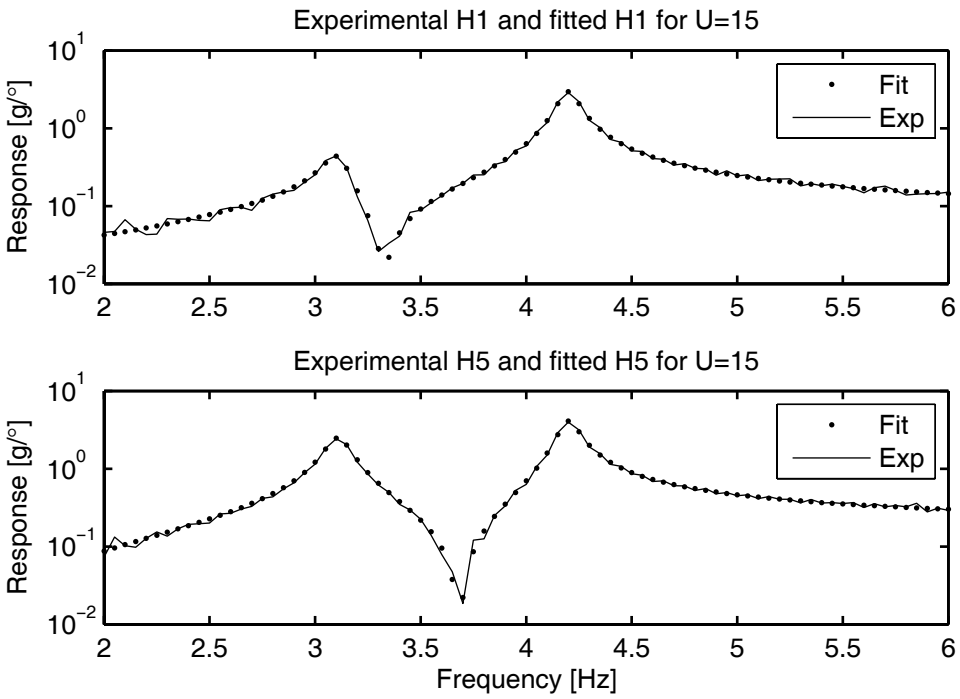

Figure 71. Fit results for 15 m/s.

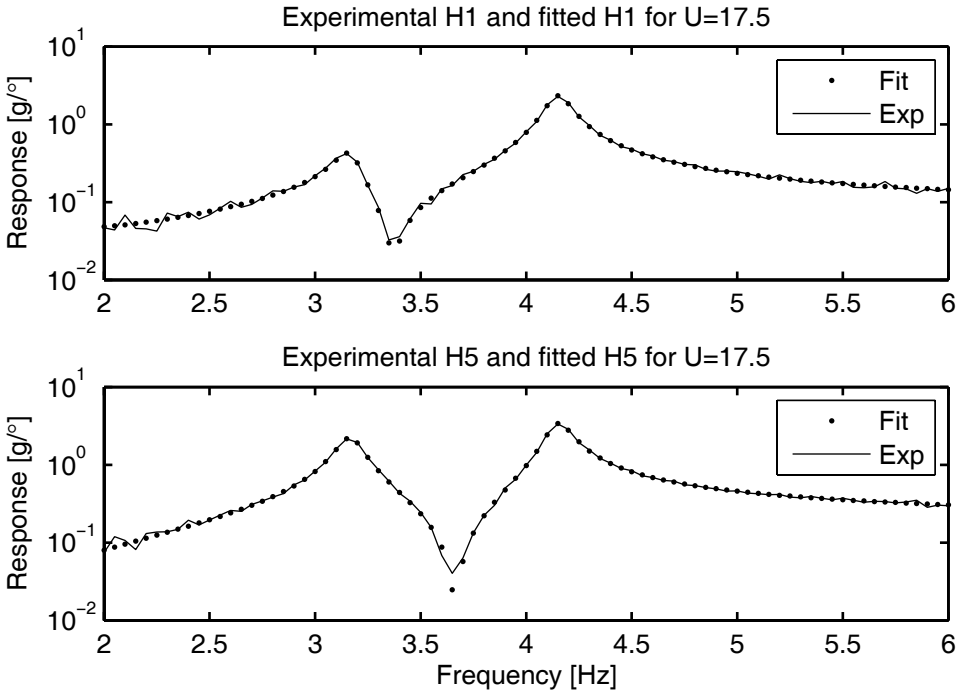

Figure 72. Fit results for 17.5 m/s.

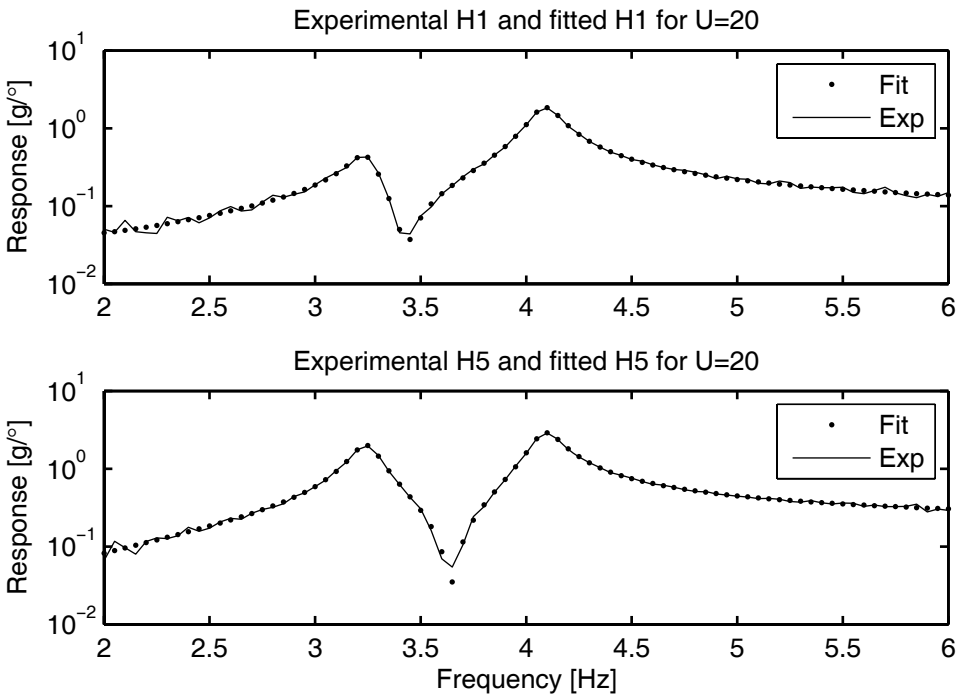

Figure 73. Fit results for 20 m/s.

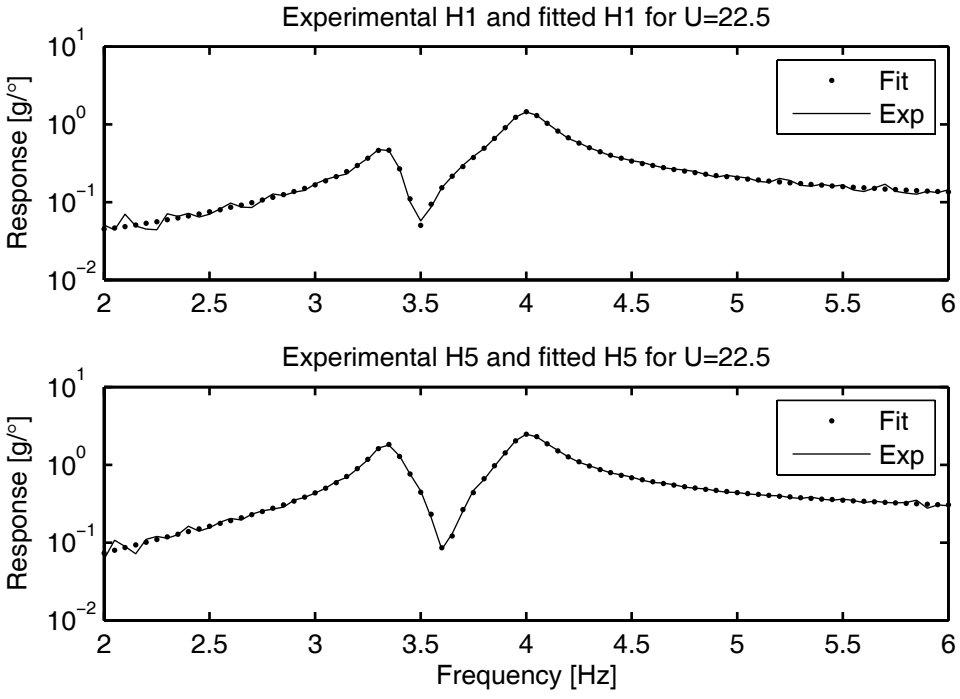

Figure 74. Fit results for 22.5 m/s.

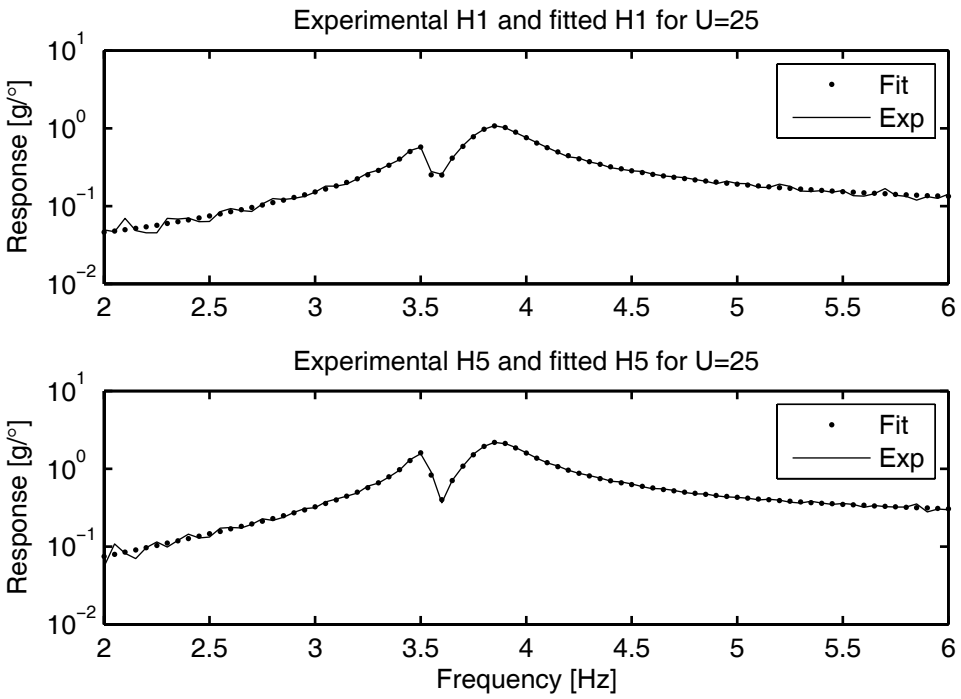

Figure 75. Fit results for 25 m/s.

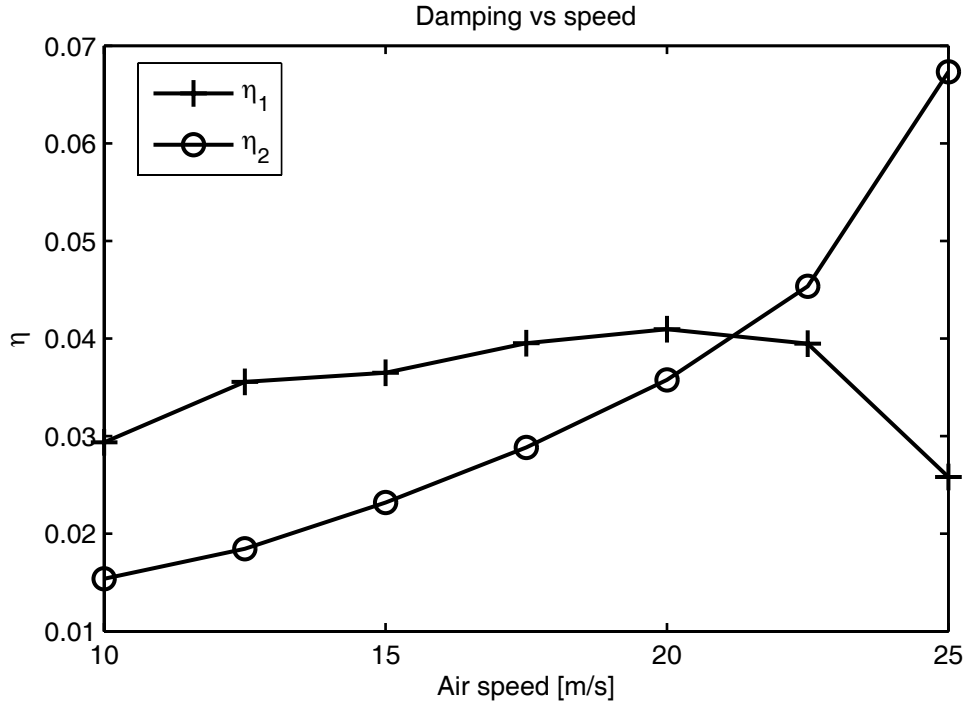

Figure 76. Damping versus speed graph.

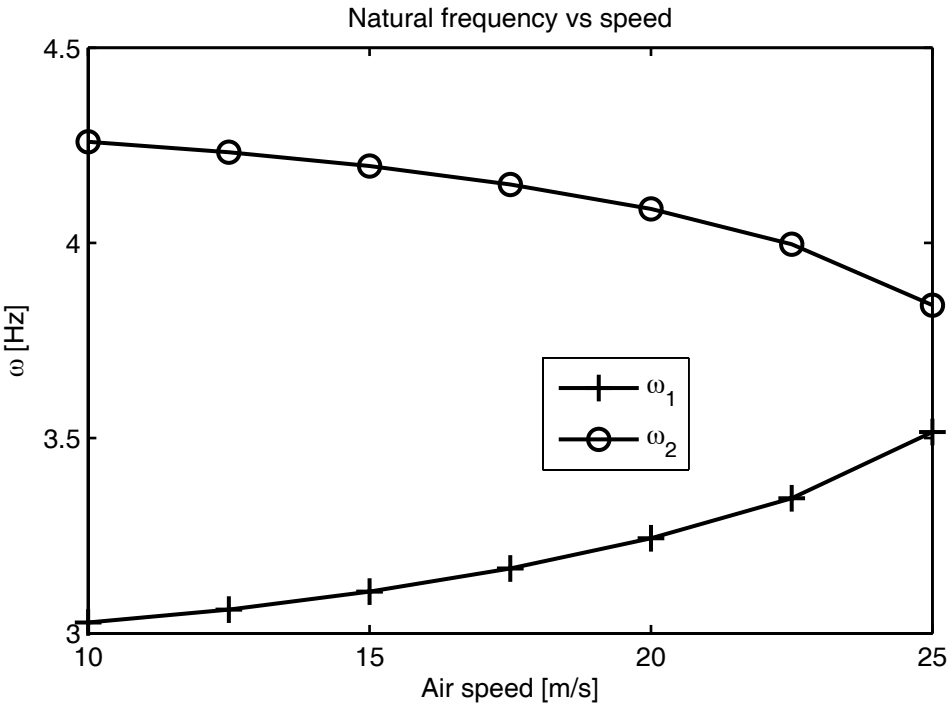

Figure 77. Natural frequency versus speed graph.

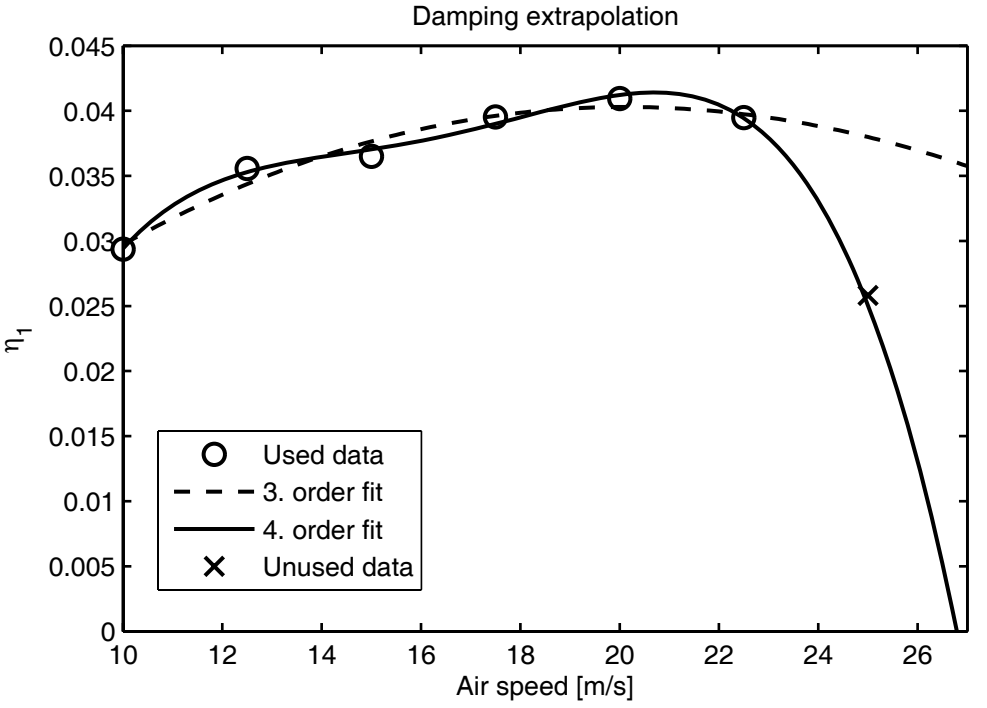

Figure 78. Damping extrapolation result with 6 data.

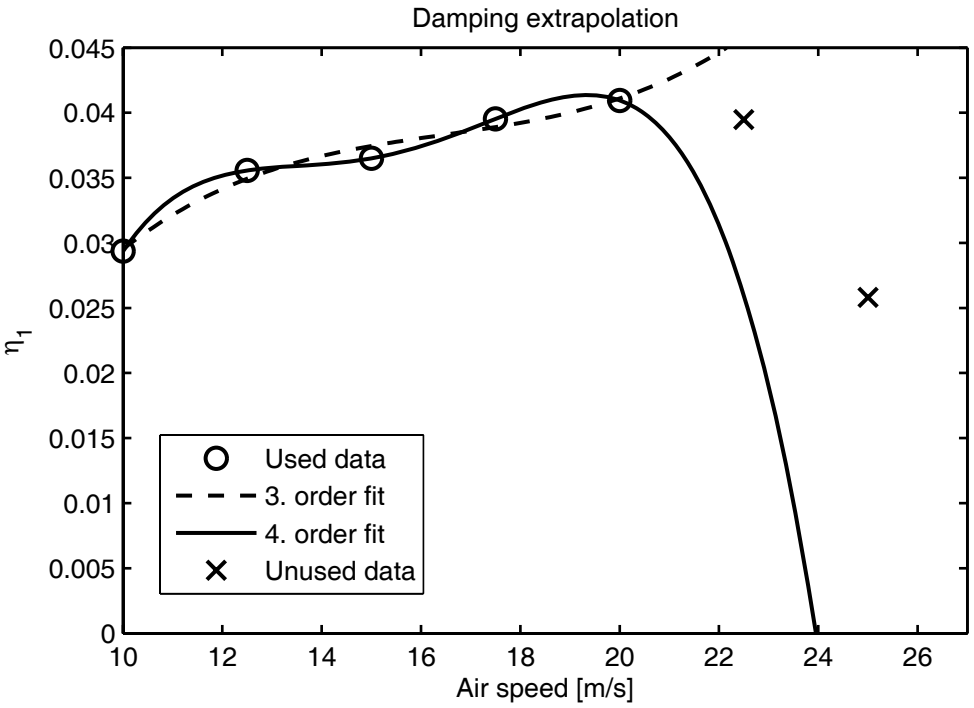

Figure 79. Damping extrapolation result with 5 data.

Table 12. Summary of modal extraction.

U [m/s]	10	12.5	15	17.5	20	22.5	25
η_1	0.0294	0.0356	0.0365	0.0395	0.0409	0.0395	0.0258
η_2	0.0154	0.0185	0.0232	0.0288	0.0358	0.0453	0.0673
ω_1 [Hz]	3.0277	3.0604	3.1068	3.1657	3.2433	3.3459	3.5153
ω_2 [Hz]	4.2587	4.232	4.1971	4.1496	4.0869	3.9964	3.8406

Although the change in damping is steep, the extrapolation with 4^{th} order fit gives very reliable estimates. Higher order fits are expected to give more conservative estimates provided that these fits are concave down in the speed range of interest. The most conservative value, 24 m/s, is selected to be the result of the damping extrapolation method.

3.3.2 Flutter Prediction with Envelope Function

The response of the ATS to nearly impulsive angular base input is directly used to calculate the shape parameters at each speed. The results of the mild flutter case are very satisfying. However, the results for ATS are disappointing. The calculated envelope functions for the trailing edge sensor are given in Figure 80 and Figure 81. Some highly coupled modes result in oscillatory envelopes at low speeds as in the mild flutter case. However, the envelopes for all sensors are found to be decreasing with increasing speed. The method becomes useless in such cases. Recall that in the mild flutter case, the envelopes just after the impact are increasing with increasing speed, Figure 42. That phenomenon becomes very useful if it can be generalized. However, it is not observed in ATS case, Figure 81. There seems to be an increase in the envelope just after the impact as speed increases, but increase is not significant compared to mild flutter case even at 25 m/s speed. The special case observed in mild flutter case affects the shape parameter change as the time limit is changed. However, the shape parameter change in ATS is found to be not affected by the time limit. The shape parameter change with 10 s of time limit is given in Figure 82. As seen from the figure, the shape parameters do not converge. All shape parameters, except the one related with sensor 2, monotonically increases as the air speed increases. Sensor 2 is very close to the elastic axis and thus measures mainly the plunge motion. This is because, the envelopes of sensor 2 are always much smaller than the other sensor's envelopes, and the sensor does not represent the overall system.

It can be concluded that the envelope function method is not working with the ATS. This might be the case for all explosive type flutter systems. But the generality of this statement must be further investigated.

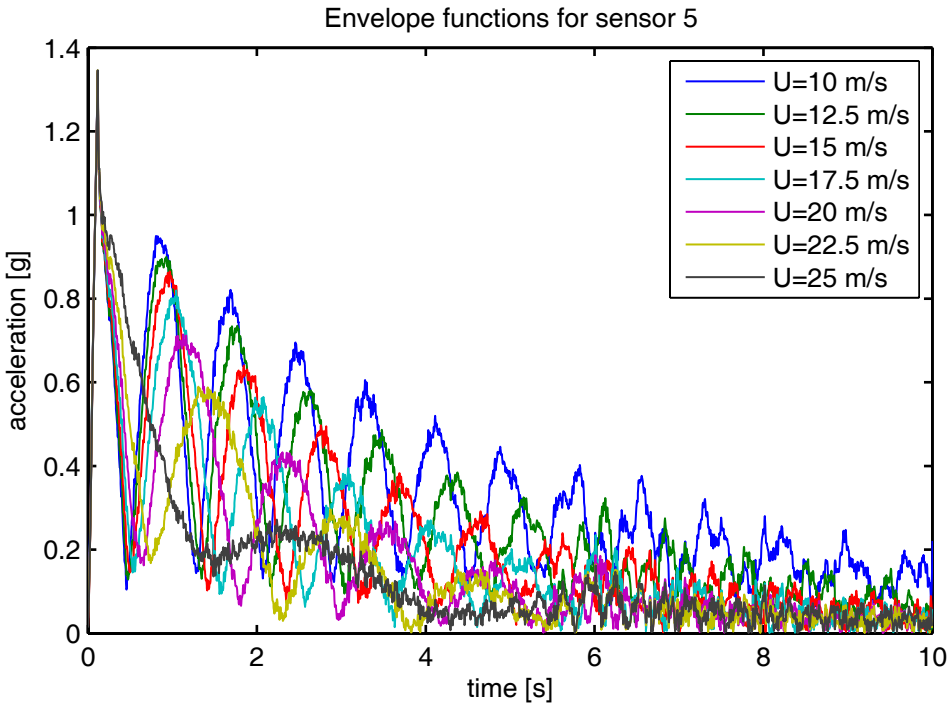

Figure 80. Envelope functions for the trailing edge accelerometer.

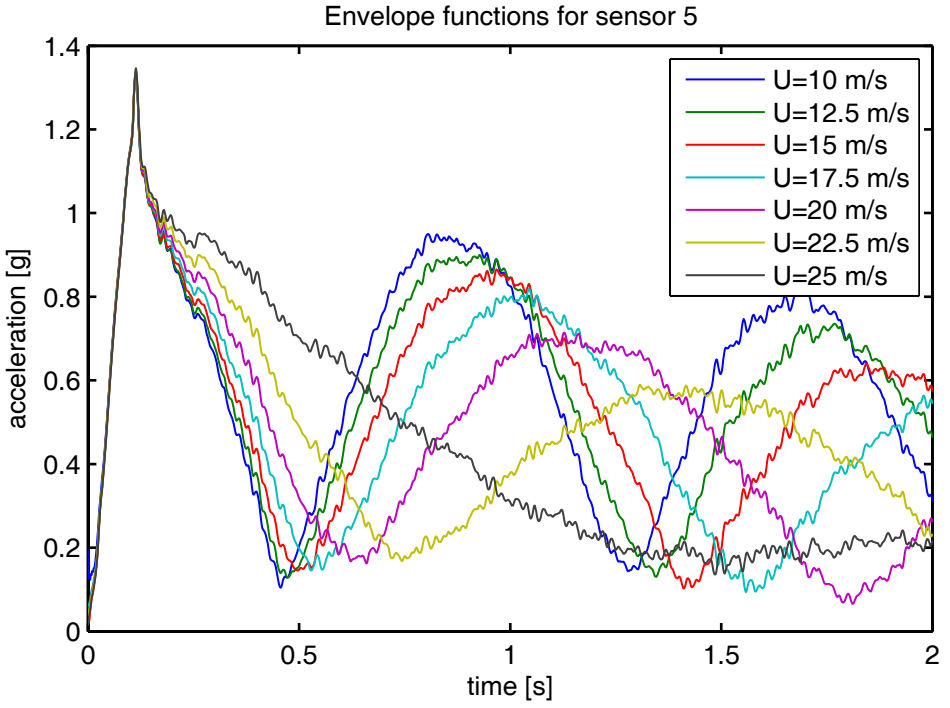

Figure 81. Envelope functions for the trailing edge accelerometer, zoomed.

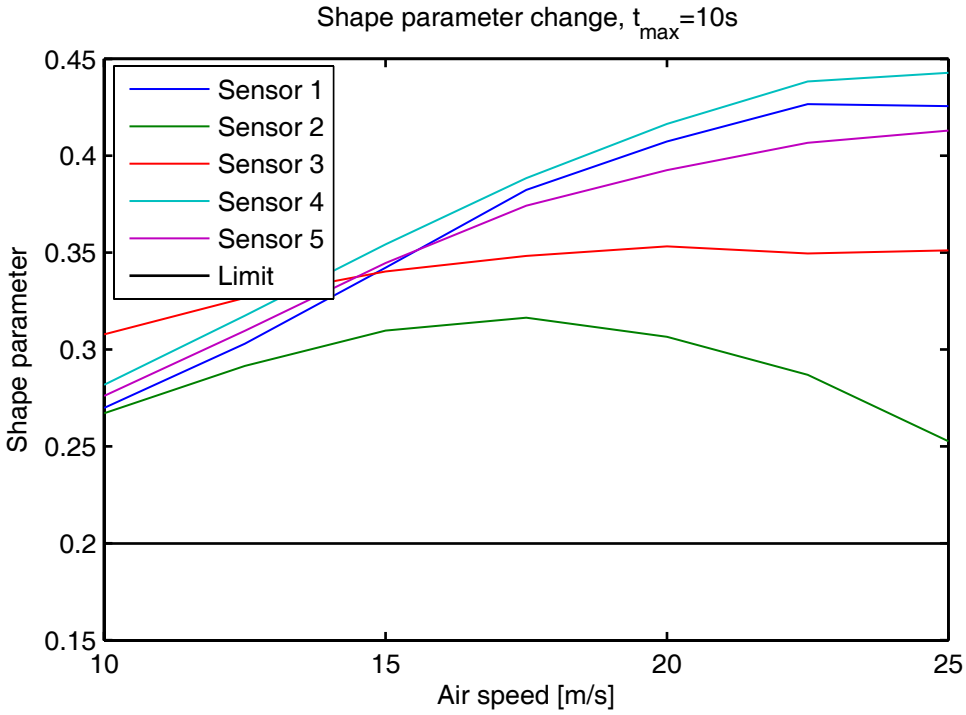

Figure 82. Variation of shape parameters with speed, t_{max}=10s.

3.3.3 Flutter Prediction with Flutter Margin

The flutter margin method is expected to work with explosive type flutter systems. Since ATS is a 2-DOF system, the method should give perfect results. The modal parameters, which are necessary to apply the method, are given in Table 12. The result is given in Figure 83 and Figure 84 with different number of data pairs used. The variation of Flutter Margin is almost linear as expected. There is no need to discard low speed data as in the mild flutter case. The 1st order fit with 6 data pairs results in a flutter speed of 26.7 m/s. The 2nd order fit with 6 data pairs results in a flutter speed of 25.4. When the first 5 data pairs are used, the flutter speed is estimated to be 27.4 m/s with the 1st order fit and 25.4 m/s with the 2nd order fit. All results, especially the results of the 2nd order fits, are very close to the actual value, 25.7 m/s.

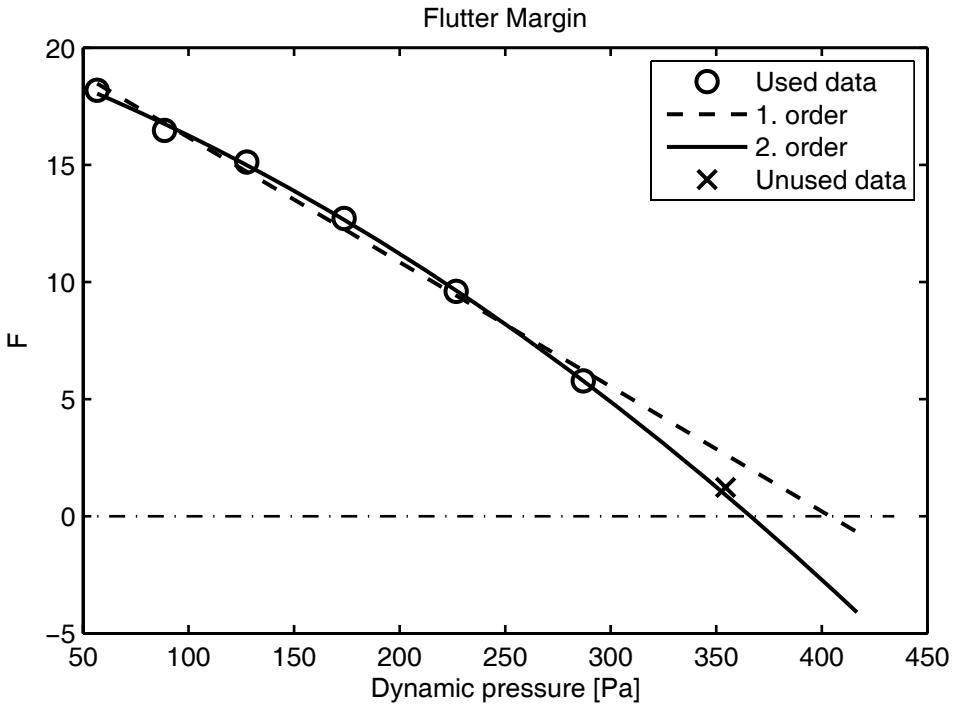

Figure 83. Flutter Margin fit for 6 data points.

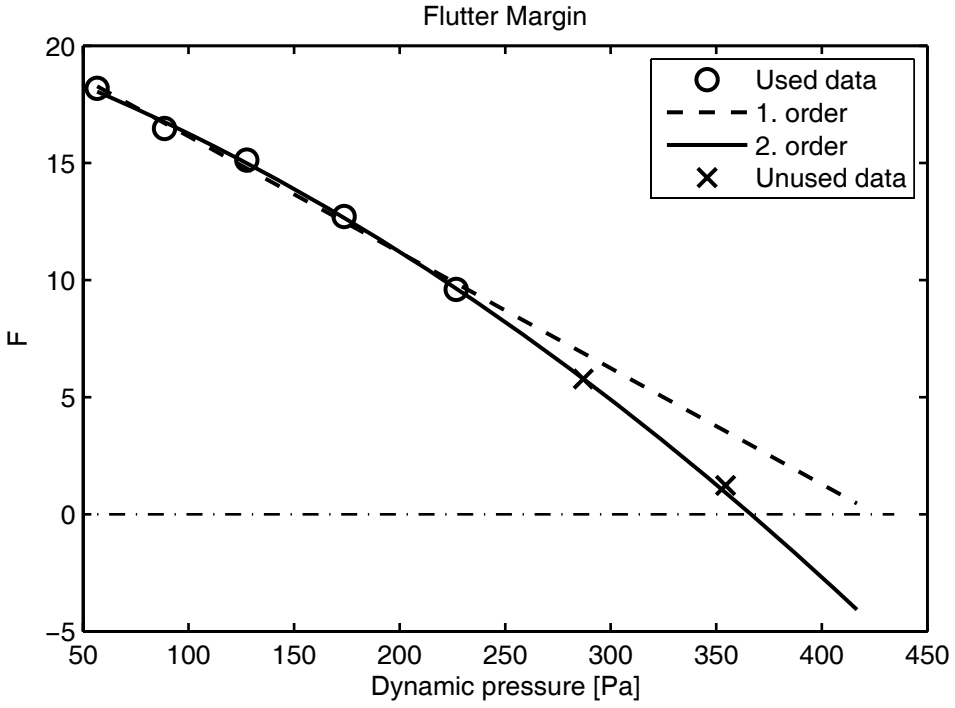

Figure 84. Flutter Margin fit for 5 data points.

The most conservative value, 25.4 m/s, is selected to be the result of the Flutter Margin method.

3.3.4 Flutter Prediction with ARMA Modeling

The discrete time ARMA modeling requires a random excitation. The ATS model is excited with random angular base inputs ranging from -5° to 5° at various speeds. Since the excitation is assumed to be always present on the structure in this method, more test points can be defined. The response of the ATS at speeds 10, 11.25, 12.5, 13.75, 15, 16.25, 17.5, 18.75, 20, 21.25, 22.5, 23.75, and 25 m/s are recorded for processing. The response of the ATS at speed 25.7 m/s, which is the critical flutter speed and at speeds 26 m/s and 27 m/s, which are above the critical flutter speed, are also recorded. The ARMA models of system order 4 and noise order 3 are used to fit the models as in the mild flutter case. Calculated stability indices, *Fz*, for each sensor at various speeds are given in Figure 85. As seen from the figure, the stability curves are almost flat up to the flutter speed. The stability curves rapidly decrease beyond the flutter speed. Obviously it is not possible to perform an extrapolation procedure to estimate the flutter speed with the data presented. It can be concluded that the method is not working with the ATS model as the envelope function method. It is known that flutter mode dominates the response at speeds close to the flutter speed. However the FRF plots of the ATS show that both modes of the structure are still dominant even at 25 m/s speed. This is because of the high coupling of the structural modes. The flutter mode dominates the response only at speeds very close to the flutter speed. This seems to be the reason for the failure of the envelope function and ARMA methods.

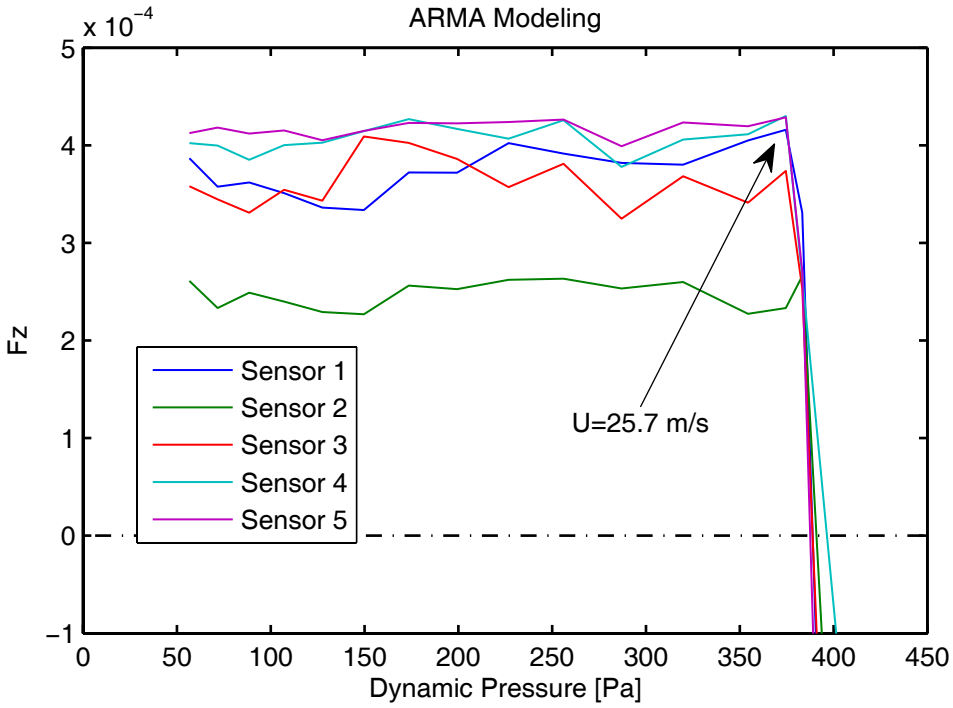

Figure 85. Variation of ARMA Fz with dynamic pressure.

3.3.5 Flutter Prediction with Flutterometer

The nominal flutter analysis of the ATS with the μ method results in a flutter speed of 25.7 m/s, which is the true flutter speed. The real part of the associated pole with respect to speed is given in Figure 86. The comparison of Figure 86 with Figure 56 explains the difference between the mild and explosive flutter.

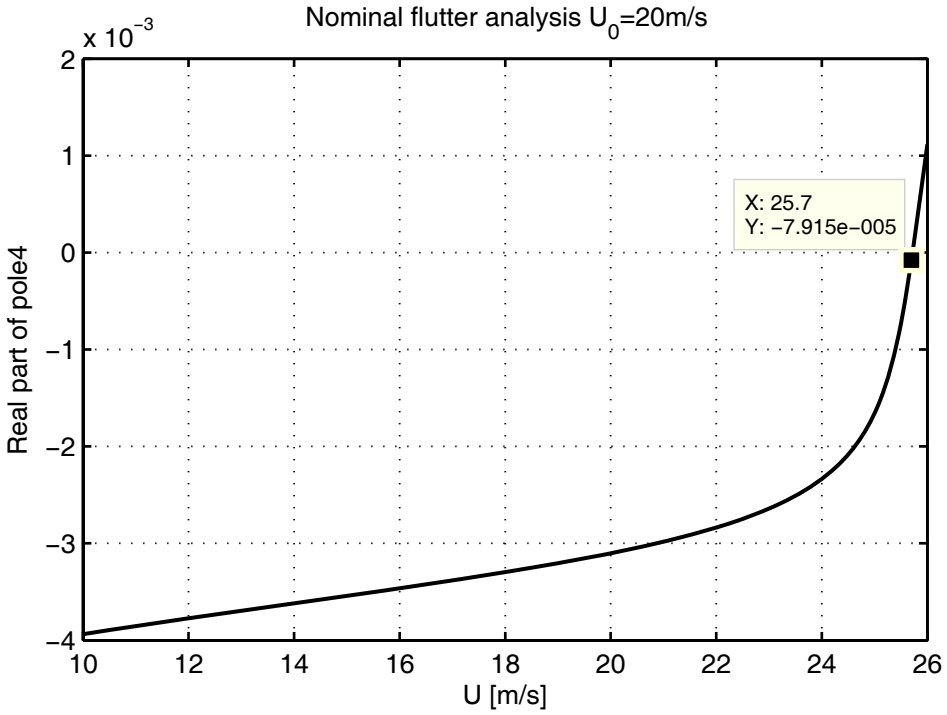

Figure 86. Nominal flutter analysis of the ATS.

Since the parameter "*a*" for ATS is different than the previous model, the acceleration of the trailing edge must be redefined as follows.

$$y = -h'' - 1.6b\alpha'' = \begin{bmatrix} -1 & -1.6b \end{bmatrix} \begin{Bmatrix} h'' \\ \alpha'' \end{Bmatrix} = \left[T_1\right]\{\eta''\} \tag{3-45}$$

The forcing is also different than the previous model. It is an impulsive force on the trailing edge affecting both directions. However, in the ATS, the forcing is an angular base displacement in pitch direction. The new forcing expression is given in Equation 3-46.

$$\{f\} = \begin{bmatrix} 0 \\ K_\alpha \end{bmatrix} x^e = \left[T_2\right] x^e \tag{3-46}$$

where x^e is the external pitch input in radians. The equation of motion of ATS in state space form for robust flutter analysis is given in Equation 3-47.

$$\begin{Bmatrix} \{\eta'\} \\ \{\eta''\} \\ \{x'\} \\ \hline \{z\} \\ \{z_K\} \\ \{z_{c_1}\} \\ \{z_{c_2}\} \\ \{z_{c_3}\} \\ \{z_{c_4}\} \\ y \end{Bmatrix} = \left[\begin{array}{ccc|ccccccc} [0] & [I] & [0] & [0] & [0] & [0] & [0] & [0] & [0] & [0] \\ -[M]^{-1}([K_0]/q_0+[K_a]) & -[M]^{-1}[C] & -[M]^{-1}[D_0] & -[I] & -[I] & -[I] & -[I] & [0] & [0] & [M]^{-1}[T_2]/q_0 \\ [E_2] & [E_1] & [F_0] & [0] & [0] & [0] & [0] & [I] & [I] & [0] \\ \hline -[M]^{-1}[K_0]W_q/q_0^2 & [0] & [0] & -W_q/q_0[I] & -W_q/q_0[I] & [0] & [0] & [0] & [0] & [M]^{-1}[T_2]W_q/q_0^2 \\ [M]^{-1}[W_K]/q_0 & [0] & [0] & [0] & & \cdots & & & & [0] \\ [0] & [0] & [M]^{-1}[D_3] & & & & & & & \\ [0] & [0] & [M]^{-1}[D_2] & \vdots & & \ddots & & & & \vdots \\ [0] & [0] & [F_2] & & & & & & & \\ [0] & [0] & [F_1] & [0] & & \cdots & & & & [0] \\ -[T_i][M]^{-1}([K_0]/q_0+[K_a]) & -[T_i][M]^{-1}[C] & -[T_i][M]^{-1}[D_0] & -[T_i] & -[T_i] & -[T_i] & -[T_i] & -[T_i] & -[T_i] & [T_i][M]^{-1}[T_2]/q_0 \end{array}\right] \begin{Bmatrix} \{\eta\} \\ \{\eta'\} \\ \{x\} \\ \hline \{w\} \\ \{w_K\} \\ \{w_{c_1}\} \\ \{w_{c_2}\} \\ \{w_{c_3}\} \\ \{w_{c_4}\} \\ x^e \end{Bmatrix}$$

(3-47)

A set of flutterometer solutions are obtained at speeds of 15 m/s and 20 m/s. The parameters of the ATS are perturbed as in the mild flutter case according to Table 10. The uncertainty description is defined to be complex for the stiffness matrix and real for the aerodynamic coefficients. The initial uncertainty is defined as 1% as in the mild flutter case. The validation norm for 15 m/s speed and 1% uncertainty is given in Figure 87. The validation norm is approximately 0.5, which means that the uncertainty description must be doubled in order not to invalidate the mathematical model. So, the uncertainty is scaled accordingly and a robust flutter analysis is performed. The results for 15 m/s speed are given in Figure 88. The flutter speed is calculated according to Equation 3-43, as 19.7 m/s. The solution at 20 m/s is given in Figure 89. The flutter estimation with the flutterometer method at 20 m/s speed is calculated as 24 m/s. Both estimates are below the true value, 25.7 m/s, as expected.

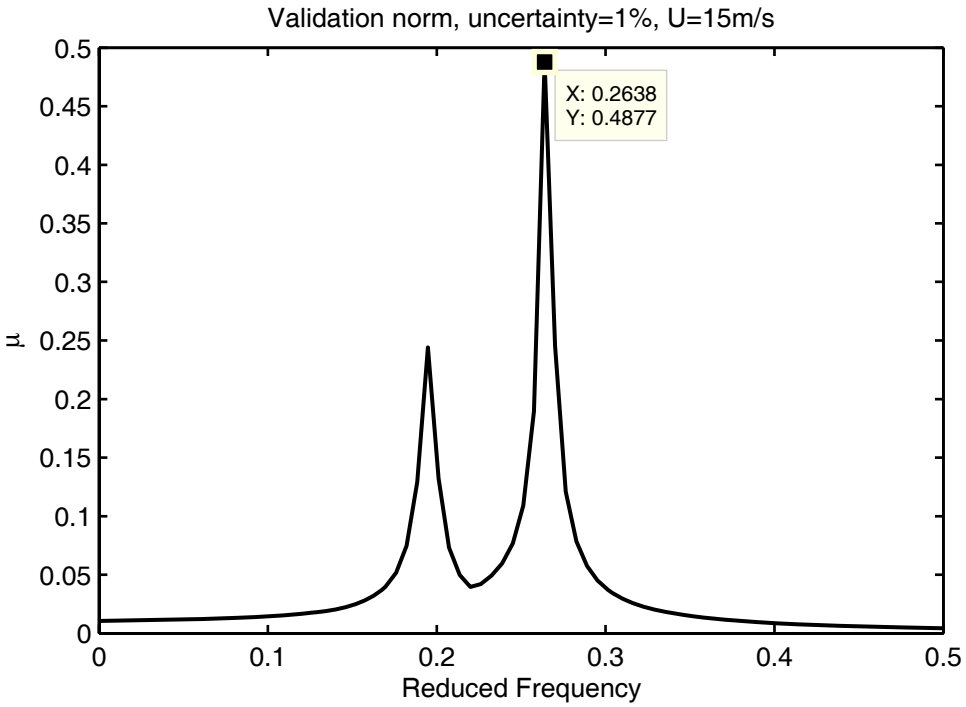

Figure 87. Validation norm, uncertainty=1%, U=15 m/s.

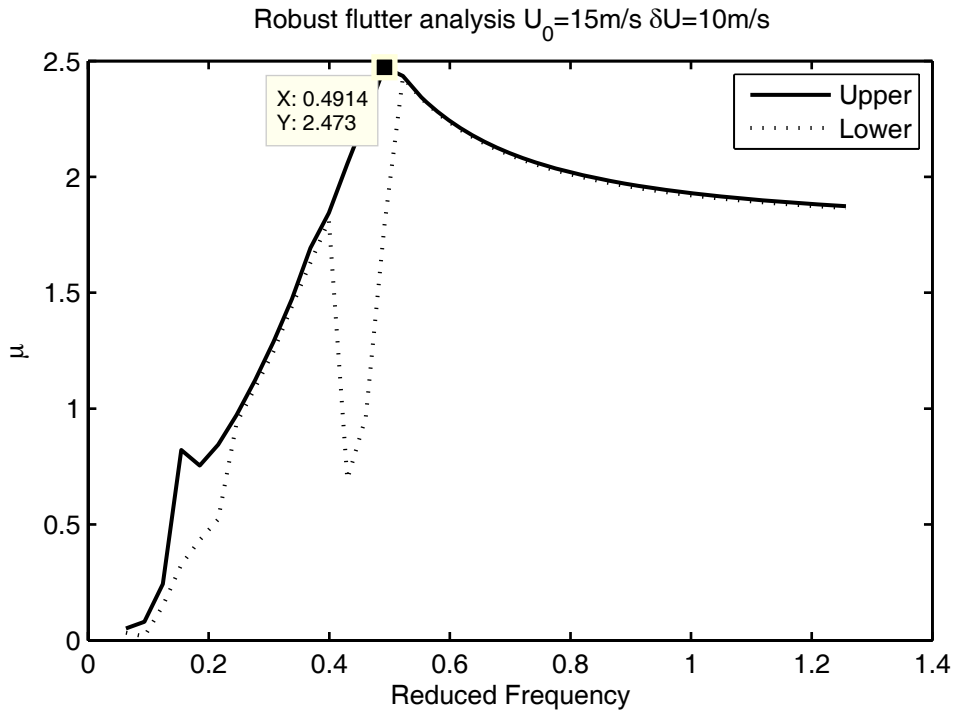

Figure 88. Flutterometer result for U=15 m/s.

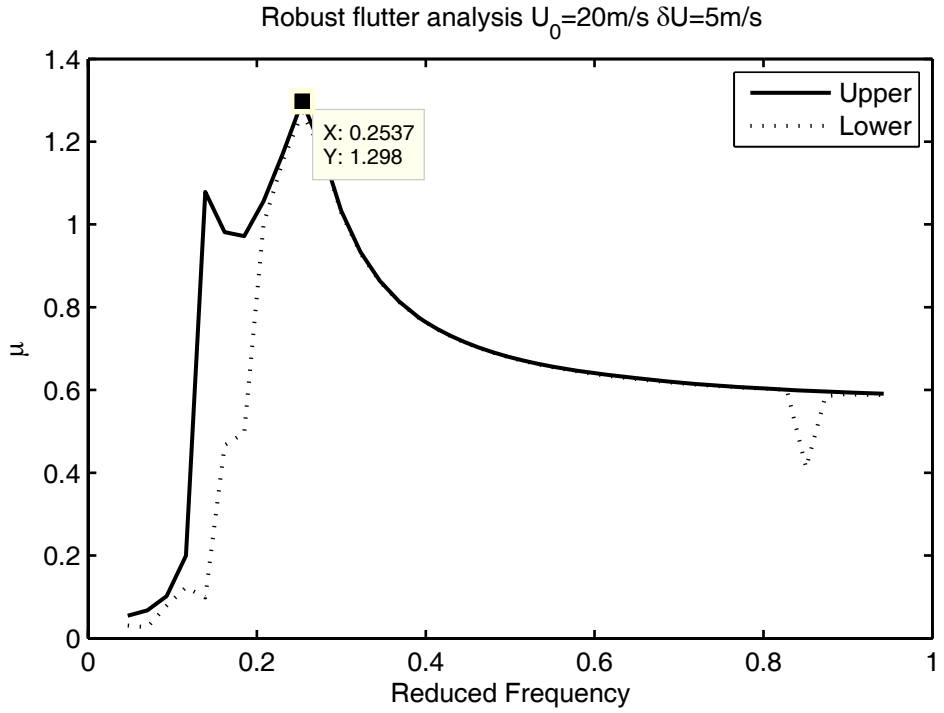

Figure 89. Flutterometer result for U=20 m/s.

3.4 Comparison of Results and Summary

The simulation results show that there is no best method for flutter estimation. Therefore, multiple results obtained from different methods should be monitored simultaneously during a flight testing. Despite the advantages of the flutterometer, an extensive modeling work is necessary to get a meaningful result. As stated in the literature, the flutterometer seems to be the most reliable method for low speeds in the beginning of the flight testing. Classical methods are useless for low speeds because of extrapolation involved in them. The flutterometer can be easily applied to more complex structures where the degree of freedom of the structure is high. However, classical methods such as flutter margin and ARMA are based on two degrees of freedom models, which may not work properly with higher order systems. Further demonstrations with complex structures might show the actual effectiveness levels of these methods. The envelope function and ARMA methods seem to have a problem with explosive type flutter systems. However, a good aeroelastic and

aeroservoelastic design should never experience an explosive type flutter. Although, the flutterometer method seems to be promising, it is seen that there are still some points to work on. One of these points is about the model validation algorithm. The method scales the entire uncertainty description. However, there might be different combinations of scales that better validate the model with less conservatism. Each uncertainty description can be scaled independently. Recent studies [68, 69] about flutterometer indicate that different scales in uncertainty descriptions and model updating can be used to reduce the conservatism of the method. Another point to be studied is the μ norm calculation. A new aeroelastic problem specific implementation of μ norm calculation can be developed to replace Matlab's standard functions to ignore the lower dynamic pressure bound in aeroelastic analysis, if the lower dynamic pressure bound appears to be negative at low speeds. In aeroservoelastic cases the lower bound of dynamic pressure should be checked, but not for negative valued dynamic pressures.

Table 13. Comparison of methods for the mild flutter case.

Method	Best estimate [m/s]	Flight Conditions [m/s]	Error [%]
Damping Extrapolation	90.42	20, 30, 40, 50, 60, 70	4.6
Envelope Function	95.12	20, 30, 40, 50, 60, 70	10.0
Flutter Margin	86.81	40, 50, 60, 70	0.4
ARMA	89.40	50, 55, 60, 65	3.4
Flutterometer	83.30	60	-3.7

Table 14. Comparison of methods for the ATS case.

Method	Best estimate [m/s]	Flight Conditions [m/s]	Error [%]
Damping Extrapolation	26.8	10, 12.5, 15, 17.5, 20, 22.5	4.3
Envelope Function	No solution	--	--
Flutter Margin	25.4	10, 12.5, 15, 17.5, 20	-0.05
ARMA	No solution	--	--
Flutterometer	24	20	-6.6

CHAPTER 4

NONLINEAR AEROELASTIC SYSTEMS

4.1 Introduction

In the previous chapter, an investigation of various flutter prediction methods for linear systems is presented. However, it is known that some fighter aircraft with certain external store configurations encounter limit cycle oscillation (LCO) problems which are only possible in nonlinear systems [46]. Fighter aircraft usually encounter LCOs because of aerodynamic nonlinearities. The shock induced by moving aerodynamic loads and trailing edge separation plays a dominant role in the development of these LCOs. The LCO phenomenon in aeroelastic systems is related to the buffeting but has characteristics similar to the classical flutter. As in flutter case, the LCO usually occurs at a single frequency. LCO is not a severe problem as long as the amplitude and frequency of oscillations do not interfere with the subsystems of the aircraft. From an operational point of view, an LCO results in an undesirable airframe vibration that limits the pilot's functional abilities and causes an extreme discomfort and anxiety; more importantly, the targeting accuracy is degraded. The F-16 fighter aircraft, which is also used by Turkish Air Forces, has a LCO problem with asymmetric external store configurations [47].

In this chapter, the influence of nonlinearities on the performances of the flutter prediction methods is investigated. A nonlinear typical section model with backlash is developed for data generation. It is seen that this type of nonlinearity greatly decreases the performance of data based prediction methods. An LCO prediction tool is developed based on wavelet analysis and its use is demonstrated on simulated

measurements. To increase the performance of the flutter prediction methods, a Volterra series representation of measurements is utilized. It is seen that the effect of nonlinearity can be decreased with the use of identified first order Volterra kernels.

4.2 Analysis of Nonlinear Aeroelastic Systems

The analysis of nonlinear systems is not as straightforward as for the linear case. There are various nonstandard methods to analyze nonlinear system outputs like Hilbert transform, but these are not applicable to all systems. A review of the nonlinear system identification methods used in structural dynamics can be found in reference [48]. The analysis of nonlinear aeroelastic systems is not much studied in the literature since linear methods still need some improvements. It is possible to fit a linear model on measurements and use a data based flutter prediction method. However, it is not possible to predict LCOs with such an approach. Unlike data based methods, the model based methods like flutterometer can be directly used with nonlinear systems, since the nonlinearity is handled in the uncertainty description. However, this approach will further increase the conservatism of the method. To predict LCOs and flutter, a high order spectral analysis or nonlinear modeling is required. Such analyses are computationally very expensive and it is usually not possible to utilize them online. On the other hand, there are some tools that are used in the literature to predict LCOs and flutter.

The wavelet analysis is one of the most popular recent tools for both linear and nonlinear signal analysis. Wavelets are used for signal denoising, tracking the frequency content change with time, compressing signals and image processing. In the field of aeroelasticity, wavelets are used for identification and LCO prediction. Flight test measurements usually contain highly transient signals, higher order nonlinear dynamics, and noise. By wavelet filtering, the unwanted features are removed from the signal. Although Fourier methods are the most commonly used signal analysis tools, wavelets have some advantages due to the inherently transient nature of inflight aeroelastic dynamics. The infinite and at least locally periodic

waveform assumption in Fourier analysis can not adequately describe the intermittency, modulation (amplitude, phase, or frequency), non-periodicity, non-stationary behavior, time variance, or nonlinearity in the measurements. By wavelet transform, a signal can be investigated in time and frequency domain, simultaneously. Brenner [49] demonstrated the use of Morlet wavelets on improving the input and output signals obtained from F/A-18 Systems Research Aircraft during flight tests. The measurement signals were cleaned with the help of wavelets. The cleaned signals were used to identify the transfer functions of the aircraft. Brenner [50] also used wavelets with SVD to estimate the instantaneous modal parameters of the NASA DAST (Drone for Aerodynamic and Structural Testing) vehicle and F-18 aircraft with inflight measurements. In his work, standard SVD and transformed SVD are used to identify the dominant scales of the wavelet coefficients for filtering. A wavelet filtering is used to reduce the conservatism of flutterometer by Brenner and Lind [51, 52]. The filtered signals are used to update the uncertainty model. Freudinger *et al*. [53] and Johnson *et al*. [54] used the wavelet transform with correlation filtering to identify the modal properties during flight test. Both used the Laplace wavelet which is a complex, analytical, and damped exponential, similar to the response of a damped structure. A set of natural frequencies and damping values are correlated to the measured data and best correlated values are marked as modal parameters of the system.

The application of wavelet transform for LCO prediction was first introduced by Lind *et al*. [55, 56]. The response of the system to an impulse input was decomposed into wavelet coefficients and the behavior of the dominant scales was observed. The derivative of the dominant scale change was used to construct a prediction function. The method was successfully demonstrated on a nonlinear testbed which has continuous nonlinear springs. The method was used with pitch angle measurements. However, it is not always possible to measure the displacements directly during flight test. In this study, the method of Lind is applied to the acceleration measurements with discontinuous nonlinearities such as backlash.

In addition to the LCO prediction, the flutter speed of the nonlinear system should also be predicted for a safe testing. The Fourier analysis, which is the main tool for transfer function estimation, yields very poor transfer function estimates so that the classical flutter prediction methods generally fail to predict the flutter speed. Separating the linear part of the signal and predicting the flutter from this linear part constitutes another approach for flutter prediction. The separation of the linear part can be performed by representing the system's output by Volterra series. First order Volterra kernels can be used to represent the system's first order dynamics, which is expected to be the linear part of the output. While Volterra theory has a strong foundation in both the biological and electrical engineering fields, it has received little attention in the field of aeroelasticity. Prazenica *et al*. [57, 58] used Volterra approach to identify the linear output. In his work, the calculated linear output of the system was used to update the uncertainty modeling in the flutterometer. If the dynamics of the system is known, a Volterra based structural model can be constructed for analytical flutter predictions [59-62]. The Volterra series representation of a nonlinear system can be obtained in the frequency domain as well. To identify the frequency domain kernels, a set of sinusoidal signals can be used [63]. A standard method called harmonic probing is commonly used in the identification of higher order frequency domain kernels [64]. However, such an approach requires a large number of test points, which is not possible during flight testing. There exist truncated approaches [65], but the identification in frequency domain is not a feasible method for flight testing because of its computational costs. Complete technical details on Volterra approach can be found in reference [66]. In this study, a time series approach is used to identify the Volterra kernels. The linear parts of measurements are extracted by the help of these kernels and used in the flutterometer method. The nonlinear measurements are also used to predict the flutter speed for comparison.

4.3 Nonlinear Typical Section Model

The mathematical model used to generate the measurements is modified to reflect the effect of backlash in pitch degree of freedom. The ATS is actuated by a stiff servomotor in pitch direction. Thus, the external forcing is only in the pitch direction as an angular base displacement. The equation of motion of the linear system is the same as the previous mathematical model used in this thesis. The only difference is in the forcing terms.

For the computer simulations, considering the nonlinear model, the typical section parameters are changed to get distinct natural frequencies and limit cycle oscillations. The selected parameters are listed below.

m = 28 kg : Total mass of moving parts of the system (airfoil and base).
$m_{airfoil}$ =11 kg : Mass of the rotating parts (airfoil).
I_α = 0.05 kg.m^2 : Moment of inertia of rotating parts.
K_h = 10,000 N/m : Flexural stiffness of the airfoil.
K_α = 55 N.m/rad : Torsional stiffness of the airfoil.
a = -0.6 : Normalized distance between the elastic axis and midchord.
b = 0.15 m : Semichord length of the airfoil.
l = 0.6 m : Span of the airfoil.
x_α = 0.5 : Normalized distance between the elastic axis and mass center of airfoil.

The new system has a linear flutter speed of 32.2 m/s. The new natural frequencies are 2.79 and 7.43 Hz. The acceleration of the trailing edge for a = -0.6 is given in Equation 3-45 and repeated here as follows.

$$y = -h'' - 1.6b\alpha'' = \begin{bmatrix} -1 & -1.6b \end{bmatrix} \begin{Bmatrix} h'' \\ \alpha'' \end{Bmatrix} = [T_1]\{\eta''\} \tag{4-1}$$

The forcing term for the angular base displacement is given in Equation 3-46 and repeated here as follows.

$$\{f\} = \begin{bmatrix} 0 \\ K_\alpha \end{bmatrix} x^e = [T_2] x^e \tag{4-2}$$

where x^e is the external pitch input in radians. The linear equations of motion for the ATS to be used with robust flutter analysis is given Equation 3-47 and repeated here as follows.

$$\begin{Bmatrix} \{\eta'\} \\ \{\eta^*\} \\ \{x'\} \\ \hline \{z\} \\ \{z_K\} \\ \{z_{c_1}\} \\ \{z_{c_2}\} \\ \{z_{c_3}\} \\ \{z_{c_4}\} \\ y \end{Bmatrix} = \left[\begin{array}{ccc|ccccccc} [0] & [I] & [0] & [0] & [0] & [0] & [0] & [0] & [0] & [0] \\ -[M]^{-1}([K_0]/q_0+[K_a]) & -[M]^{-1}[C] & -[M]^{-1}[D_0] & -[I] & -[I] & -[I] & -[I] & [0] & [0] & [M]^{-1}[T_2]/q_0 \\ [E_2] & [E_1] & [F_0] & [0] & [0] & [0] & [0] & [I] & [I] & [0] \\ \hline -[M]^{-1}[K_0]W_g/q_0^2 & [0] & [0] & -W_g/q_0[I] & -W_g/q_0[I] & [0] & [0] & [0] & [0] & [M]^{-1}[T_2]W_g/q_0^2 \\ [M]^{-1}[W_K]/q_0 & [0] & [0] & [0] & & \cdots & & & & [0] \\ [0] & [0] & [M]^{-1}[D_3] & & & & & & & \\ [0] & [0] & [M]^{-1}[D_2] & \vdots & & \ddots & & & & \vdots \\ [0] & [0] & [F_2] & & & & & & & \\ [0] & [0] & [F_1] & [0] & & \cdots & & & & [0] \\ -[T_1][M]^{-1}([K_0]/q_0+[K_a]) & -[T_1][M]^{-1}[C] & -[T_1][M]^{-1}[D_0] & -[T_1] & -[T_1] & -[T_1] & -[T_1] & -[T_1] & -[T_1] & [T_1][M]^{-1}[T_2]/q_0 \end{array}\right] \begin{Bmatrix} \{\eta\} \\ \{\eta'\} \\ \{x\} \\ \hline \{w\} \\ \{w_K\} \\ \{w_{c_1}\} \\ \{w_{c_2}\} \\ \{w_{c_3}\} \\ \{w_{c_4}\} \\ x^e \end{Bmatrix}$$

(4-3)

The Simulink model, which is used to generate the experimental data with transfer functions, is adapted such that the effect of backlash is modeled as another external forcing that depends on the pitch displacement of the system. A special care must be taken while calculating the nonlinear forces for backlash type nonlinearities, since this kind of nonlinearities do not have a linear component that can be included in the equations as a linear stiffness. The nonlinear torsional spring force with a backlash amount δ, spring deflection α, and input x^e can be expressed as follows.

$$T_\alpha\left(\alpha, x^e\right) = \begin{cases} 0 & \text{for} \quad \left|x^e - \alpha\right| \le \delta \\ K_\alpha\left(x^e - \alpha - \delta\right) & \text{for} \quad x^e - \alpha > \delta \\ K_\alpha\left(x^e - \alpha + \delta\right) & \text{for} \quad x^e - \alpha < -\delta \end{cases} \tag{4-4}$$

As seen from Equation 4-4, there is no common linear term that can be treated as a linear stiffness. The nonlinear force can be rewritten by adding and subtracting linear terms as follows

$$T_\alpha\left(\alpha, x^e\right) = K_\alpha\left(x^e - \alpha\right) + T_\alpha\left(\alpha, x^e\right) - K_\alpha\left(x^e - \alpha\right) \tag{4-5}$$

The first term in Equation 4-5 is a linear term and it is already used in the simulation model. The remaining two terms can be kept at the right rand side of the equation of motion as an external force. So, the correction term for backlash as an external force becomes

$$n_\alpha = T_\alpha\left(\alpha, x^e\right) - K_\alpha\left(x^e - \alpha\right) \tag{4-6}$$

The Simulink model given in Appendix B is modified accordingly. The correction force given in Equation 4-6 is applied to the transfer functions G_{12} (transfer function from pitch input to plunge output) and G_{22} (transfer function from pitch input to pitch output) in addition to the external input. Since there is no external forcing or no nonlinearity correction on plunge direction, the transfer functions G_{11} (transfer function from plunge input to plunge output) and G_{21} (transfer function from plunge input to pitch output) can be omitted. The new Simulink model is given in Figure 90. The details of the nonlinearity block are given in Figure 91.

The amount of backlash in pitch direction is selected as ±1°. With this backlash, the system produces LCOs at a flow speed of 23.3 m/s. The flutter speed of the nonlinear system is 32 m/s, which is very close to the flutter speed of the linear part of the system (32.2 m/s). Since the effect of backlash decreases with increasing oscillation amplitude, the nonlinear flutter speed remains almost the same. Figure 92 shows the simulation results for a flow speed of 25 m/s. The input to the system is a 10 Hz pulse shaped as a shifted half cosine function. The LCO has a frequency of 3.1 Hz.

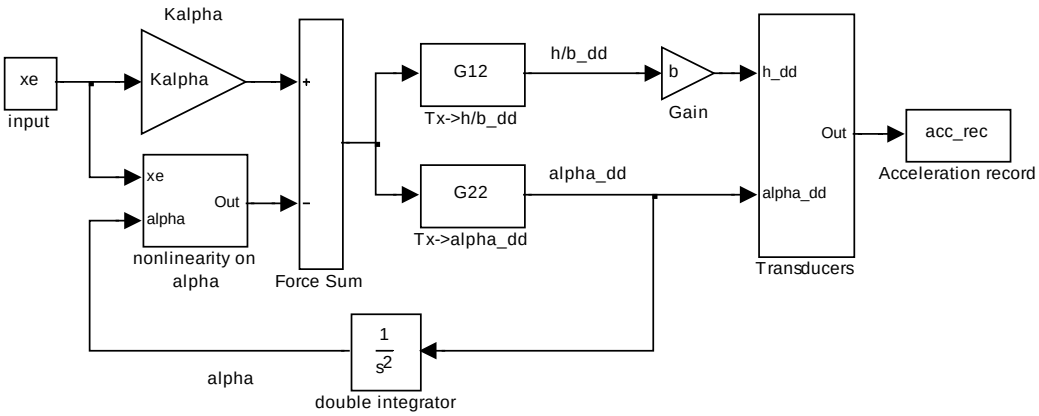

Figure 90. Nonlinear aeroelastic Simulink model.

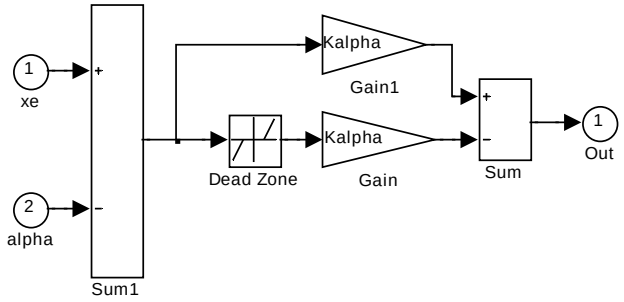

Figure 91. Nonlinear correction force block.

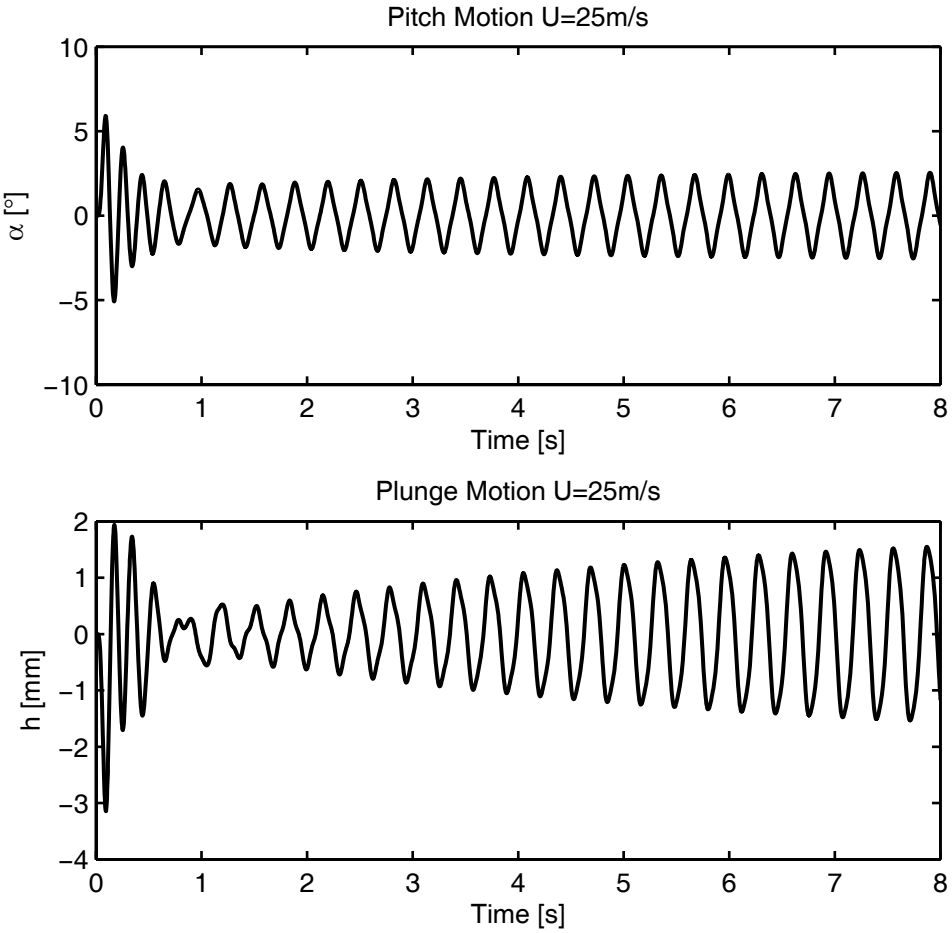

Figure 92. Nonlinear simulation results for U=25 m/s.

4.4 LCO Prediction with Wavelet Analysis

A wavelet is a waveform of effectively limited duration that has an average value of zero. The wavelet analysis is simply an expression of a signal in terms of summed wavelets with different scales and time shifts. The wavelet analysis is similar to Fourier analysis, but has more advantages. Sinusoids, which are the basis of Fourier analysis, do not have limited duration. Sinusoids are smooth and predictable, whereas wavelets tend to be irregular and asymmetric. A Fourier analysis consists of breaking up a signal into sine waves of various frequencies. Similarly, a wavelet analysis is the breaking up of a signal into shifted and scaled versions of the original (or mother) wavelet. Signals with sharp changes might be better analyzed with an irregular wavelet than with a smooth sinusoid. Local features can be described better

with wavelets than sinusoids. Actually, it is possible to analyze a signal locally by short time Fourier transforms. However, the drawback is that once a particular size for the time window is chosen, that window is the same for all frequencies. Many signals require a more flexible approach where the window size can be varied to determine both the local and wide components in the signal.

Figure 93 shows a commonly used mother wavelet, called Morlet wavelet. A wavelet is a function of scale (stretching), *a,* time shift (position), τ, and time. The scale acts like stretching of the wavelet. The Morlet wavelet shown in Figure 93 has a dominant sinusoid component with a period of 1.2 s. When this wavelet is stretched such that a=2, its period becomes 2.4 s. Thus, the scale is related to the periodicity and inversely proportional to the sinusoidal frequency. The expression of the mother Morlet Wavelet is given in Equation 4-7.

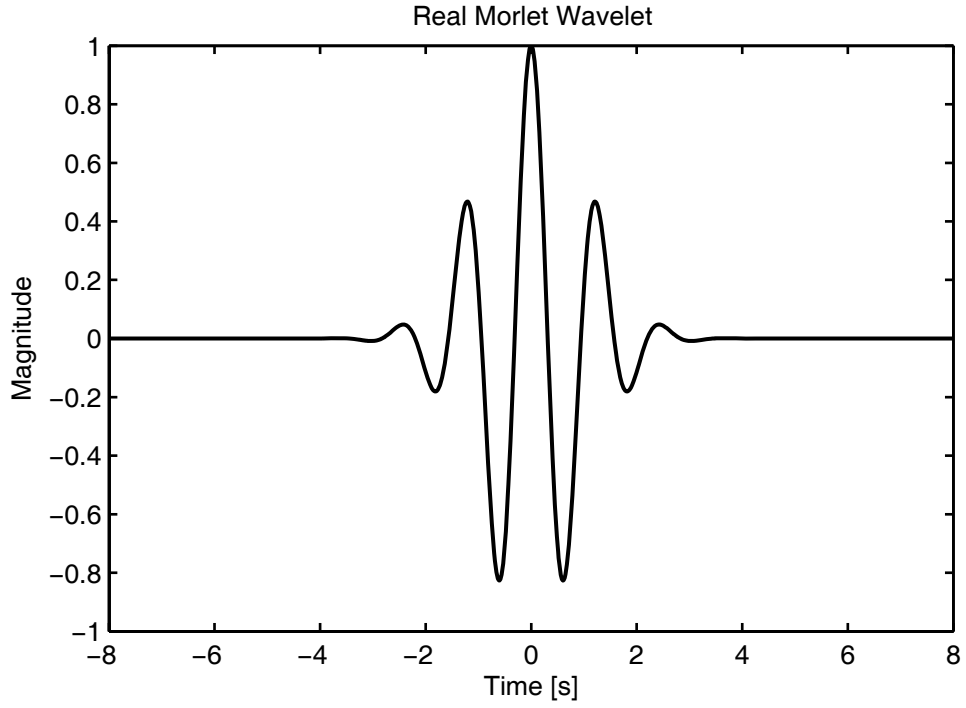

Figure 93. Real Morlet Wavelet for a=1 and τ=0.

$$\psi(t) = e^{-(1/2)t^2} \cos(5t) \tag{4-7}$$

The wavelet elements can be explicitly written in terms of the mother wavelet as follows.

$$\psi_{a,\tau}(t) = \frac{1}{\sqrt{a}}\psi\left(\frac{t-\tau}{a}\right) \tag{4-8}$$

The wavelet transform is the correlation of wavelet elements to the signal, *x(t)*, through the mapping given by

$$W(a,\tau) = \int_{-\infty}^{\infty} x(t)\psi_{a,\tau}(t)\,dt \tag{4-9}$$

The work of Lind [55, 56] showed that wavelet transforms can be used to predict LCOs for continuous structural nonlinearities. Lind used the pitch angle measurements to analyze his system with the wavelet transform. However, it is not always possible to measure the displacements directly. Recall that the main sensors for a flight test are the accelerometers. An accelerometer data can show some steep changes in the presence of discontinuous nonlinearities although the displacement data may seem to be smooth. The nonlinearities originating from aerodynamics may be continuous and smooth in nature, but the structural nonlinearities can be very severe and discontinuous as in the case of backlash. The applicability of the method developed by Lind *et al*. to general nonlinear systems is not known and left as a future work. In this study, the applicability of this method to backlash type nonlinearity using acceleration data is investigated and an appropriate prediction function is derived.

A set of simulations are performed with various flow speeds. The pulse response of the system is recorded and the acceleration data of the trailing edge is used to perform the wavelet transform. Figure 94, Figure 95, and Figure 96 show the results of wavelet transforms for increasing flow speeds. The transition to LCO is clearly observed. The dominant scales shift upwards with increasing slopes as the flow speed increases. Finally, scales reach the LCO frequency beyond the critical speed.

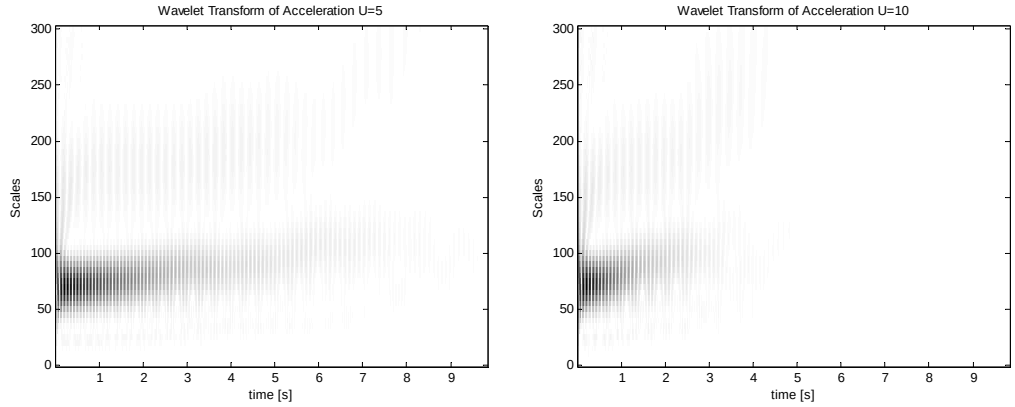

Figure 94. Wavelet transforms, left U=5 m/s, right U=10 m/s.

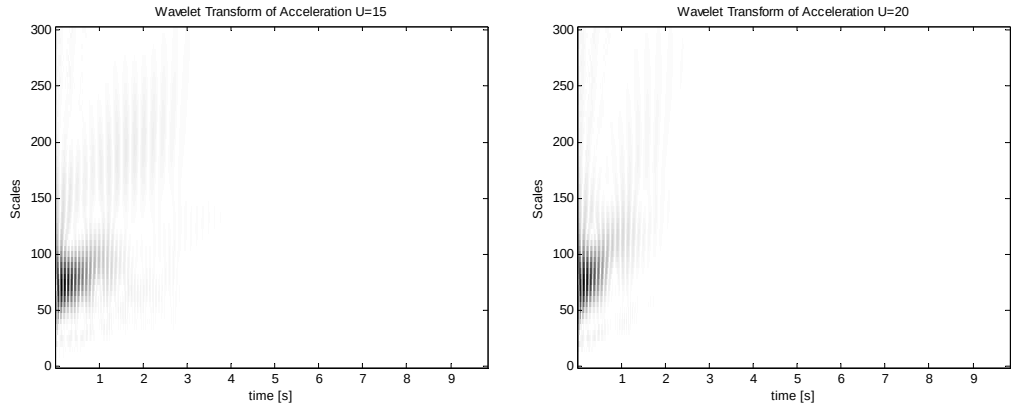

Figure 95. Wavelet transforms, left U=15 m/s, right U=20 m/s.

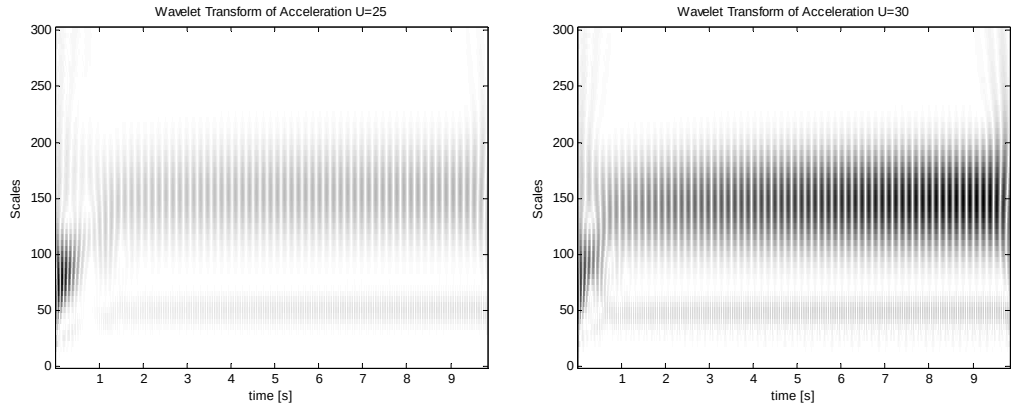

Figure 96. Wavelet transforms, left U=25 m/s, right U=30 m/s.

Lind used the maximum slope of the dominant scales and corresponding time to construct the prediction function. Figure 97 shows the magnitudes of the dominant scales. As seen from the figure, the dominant scales are oscillatory. Thus, the envelope of the dominant scales should be determined.

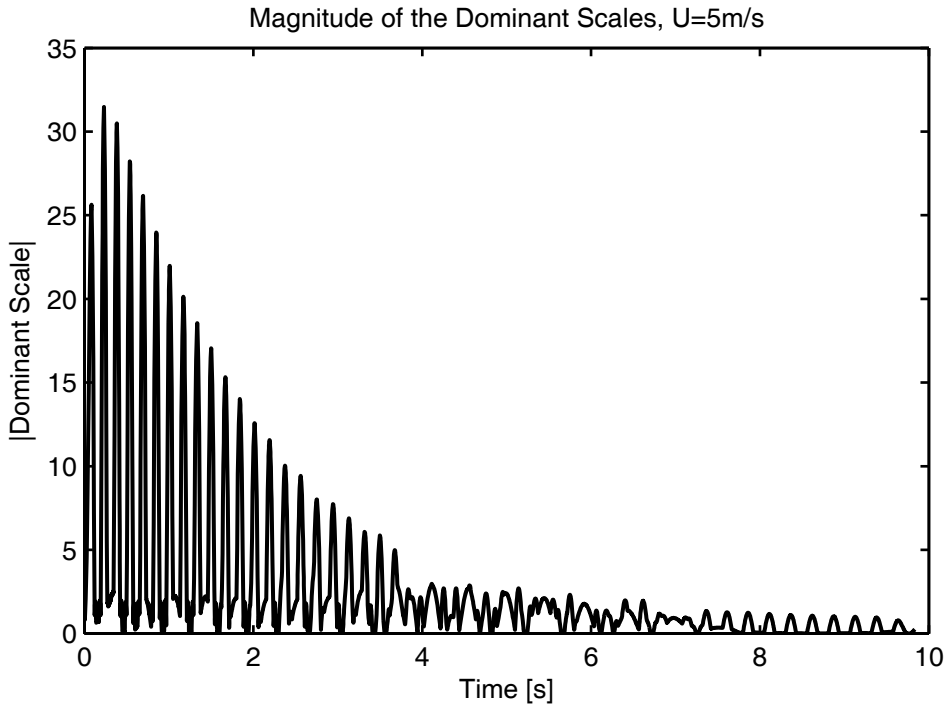

Figure 97. Magnitude of dominant scales for U=5 m/s.

Lind manually constructed the envelope of the dominant scales. However, this process can be automatically performed by means of Hilbert transform. Recall that the Hilbert transform is used in the envelope function method for flutter prediction. However, the magnitude plot is not suitable for Hilbert transform since there are many discontinuities. Instead of the magnitude of the dominant scales, numerical values of the dominant scales can be used. Figure 98 shows the numerical values of the dominant scales. In fact, Figure 97 is obtained by taking the magnitude of the Figure 98. Figure 98 is more suitable for the application of Hilbert transform. The Hilbert transform introduces an additional 90° shift to the original signal, converting it to a complex valued signal. The amplitude of this complex valued signal should

describe the envelope of the original signal. The left plot of Figure 99 shows the result of the Hilbert transform. The right plot of Figure 99 shows the polynomial curve of order 12 that is fitted to the Hilbert transform data. Clearly, the slope of the dominant scales can be derived from curve fit results.

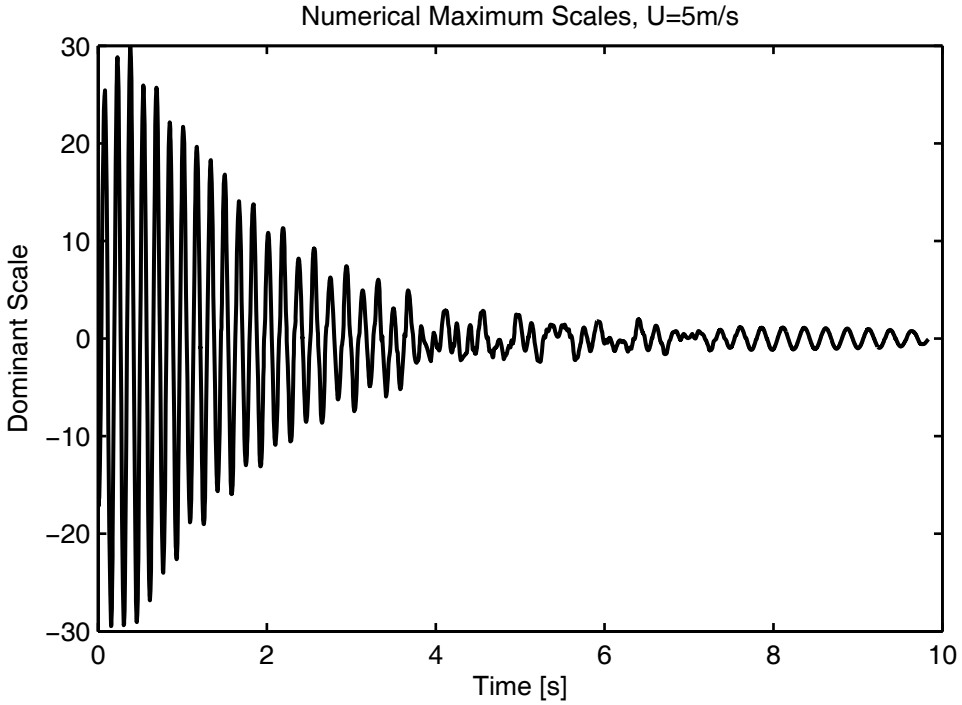

Figure 98. Dominant scales for U=5 m/s.

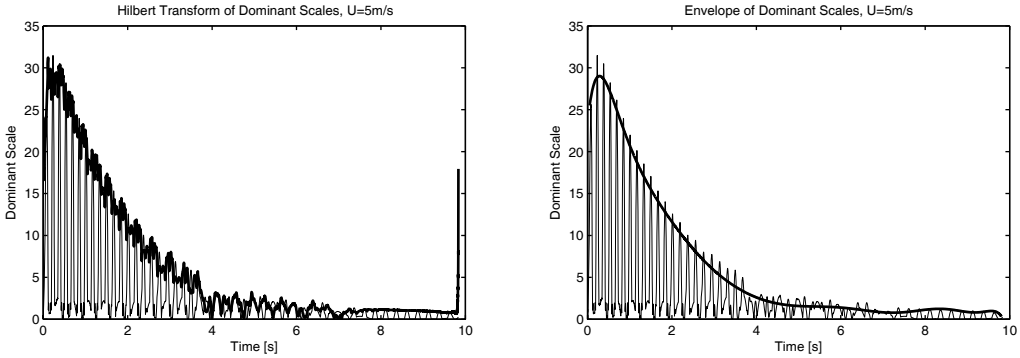

Figure 99. Envelope of the dominant scales for U=5 m/s, left: pure Hilbert, right: curve fit.

Figure 100 shows the dominant scales and their derivatives for all speeds. As seen from the figure, as the speed increases, the negative slope also increases and the instant when the maximum negative slope occurs decreases. Hence, a prediction function can be derived with these values. Figure 101 indicates the maximum slope and maximum slope instant with respect to speed.

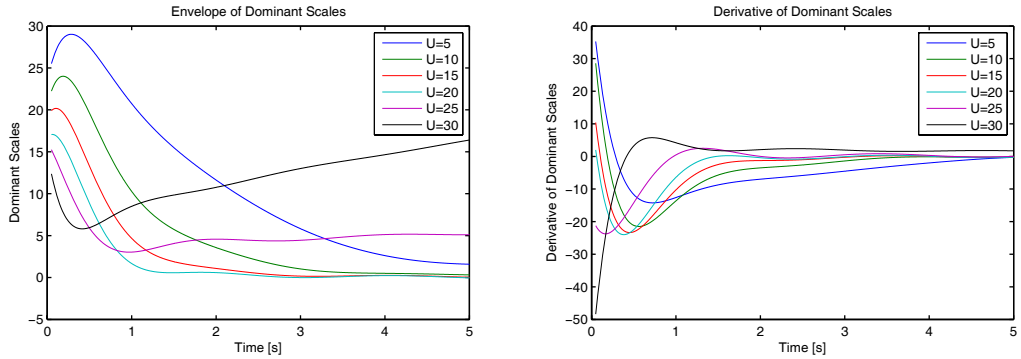

Figure 100. Left: Envelope of dominant scales. Right: Derivative of dominant scales.

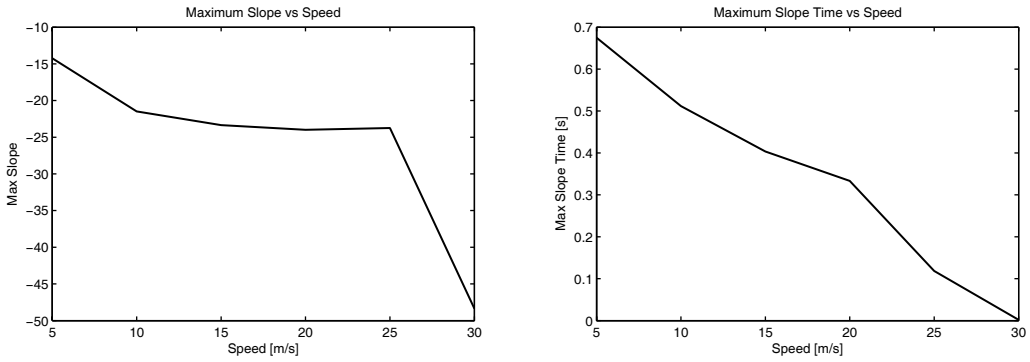

Figure 101. Maximum slope and maximum slope time results.

A prediction function can be derived from Figure 101 such that

$$\phi(U) = \frac{\text{max slope time}}{\text{max slope}} \tag{4-10}$$

Lind used the inverse of the prediction function derived here since the behavior of Lind's system was different than the system under consideration here. Lind used softening springs. Figure 102 shows the values of prediction function for speeds below the critical LCO speed. It is seen that the shape of the prediction function deviates from linearity as the LCO speed is attained. A similar behavior was also observed by Lind [55].

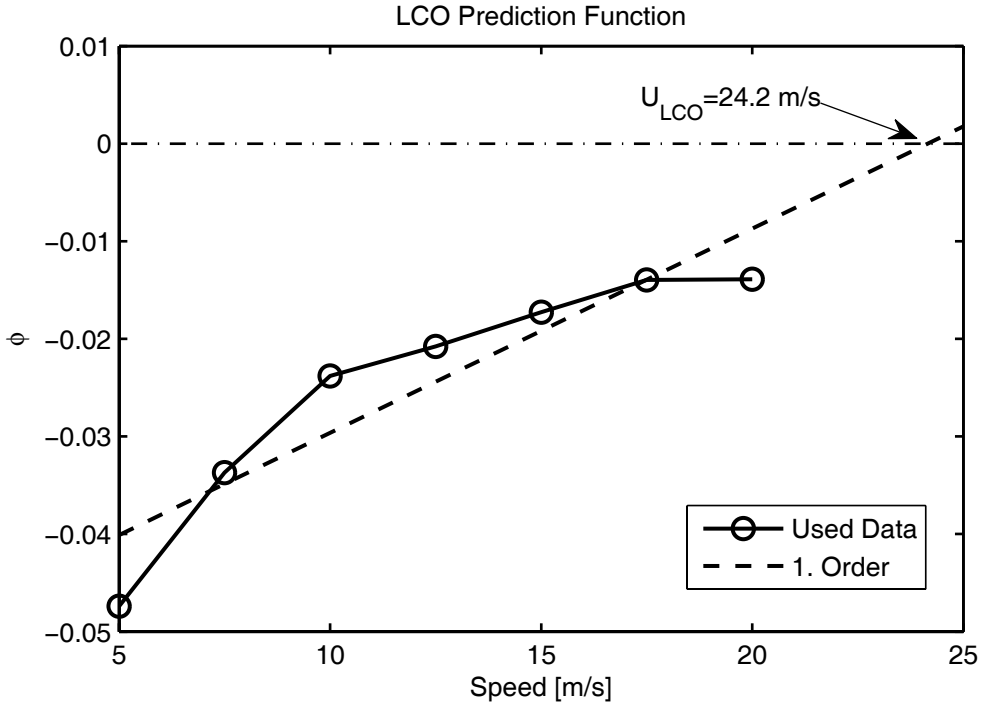

Figure 102. LCO prediction function.

A first order fit to the prediction function using the speeds 5, 7.5, 10, 12.5, 15, 17.5, and 20 m/s results in prediction function given in Equation 4-11.

$$\phi(U) = -5.057\text{x}10^{-2} + 2.093\text{x}10^{-3}\text{U} \tag{4-11}$$

The prediction function 4-11 predicts LCO at a speed of 24.2 m/s. The true value is 23.3 m/s. If the speed data at 20 m/s is discarded from the first order fit, the LCO speed is predicted as 21.7 m/s. Results are sufficiently close to the true value.

4.5 Volterra Series

The nonlinear Volterra theory was developed in the 1880's by Vito Volterra. The theory quickly received a great deal of attention in the field of electrical engineering, and later in the biological field, as a powerful approach to the modeling of nonlinear system behavior. The Volterra theory is a generalization of the linear convolution integral approach often applied to LTI systems. The theory states that any time-invariant nonlinear system can be modeled as an infinite sum of multidimensional convolution integrals of increasing order. This is represented symbolically by the series of integrals,

$$y(t) = h_0 + \int_0^\infty h_1(\tau_1)u(t-\tau_1)d\tau_1 + \int_0^\infty \int_0^\infty h_2(\tau_1,\tau_2)u(t-\tau_1)u(t-\tau_2)d\tau_1 d\tau_2 + ... \quad (4\text{-}12)$$

which is known as the Volterra series. Here, *u(t)* represents the system input while *y(t)* represents the system response. Each of the convolution integral terms contains a "kernel", either linear (h_1) or nonlinear ($h_2,..,h_n$), which corresponds to the impulse response of the system. Once these kernels are identified, then the response to any arbitrary input can be calculated. The first integral term of the series represents the linear convolution integral. Weakly nonlinear systems are well represented by the first, second, or third order Volterra series. All higher-order terms usually tend to vanish quickly, and are therefore negligible in most system representations. A discrete time version of continuous Volterra series with memory length of *M* is given as

$$y(n) = h_0 + \sum_{k_1=0}^{M-1} h_1(k_1)\,x(n-k_1) + \\ + \sum_{k_1=0}^{M-1}\sum_{k_2=0}^{M-1} h_2(k_1,k_2)\,x(n-k_1)\,x(n-k_2) \\ + \sum_{k_1=0}^{M-1}\sum_{k_2=0}^{M-1}\sum_{k_2=0}^{M-1} h_3(k_1,k_2,k_3)\,x(n-k_1)\,x(n-k_2)\,x(n-k_3)+\cdots \tag{4-13}$$

The kernel $h_j(k_1...k_i)$ is symmetric if the indices can be interchanged without affecting its value. It is obvious that $x(n-k_1)x(n-k_2)$ is the same as $x(n-k_2)x(n-k_1)$, so the associated kernels $h_2(k_1,k_2)$ and $h_2(k_2,k_1)$ are the same. For symmetric kernels of memory M, the second order Volterra kernel requires the determination of $M(M+1)/2$ coefficients, while the third order kernel needs $M(M+1)(M+2)/6$ coefficients. The second order Volterra kernel is a symmetric $(M\times M)$ matrix. The third order kernel is composed of M symmetric matrices having the dimension $(M\times M)$.

Volterra kernels are the backbone of any Volterra series. Volterra kernels, both linear and nonlinear, are input dependent. As an example to this, consider the case where the response of a linear system to an arbitrary input is desired. Here, the unit impulse response of the system to that type of input must first be defined. The first order kernel, h_1, represents the linear unit impulse response of the system. This term is comparable to the basic frequency response function (FRF) of a linear system, transformed into the time domain. However, the kernel h_1 gives a more accurate representation of a system's linear response than does the FRF. This is because h_1 exists with the knowledge of higher-order, nonlinear terms while the FRF assumes a completely linear response. The second order kernel, h_2, is a two-dimensional function of time. It represents the response of the system to two separate unit impulses applied at two varying instants in time. Therefore the kernel is a function of both time and time lag. Similarly, h_3 is a three-dimensional function of time, representing the response of the system to three separate unit impulses applied at three varying instants in time. Here, the kernel is a function of time and two distinct

time lags. It is through these time lags that nonlinear kernels represent the effect of a previous response as it is carried through time in the system.

The identification of the kernels is generally an ill-conditioned inverse problem. For large memory lengths, the number of third order kernels increases so much that it is almost impossible to store the solution. Table 15 shows some examples for the number of kernels that must be determined for different memory lengths. Clearly, the number of third order kernels increases geometrically for large memory lengths. For this reason, usually only second order approximations are used in practice. However, for impulsive inputs, the solution matrix becomes very sparse, since most of the input multiplications vanish. In such cases, higher order kernels can be also determined.

Table 15. Number of kernels to be identified for sample memory lengths.

M	Number of 1st order kernels	Number of 2nd order kernels	Number of 3rd order kernels	Total for 1st to 3rd	Total for 1st to 2nd
10	10	55	220	286	66
50	50	1,275	22,100	23,426	1,326
100	100	5,050	171,700	176,851	5,151
150	150	11,325	573,800	585,276	11,476
200	200	20,100	1,353,400	1,373,701	20,301
300	300	45,150	4,545,100	4,590,551	45,451

The memory length corresponds to the number of samples that describes the impulse response until the response vanishes sufficiently. The memory length should be kept as small as possible for computational reasons. The only way to decrease the necessary memory length is to decrease the sampling frequency. The measured data should be down-sampled to a frequency such that the frequency range of interest is

still covered. The highest natural frequency of the system studied in this Chapter is 7.4 Hz, so a sampling frequency of at least 15 Hz is necessary according to the Nyquist criterion. However, a down sampling to that level would decrease the resolution of kernels, thus the resolution of the estimated transfer functions, beyond any practical use. The simulated measurements are sampled at 600 Hz, so a down-sampling of ratio 10 is used corresponding to a 60 Hz sampling. Because of the odd nonlinearity, it is expected to have a response at the third harmonic of the natural frequency which is 22.2 Hz (3x7.4 Hz). This value would certainly change with the flow speed but it would decrease with speed. Thus, a sampling frequency of 60 Hz would at least cover the first odd higher harmonic. Figure 103 shows the original and down-sampled data of the pitch motion for the defined pulse input. The memory length of the system is chosen as 2.5 s, which corresponds to 150 discrete data points and is sufficiently long to represent the system.

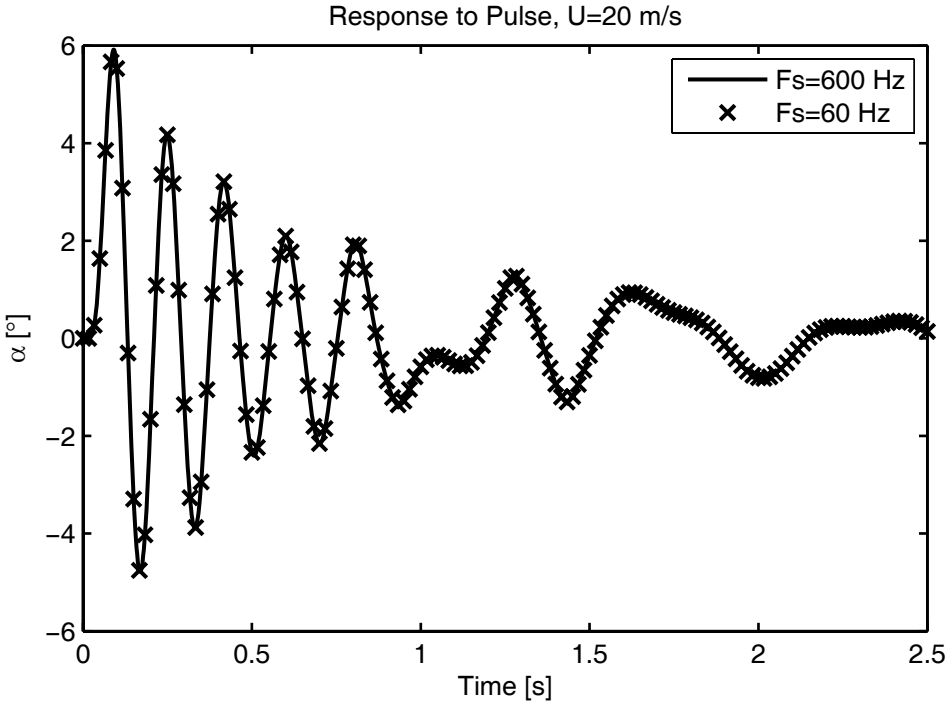

Figure 103. Pitch response U=20 m/s.

Kernels are determined by the solution of an underdetermined problem since there are usually not enough data points. The solution is obtained in a least squares sense. To formulate the problem in matrix form, the matrix of delayed inputs and higher order inputs must be constructed. Let the array of first order inputs be defined as follows

$$\{X_1\} = \{x_n \quad x_{n-1} \quad \cdots \quad x_{n-M+1}\} \tag{4-14}$$

So the second order input array can be constructed from the upper triangular of matrix as

$$[X_2] = \{X_1\}^T \{X_1\} \tag{4-15}$$

Considering the symmetry conditions, third order input arrays can be further constructed by using the upper triangular parts of the matrices defined as

$$\begin{aligned} \left[X_{3_n}\right] &= [X_2] x_n \\ \left[X_{3_{n-1}}\right] &= [X_2] x_{n-1} \\ &\vdots \\ \left[X_{3_{n-M+1}}\right] &= [X_2] x_{n-M+1} \end{aligned} \tag{4-16}$$

Then, for each output, *y(n)*, an equation can be written in form of

$$y(n) = \{X(n)\}\{H\} \tag{4-17}$$

where

$$\{X(n)\} = \{1 \quad x_n \quad x_{n-1} \quad \cdots \quad x_n^2 \quad x_n x_{n-1} \quad \cdots \quad x_n^3 \quad x_n^2 x_{n-1} \quad \cdots \quad x_{n-M+1}^3\}$$
$$\{H\} = \{h_0 \quad h_{1_0} \quad h_{1_1} \quad \cdots \quad h_{2_{0,0}} \quad h_{2_{0,1}} \quad \cdots \quad h_{3_{0,0,0}} \quad \cdots \quad h_{3_{n-M+1,n-M+1,n-M+1}}\}^T \tag{4-18}$$

Consider a memory length of 3. Then input arrays can be defined according to Equations 4-14 to 4-16 as follows.

$$\{X_1\} = \{x_n \quad x_{n-1} \quad x_{n-2}\} \tag{4-19}$$

$$[X_2] = \begin{bmatrix} x_n^2 & x_n x_{n-1} & x_n x_{n-2} \\ \cdots & x_{n-1}^2 & x_{n-1} x_{n-2} \\ \cdots & \cdots & x_{n-3}^2 \end{bmatrix} \tag{4-20}$$

$$[X_{3_n}] = [X_2] x_n = \begin{bmatrix} x_n^3 & x_n^2 x_{n-1} & x_n^2 x_{n-2} \\ \cdots & x_n x_{n-1}^2 & x_n x_{n-1} x_{n-2} \\ \cdots & \cdots & x_n x_{n-2}^2 \end{bmatrix}$$

$$[X_{3_{n-1}}] = [X_2] x_{n-1} = \begin{bmatrix} \cdots & \cdots & \cdots \\ \cdots & x_{n-1}^3 & x_{n-1}^2 x_{n-2} \\ \cdots & \cdots & x_{n-1} x_{n-2}^2 \end{bmatrix} \tag{4-21}$$

$$[X_{3_{n-2}}] = [X_2] x_{n-2} = \begin{bmatrix} \cdots & \cdots & \cdots \\ \cdots & \cdots & \cdots \\ \cdots & \cdots & x_{n-2}^3 \end{bmatrix}$$

The empty entries in the equations above correspond to symmetric terms and are not included in the solution. Then, *{X(n)}* is the collection of terms in Equations 4-19, 4-20, and 4-21. If there exists a zero order term h_0, which corresponds to a bias, then the constant "1" should be included in the *{X(n)}* array. The equations can be collected in matrix form as

$$\{Y\} = \begin{Bmatrix} y_1 \\ y_2 \\ \vdots \\ y_n \end{Bmatrix} = \begin{bmatrix} X(1) \\ X(2) \\ \vdots \\ X(n) \end{bmatrix} \{H\} = [A_X]\{H\} \tag{4-22}$$

The column size of the delayed input matrix, $[A_X]$, is the total number of kernels. The row size is the number total data points. Note that $\{X(1)\}$ requires past data, which can be set to zero.

Equation 4-22 can be solved by various ways. In this study, an iterative least squared method is used. Although there are no constraints, the solution of Equation 4-22 requires a considerable computation time with direct methods. For impulse inputs, the input matrix $[A_X]$ is very sparse and the solution should converge very rapidly with iterative methods. So, the problem reduces to the minimization of the 2-norm of the error defined by

$$\min_{\{H\}} \frac{1}{2} \left\| [A_X]\{H\} - \{Y\} \right\|_2^2 \tag{4-23}$$

Matlab functions are prepared to construct the input matrix with a desired memory length and Volterra order. It is not possible to obtain all kernels with impulsive inputs, since cross products of inputs vanish for most of the terms. Therefore, a sine sweep signal is used to test the algorithms. Results are given for a flow speed of 25 m/s. It is known from Figure 92 that there exists an LCO for this speed with a frequency of 3.1 Hz. Figure 104 shows the identified first order kernel. This first order kernel is also the ideal impulse response. The last index 150, which is the memory length, corresponds to 2.5 s.

Figure 105 shows the estimated FRF using the first order kernel data given in Figure 104 and actual measurements. Note that the FRF derived from nonlinear data estimates a peak at 3.1 Hz. Both LCO and the linear mode close to that frequency

contribute to the amplitude. However the Volterra estimation truncates the peak, removing the effect of LCO.

Figure 106 shows the identified second order kernel. Note that numerical values are comparable to first order kernel. This is an indication of a strong nonlinearity.

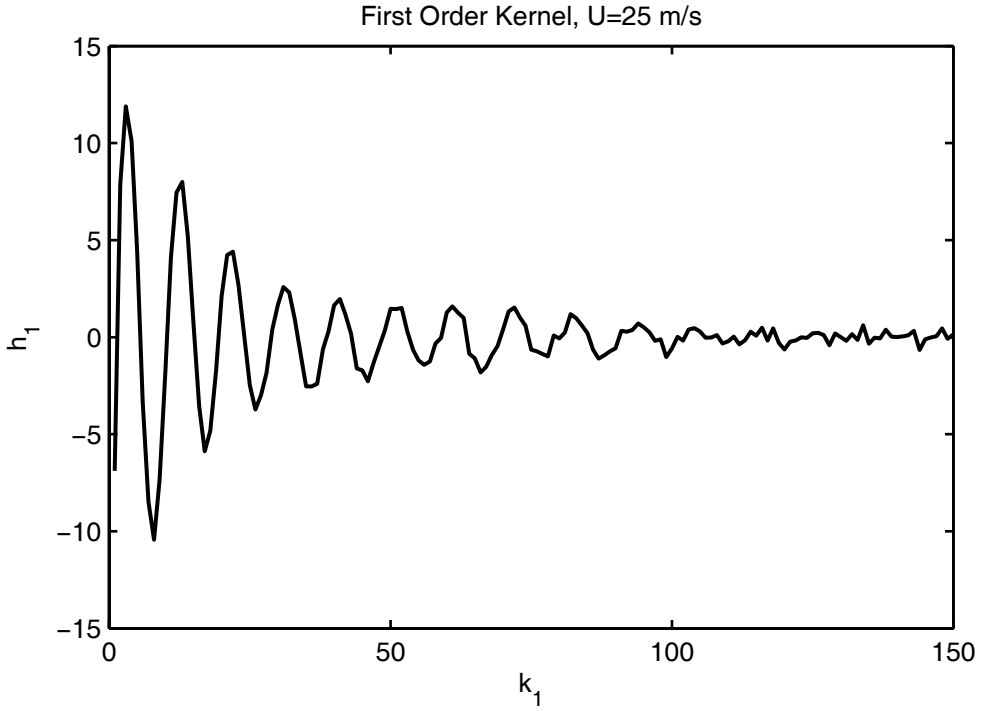

Figure 104. Identified first order kernel, U=25 m/s.

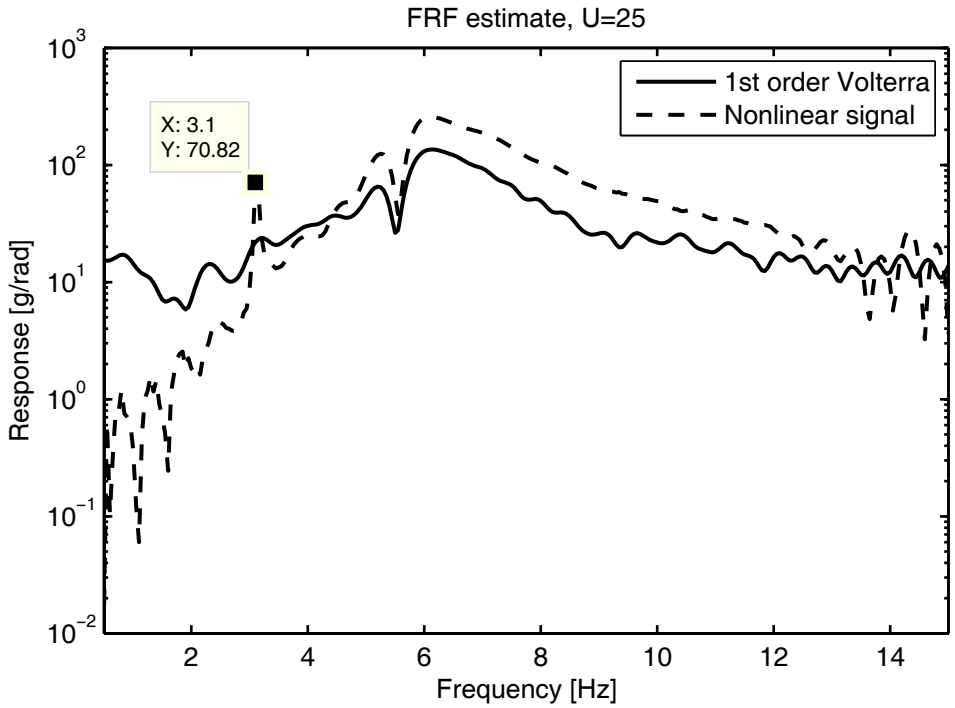

Figure 105. Derived FRF, U=25 m/s.

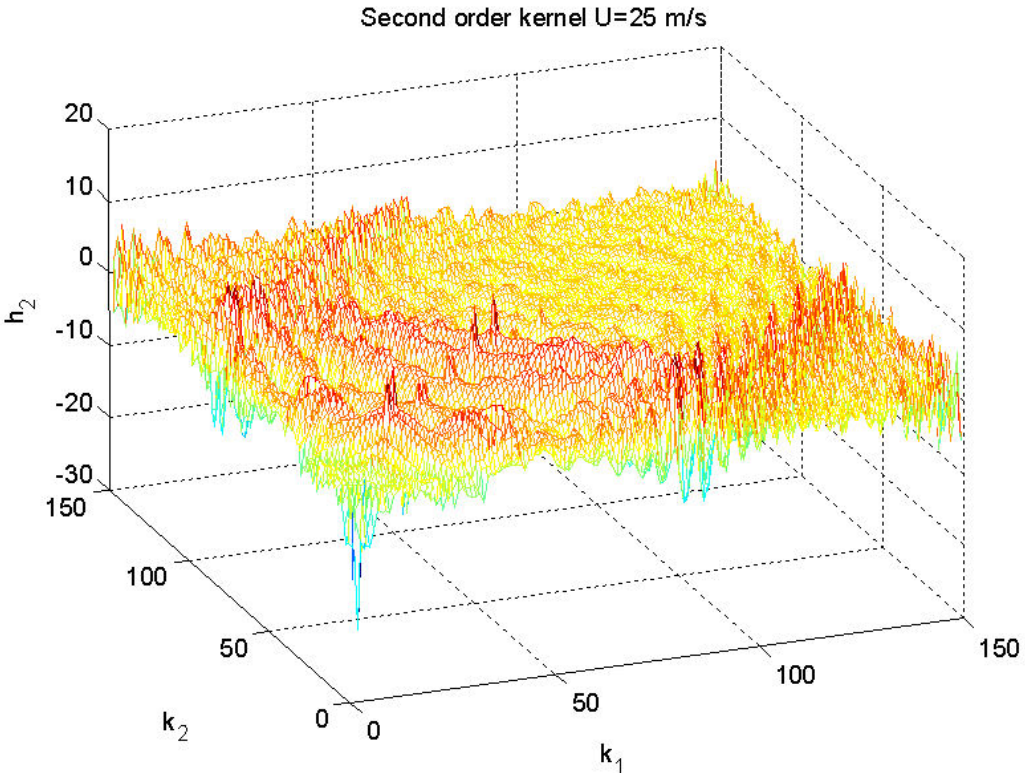

Figure 106. Identified second order kernel, U=25 m/s.

4.6 Nonlinear Flutter Prediction

A series of flutter predictions are performed with direct and processed measurements. The processed measurements are simply the identified first order Volterra kernels. Figure 107 shows the estimated transfer functions for various speeds directly using the measured data. As seen from the figure, the qualities of FRFs are not comparable to the linear cases; for instance, those obtained in Section 3.3.1. The high speed FRFs seem to be much better than the low speed ones. However, the distinct peaks at high speeds are due to the LCOs.

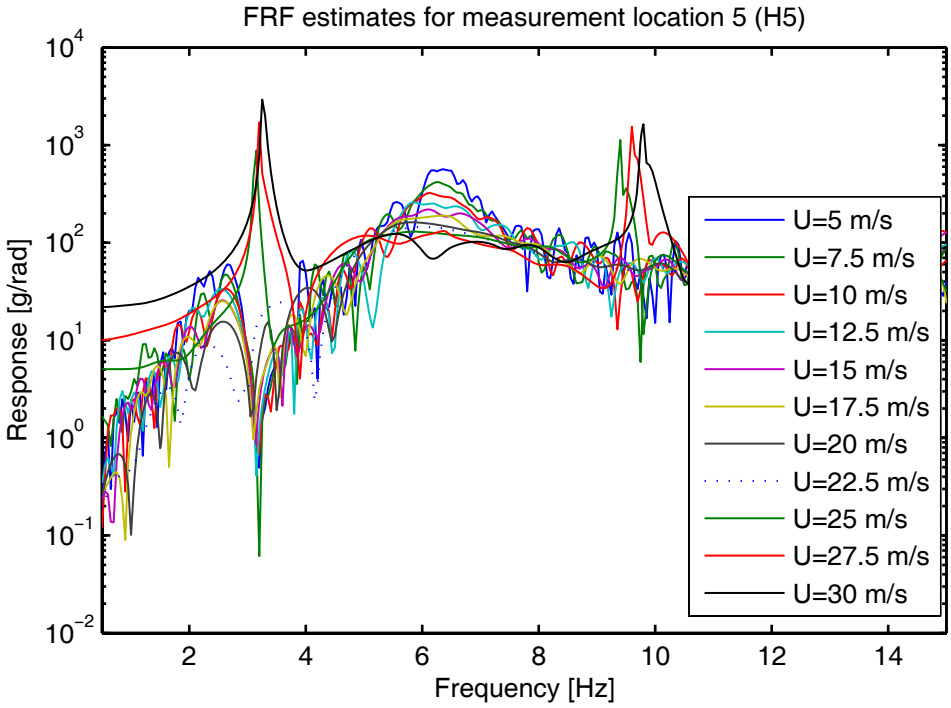

Figure 107. FRF estimates for all speeds.

The damping estimations with these FRF are not supposed to be reliable. Figure 108 shows one of the curve fit results. It is not even possible to fit an appropriate curve to the FRF in the case of LCO. So, the results of speeds 25, 27.5, and 30 m/s are not included in the damping extrapolation solution. Figure 109 shows the estimated damping with respect to the flow speed.

Obviously, it is not possible to predict flutter with the curves given in Figure 109. Recall that the flutter margin method is very successful in case of damping scatter. Figure 110 shows the flutter margin solution. It is hard to say that a trend exists.

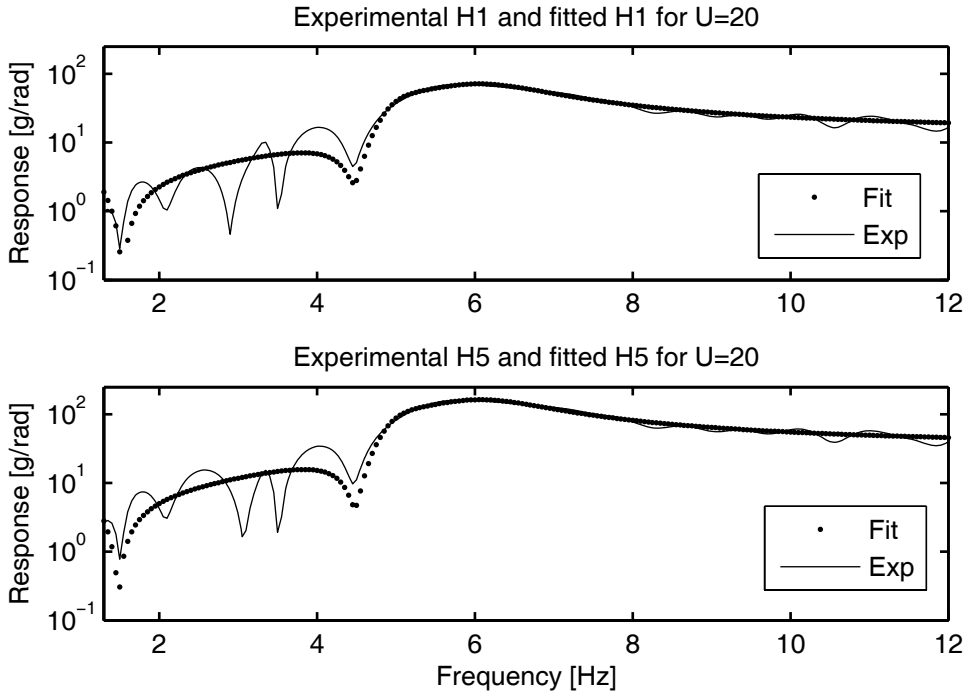

Figure 108. Curve fit result for damping extrapolation, U=20 m/s.

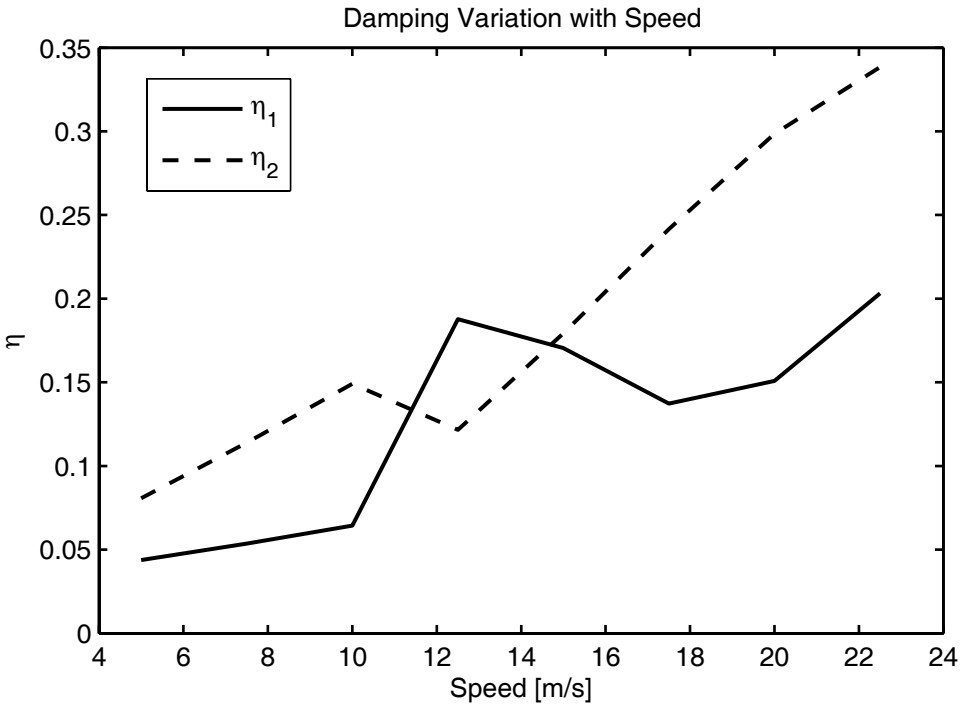

Figure 109. Estimated damping variation.

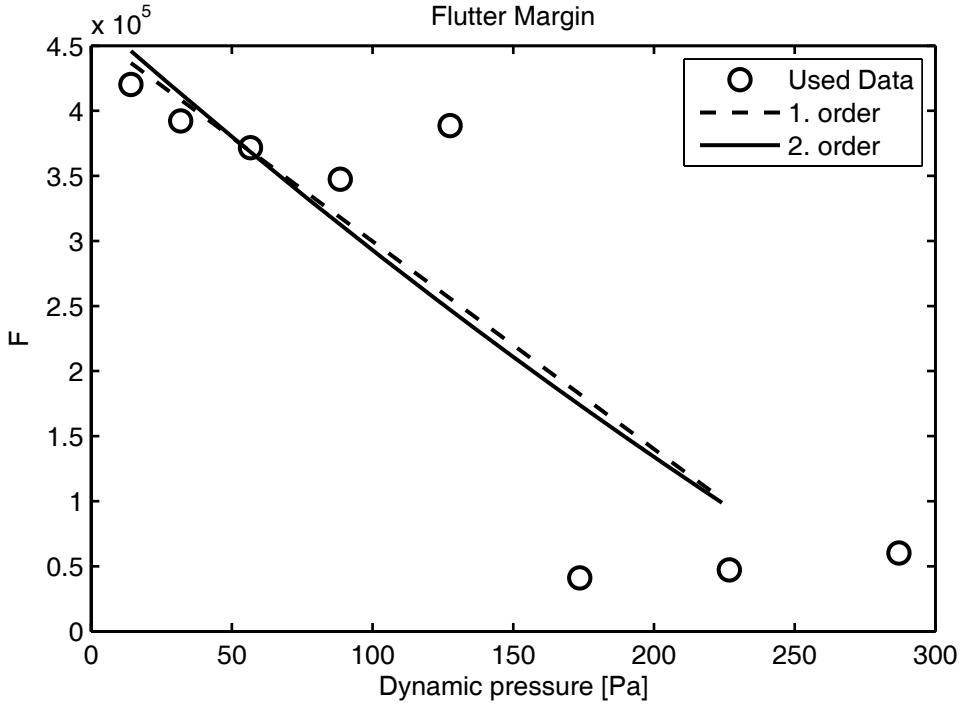

Figure 110. Flutter margin solution.

It is observed that Volterra processing of nonlinear data does not increase the reliability of the data based methods. Despite the failure of data based methods, the flutterometer method should be able to provide an answer even with the nonlinear data. Note that the deviation from linear response is handled by an uncertainty modeling in the flutterometer method. Thus, the success of the method directly depends on this uncertainty modeling. To test the capability of the flutterometer method to handle the nonlinear data successfully, a case study is performed. The initial uncertainty description is kept the same as in previous studies. Parameter variations that are used for robust flutter analysis are given in Table 10. An uncertainty validation is performed with both nonlinear and processed data. Flutterometer solutions are given in Table 16.

Table 16. Flutterometer solutions.

	1/uncertainty scaling		Predicted flutter speed [m/s]	
U [m/s]	Volterra	Nonlinear	Volterra	Nonlinear
12.5	0.978	0.269	16.97	15.05
15	0.703	0.443	19.78	19.4
17.5	1.351	0.487	24.16	22.61
20	0.279	0.269	23.14	23.04
22.5	0.519	0.483	27.86	27.52
25	0.569	0.386	30.03	28.55
27.5	1.048	0.402	33.39	29.9
30	0.904	0.524	32.45	32.41

As seen from Table 16, a Volterra processing results in a smaller scaling, thus decreasing the conservatism. The effect of Volterra processing is more effectively

seen at speeds where an LCO exists. Since the LCO signal is filtered from the measurement, the uncertainty description becomes less conservative. Recall that the true flutter speed is 32 m/s. Despite the conservatism of the method, some predictions are above the true value, not only with the Volterra processing but also with the direct measurements.

4.7 Summary

In this chapter, the effect of nonlinearity on flutter prediction is investigated. It is seen that the backlash type severe nonlinearity distorts the estimated FRF seriously not only in the case of LCO but also at low speeds where no LCO occurs. The Fourier analysis is the main tool for classical flutter prediction methods. Thus, the failure in Fourier transform operation degrades the performance of these methods. It is not possible to predict flutter speed or LCO with data based methods. This clearly implies that more attention must be given to model based methods. It is possible to observe the onset of LCO with the help of wavelet analysis, even in the case of severe nonlinearities.

The nonlinear signals in the response of the system can be identified by the application of Volterra series approach. The accuracy of the extracted linear part of the signal depends on the order of kernels used in the series. The quadratic type nonlinearities can be clearly observed by the second order kernels. The odd type nonlinearities such as backlash and cubic stiffness can be observed with third or even higher order kernels. However, the implementation of the third and higher order kernels increases the computational cost of the solution beyond the practical use in a flight test with the current computational power. On the other hand, the second order kernels can be used with such nonlinearities, but the truncation of higher order kernels introduces some errors in both second and first order kernels. The FRFs that are estimated directly from the response of the nonlinear systems usually can not be used with the most of the flutter estimation methods. However, the linear part of the system response can be extracted from the nonlinear response by using the Volterra

kernels. The FRFs that are estimated from the linear part of the system response can be used for more accurate and less conservative flutter estimation. The success of Volterra filtering directly affects the performance of the classical data based flutter estimation methods. However, the flutterometer method is able to predict a flutter speed even in the case of severe nonlinearity. It is shown that the conservatism of the method can be decreased by using the FRF obtained from the first order Volterra kernels.

CHAPTER 5

EXPERIMENTAL STUDIES

5.1 The Aeroservoelastic Test Setup (ATS)

The ATS was designed and produced for the aeroelastic and aeroservoelastic experiment requirements of TÜBİTAK-SAGE [67]. The setup was designed to fit into the test room of Ankara Wind Tunnel. The setup consists of a rigid airfoil, a base that holds the airfoil, linear guides for plunge degree of freedom, a servomotor with backlash-free gear head, and a frame. The base provides two degrees of freedom to the airfoil. The torsional DOF of the airfoil is guided with a couple of ball bearings installed in the base. The servo system is also installed on the base and the torsional DOF of the airfoil is connected to the servo system via a torsional spring. The whole base subsystem, including the airfoil and the servo system, is installed on the structure via linear guides, which permits the plunge DOF. Two linear springs are placed between the base subsystem and the frame.

The ATS is instrumented with a resolver, a position transducer, and four accelerometers. The resolver is used to measure the angular displacement of the airfoil about the pitch axis located vertically. The servomotor also includes a resolver, which is used for commutation of the servomotor and control feedback. The position transducer is used to measure the plunge motion of the airfoil perpendicular the direction of airflow. The accelerometers are placed close to the four corners of the airfoil. The sensors of the ATS monitor all the motions of the system. The accelerometers are redundant sensors. They are used to generate data similar to the ones that are obtained in real flight tests. Acceleration data is usually the only data available during flight tests.

The servomotor of the system is controlled by a PC, that is running Matlab's real time xPC Target operating system. The PC is equipped with necessary PCI input/output cards that are compatible with Matlab xPC Target. The servomotor position is measured from the driver of the servomotor and fed to the controller. The controller calculates the necessary current to track the position command in real time. The calculated current is commanded to the servomotor driver through a digital to analog card. The xPC Target system is also used for data acquisition from the sensors of the ATS.

Components of the ATS are shown in Figure 111, Figure 112 and Figure 113. The view of the ATS as installed into the test room is given in Figure 114.

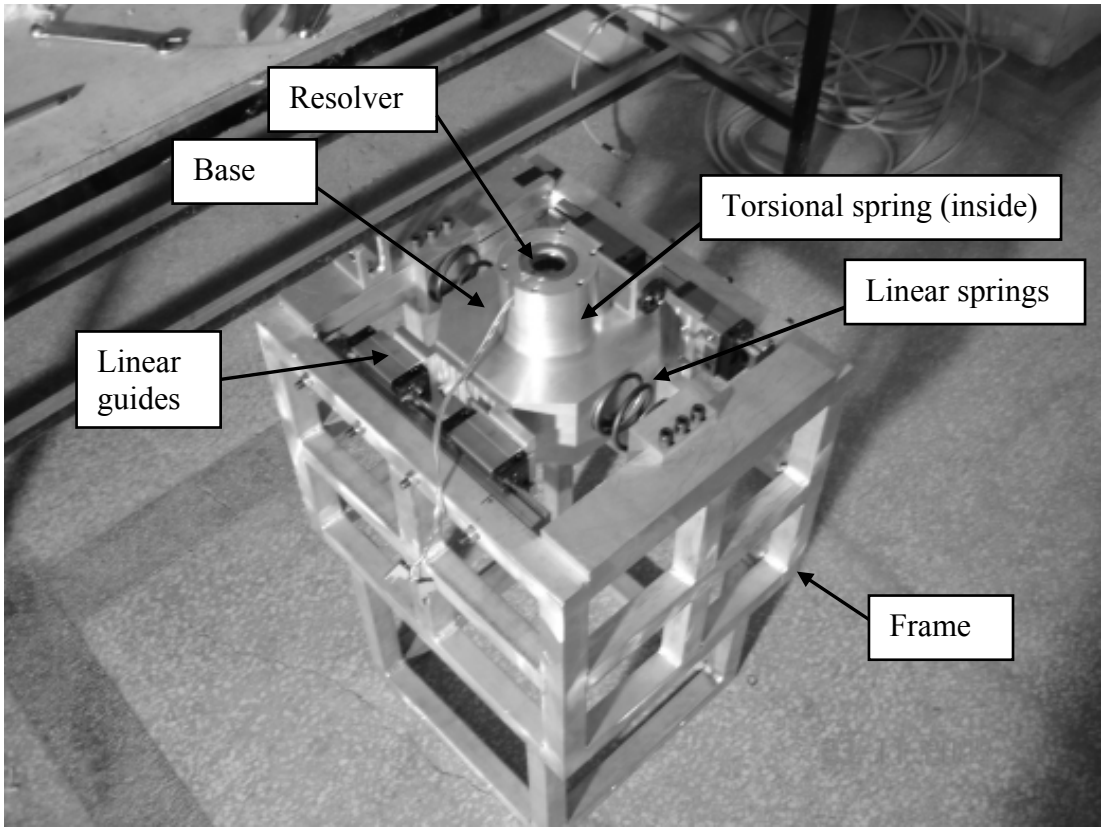

Figure 111. Uninstalled ATS.

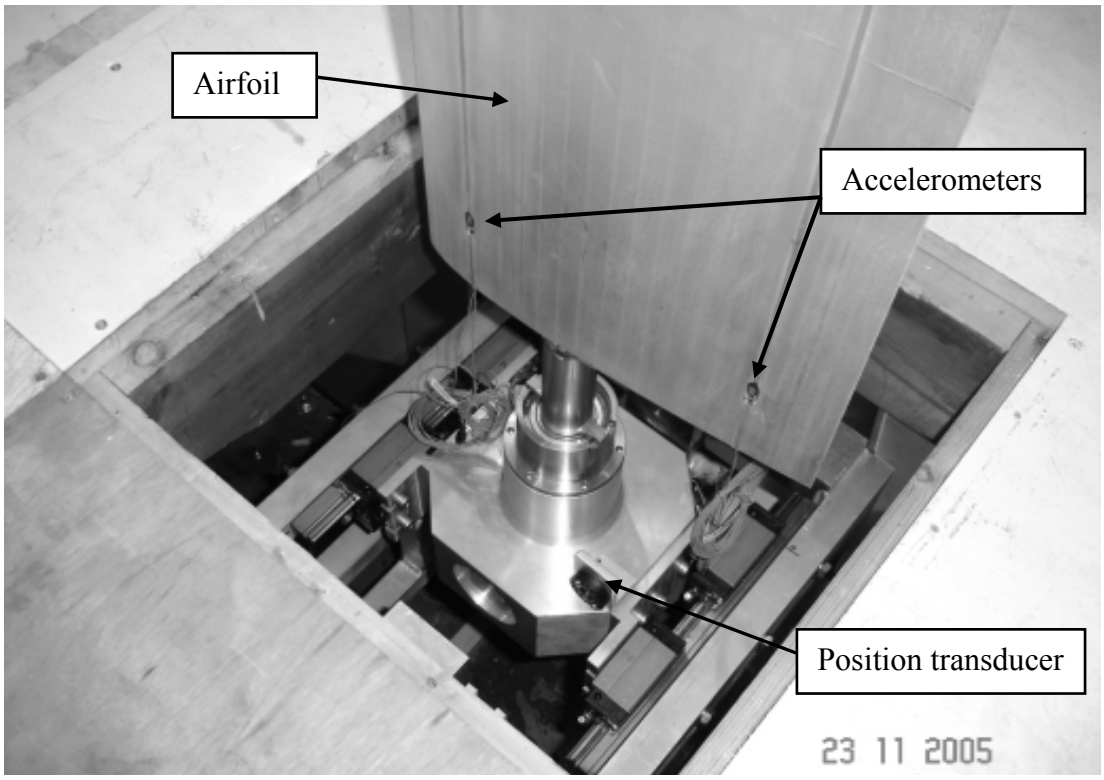

Figure 112. View of ATS from test room.

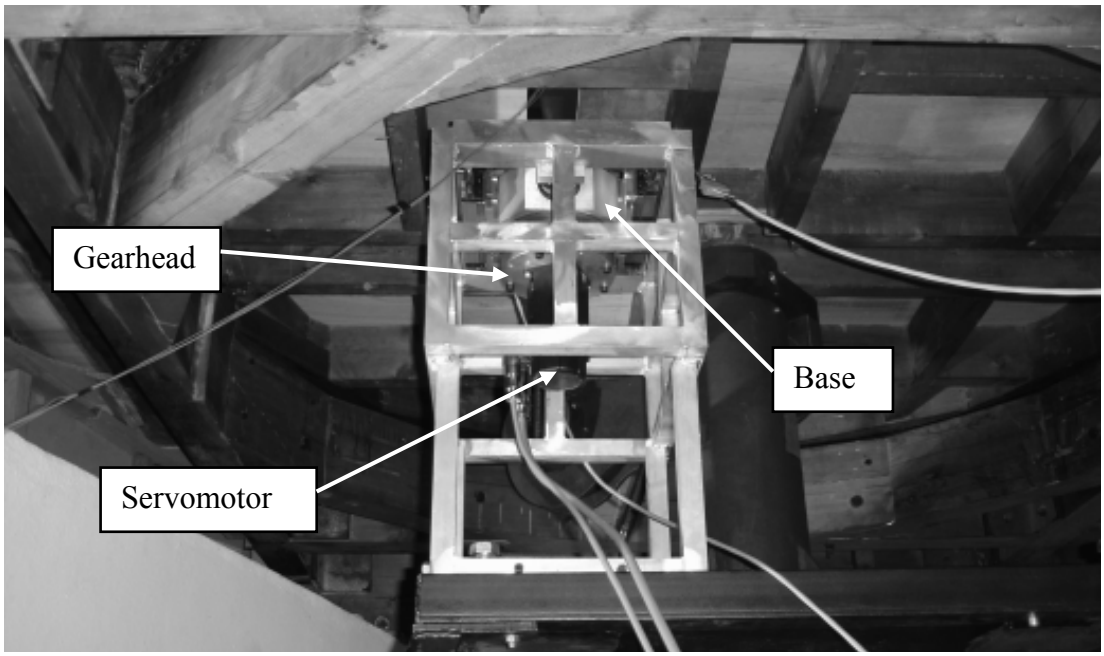

Figure 113. View of ATS below the test room.

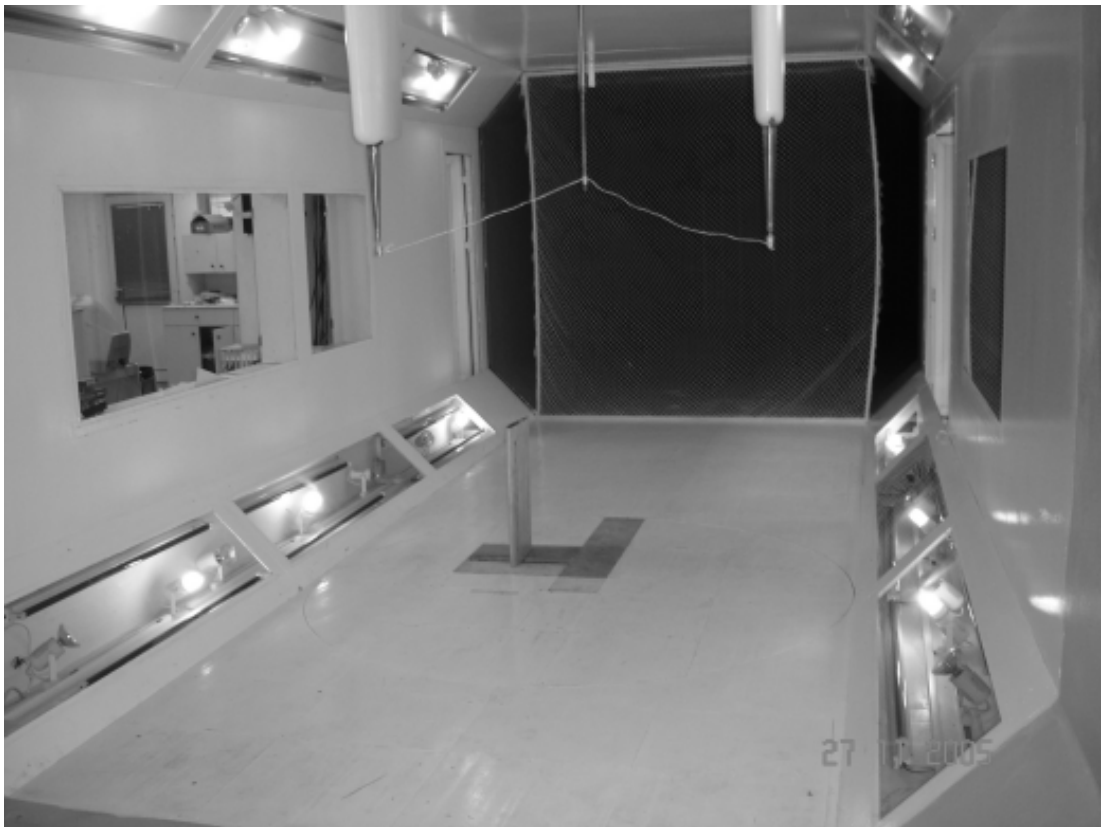

Figure 114. Installed ATS.

The original linear guides of the ATS were preloaded re-circulating ball type heavy duty guides. The guides had serious stick slip friction problem under light loads. Because of that high dry friction, it was not possible to observe any flutter within the operation range of the wind tunnel. However, it was possible to observe some limit cycle oscillations when large disturbances were applied to the setup. In order to enhance the behavior of the system (i.e., to convert the system more flutter-prone), the linear guides are replaced with low friction guides. Linear springs are also replaced by new ones to increase the preload on them. So the linear springs never separate from the base during motion. Despite all these enhancements, FRF measurements of the setup showed that there is still some dry friction on the setup.

5.2 Experiment

The servo system installed on the ATS allows to excite the system in pitch DOF in any form. A set of pulse and sinesweep excitations are performed at various air speeds. The measurements are recorded at each air speed for post processing. The experiment is started with a wind tunnel speed of 10 m/s. The air speed in the wind tunnel is increased gradually and the data is recorded at speeds of 15, 19.9, 24.8, 29.9, 34.9, and 37.6 m/s. The system is observed to be stable at these speeds. The flutter is observed at 40.1 m/s. Tests are repeated around 40 m/s to accurately determine the critical flutter speed. As a coincidence, it is seen that the flutter speed for the ATS is very close to 40.1 m/s. Recall that the theoretical flutter speed is 25.7 m/s. The theoretical calculations assume that the airfoil thickness is zero and the nondimensional lift slope is 2π, which is the theoretical maximum for infinite span. Any deviation from these assumptions is expected to cause the lift to decrease. The lift for finite span wings is known to decrease, especially if the aspect ratio is small. The setup has still a slight stick slip friction problem which also introduces a weak nonlinear damping to the setup. Additional damping shifts the damping versus speed graph upwards, thus increasing the flutter speed. The aim of the experiment is not to validate or update the theoretical flutter calculations, but to estimate the flutter speed from the real test data. So the real flutter speed of the ATS is determined to be just below 40.1 m/s. The response plots of the system at 15 m/s to the pulse excitation described in Figure 115 are given in Figure 116, Figure 117, Figure 118, and Figure 119. As seen from the acceleration graphs, noise levels are comparable to the response. The filtered acceleration data with 20 Hz cutoff 2^{nd} order Butterworth filter is given in Figure 120. As seen from the figure, noise can be filtered considerably. The performance of the servo system is observed to be successful as seen from Figure 115. The figure implies that the base of the torsional spring does not move after the command is set to zero, even during the oscillations of the system. Otherwise, a coupling between the aeroelastic system and servo system would occur and this interaction of the control system with the elastic system would affect the flutter speed.

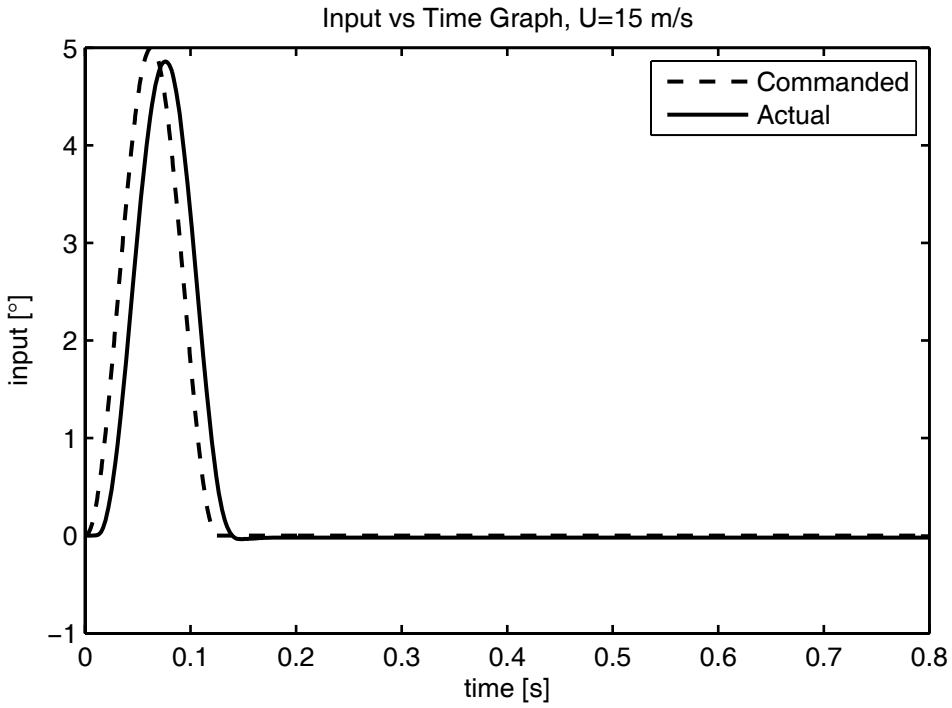

Figure 115. Excitation at 15 m/s.

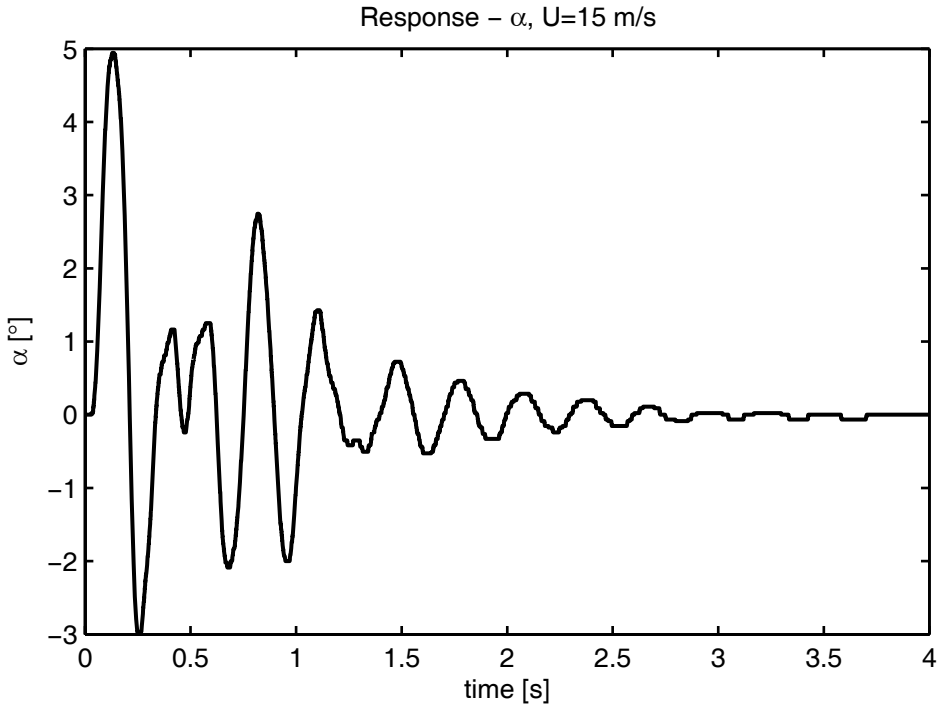

Figure 116. Torsional response at 15 m/s.

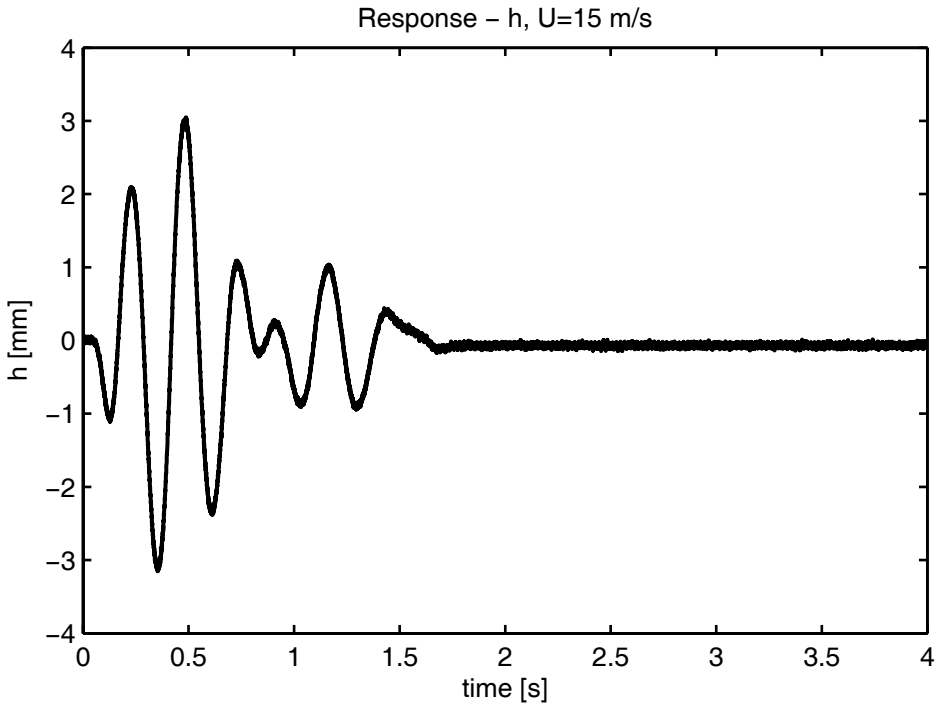

Figure 117. Plunge response at 15 m/s.

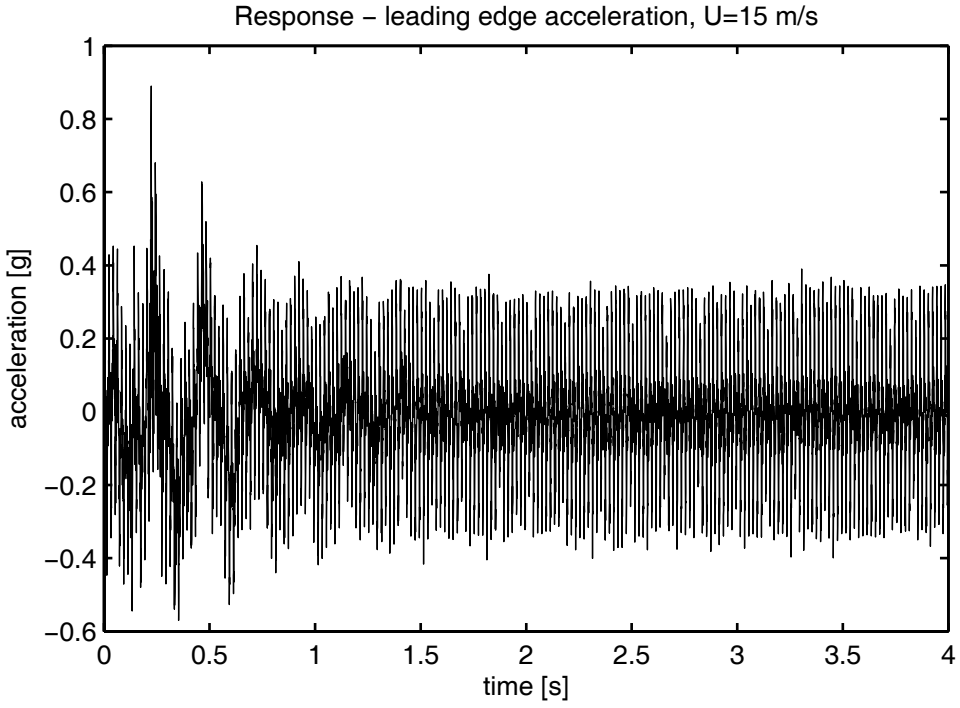

Figure 118. Leading edge accelerometer data at 15 m/s.

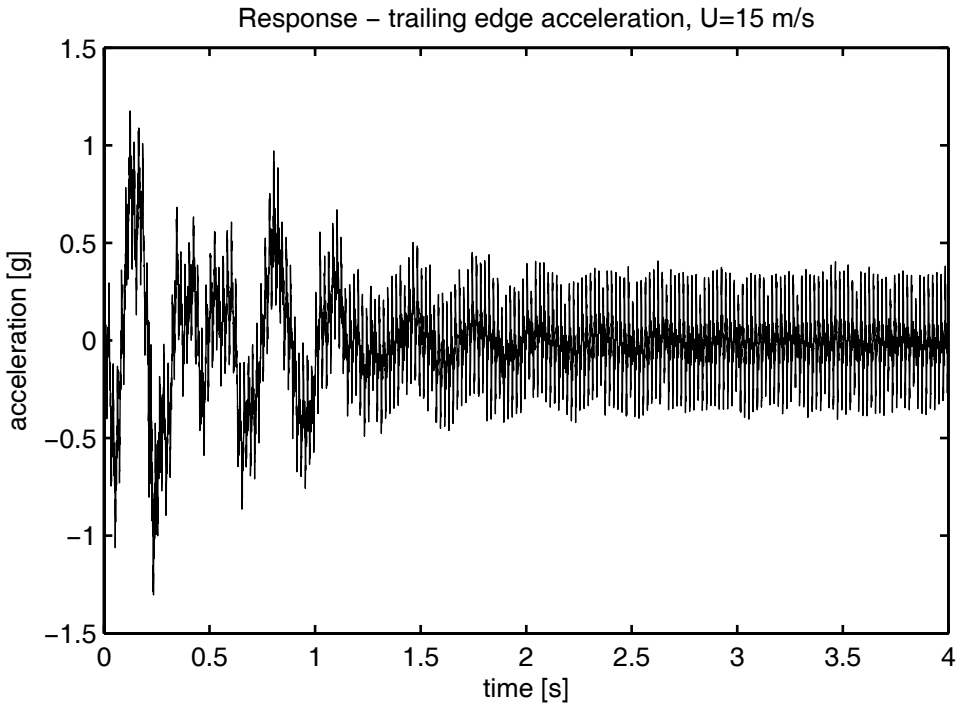

Figure 119. Trailing edge accelerometer data at 15 m/s.

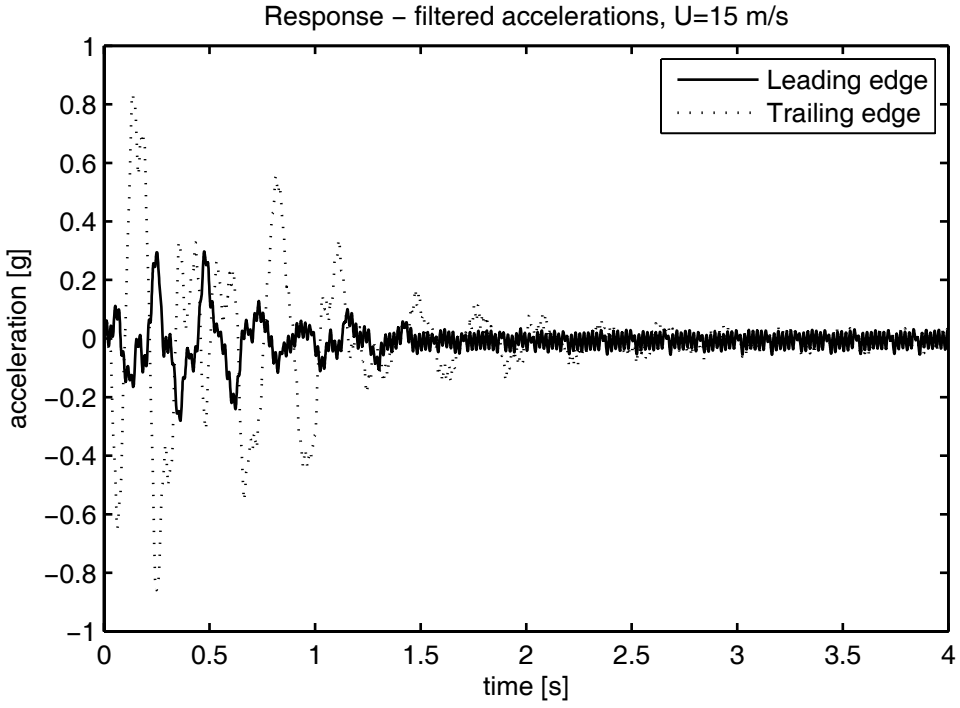

Figure 120. Filtered accelerometer data at 15 m/s.

The response of the system just before the flutter speed is given in Figure 121 and Figure 122. As seen from the figures, this response is similar to the response of a single-DOF system, which is expected at speeds close to the flutter speed. However, there is no clear indication about the decrease in damping when the response is compared with the response at 15 m/s air speed. The response of the system at just above the flutter speed is given in Figure 123 and Figure 124. The exponential divergence of the response can be clearly observed.

The experiment process is concluded to be successful with the observation of flutter within the operation speed range of the wind tunnel.

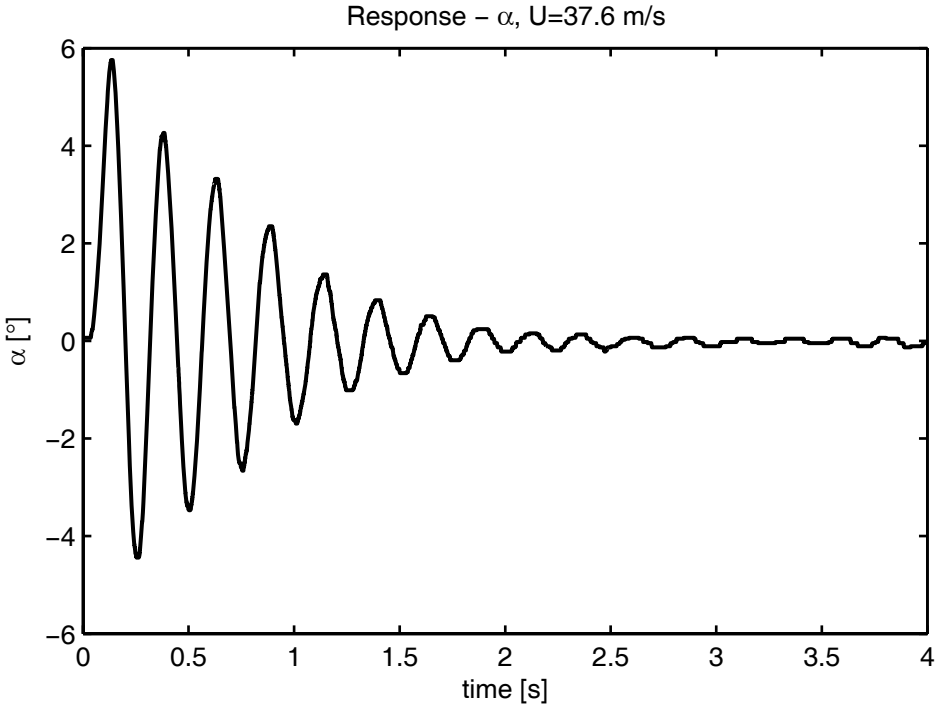

Figure 121. Torsional response at 37.6 m/s.

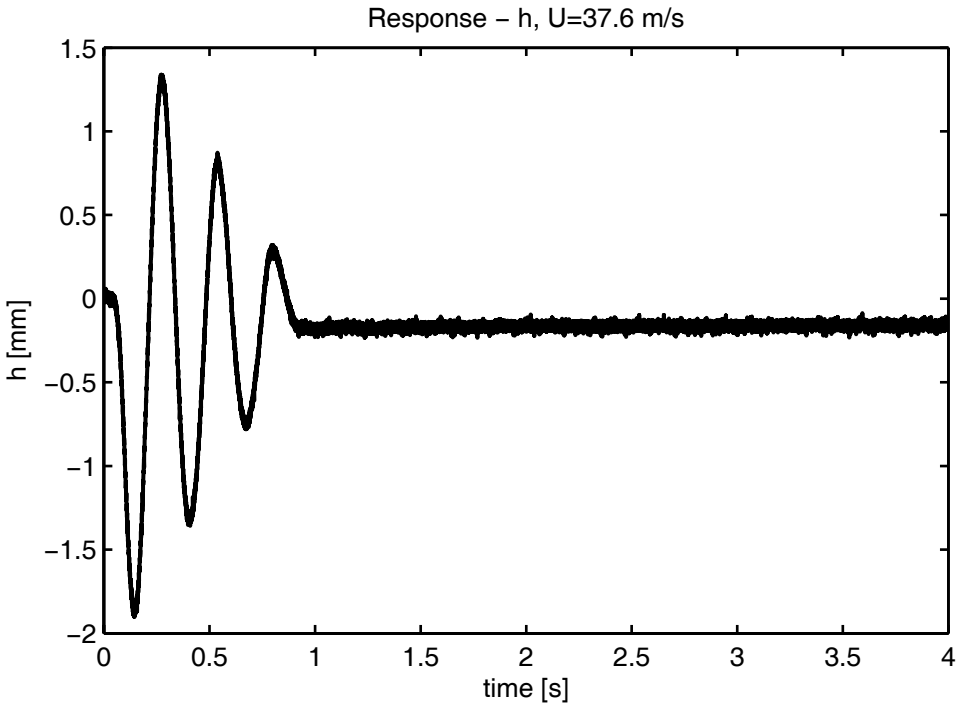

Figure 122. Plunge response at 37.6 m/s.

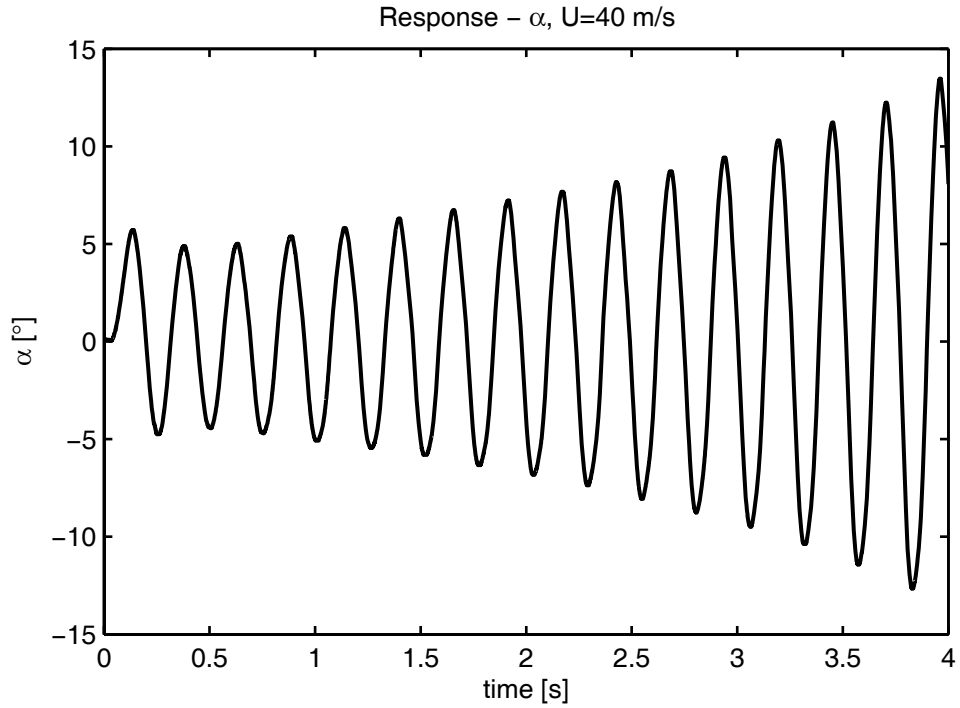

Figure 123. Torsional response at 40 m/s.

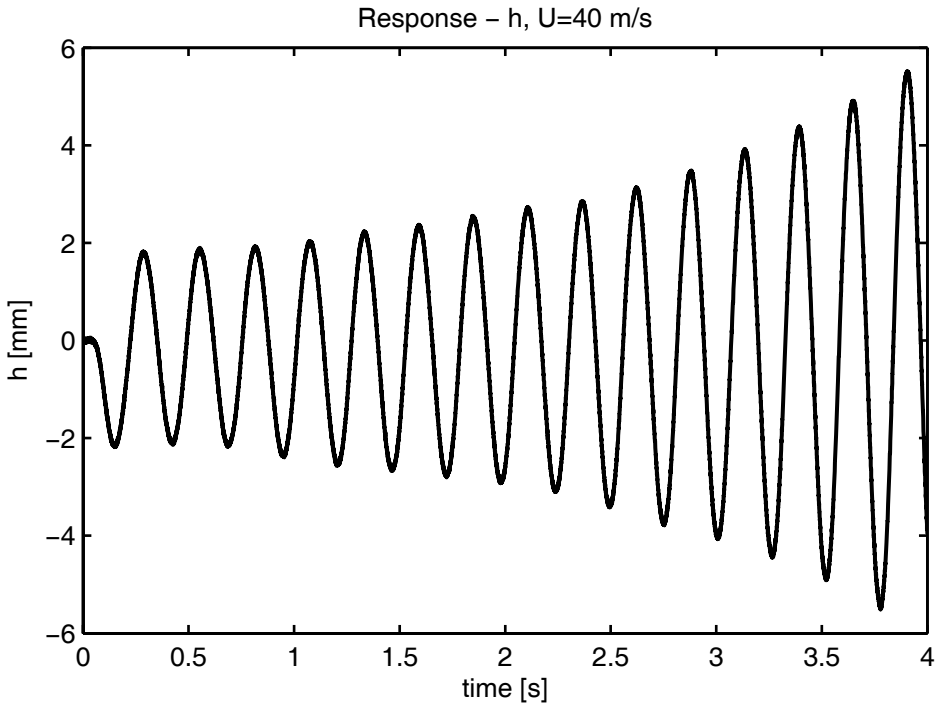

Figure 124. Plunge response at 40 m/s.

5.3 Flutter Estimation

The first step in flutter estimation is to determine the FRF of the system. Both impulse and sinesweep excitations are applied during the tests. The FRF estimations with impulsive input are given in Figure 125 and Figure 126. As seen from the figures, the FRFs are completely useless. Even the peaks of the system are not distinguishable. Although the friction problem of the ATS is greatly solved, the remaining slight dry friction disturbs the FRFs significantly. It is not possible to perform modal fits to these FRFs, but they can be directly used with the flutterometer method. However, some successful modal fits are necessary for damping extrapolation and flutter margin methods. Sinesweep excitation is a useful excitation type in case of weak nonlinearities. If the input energy can be concentrated in a single frequency for a sufficient duration, very successful output measurements can be obtained. The frequency range of interest can be swept with discrete frequency lines. Such excitations are called as the “stepped sine testing”. However, the

acquisition time for a stepped sine input testing is longer than the other types of inputs. Instead of a stepped sine input, a continuously but slowly varying sinesweep is used as input. The speed of the sweep determines the accuracy of the peak of the response, which is directly related to the accuracy of the damping estimation. Slower sweeps always result in better accuracies. Figure 127 and Figure 128 show the estimated FRF with a sinesweep excitation. The performed sweeps start at 1 Hz and end at 6 Hz within 200 s. This sweep rate is sufficiently small and appropriateness of this rate is verified by using various sweep rate tests. As seen from the figures, the FRF estimates are much better than the ones that obtained with the impulsive inputs. It is possible to perform successful modal fits to these FRFs.

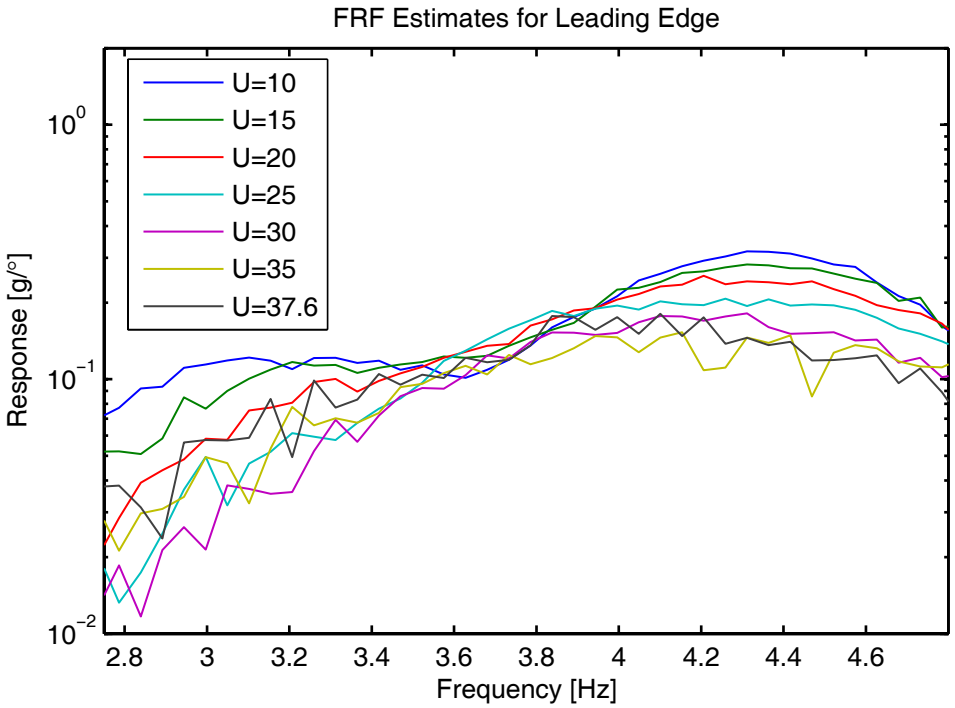

Figure 125. FRF estimations for leading edge with impulsive input.

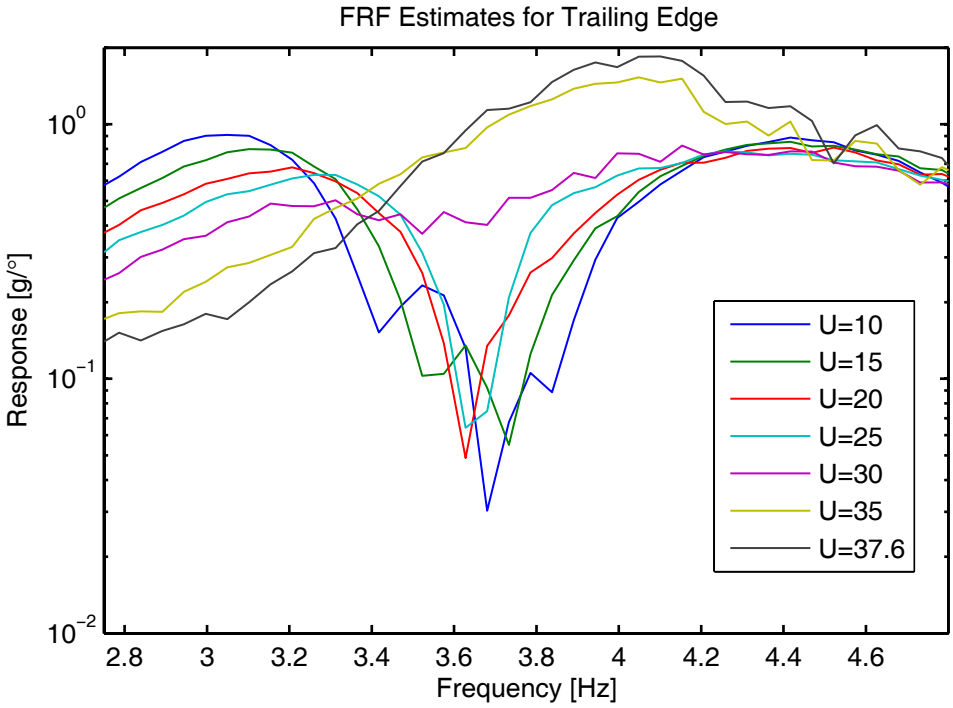

Figure 126. FRF estimations for trailing edge with impulsive input.

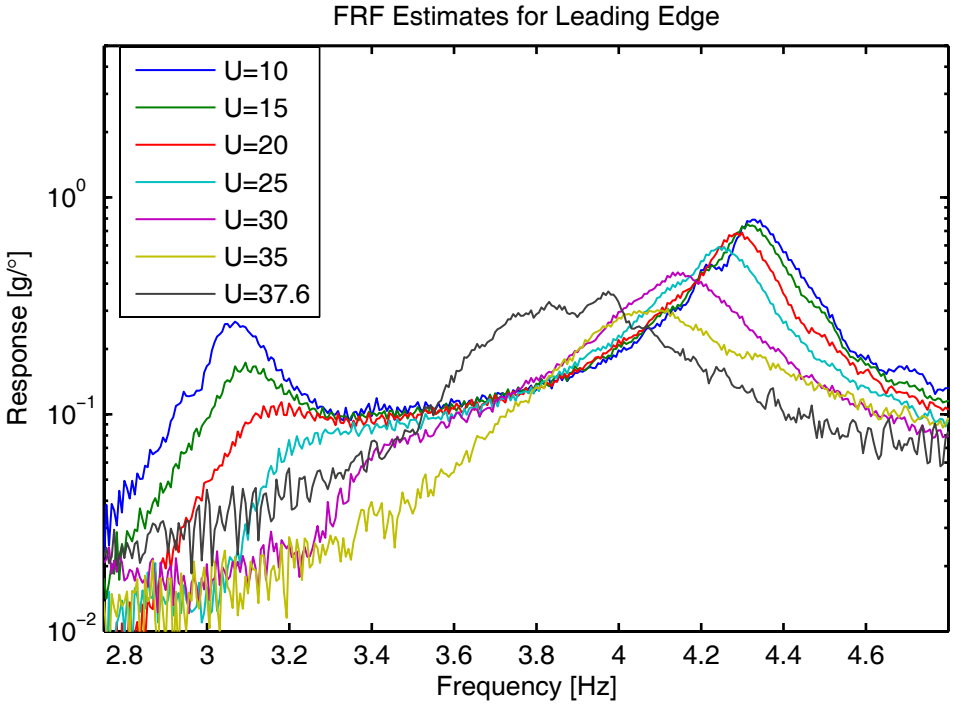

Figure 127. FRF estimations for leading edge with sinesweep input.

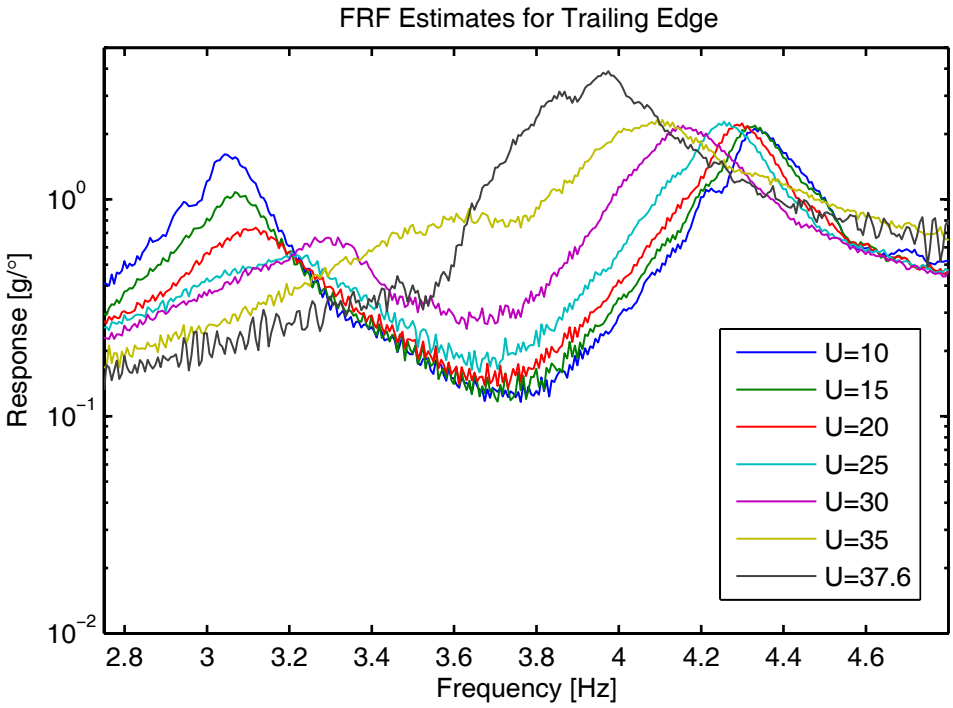

Figure 128. FRF estimations for trailing edge with sinesweep input.

5.3.1 Flutter Prediction with Damping Extrapolation

The modal fit results are given in Figure 129 to Figure 135 at each wind tunnel speed. As seen from the figures, these fits are successful. A summary of modal extraction is given in Table 17. The V-g plots are given in Figure 136 and Figure 137. The damping variation of the ATS, which is given in Figure 136, is one of the most difficult type to interpret. If the true flutter speed were not known, the estimate would cause some catastrophic results. Because the damping of the 1st mode seems to increase enormously at the speed just before the flutter. In an actual flight test, the test engineer may consider such a variation as a scatter. Since the damping trends for both modes seem to increase exponentially, the test engineer would probably consider a large speed increment for the next test point. Clearly, it is not possible to perform a concave down curve fit to the damping graphs if the first 6 data pairs are used. If the first 5 data pairs are used in Figure 138, it is possible to estimate a flutter speed of 36.7 m/s for 3rd order fit and 34.7 m/s for 4th order fit.

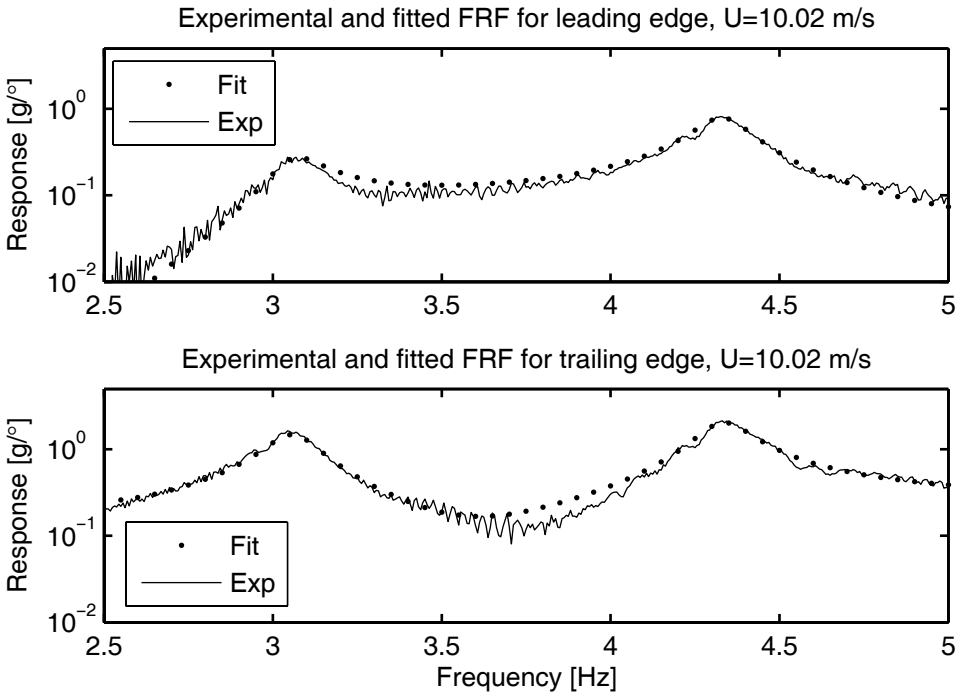

Figure 129. Fit results for 10 m/s.

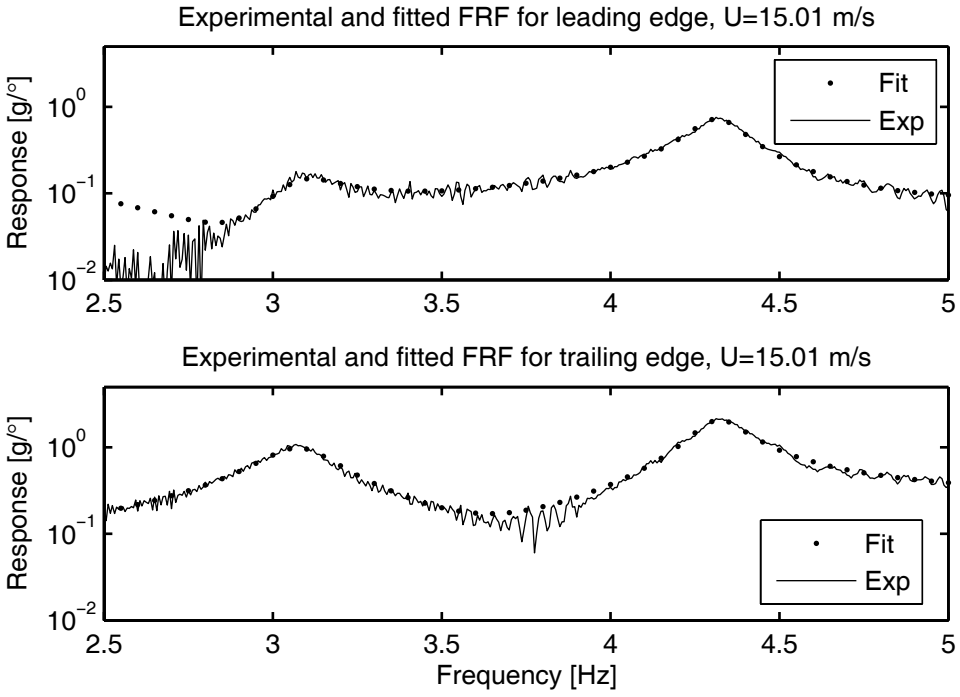

Figure 130. Fit results for 15 m/s.

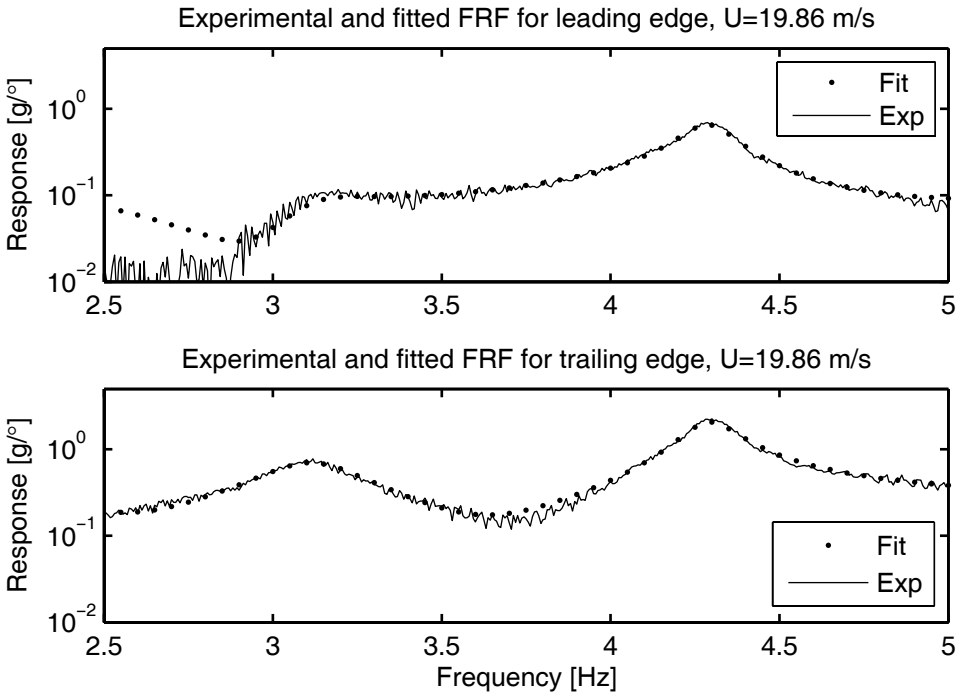

Figure 131. Fit results for 19.9 m/s.

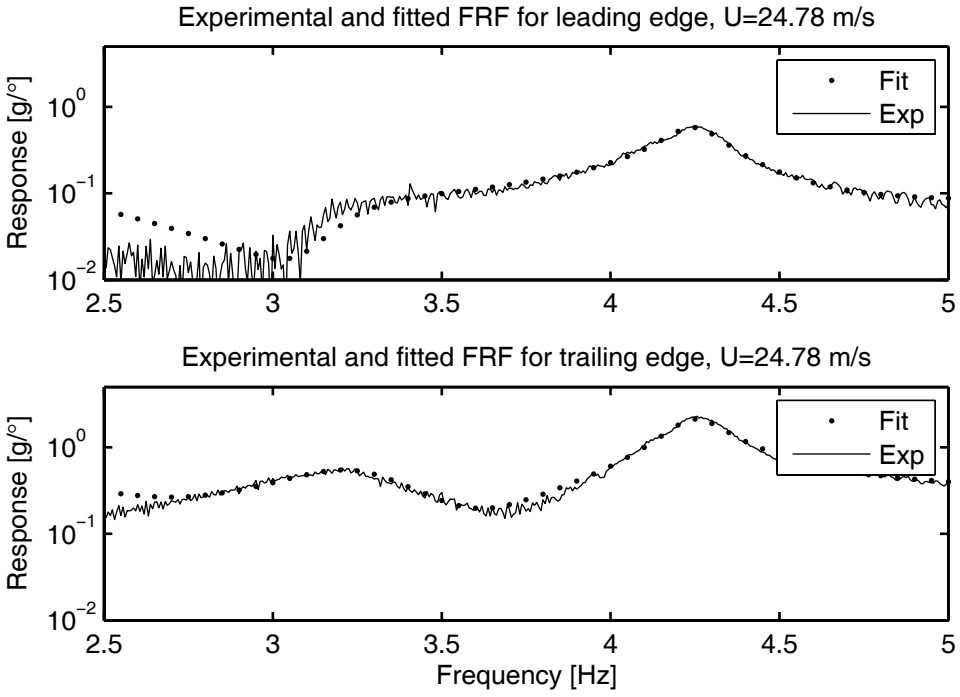

Figure 132. Fit results for 24.8 m/s.

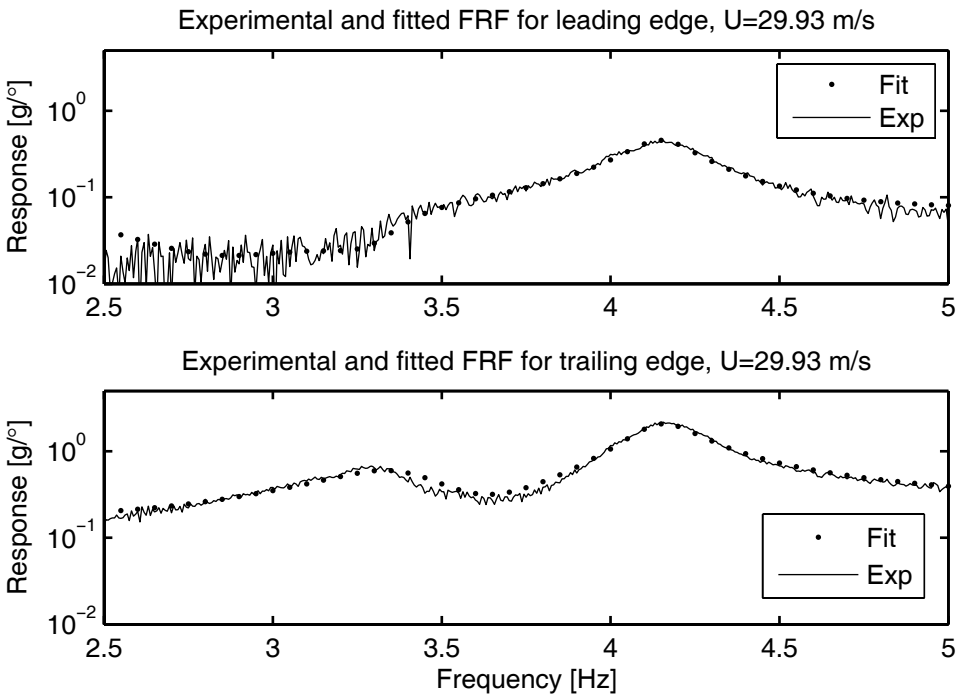

Figure 133. Fit results for 29.9 m/s.

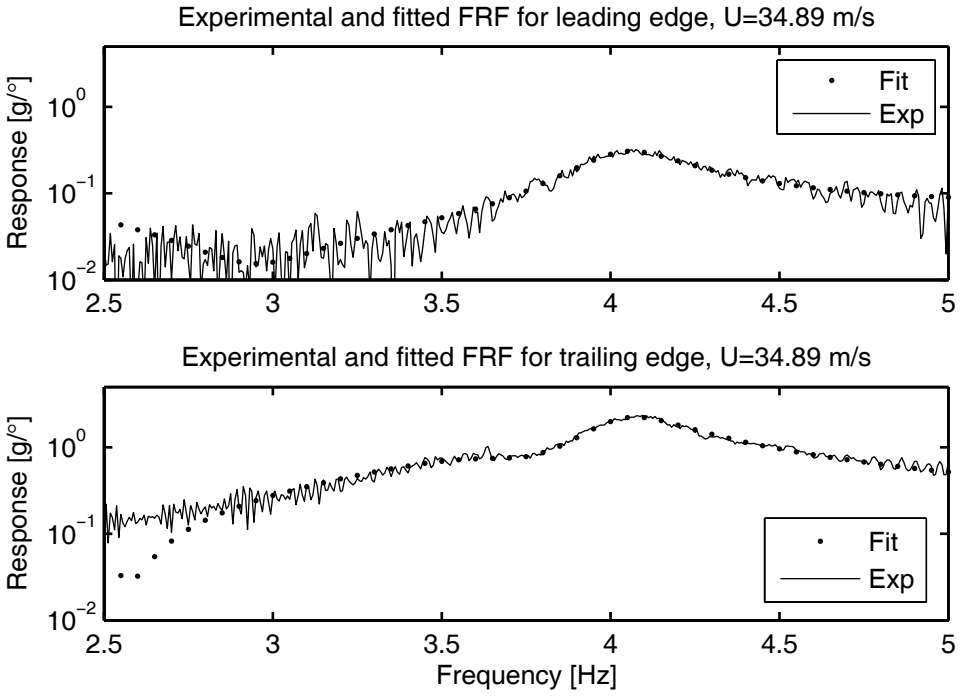

Figure 134. Fit results for 34.9 m/s.

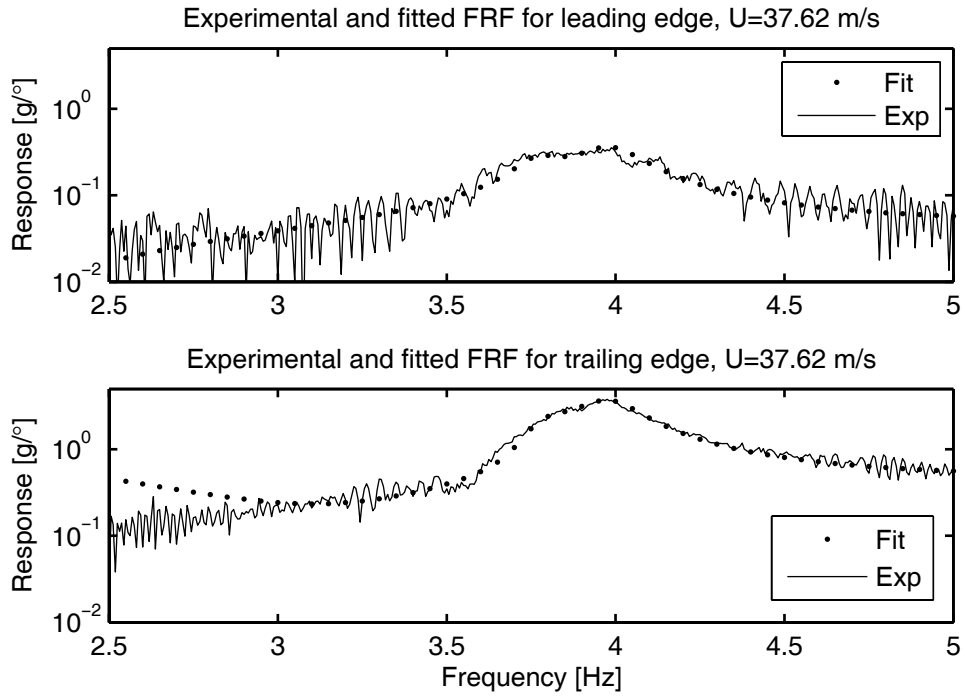

Figure 135. Fit results for 37.6 m/s.

Table 17. Summary of modal extraction.

U [m/s]	10	15	19.9	24.8	29.9	34.9	37.6
η_1	0.0495	0.0695	0.0966	0.1224	0.1096	0.1766	0.0388
η_2	0.0362	0.0354	0.0376	0.0419	0.0509	0.0763	0.0501
ω_1 [Hz]	3.0595	3.0756	3.1129	3.2334	3.3669	3.6757	3.7717
ω_2 [Hz]	4.332	4.3171	4.2889	4.2473	4.1495	4.0411	3.9784

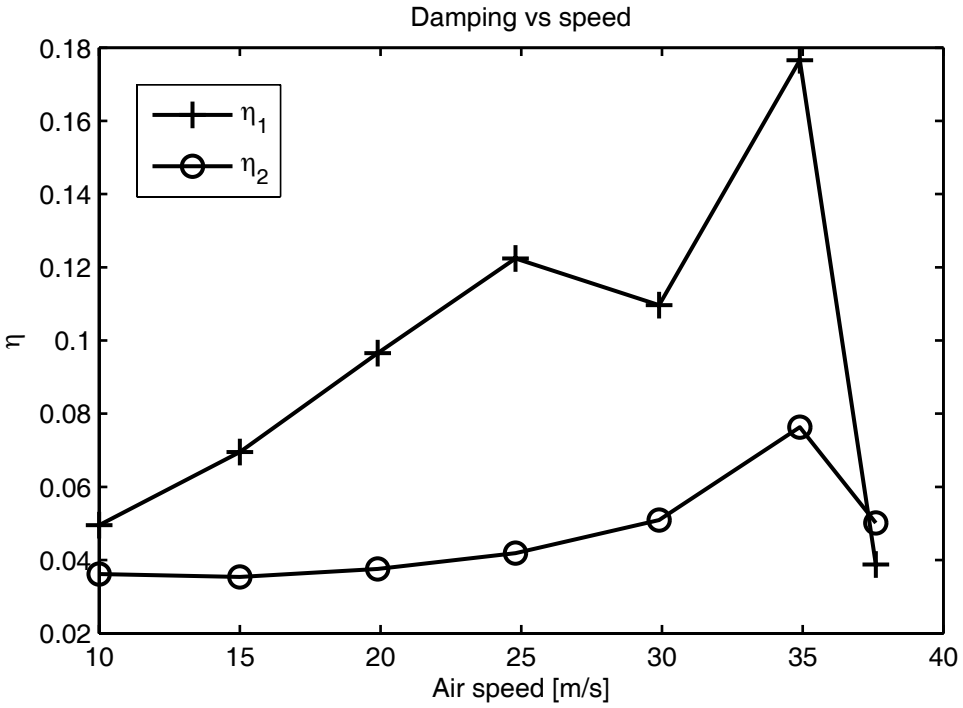

Figure 136. Damping versus speed graph.

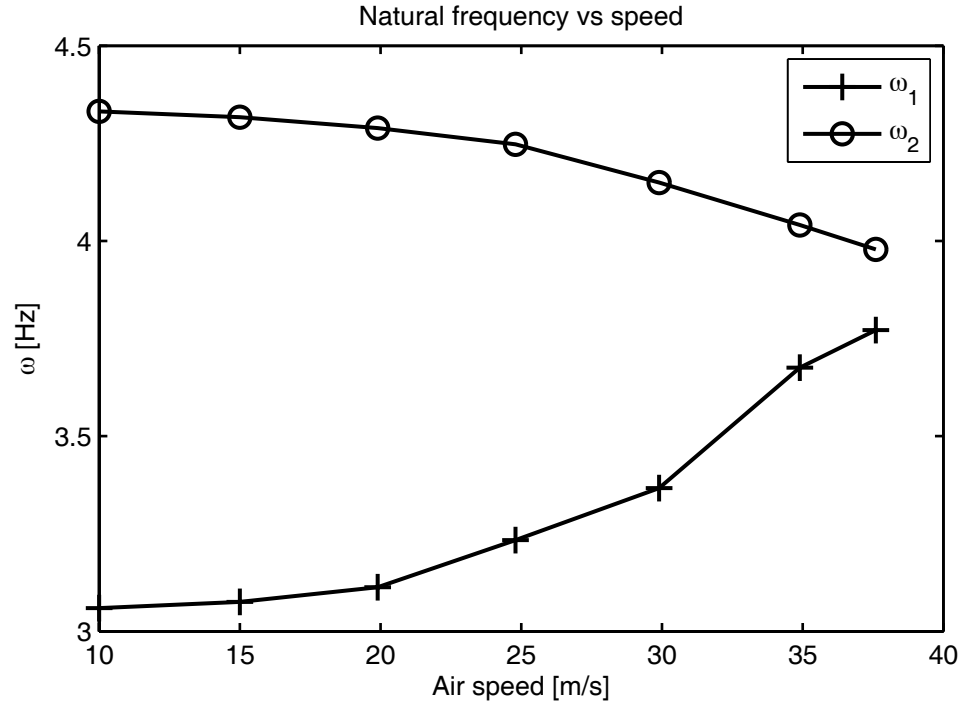

Figure 137. Natural frequency versus speed graph.

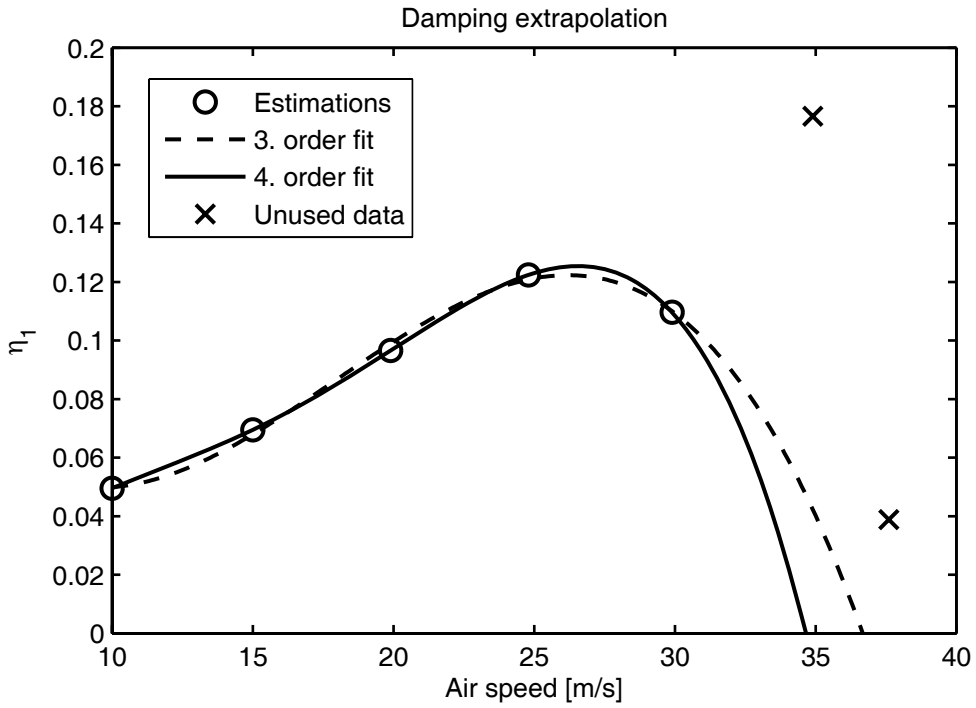

Figure 138. Damping extrapolation result with 5 data pairs.

The solution presented in Figure 138 is not acceptable, since further speed increments may mislead the test engineer. Thus, the damping extrapolation method is concluded to fail with the real ATS.

5.3.2 Flutter Prediction with Envelope Function

The response of the ATS to nearly impulsive excitations are available at each test point. The calculated envelopes are given in Figure 139. When the envelopes are compared with the simulated ATS's envelopes, which are given in Figure 80, the real decay rate of the system is observed to be much higher than the decay rate observed in the simulation results. This is an indication of higher damping. However, the behavior of the system is similar to the simulated one. The envelope at just below the flutter speed is still highly damped. The time limit is selected as 3 s, since envelopes vanish considerably in 3 s. The resulting shape parameter variations are given in Figure 140.

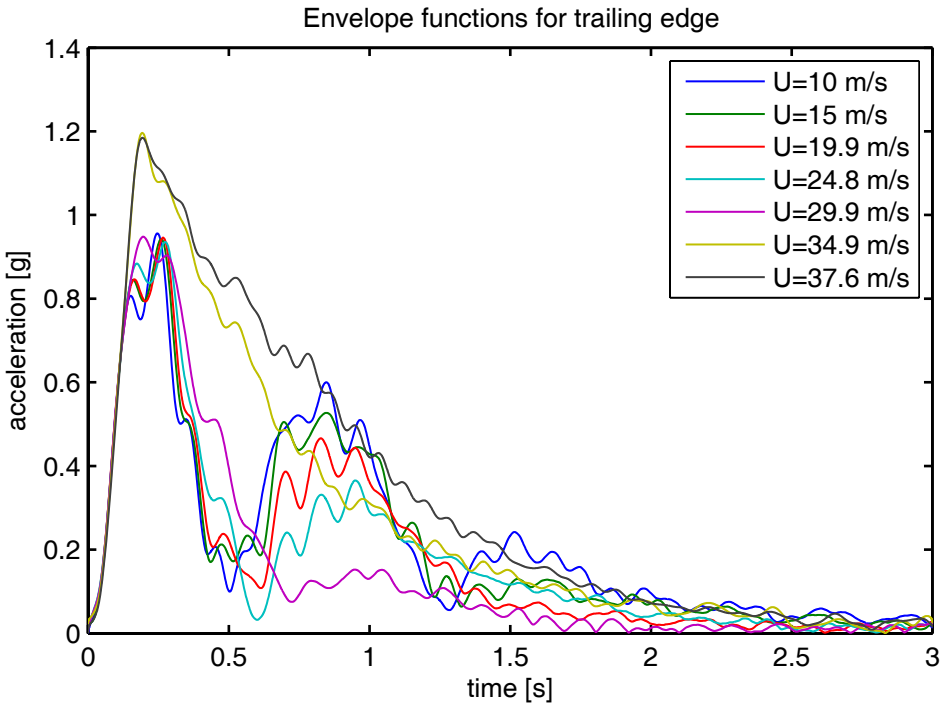

Figure 139. Envelope functions for trailing edge accelerometer.

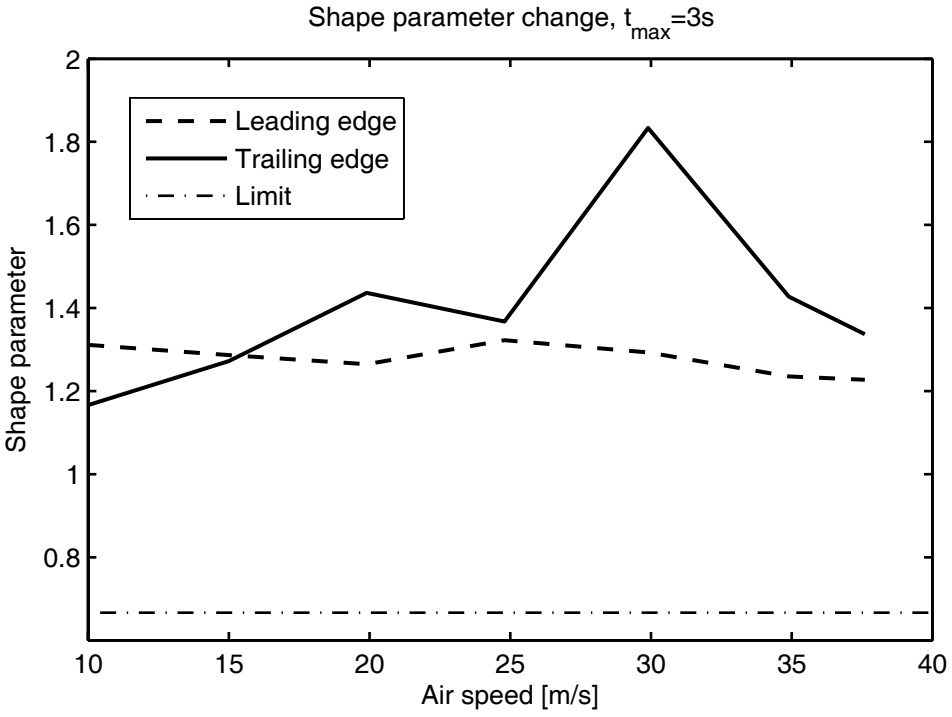

Figure 140. Variation of shape parameter with speed, t_{max}=3s.

It is not possible to estimate the flutter speed of real ATS with the envelope function method, similar to the simulated ATS case. The variation of the shape parameter is not smooth enough to perform curve fits. So the envelope function is concluded to fail with the real ATS.

5.3.3 Flutter Prediction with Flutter Margin

The flutter margin method is expected to be very successful with the real ATS results, similarly to the simulated ATS case. The extracted modal parameters given in Table 17 are used to calculate the flutter margin. The result is given in Figure 141. The damping scatter seen in damping extrapolation method is not observed with the flutter margin method as expected. The solution of the flutter speed with the first 5 data pairs results in a flutter speed of 36.1 m/s. This result is obtained by extrapolating the 1st order fit.

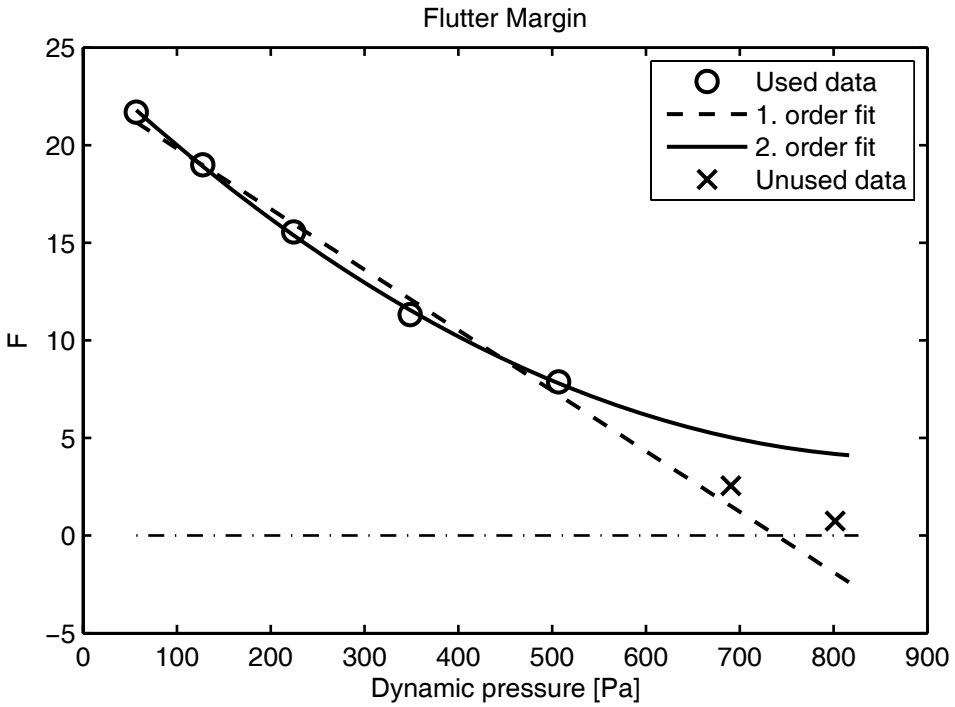

Figure 141. Flutter Margin fit for 5 data points.

When the data corresponding to 35 m/s air speed (6th data pair) is also used in the estimation procedure, the accuracy of the estimation improves further, as expected. The solution obtained when the first 6 data pairs are used is given in Figure 142. The flutter estimation is extrapolated as 36.7 m/s with the 1st order fit and 38.1 m/s with the 2nd order fit.

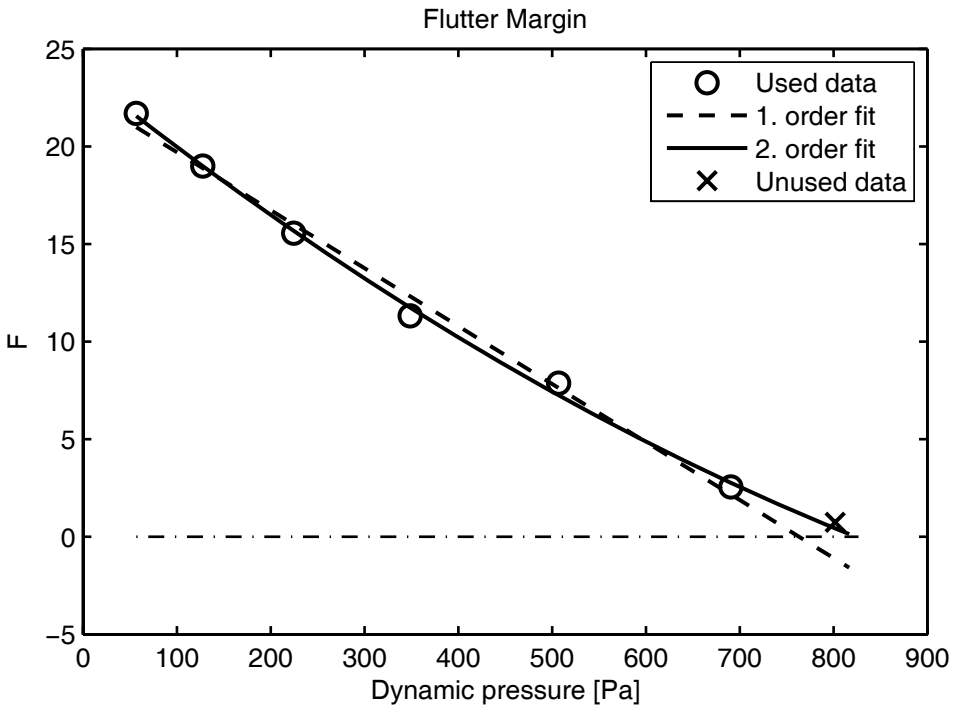

Figure 142. Flutter Margin fit for 6 data points.

The flutter speed estimation of the real ATS with the flutter margin method is selected as 36.1 m/s, which is obtained from the first 5 data point fit.

5.3.4 Flutter Prediction with ARMA Modeling

The discrete time ARMA modeling method assumes a random aerodynamic excitation on the aeroelastic structure. However, the flow in the wind tunnel's test room is always a high quality flow, that is nearly laminar flow. The friction also precludes the motion of the airfoil when forcing is small. The airfoil is observed to

remain stationary under flow when base excitation is not present. Therefore, it is not possible to perform a flutter estimation with the real ATS. However, the method is not expected to work with the real ATS as in simulated ATS case, because of the explosive flutter behavior.

5.3.5 Flutter Prediction with Flutterometer

The accelerometers of the ATS are mounted 50 mm inside the edges of the airfoil, because of geometrical limitations. Accelerometers are located inside blind holes drilled on the surface of the airfoil and covered with paste. The external contour of the airfoil is thus kept smooth. The thickness of the airfoil is sufficient at the accelerometer locations to permit such mounting. Thus, the trailing edge accelerometer is located 190 mm aft of the elastic axis. So, the acceleration of the trailing edge must be redefined as follows.

$$y = -h'' - 0.19\alpha'' = \begin{bmatrix} -1 & -0.19 \end{bmatrix} \begin{Bmatrix} h'' \\ \alpha'' \end{Bmatrix} = [T_1]\{\eta''\} \tag{5-1}$$

The mathematical model used with the flutterometer, which is called as the “nominal plant”, is a simulated ATS model. The comparison of the results obtained by using the nominal plant with the experimental results at various speeds are given in Figure 143 to Figure 146. As seen from the figures, the nominal plant represents the ATS well at low air speeds. As the air speed increases, the behavior of the nominal plant deviates from the actual dynamics of the ATS. Recall that in the flutterometer method this deviation is compensated by scaling the defined uncertainty description according to the experimental data. Each deviation from the nominal plant introduces a certain amount of conservatism to the method. For this reason, an accurate modeling is very important for this method as stated before.

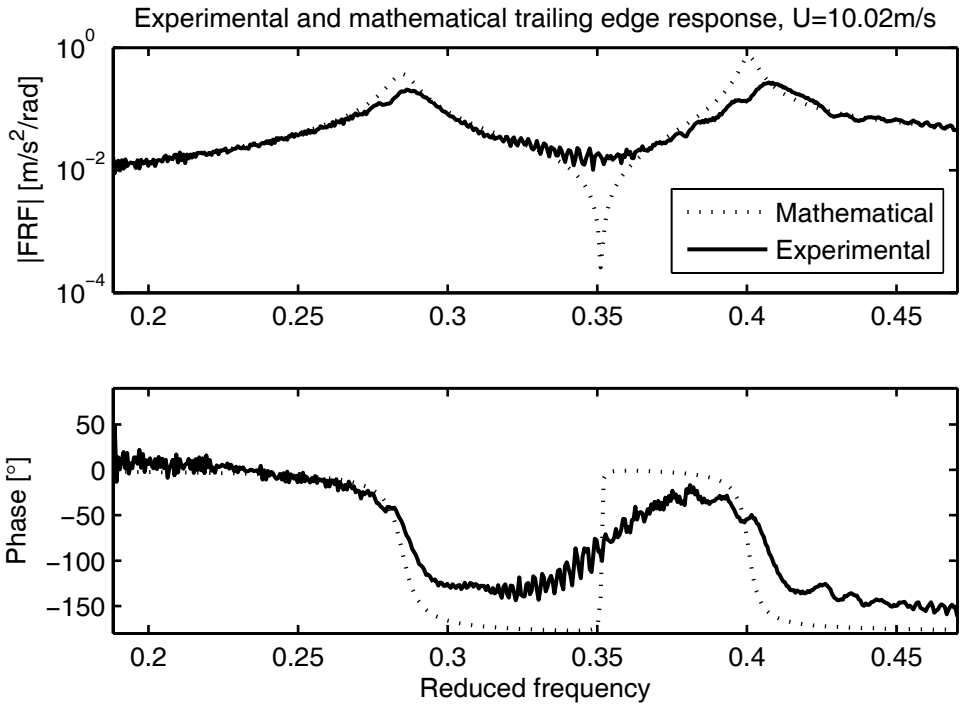

Figure 143. Nominal plant and ATS FRF at 10 m/s.

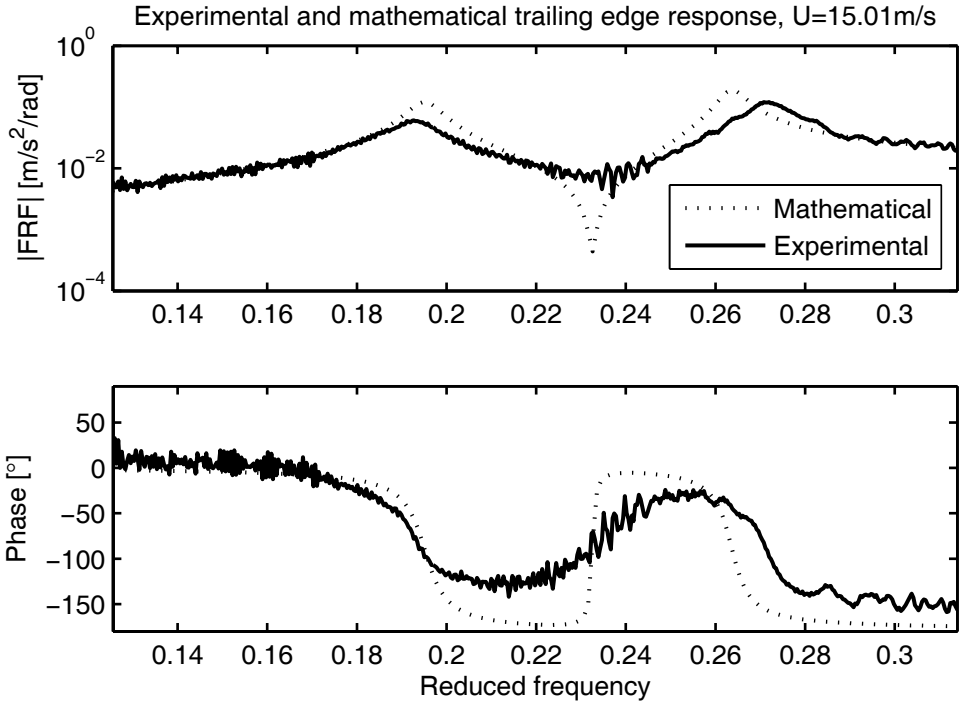

Figure 144. Nominal plant and ATS FRF at 15 m/s.

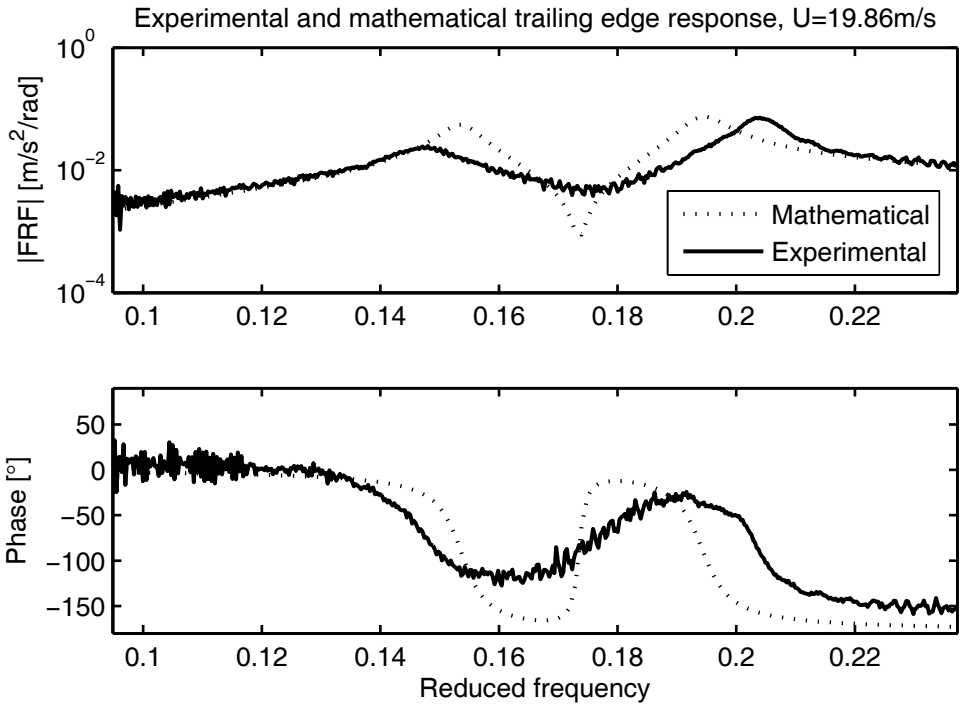

Figure 145. Nominal plant and ATS FRF at 19.9 m/s.

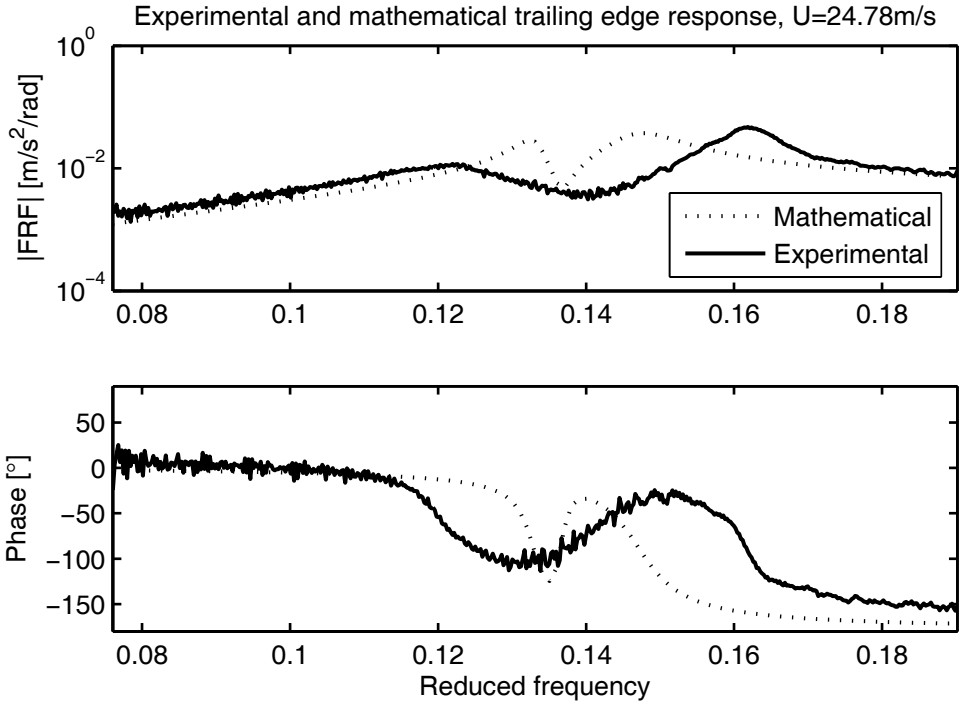

Figure 146. Nominal plant and ATS FRF at 24.8 m/s.

The uncertainties for the aerodynamic coefficients and for the stiffness matrix are defined as real parametric uncertainty. Flutter estimates are obtained at wind tunnel speeds of 10, 15, and 19.9 m/s. The necessary scaling of the uncertainty for 10 m/s is given in Figure 147. The validation norm, which is approximately 0.04 at 10 m/s wind tunnel speed, dictates that the uncertainty should be increased by a factor of 25. This corresponds to 25% uncertainty since base uncertainty is 1%. Recall that the uncertainty description for the ATS involves both aerodynamic coefficients and stiffness matrix. The stiffness properties of the ATS are determined experimentally. So, the increase in uncertainty is most probably due to aerodynamic coefficients. The predicted flutter speed at 10 m/s wind tunnel speed is 20.8 m/s. The robust flutter solution graph is given in Figure 148. Recall that the flutter speed is calculated by scaling down the dynamic pressure perturbation by the μ norm. If the μ norm is smaller than unity then the dynamic pressure perturbation is increased. Then the flutter speed is calculated from the corrected dynamic pressure.

Figure 149 shows the validation norm for wind tunnel speed of 15 m/s. The required uncertainty scaling is similar to the one obtained for 10 m/s wind tunnel speed. The robust flutter solution at this speed is given in Figure 150, which corresponds to a flutter speed of 21.5 m/s. Solutions for the wind tunnel speed of 19.9 m/s are given in Figure 151 and Figure 152, which corresponds to a flutter speed of 25.9 m/s.

Note that flutterometer estimates are all considerably below the flutter speed of the nominal plant. This is an expected result since each uncertainty and deviation from the nominal plant further decrease the flutter speed of the robust plant. For this reason, the conservatism of the method does not decrease as the speed approaches the flutter speed. A certain amount of conservatism is necessary for a safe flutter flight test, but the test time should also be minimized. In any case, an accurate mathematical model is required by the flutterometer method for an effective testing.

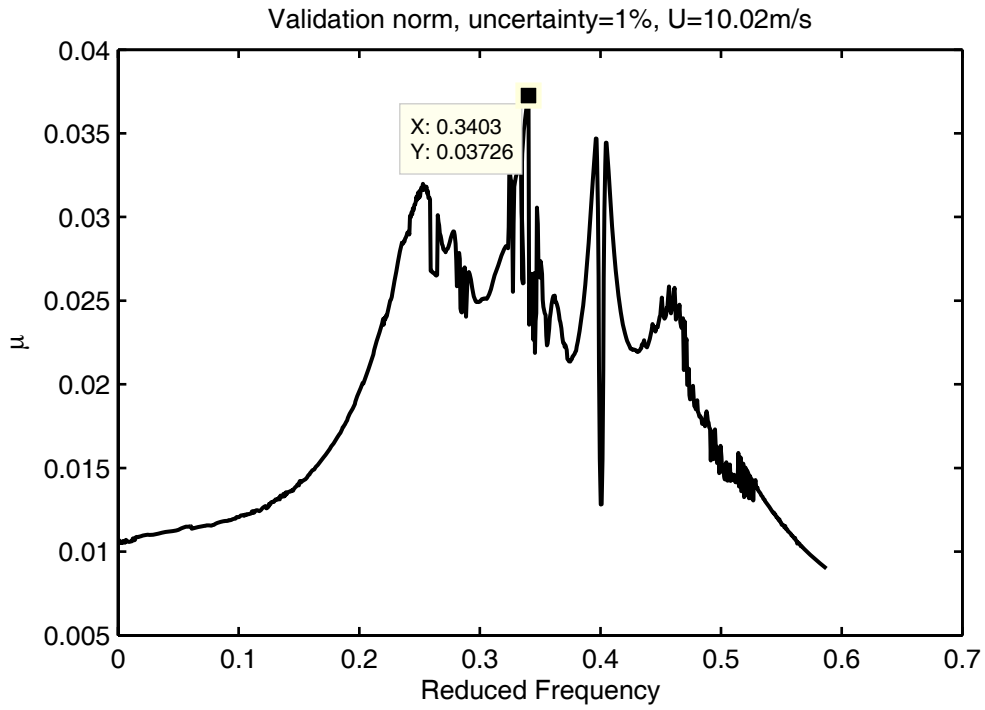

Figure 147. Validation norm, uncertainty=1%, U=10m/s.

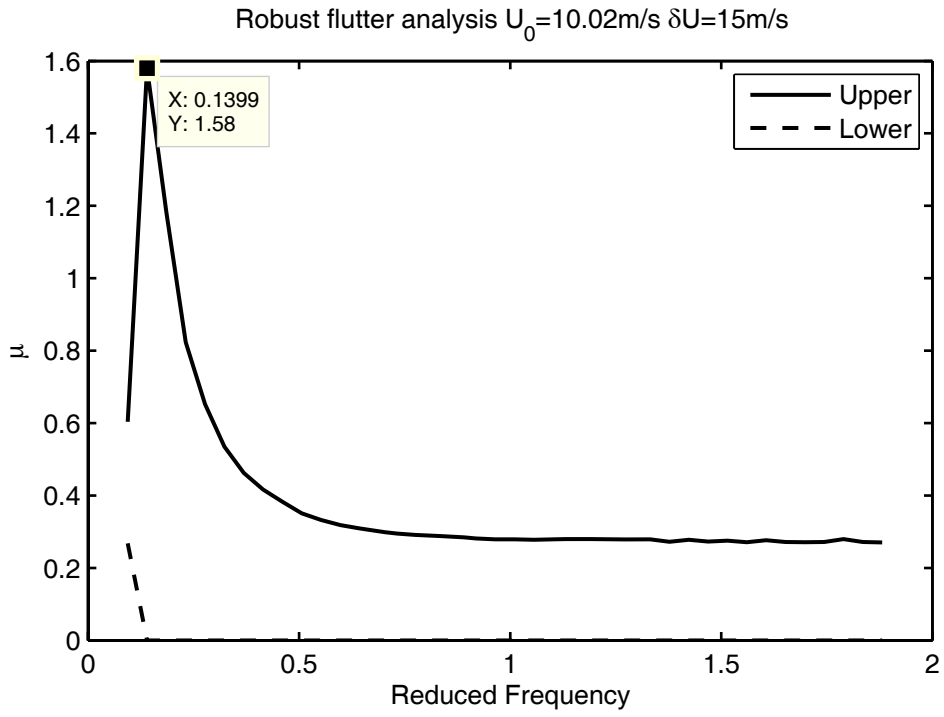

Figure 148. Flutterometer result for U=10m/s.

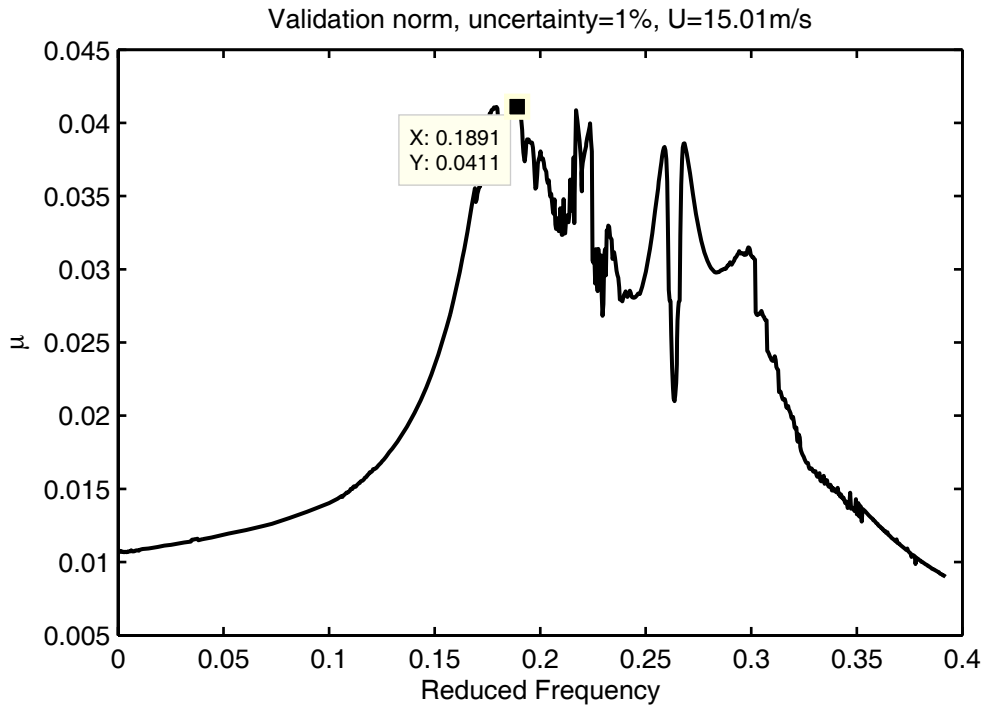

Figure 149. Validation norm, uncertainty=1%, U=15m/s.

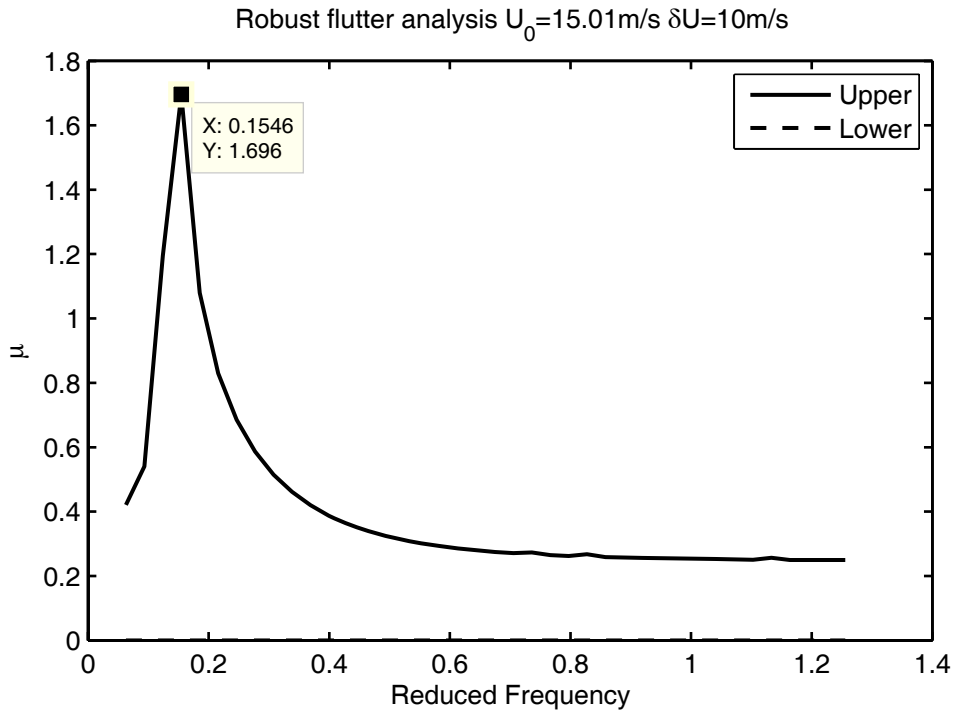

Figure 150. Flutterometer result for U=15m/s.

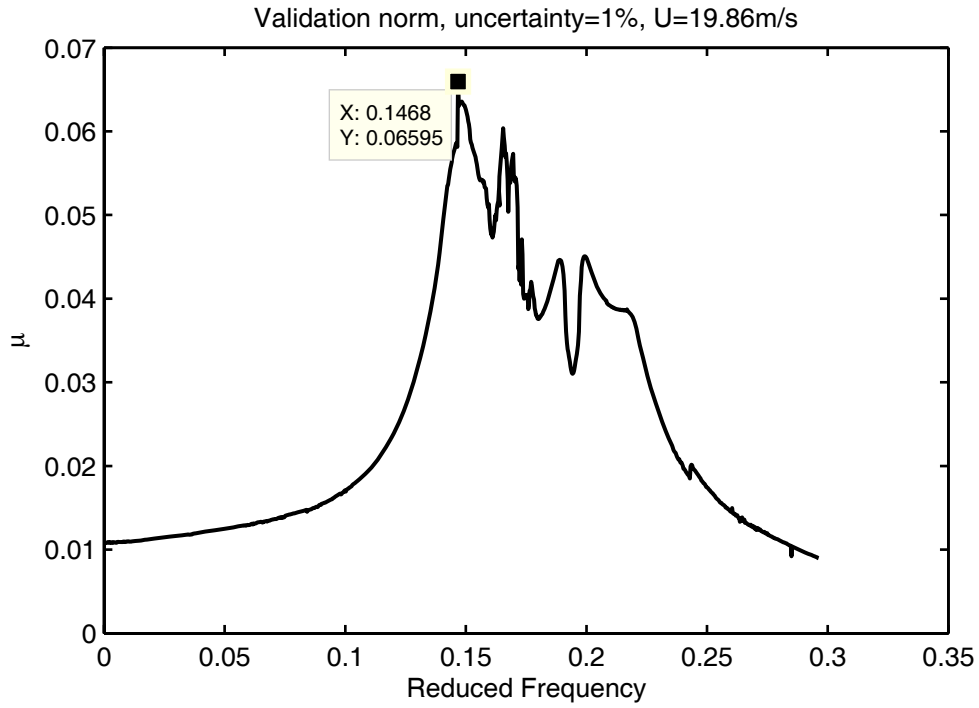

Figure 151. Validation norm, uncertainty=1%, U=19.9m/s.

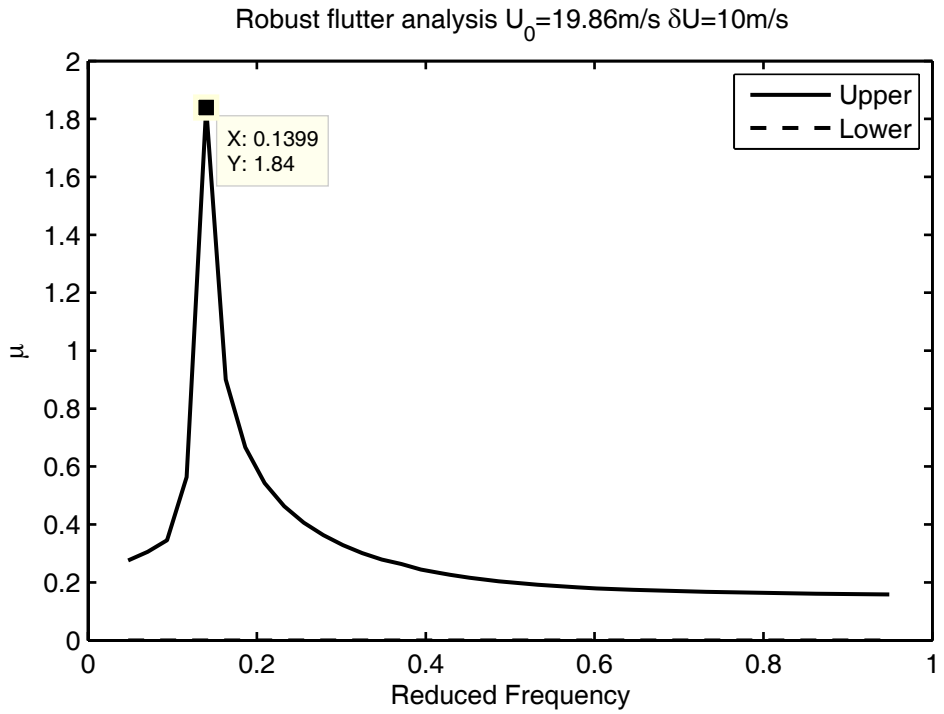

Figure 152. Flutterometer result for U=19.9m/s.

5.4 Summary

The experiments show that the data based methods, except the flutter margin method, are not effective when the test structure has an explosive type flutter instability. It is demonstrated that the flutter margin method accurately estimates the flutter speed despite the increasing damping trend prior to flutter. It is proven again that the damping alone is not a good indicator of stability for such systems. The flutterometer, as a model based method, is able to estimate a flutter speed, but the estimated speeds are extremely conservative. It is possible to model the unsteady aerodynamics more accurately with the doublet-lattice methods for finite wings. Such a modeling would decrease the conservatism of the method and estimations with less error could be performed. A summary of the results is presented in Table 18.

Table 18. Comparison of methods for the real ATS.

Method	Best estimate [m/s]	Flight Conditions [m/s]	Error [%]
Damping Extrapolation	No solution	--	--
Envelope Function	No solution	--	--
Flutter Margin	36.1	10, 15, 19.9, 24.8, 29.9	-9.8
ARMA	Not applicable	--	--
Flutterometer	25.9	19.9	-35.4

The results may seem to be discouraging, since only two of the methods work properly. However, the real aeroelastic systems usually experience mild flutter and not explosive flutter. Recall that all methods successfully estimate the flutter speed in the simulated mild flutter case.

For aircraft structures with linear behavior, it is generally possible to generate accurate structural models with the ground vibration test data of the aircraft. Generally, doublet-lattice codes are used to generate the aerodynamic data for flutter analysis, but it is not easy to verify the aerodynamic data with the wind tunnel tests. The conservatism of flutterometer method would decrease considerably when accurate aeroelastic models are obtained.

CHAPTER 6

SUMMARY AND CONCLUSIONS

6.1 Summary

There is an increasing demand on certifying new external stores or onboard equipment to aircraft. The flutter flight test is one of the most important certification tests. It has not only some serious safety issues but also it involves a huge amount of preliminary work that must be performed for an effective testing. The flutter flight test also requires some serious human intervention. The test engineer should have experience on system dynamics, system identification, aeroelasticity, modal testing, data acquisition, digital signal processing and mission critical programming.

The aim of this study is to gain a theoretical and practical background on some of these engineering fields from the flutter flight test point of view. The study mainly focuses on the flutter estimation methods, which is the core for all flutter flight tests. An extensive literature survey on the flutter estimation methods is performed. Most commonly used methods are investigated in detail. The mathematical theory behind these methods are investigated and implemented on computer. The effectiveness of these methods are theoretically and practically studied. Some improvement issues that are pointed out by the aeroelasticity community such as modal filters and singular value decomposition are also investigated in the study.

The methods are extended to nonlinear aeroelastic systems. Effect of nonlinearities on flutter estimation is investigated. Wavelet and Volterra series approaches are utilized in processing of measurement signals. Severe nonlinearity cases, which can

cause limit cycle oscillations are not well studied in literature. Some aircraft are known to exhibit limit cycle oscillations with some external store combinations. Wavelets are successfully utilized to predict speeds at which such limit cycle oscillations can occur. An automation procedure is developed for the prediction of LCOs. Volterra series approach is successfully utilized to filter out the nonlinear components of the response signals. The filtered responses are used to predict flutter speed with less conservatism.

The methods presented in the study are first implemented, then demonstrated with simulations, and are further investigated by conducting some wind tunnel tests for practical demonstrations.

6.2 Conclusions and Contributions

The main conclusion derived from this study is that, there is no perfect method that can be used for flutter prediction with all kinds of aeroelastic systems. Each method has some advantages and drawbacks that must be considered during the planning of flight tests.

The damping extrapolation method, as the oldest method, is still widely used in the aeroelasticity community. The method evolved from the logarithmic decrement calculations to some complex modal identification techniques as the computational resources developed. However, the method still depends on the most spectacular parameter of a structure, the damping, which is very difficult to measure accurately. The method does not have a standard modal extraction procedure. Any modal analysis tool can be used with the method. There exist very sophisticated modal analysis methods. However, it is not always possible to apply these methods on a flying aircraft because of the low signal to noise ratio of measurements, insufficient number of measurements and limited test time. A simple modal analysis method should be selected that requires a minimum human intervention. It is seen that the

method works well if the structure does not experience any explosive flutter and the scatter on damping is low.

The envelope function method was originally proposed as an auxiliary tool. The method calculates the overall damping trend of the system extremely fast. However, effectiveness of this method depends on the same conditions that are stated for the damping extrapolation method. It is a very easy to implement envelope function tool, so it can be monitored in any test.

The flutter margin is a valuable method, not only because of its easy implementation but also because of its approach to solve the problem. This method uses the roots of the system to monitor the overall stability of the system. The method considers both damping and natural frequencies of the system. Thus, in contrast to the damping extrapolation and envelope function methods, it is not affected by damping scatter. If the number of modes that are related to flutter mechanism is two, then the method results in very accurate flutter estimates even at low speeds. It is seen that the method is not affected by the type of flutter mechanism. The decrease in the overall stability of the system as speed increases can be monitored clearly even in the explosive flutter case.

The discrete time ARMA modeling uses a similar approach to the flutter margin method, but it employs discrete time models. The applicability of the method depends on the existence of turbulence and the number of modes that interact. It is not always possible to obtain turbulent flow around the test area. The excitation due to turbulence should be high enough to distinguish response data from noise. It is seen that the method converges to improper roots if the measurement data is not filtered accordingly. The calculated roots of the system should be checked at each run to ensure that complex conjugate poles are obtained.

The flutterometer is a recent method that utilizes the concept of robust control. The method uses both mathematical models and flight data. The effectiveness of the

method depends on the accuracy of the mathematical model. The method is able to predict a flutter speed even in the case of an inaccurate mathematical model or in the presence of nonlinearities. However, the conservatism of the method in that case may result in flutter speeds that are short of any practical use.

Contributions to the Literature

There are several contributions to the literature within the study. They are listed below.

- Modal filters are proposed by senior aeroelasticians to improve the quality of modal extraction. However, their practical use in flight testing is not reported in the literature. The method is usually used in ground testing and control of elastic systems. The modal filters can be constructed with the modal parameters extracted in ground vibration tests. It is not feasible to construct modal filters during flight since modal data is required to construct the filters. Once the modal analysis is performed, a flutter prediction can be performed without the need of modal filters. However, if the modal filter is available, then the modal extraction procedure becomes very easy and damping can be estimated more accurately. If the mode shapes of the vehicle do not change considerably during flight, then the modal filter constructed from ground vibration data can be used to decouple the modes. However it is observed that mode shapes of the aeroelastic system change considerably as the speed changes. Aerodynamic damping affects the complex valued mode shapes of the structure, and the phase difference between the modes change as the speed changes. Modal filters constructed at zero speed fail to decouple the frequency response functions as speed increases. So the method is concluded to be useless with flutter flight test.

- An important behavior of the envelope function method is observed, which is not stated in the literature. It is observed that at speeds close to the flutter speed, the envelopes show a characteristic change after the impulse input and this change

improves the estimate as the time limit is decreased. This behavior is not observed in explosive flutter cases up to speeds that are very close to the flutter speed. The behavior could not be generalized, but is considered to be likely to occur in mild flutter cases. In such cases, the envelope function becomes very useful. This behavior should be searched during flight tests, since very reliable flutter estimates can be performed with this simple method.

- The flutterometer method is commonly used with dimensional time domain mathematical models. However, the unsteady aerodynamic coefficients are Mach and reduced frequency dependent. The original work by Lind converts the parameters defined in reduced frequency domain to dimensional frequency domain. This introduces some explicit speed terms in the equation of motion, besides the dynamic pressure terms. The perturbation to dynamic pressure is applied to search for stability. However, the speed is kept constant during this perturbation, which implies a change in the air density. When the density changes, the Mach number changes. A Mach number change requires updates in the aerodynamic coefficients. So an iterative procedure must be used with the original method increasing the computational load of the method, which is already high. In this study, a different equation of motion formulation based on nondimensional time and reduced frequency is developed. The resulting equations of motion for the typical section is such that the speed terms are all grouped in dynamic pressure terms, thus eliminating the need for an iterative solution.

- Another contribution to the literature is the application of wavelet technique to the limit cycle prediction in the presence of backlash type nonlinearity. The technique is successfully utilized herein with severe backlash type nonlinearity. It is found that the prediction function derivation is problem dependent. Finally, the processing of wavelets are also automated in this study with the use of Hilbert transform.

6.3 Recommended Future Work

Two future areas are pointed out in the study, which have the potential of improving the flutterometer method further. The first one is about the dynamic pressure perturbation used in the flutterometer method for stability search. Although a structure of the uncertainty matrix is considered in the μ analysis, the deviations are assumed to be symmetric. A symmetric deviation in the dynamic pressure is not required in the flutter prediction. Such symmetric deviations can cause some negative dynamic pressures at low speeds. If the system is unstable at these negative dynamic pressures, which is physically not meaningful but mathematically possible, the method inherently accounts for the physically meaningless instabilities. In case of aeroservoelastic analysis, the lower bound of the dynamic pressure should be checked. However, for aeroelastic cases, the lower bound of dynamic pressure is not important. It is known that the system is always stable below the critical flutter speed. A new μ calculation procedure can be implemented for aeroelastic cases, where the dynamic pressure is perturbed towards the upper bound. Another improvement area is in the scaling of the uncertainty matrix. The current implementation of the flutterometer method scales the entire uncertainty matrix. This increases the conservatism further. Each element of the uncertainty matrix can be scaled optimally such that the model is not invalidated by the measured data. An optimally scaled uncertainty would have less effect on the nominal model so that less conservative estimates can be obtained. However, the optimal scaling of the uncertainty matrix can be computationally very expensive. The computation time should also be considered if such a potential improvement is undertaken.

There exists several sophisticated system identification methods such as “eigensystem realization algorithms” (ERA), the “eigensystem realization algorithm with data correlation” (ERA/DC), and the “instrumental variables output error method” (IV/OEM), which are also used in the aeroelasticity community to predict the flutter speed. The ERA methods use the time domain data, where as the IV/OEM uses the frequency domain data to identify the system. Application of these methods

to aeroelastic systems is demonstrated in the literature, but the application of these methods can be investigated and improved further for more accurate to flutter predictions.

The “operational modal analysis” (OMA) is a developing area, which attract the attention of the modal analysis community. The methods developed for OMA can be used to identify the system where the excitation is not known, as in the ARMA method.

The system identification methods that are recommended above and investigated in this study and are still used to predict the modal parameters of the system. Once the modal properties of the system are determined accurately the damping extrapolation method is used to predict the flutter speed. However it is seen that damping is not a proper indicator of stability. If it were possible to derive a single stability parameter from all modal parameters of the system, then that stability parameter would be the perfect indicator for the flutter prediction. The flutter margin and ARMA methods use such stability parameters but only by using the two modes of the system. The flutterometer method uses a single stability parameter considering all modes of the system but requires a nominal mathematical model. So an effort on deriving such a single stability parameter is strongly recommended

REFERENCES

1. Bisplinghoff, R. L., Ashley, H., and Halfman, R. L., Aeroelasticity, Dover Publications, New York, 1996.

2. Fung, Y. C., An Introduction to the Theory of Aeroelasticity, Dover Publications, New York, 1993.

3. Kehoe, M. W., A Historical Overview of Flight Flutter Testing, NASA Technical Memorandum 4720, October 1995.

4. Cooper, J.E., Parameter Estimation Methods for Flight Flutter Testing, AGARD CP-566, Paper No 10, 1995.

5. Brenner, M.J., Lind, R.C., Voracek, D.F., Overview of Recent Flight Flutter Testing Research at NASA Dryden, NASA TM-4792, 1997.

6. Cooper, J.E., Towards Faster and Safer Flight Flutter Testing, RTO-MP-089, Paper No 43, 2002.

7. Cooper, J.E., Desforges M.J., Emmet P.R., Wright J.R., Advances in the Analysis of Flight Flutter Test Data, AGARD CP-566, Paper No 13, 1995.

8. Dimitriadis, G., Cooper, J.E, Flutter Prediction from Flight Flutter Test Data, Journal of Aircraft, Vol. 38, No. 2, pp. 355-367, 2001.

9. Kehoe, M.W., Aircraft Flight Flutter Testing at the NASA Ames-Dryden Flight Research Facility, NASA TM-100417, 1988.

10. Ramsay, R.B., Flight Flutter Testing of Combat Aircraft, AGARD CP-566, Paper No 18, 1995.

11. Lind, R., Brenner, M., Flight Test Evaluation of Flutter Prediction Methods, AIAA Paper 2002-1649, 2002.

12. Lind, R., Flight Test Evaluation of Flutter Prediction Methods, Journal of Aircraft, Vol. 40, No. 5, pp. 964-970, 2003.

13. Cooper, J.E., Emmett, P.R., Wright, J.R., Schofield, M.J., Envelope Function: A Tool for Analyzing Flutter Data, Journal of Aircraft, Vol. 30, No. 5, pp. 785-790, 1993.

14. Zimmerman, N.H., Weissenburger, J.T., Prediction of Flutter Onset Speed Based on Flight Testing at Subcritical Speeds, Journal of Aircraft, Vol. 1, No. 4, pp. 190-202, 1964.

15. Torii, H., Matsuzaki, Y., Flutter Margin Evaluation for Discrete Time Systems, Journal of Aircraft, Vol. 38, No. 1, pp. 42-47, 2001.

16. Lind, R., Brenner, M., Flutterometer: An On Line Tool to Predict Robust Flutter Margins, Journal of Aircraft, Vol. 37, No. 6, pp. 1105-1112, 2000.

17. Lind, R., Flight Testing with the Flutterometer, Journal of Aircraft, Vol. 40, No. 3, pp. 574-970, 2003.

18. Lind, R., Brenner, M., Robust Flutter Margin Analysis That Incorporates Flight Data, NASA/TP-1998-206543.

19. Lind, R., Brenner, M., Incorporating Flight Data into a Robust Aeroelastic Model, Journal of Aircraft, Vol. 35, No. 3, pp. 470-477, 1998.

20. Lind, R., Brenner, M., Robust Flutter Margins of an F/A-18 Aircraft from Aeroelastic Flight Data, Journal of Aircraft, Vol. 20, No. 3, pp. 597-604, 1997.

21. Ewins, D.J., Modal Testing: Theory, Practice and Application, Research Studies Press Ltd., Baldock, Hertfordshire, England, 2000.

22. Koenig K., Flight Vibration Test Analysis-Methods, Theory and Application, AIAA Paper 1983-2752, 1983.

23. Flutter Testing Techniques, NASA SP-415, 1975.

24. Bennett, R.M., Abel, I., Application of a Flight Test and Data Analysis Technique to Flutter of a Drone Aircraft, AIAA Paper 1981-0652, pp. 811-820, 1981.

25. Smith, W.R., Least-Squares Time-Domain Method for Simultaneous Identification of Vibration Parameters from Multiple Free-Response Records, AIAA Paper 1991-0530, pp. 194-201, 1981.

26. Nissim, E., Gilyard, G.B., Method for Experimental Determination of Flutter Speed by Parameter Identification, AIAA Paper 1989-1324-CP, pp. 1427-1441, 1989.

27. Van der Auwerear, H., Guillaume, P., A Maximum Likelihood Parameter Estimation Technique to Analyse Multiple Input/Multiple Output Flutter Test Data, AGARD CP-566, Paper No 12, 1995.

28. Shelly, S.J., Freudinger, L.C., Allemang R.J., Development of an Online Parameter Estimation System Using the Discrete Modal Filter, Proceedings of the 10th IMAC, 1992.

29. Price, S.J., Lee, B.H.K., Development and Analysis of Flight Flutter Prediction Methods, AIAA Paper 1992-2101-CP, pp. 188-200, 1992.

30. Price, S.J., Lee, B.H.K., Evaluation and Extension of the Flutter-Margin Method for Flight Flutter Prediction, Journal of Aircraft, Vol. 30, No. 3, pp. 395-402, 1993.

31. Lind, R., Flight-Test Evaluation of Flutter Prediction Methods, Journal of Aircraft, Vol. 40, No. 5, pp. 964-970, 2003.

32. Matsuzaki, Y., Ando, Y., Estimation of Flutter Boundary from Random Responses Due to Turbulence at Subcritical Speeds, Journal of Aircraft, Vol. 18, No. 10, pp. 862-868, 1981.

33. Torii, H., Matsuzaki, Y., Flutter Boundary Prediction Based on Nonstationary Data Measurement, AIAA Paper 1995-1487-CP, pp. 3012-3018, 1995.

34. Torii, H., Matsuzaki, Y., Flutter Boundary Prediction Based on Nonstationary Data Measurement, Journal of Aircraft, Vol. 34, No. 3, pp. 427-432, 1997.

35. Torii, H., Matsuzaki, Y., Flutter Margin Evaluation in Discrete-Time System, AIAA Paper 1998-1724, pp. 229-236, 1998.

36. Torii, H., Matsuzaki, Y., Application of a New Aeroelastic Stability Criterion for Real-Time Flutter Prediction, AIAA Paper 1999-1351, pp. 1314-1320, 1999.

37. Lind, R., Brenner, M., Robust Flutter Margins of an F/A-18 Aircraft from Aeroelastic Flight Data, Journal of Guidance, Control, and Dynamics, Vol. 20, No. 3, pp. 597-604, 1997.

38. Lind, R., Brenner, M., Worst-Case Flutter Margins from F/A-18 Aircraft Aeroelastic Data, AIAA Paper 1997-1266, pp. 738-748, 1997.

39. Lind, R., Brenner, M., Utilizing Flight Data to Update Aeroelastic Stability Estimates, AIAA Paper 1997-3714, pp. 605-614, 1997.

40. Lind, R.C., A Presentation on Robust Flutter Margin Analysis and a Flutterometer, NASA TM-206220, 1997.

41. Lind, R., Flight Testing with the Flutterometer, AIAA Paper 2001-1654, 2001.

42. Potter, S., Lind, R., Developing Uncertainty Models for Robust Flutter Analysis Using Ground Vibration Test Data, AIAA Paper 2001-1585, 2001.

43. Karpel, M., Design for Active Flutter Suppression and Gust Alleviation Using State Space Aeroelastic Modeling, Journal of Aircraft, Vol. 19, No. 3, pp. 221-227, 1982.

44. Berman, A., Nagy, E. J., Improvement of a Large Analytic Model Using Test Data, AIAA Journal, Vol. 21, No. 8, pp. 1168-1173, 1983.

45. Kumar, A., Balas, G.J., An Approach to Model Validation in the mu Framework, Proceedings of the American Control Conference, Baltimore, Maryland, June 1994, pp. 3021-3026.

46. Meijer, J.J., Cunningham, A.M., Understanding and Development of a Prediction Method of Transonic Limit Cycle Oscillation Characteristics of Fighter Aircraft, AIAA Paper 1992-4501-CP, pp. 446-457, 1992.

47. Dawson, K.S., Maxwell, D.L., Limit Cycle Oscillation Flight Test Results for Asymmetric Store Configurations, AIAA Paper 2003-1427, 44th AIAA/ASME/ASCE/ AHS Structures, Structural Dynamics, and Materials Conference, Norfolk, Virginia, 7-10 April 2003.

48. Kerschen, G., Worden, K., Vakakis A. F., Golinval J. C., Past Present and Future of Nonlinear System Identification in Structural Dynamics, Mechanical Systems and Signal Processing, No. 20, pp. 505-592, 2006.

49. Brenner, M., Wavelet Analyses of F/A-18 Aeroelastic and Aeroservoelastic Flight Test Data, NASA Technical Memorandum 4793, 1997.

50. Brenner, M., Nonstationary Dynamics Data Analysis with Wavelet-SVD Filtering, AIAA Paper 2001-1586, 42nd AIAA/ASME/ASCE/AHS/ASC Structures, Structural Dynamics, and Materials Conference and Exhibit, Seattle, WA, 16-19 April 2001.

51. Brenner, M., Lind, R., Wavelet-Processed Flight Data for Robust Aeroservoelastic Stability Margins, Journal of Guidance, Control, and Dynamics, Vol. 21, No. 6, pp. 823-829, 1998.

52. Brenner, M., Lind, R., On-Line Robust Modal Stability Prediction using Wavelet Processing, NASA TM-1998-206550, 1998.

53. Freudinger, L.C., Lind, R., Brenner, M.J., Correlation Filtering of Modal Dynamics Using the Laplace Wavelet, Proceedings of the 16th International Modal Analysis Conference, Vol. 2, pp. 868-877, February 1998.

54. Johnson, J.D., Lu, J., Dhawan, A.P., Lind, R., Real-Time Identification of Flutter Boundaries Using the Discrete Wavelet Transform, Journal of Guidance, Control, and Dynamics, Vol. 25, No. 2, pp. 334-339, 2002.

55. Lind, R., Snyder, K., Brenner, M., Investigating Transient and Limit Cycle Behaviors of a Nonlinear Structure by Wavelet Transform, AIAA Paper 1998-1808.

56. Lind, R., Snyder, K., Brenner, M., Wavelet Analysis to Characterize Non-Linearities and Predict Limit Cycles of an Aeroelastic System, Mechanical Systems and Signal Processing Vol. 15, No. 2, pp. 337-356, 2001.

57. Prazenica, R.J., Lind, R., Kurdila, A.J., Uncertainty Estimation From Volterra Kernels for Robust Flutter Analysis, AIAA Paper 2002-1650, 43rd AIAA/ASME/ASCE/AHS/ASC Structures, Structural Dynamics, and Materials Conference, Denver, Colorado, 22-25 April 2002.

58. Prazenica, R J., Lind, R., Kurdila, A.J., Uncertainty Estimation From Volterra Kernels for Robust Flutter Analysis, Journal of Guidance, Control, and Dynamics, Vol. 26, No. 2, pp. 331-339, 2003.

59. Lind, R., Prazenica, R.J., Brenner, M.J., Baldelli, D.H., Identififying Parameter-Dependent Volterra Kernels to Predict Aeroelastic Instabilities, AIAA Paper 2004-1517, 45th AIAA/ASME/ASCE/AHS/ASC Structures, Structural Dynamics & Materials Conference, Palm Springs, California, 19-22 April 2004.

60. Lind, R., Prazenica, R J., Brenner, M.J., Baldelli, D.H., Identififying Parameter-Dependent Volterra Kernels to Predict Aeroelastic Instabilities, AIAA Journal, Vol. 43, No. 12, December 2005.

61. Lind, R., Prazenica, R.J., Brenner, M.J., Estimating Nonlinearity Using Volterra Kernels in Feedback with Linear Models, Nonlinear Dynamics, No. 39, pp. 3-23, 2005.

62. Marzocca, P., Librescu, L., Volterra Series Approach For Nonlinear Aeroelastic Response of 2-D Lifting Surfaces, AIAA Paper 2001-1459, 2001.

63. Zhang, P., Song, Y., Discrete Frequency-Domain Modeling and Measuring of Mildly Nonlinear Volterra Transfer Functions with a Set of Special Sinusoid Signals, IEEE Pacific Rim Conference on Communications, Computers and Signal Processing, June 1st-2nd, 1989.

64. Boyd, S., Tang, Y.S., Chua, L., Measuring Volterra Kernels, IEEE Transactions on Circuits and Systems, Vol. 30, No. 8, August 1983.

65. Németh, J.G., Kollár, I., Schoukens, J., Identification of Volterra Kernels Using Interpolation, IEEE Transactions on Instrumentation and Measurement, Vol. 51, No. 4, pp. 770-775, August 2002.

66. Rugh, W.J., Nonlinear System Theory – The Volterra/Wiener Approach, The Johns Hopkins University Press, 1981, ISBN O-8018-2549-0.

67. Ünal, S.U., Design, Construction and Preliminary Testing of an Aeroservoelastic Test Apparatus to be Used in Ankara Wind Tunnel, Master Thesis, METU, Ankara, Turkey, 2005.

68. Brenner, M.J., Aeroservoelastic Model Uncertainty Bound Estimation from Flight Data, Journal of Guidance, Control, and Dynamics, Vol. 25, No. 4, pp. 748-754, 2002.

69. Lind, R., Mortagua, J.P, Reducing Conservatism in Flutterometer Predictions Using Volterra Modeling with Modal Parameter Estimation, Journal of Aircraft, Vol. 42, No. 4, pp. 998-1004, 2005.

Appendix A

Lift and Moment on A Typical Section for Incompressible Flow

Incompressible flow is the simplest flow type to analyze among all flow regimes. It has been well studied for years and some closed form expressions are available for both steady and unsteady cases.

A 1 Steady Flow

Steady lift and moment for thin airfoils per unit span are given as [1]

$$L = 2\pi\rho U^2 b\alpha \tag{A-1}$$

$$M_y = -L\left(ba + \tfrac{1}{2}b\right) \tag{A-2}$$

These expressions are linear in angle of attack, α. When α becomes too large, the flow starts to separate from the airfoil and the lift decreases. These expressions can be safely used for angle of attack values within the range of ± 15 degrees.

Equation A-2 implies that the aerodynamic center (zero hinge moment) at steady state is at the quarter-chord point (a = - ½).

A 2 Unsteady Flow

Calculating the unsteady forces on an oscillating airfoil is a difficult task. The complete motion of the airfoil must be known in every direction in order to be able to calculate the forces. Harmonically oscillating airfoils have a special advantage in calculating the unsteady forces. Since their motion is harmonic, their motion history is fully described. Position, velocity and acceleration information is available at any required time since the motion repeats itself continuously. By solving the potential flow equations with harmonically oscillating boundary conditions, the analytical expressions for lift and moment can be found for harmonically oscillating thin airfoils. These expressions will be in the frequency domain. To find the forces for an arbitrary motion, one can convert these frequency domain expressions to time domain expressions by inverse Fourier transformation.

A 3 Harmonic Motion

Unsteady force expressions contain the phase lag information. In the frequency domain, the phase lag is expressed by complex quantities. Therefore, lift and moment expressions become complex quantities. The complex lift and moment equations for an oscillating airfoil are given as follows [1].

$$L = \pi\rho b^2 l\left[\ddot{h} + U\dot{\alpha} - ba\ddot{\alpha}\right] + 2\pi\rho U b l C(k)\left[\dot{h} + U\alpha + b\left(\tfrac{1}{2} - a\right)\dot{\alpha}\right] \tag{A-3}$$

$$\begin{aligned} M_y = {} & \pi\rho b^2 l\left[ba\ddot{h} - Ub\left(\tfrac{1}{2} - a\right)\dot{\alpha} - b^2\left(\tfrac{1}{8} + a^2\right)\ddot{\alpha}\right] \\ & + 2\pi\rho U b^2 l\left(a + \tfrac{1}{2}\right)C(k)\left[\dot{h} + U\alpha + b\left(\tfrac{1}{2} - a\right)\dot{\alpha}\right] \end{aligned} \tag{A-4}$$

C(k) terms in these equations are complex quantities.

These lift and moment expressions have both circulatory and noncirculatory parts. Here, the circulatory part is the terms in the second braces that cause the steady lift and moment, as *k* tends to zero. In these equations, the reduced frequency defined as

$$k = \frac{\omega b}{U} \tag{A-5}$$

is one of the most important nondimensional parameters. The function *C(k)* is called as the Theodorsen's function, which is complex itself, and is another important quantity. Its exact expression is given by [1]

$$C(k) = F(k) + iG(k) = \frac{H_1^{(2)}(k)}{H_1^{(2)}(k) + iH_0^{(2)}(k)} \tag{A-6}$$

where *H* is the Hänkel function. Hänkel function is a combination of Bessel functions of first and second kinds in the following manner

$$H_n^{(2)} = J_n - iY_n \tag{A-7}$$

F(k) and *G(k)* represent the real and imaginary parts of the Theodorsen's function, respectively. Usually, the flowing approximations for Theodorsen's function, *C(k),* are used [2] depending on the value of *k* as

$$C(k) = 1 - \frac{0.165}{1 - i\frac{0.0455}{k}} - \frac{0.335}{1 - i\frac{0.3}{k}} \quad \text{for} \quad k < 0.5 \tag{A-8}$$

$$C(k) = 1 - \frac{0.165}{1 - i\frac{0.041}{k}} - \frac{0.335}{1 - i\frac{0.32}{k}} \quad \text{for} \quad k \geq 0.5 \tag{A-9}$$

The aerodynamic matrix of a typical section for harmonic motion in incompressible flow can be constructed in the following manner. The harmonic motion assumption implies that

$$q = \bar{q} e^{i\omega t} \ , \tag{A-10}$$

where

$$\bar{q} = \begin{Bmatrix} \bar{h}/b \\ \bar{\alpha} \end{Bmatrix}. \tag{A-11}$$

The linear aerodynamic model permits to represent the aerodynamic force vector as a multiplication of the complex displacement vector by the aerodynamic matrix as

$$\{\bar{a}\} = \begin{Bmatrix} -\bar{L} \\ \bar{M}_y \end{Bmatrix} = [A]\{\bar{q}\} \tag{A-12}$$

Since the lift and moment equations involve first and second derivatives in addition to the displacements, the aerodynamic matrix can be written as the summation of the virtual mass, damping and stiffness matrices as follows.

$$[A] = -\omega^2 [A_M] + i\omega [A_C] + [A_K] \tag{A-13}$$

$$[A_M] = \pi \rho b^3 l \begin{bmatrix} -1 & a \\ ba & -b\left(\frac{1}{8} + a^2\right) \end{bmatrix} \tag{A-14}$$

$$[A_C] = \pi \rho U b^2 l \begin{bmatrix} -2C(k) & -1 - 2\left(\frac{1}{2} - a\right)C(k) \\ 2b\left(a + \frac{1}{2}\right)C(k) & b\left(\frac{1}{2} - a\right)\left(-1 + 2\left(a + \frac{1}{2}\right)C(k)\right) \end{bmatrix} \tag{A-15}$$

$$[A_K] = 2\pi\rho U^2 blC(k)\begin{bmatrix} 0 & -1 \\ 0 & b\left(a+\frac{1}{2}\right) \end{bmatrix} \tag{A-16}$$

These frequency domain expressions can be used to derive the analytical frequency response function of the aeroelastic system much faster than time domain simulations.

A 4 Arbitrary Motion

The simulation in the time domain requires that the lift and moment expressions should be known at each integration instant. However, the circulatory part of the harmonic lift and moment contains the frequency information, *k*. The term in the circulatory part of the harmonic lift and moment equations, which can be written as

$$w_{\frac{3}{4}c}(t) = -\left[\dot{h} + U\alpha + b\left(\frac{1}{2} - a\right)\dot{\alpha}\right] \tag{A-17}$$

is the instantaneous vertical velocity of the fluid particle in contact with the three-quarter-chord point of the airfoil. Both the circulatory lift and moment can be expressed in terms of this quantity. The time domain expressions can be obtained by using inverse Fourier transform of the harmonic lift and moment expressions. To handle the integrals within the inverse Fourier transformation, Wagner defined a problem of the step change in angle of attack [1]

$$w_{\frac{3}{4}c} = \begin{cases} 0, & t < 0, \\ -U\alpha_{0,} & t > 0. \end{cases} \tag{A-18}$$

and calculated lift as

$$L = \pi\rho U^2 bl\alpha_0\phi(s) \tag{A-19}$$

where

$$s = \frac{Ut}{b} \tag{A-20}$$

is the distance in semichords traveled by the airfoil after the sudden step. It is in fact a nondimensional time quantity used to simplify the expressions. Equation A-19 gives the time history of the lift when the airfoil is subjected to a sudden change in angle of attack. The function, $\phi(s)$, is called as the Wagner function. Wagner computed $\phi(s)$ to be

$$\phi(s) = \frac{2}{\pi}\int_0^\infty \frac{F(k)}{k}\sin(ks)dk = 1 + \frac{2}{\pi}\int_0^\infty \frac{G(k)}{k}\cos(ks)dk\,. \tag{A-21}$$

Although $\phi(s)$ has a simple form, it is not expressible in terms of simple functions. Therefore, some approximations for $\phi(s)$ are often used. There are two kinds of approximations for the Wagner's function as follows [2].

$$\phi(s) \cong 1 - 0.165e^{-0.0455s} - 0.335e^{-0.3s} \tag{A-22}$$

$$\phi(s) \cong \frac{s+2}{s+4} \tag{A-23}$$

Since the expression given by Equation A-22 has a simple Laplace transform, it is useful in solving the equations whereas the latter shows better asymptotic behavior.

Wagner's function expresses the history of aerodynamic lift due to a sudden change of angle of attack; but it can also be used to calculate the lift due to arbitrary motions of the airfoil. Instead of calculating the Fourier integral, one can use the Wagner's function to calculate the circulatory lift and moment by the use of Duhamel or

superposition integral. Lift and moment for zero initial conditions are given by the following equations.

$$L = \pi\rho b^2 l\left[\ddot{h} + U\dot{\alpha} - ba\ddot{\alpha}\right] - 2\pi\rho U b l \int_0^s \frac{dw_{\frac{3}{4}c}(\sigma)}{d\sigma}\phi(s-\sigma)d\sigma \qquad \text{(A-24)}$$

$$M_y = \pi\rho b^2 l\left[ba\ddot{h} - Ub\left(\tfrac{1}{2} - a\right)\dot{\alpha} - b^2\left(\tfrac{1}{8} + a^2\right)\ddot{\alpha}\right] - 2\pi\rho U b^2 l\left(a + \tfrac{1}{2}\right)\int_0^s \frac{dw_{\frac{3}{4}c}(\sigma)}{d\sigma}\phi(s-\sigma)d\sigma \qquad \text{(A-25)}$$

These expressions are easier to handle since they are Laplace transformable due to the convolution form of the integral.

Appendix B

Simulink Model

The equations of motion (Equations 3-1 and 3-2) can be combined with the aerodynamic force expressions (Equations A-24 and A-25) to obtain the overall equations of motion of the aeroelastic system, (B-1 and B-2).

$$\begin{aligned} & m\ddot{h} + S_\alpha \ddot{\alpha} + K_h h + \pi\rho b^2 l\left[\ddot{h} + U\dot{\alpha} - ba\ddot{\alpha}\right] \\ & + 2\pi\rho U b l \int_0^s \frac{d\left[\dot{h} + U\alpha + b\left(\frac{1}{2} - a\right)\dot{\alpha}\right]}{d\sigma}\phi(s-\sigma)d\sigma = F^{ext} \end{aligned} \tag{B-1}$$

$$\begin{aligned} & S_\alpha \ddot{h} + I_\alpha \ddot{\alpha} + K_\alpha \alpha - \pi\rho b^2 l\left[ba\ddot{h} - Ub\left(\frac{1}{2} - a\right)\dot{\alpha} - b^2\left(\frac{1}{8} + a^2\right)\ddot{\alpha}\right] \\ & - 2\pi\rho U b^2 l\left(a + \frac{1}{2}\right)\int_0^s \frac{d\left[\dot{h} + U\alpha + b\left(\frac{1}{2} - a\right)\dot{\alpha}\right]}{d\sigma}\phi(s-\sigma)d\sigma = M^{ext} \end{aligned} \tag{B-2}$$

Since the damping in aeroelastic structures is very low and the aerodynamic damping is dominant, structural and viscous dampings are ignored in these equations. It is always safe to ignore the damping of structure during aeroelastic stability analysis.

The integrations in Equations B-1 and B-2 are written with respect to nondimensional time, *s*. Since Wagner's function is also function of *s*, it is convenient to convert all derivatives to those with respect to *s*. Expression of *s* is given in Equation A-20 and conversion of derivative from *t* to *s* are as follows.

$$\frac{d}{dt} = \frac{ds}{dt}\frac{d}{ds} = \left(\frac{U}{b}\right)\frac{d}{ds} \tag{B-3}$$

$$\frac{d^2}{dt^2} = \left(\frac{U}{b}\right)^2 \frac{d^2}{ds^2} \tag{B-4}$$

Replacing the first and second time derivatives with expressions given in Equations B-3 and B-4 respectively, one can obtain the equations of motion in *s* domain as

$$\begin{aligned} &\frac{mU^2}{b^2}h'' + \frac{S_\alpha U^2}{b^2}\alpha'' + K_h h + \pi\rho b^2 l\left[\frac{U^2}{b^2}h'' + \frac{U^2}{b}\alpha' - \frac{aU^2}{b}\alpha''\right] \\ &+ 2\pi\rho U b l\int_0^s \left[\frac{U}{b}h'' + U\alpha' + \left(\tfrac{1}{2} - a\right)U\alpha''\right]\phi(s-\sigma)d\sigma = F^{ext} \end{aligned} \tag{B-5}$$

$$\begin{aligned} &\frac{S_\alpha U^2}{b^2}h'' + \frac{I_\alpha U^2}{b^2}\alpha'' + K_\alpha \alpha - \pi\rho b^2 l\left[\frac{aU^2}{b}h'' - U^2\left(\tfrac{1}{2} - a\right)\alpha' - \left(\tfrac{1}{8} + a^2\right)U^2\alpha''\right] \\ &- 2\pi\rho U b^2 l\left(a + \tfrac{1}{2}\right)\int_0^s \left[\frac{U}{b}h'' + U\alpha' + \left(\tfrac{1}{2} - a\right)U\alpha''\right]\phi(s-\sigma)d\sigma = M^{ext} \end{aligned} \tag{B-6}$$

Taking the Laplace transform of Equations B-5 and B-6 with respect to *s* using the Laplace variable, *p* and using *q* for dynamic pressure and *S* for wing area, one can obtain the following final forms of equations to construct the transfer function matrix.

$$\begin{aligned} &\pi qS\left\{\left[\frac{mU^2}{b\pi qS} + 1 + 2\tilde{\phi}(p)\right]p^2 + \frac{bK_h}{\pi qS}\right\}\frac{\tilde{h}}{b} \\ &+ \pi qS\left\{\left[\frac{S_\alpha U^2}{b^2\pi qS} - a + (1-2a)\tilde{\phi}(p)\right]p^2 + \left[1 + 2\tilde{\phi}(p)\right]p\right\}\tilde{\alpha} = F^{ext} \end{aligned} \tag{B-7}$$

$$\pi qSb\left\{\left[\frac{S_\alpha U^2}{b\pi qS}-a-(1+2a)\tilde{\phi}(p)\right]p^2\right\}\frac{\tilde{h}}{b}$$
$$+\pi qSb\left\{\left[\frac{I_\alpha U^2}{b^2\pi qS}+\left(\tfrac{1}{8}+a^2\right)-\left(\tfrac{1}{2}-2a^2\right)\tilde{\phi}(p)\right]p^2+\left[\left(\tfrac{1}{2}-a\right)-(1+2a)\tilde{\phi}(p)\right]p+K_\alpha\right\}\tilde{\alpha}=M^{ext} \tag{B-8}$$

The expression for Wagner's function, $\phi(s)$, is given in Equation A-22. Its Laplace transform is.

$$\tilde{\phi}(p)=\frac{0.5p^2+0.281p+0.01365}{p(p+0.3)(p+0.0455)} \tag{B-9}$$

The form of Equations B-7 and B-8 is chosen such that the coefficients of *p* and its polynomials are nondimensional. Definitions of these nondimensional parameters are as follows.

- Mass ratio (density ratio):

$$\mu=\frac{2m}{\pi\rho bS} \tag{B-10}$$

- Ratio of uncoupled natural frequencies:

$$\Omega=\frac{\omega_h}{\omega_\alpha} \tag{B-11}$$

where

$$\omega_\alpha=\sqrt{\frac{K_\alpha}{I_\alpha}} \tag{B-12}$$

$$\omega_h=\sqrt{\frac{K_h}{m}} \tag{B-13}$$

- Reduced rotational natural frequency:

$$k_\alpha = \frac{\omega_\alpha b}{U} \tag{B-14}$$

- Dimensionless static unbalance:

$$x_\alpha = \frac{S_\alpha}{mb} \tag{B-15}$$

- Radius of gyration of typical section about elastic axis in semichords:

$$r_\alpha = \sqrt{\frac{I_\alpha}{mb^2}} \tag{B-16}$$

When these nondimensional parameters are substituted into Equations B-7 and B-8, one can construct the transfer function matrix, [*G*] in compact form as follows.

$$[H(p)]\begin{Bmatrix} \tilde{h}/b \\ \tilde{\alpha} \end{Bmatrix} = \begin{Bmatrix} F^{ext} \\ M^{ext} \end{Bmatrix} \tag{B-17}$$

$$\begin{Bmatrix} \tilde{h}/b \\ \tilde{\alpha} \end{Bmatrix} = [G(p)]\begin{Bmatrix} F^{ext} \\ M^{ext} \end{Bmatrix} \tag{B-18}$$

$$[G(p)] = \begin{bmatrix} G_{11}(p) & G_{12}(p) \\ G_{21}(p) & G_{22}(p) \end{bmatrix} = [H(p)]^{-1} \tag{B-19}$$

where

$$H_{11} = \pi q S\left\{\left[\mu + 1 + 2\tilde{\phi}(p)\right]p^2 + \mu k_\alpha^2 \Omega^2\right\} \tag{B-20}$$

$$H_{12} = \pi qS\left\{\left[\mu x_\alpha - a + (1-2a)\tilde{\phi}(p)\right]p^2 + \left[1 + 2\tilde{\phi}(p)\right]p\right\} \tag{B-21}$$

$$H_{21} = \pi qSb\left\{\left[\mu x_\alpha - a - (1+2a)\tilde{\phi}(p)\right]p^2\right\} \tag{B-22}$$

$$H_{22} = \pi qSb\left\{\left[\mu r_\alpha^2 + \left(\tfrac{1}{8} + a^2\right) - \left(\tfrac{1}{2} - 2a^2\right)\tilde{\phi}(p)\right]p^2 + \left[\left(\tfrac{1}{2} - a\right) - (1+2a)\tilde{\phi}(p)\right]p + \mu r_\alpha^2 k_\alpha^2\right\} \tag{B-23}$$

Once the transfer function of the system is found at a particular flow speed, one can solve the response of the system for any external excitation with a model such as the Simulink model given in Figure 153.

The coefficients of transfer functions are calculated symbolically and expressed in terms of flight and nondimensional airfoil parameters. A Matlab code is prepared for this purpose.

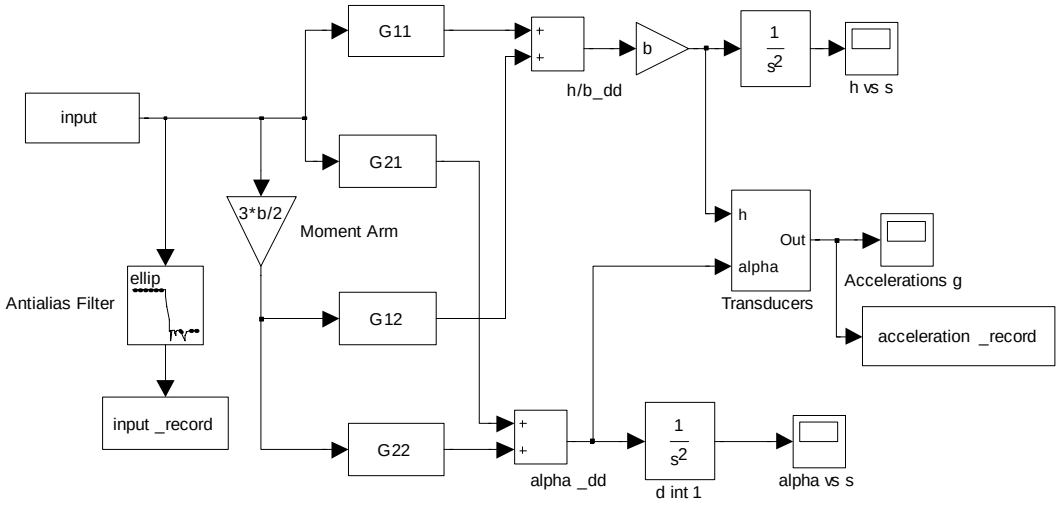

Figure 153. Simulink model for a two DOF aeroelastic system.

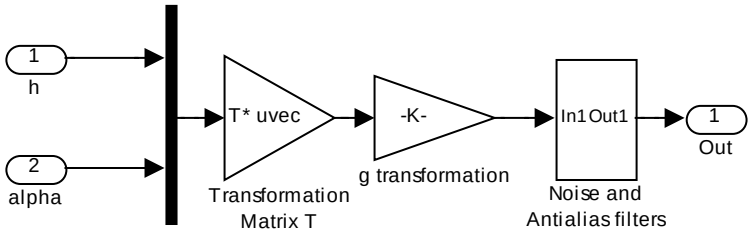

Figure 154. Detail of the "Transducers" Simulink sub-block.

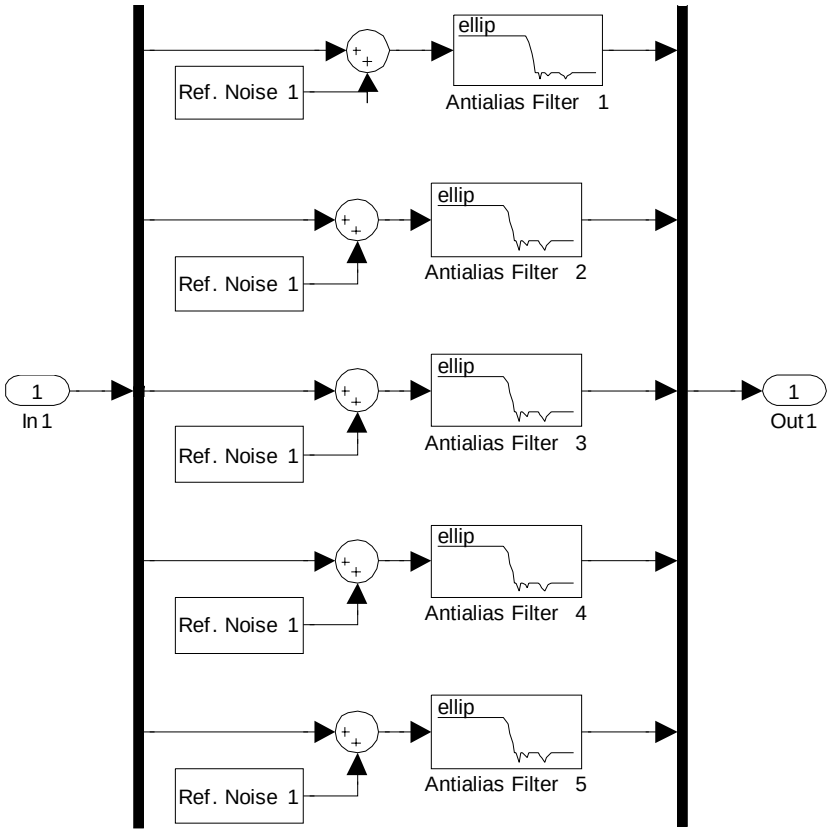

Figure 155. Detail of the "Noise and Antialias Filter" Simulink sub-block.

Although the system is a two DOF system, the order of the resulting aeroelastic system is seven. The extra three states are the aerodynamic states, which represent the approximated Wagner's function. Higher order aerodynamic approximations will result in higher order differential equations.

The “Transducers” block converts the physical displacements of the airfoil into the acceleration of several points including the estimated noise. Note that the solutions are in nondimensional time, *s*, domain. So the noise to be added should also be converted into *s* domain before polluting the acceleration data. Noise data is generated according to MIL-STD-810F.

The sampling frequency should be calculated in terms of reduced frequency. Since the frequency range of interest is up to 60 Hz, sampling frequency is chosen as 600 Hz. In order to filter the noise and to avoid antialiasing, an 11^{th} order analog elliptic filter with 300 Hz pass-band is placed on each signal with 110dB stop-band attenuation. Such specifications are common in data acquisition systems. The forcing and measurement data are saved for further processing.

CURRICULUM VITAE

PERSONAL INFORMATION

Surname, Name: Yıldız, Erdinç Nuri
Nationality: Turkish (TC)
Date and Place of Birth: 23 August 1974, Adana
Marital Status: Single
Phone: +90 312 255 85 80
Fax: +90 312 590 91 48
email: erdincnuriyildiz@yahoo.com

EDUCATION

Degree	Institution	Year of Graduation
MS	METU Mechanical Engineering	2000
BS	METU Mechanical Engineering	1997
High School	Ayas Koleji, Adana	1993

WORK EXPERIENCE

Year	Place	Enrollment
1997- Present	TÜBİTAK-SAGE	Chief Researcher
1996 August	TEMSA, Adana	Intern Engineering Student
1995 August	STFA Cıvata, Adana	Intern Engineering Student

FOREIGN LANGUAGES

Fluent English

PUBLICATIONS

1. Yıldız, E.N., Cömert, M.D., Platin, B.E., Uçuş Testlerinde Çırpıntı Hızının Kestirilmesinde Kullanılabilecek Bazı Yöntemlerin Karşılaştırılması, SAVTEK 2006, 29-30 Haziran, Ankara.

HOBBIES

Playing Bass Guitar, Computer Technologies, Programming.